A study of atmospheric oxidation chemistry in Australasia using MAX-DOAS measurements

Robert George Ryan

ORCID: 0000-0002-0806-4880

March 2020

Submitted in fulfilment of the requirements for the degree of Doctor of Philosophy (Science)

in the School of Earth Sciences,

The University of Melbourne

Abstract

Oxidation reactions provide the fundamental mechanism for chemical cycling of atmospheric constituents. Understanding the key chemical and meteorological factors determining atmospheric oxidation chemistry has important implications for air pollution and climate change. With strong but isolated urban pollution sources and endemic plants known to emit high levels of volatile organic compounds (VOCs), Australasia is a fascinating place to study atmospheric oxidation chemistry in a range of remote, coastal and urban environments. To date however, Australia is vastly underrepresented in the observational atmospheric chemistry literature.

In this thesis, the passive solar multi-axis differential optical absorption spectroscopic (MAX-DOAS) technique is used to study key molecules in the atmospheric oxidation cycle including nitrogen dioxide (NO_2), formaldehyde (HCHO), nitrous acid (HONO), glyoxal (CHOCHO) and iodine monoxide (IO). In particular, the role of these molecules in forming hydroxyl radicals (OH) and ozone (O_3), two key daytime tropospheric oxidants, is studied using urban measurements at Broadmeadows, Victoria and at Garden Island in Western Australia. In the first comprehensive study demonstrating the MAX-DOAS technique in Australasia, the technique is verified using a range of analysis sensitivity studies, inter-instrument comparison and validation against in-situ and remote sensing methods. This includes the first long term MAX-DOAS-satellite comparison in the Southern Hemisphere, where MAX-DOAS measurements were in excellent agreement with Tropospheric Monitoring Instrument (TROPOMI) results in Melbourne, Australia and at Lauder in New Zealand.

The HONO observed at Broadmeadows was consistently at daytime concentrations exceeding what is expected given the known mechanisms. The maximum daytime HONO levels correlated with soil moisture levels indicating that soil-based emissions may play a role in the missing HONO source. The exponential dependence on temperature observed for HCHO at Broadmeadows suggests that the primary formaldehyde source there is oxidation of biogenic VOCs. In contrast, glyoxal appears to be more dependent on biomass burning or anthropogenic emissions. Chemical trajectory modelling studies at Garden Island suggest that isoprene oxidation is expected to be the dominant HCHO source, while anthropogenic emissions are expected to be the dominant CHOCHO source.

At Broadmeadows, HONO photolysis was found to be the greatest boundary-layer OH source in all months, contributing on average between 45-50 % of OH production. HCHO and ozone (O_3) were often present at sufficient levels in summer to be commensurate with HONO as surface OH producers. The vertical profiling capability of the MAX-DOAS technique showed that while HONO typically dominated the OH production close to the surface, ozone and formaldehyde photolysis were the dominant mechanisms at higher altitudes. At Garden Island, a background marine boundary layer level of IO was detected which did not appear to have a locally significant O_3-destruction or OH-formation role, but nevertheless provide evidence of ubiquitous iodine chemistry in the marine boundary layer. Using the ratio of HCHO to NO_2, significant VOC emissions on hot summer days (as indicated by high observed HCHO levels), were found to shift the ozone production regime from VOC-limited to NO_x-limited. The ozone production regime was found to be mostly NO_x-limited at Garden Island. This has important implications for air pollution, for while NO_2 was not found in exceedance of guideline pollution levels, O_3 smog could still be reduced on hot days by curbing nitrogen oxide emissions.

Declaration

I, Robert Ryan, declare that this thesis, submitted in fulfilment of the requirements for the conferral of the degree Doctor of Philosophy (Science) from the University of Melbourne, is wholly my own work unless otherwise referenced or acknowledged.

This document has not been submitted for qualifications at any other academic institution.

17th of March, 2020.

Preface

This thesis is submitted as a collection of chapters, the chapters not being otherwise submitted for peer-reviewed publication.

One peer-reviewed article was published during this PhD project, namely "Daytime HONO, NO_2 and aerosol distributions from MAX-DOAS observations in Melbourne", Ryan et al. (2018).

This paper was written after four months of analysis of the Broadmeadows campaign dataset decribed initially in chapter 4 and comprehensively discussed in chapter 5. Chapter 5 discusses two and a half years of HONO and other results from Broadmeadows. To illustrate potential HONO sources and implications, the discussion and figures from the four month period in Ryan et al. (2018) have been adapted for this thesis and appear in sections 5.3.4 and 5.3.5. In addition, the DOAS sensitivity tests in section 2.4.1 and the profile retrieval sensitivity tests in section 3.4, applicable to all the work in this thesis, were published in Ryan et al. (2018).

All instances of ideas and figures adapted from Ryan et al. (2018) have been clearly referenced throughout this thesis.

Acknowledgments

Lonely and isolating as PhDs often necessarily are, I have been blessed to share this four year journey with many wonderful people. There have been travels, adventures, tears and thrills with these people; the greatest learning throughout my PhD has been stemmed from their conversations rather than from any book or paper. I view the extensive nature of these friendships and collaborations as the greatest success of my project.

Firstly, thank you to my primary supervisor Robyn Schofield for having faith in me to pursue an atmospheric science project. Thanks for giving me enough scope to explore this project thoroughly, and the guidance to help me finish it. Thank you to my chief mentor Peter Rayner for all your wisdom and words of encouragement.

I wish to thank the members of the Rayner-Schofield group for looking after me for the last four years. Thanks to Jeremy Silver for being so patient, generous with your time and programming expertise and in particular for assistance with accessing satellite data. Thanks to Steve Utembe for being so helpful in all matters related to atmospheric chemistry modelling and in particular for making your WRF simulations available. I have loved sharing the journey with my fellow students in the Rayner-Schofield group; Alex, Sonya, Yohanna, Nasimeh, Mahesh, Sushma, Imogen, Adit and others in the wider Earth Sciences community too numerous to name.

Thank you to Stephen Wilson and Nicholas Jones at the University of Wollongong for being so generous with your time and advice. I greatly enjoyed working with you both.

I also wish to thank my Masters supervisors, David Simpson and Paul Mulvaney whose early support has been fundamental to my scientific journey.

The MAX-DOAS data used in this thesis comes from several sources. Thank you to Matt Tully and Steve Rhodes for your willingness to share Bureau of Meteorology data with me, I think it has been a wonderfully fruitful collaboration. Thank you Richard Querel for hosting me at Lauder, for being so quick to respond to every question, and for your willingness to contribute NIWA data to this project. Thank you to Stephen Hoefs and the Defence Science and Technology Group for funding and hosting the AIRBOX campaign at Garden Island and for making the campaign data available for this thesis.

Thanks to Blair Trewin for providing meteorological data. Thanks Robyn for your phenomenal efforts on the AIRBOX project which have allowed me and so many others to collect amazing data and have some wonderful fieldwork experiences. I'd also like to acknowledge the hard work and good memories shared with many several fieldwork collaborators, especially Ruhi Humphries, Joel Alroe, Luke Cravigan, James Harnwell, Travis Naylor and Michal Strzelec.

I wish to acknowledge the traditional owners of the land on which this work took place, both in Australia and New Zealand. In submitting a written body of scientific work relating to Australia it is humbling to consider the unwritten spiritual and scientific knowledge gathered by the Indigenous people of this land over some 60,000+ years.

Thank you to Udo Frieß for hosting me in Heidelberg twice, and for your ongoing support and friendship. Thanks also to Johannes Lampel and Denis Pöhler at IUP Heidelberg for your invaluable technical MAX-DOAS support. Thank you to Rob Mackenzie and Jian Zhong for your help with the CiTTyCAT model and for hosting me in Birmingham.

Thank you to all my family and close friends for the constant support and love, even when you asked how the PhD was going and I wished you hadn't! Thanks for letting me vent to you about chemistry, coding and all things PhD. Special thanks to Anton, Jacob, Abi and John, Clayton, Pete and to Tanja from afar, for your valued friendship. An enormous thank you to Rudy - mate, it's been a pleasure living with you and sharing the science journey together over the last nine years.

Thank you to Maddy for your incredible love and support, strong and constant over the last three years. I can't wait to see how the next chapter unfolds!

Second last, and not entirely tongue-in-cheek, I'd like to thank myself for sticking at it. Only Mum and Dad and I know the depths of the challenges faced to get to this point; 27 years old, healthy, happy and at the end of the formal education road. Still just feeling like a kid from the bush, I'm proud of where I've come from, where I've made it to and the opportunities that await.

Finally, this thesis is primarily dedicated to Anne and George, my parents. You are my bedrock of love, faith, strength and humility; my inspiration, scientific and otherwise. The mutual pride for the three of us in this completed PhD means the world to me. The thesis is additionally dedicated to Ern and Lesley, my Grandparents, because they first sparked my passion for chemistry and Australian nature which are the underlying themes of this work. I dearly wish Granddad could have read this thesis, the fruit of that passion.

Rob,

Melbourne,

17th of March, 2020.

Contents

Abstract **1**

Declaration **3**

Preface **4**

Acknowledgments **5**

1 Australasian atmospheric chemistry – an introduction **25**
1.1 Opening remarks . . . 25
1.2 Structure of the atmosphere . . . 26
1.2.1 Vertical structure . . . 26
1.2.2 Atmospheric circulation . . . 28
1.3 Atmospheric composition . . . 30
1.3.1 Aerosols . . . 30
1.3.2 Tropospheric oxidative capacity . . . 31
1.3.3 Measuring and inferring oxidative capacity . . . 33
1.4 Tropospheric chemistry . . . 34
1.4.1 Nitrogen oxides . . . 34
1.4.2 Nitrous acid . . . 35
1.4.3 Oxidised VOCs: formaldehyde and glyoxal . . . 36
1.4.4 Tropospheric ozone production regimes . . . 39
1.4.5 Reactive halogen species . . . 41
1.5 Research motivation . . . 41
1.5.1 Australasian context . . . 42
1.6 Research aims . . . 46

2 Collection and analysis of MAX-DOAS spectra **47**
2.1 Background: atmospheric radiation and spectroscopy . . . 47
2.1.1 Radiative transfer . . . 47
2.1.2 Differential optical absorption spectroscopy . . . 50
2.2 MAX-DOAS instrumentation . . . 55
2.3 Measurement and calibration: general settings . . . 56

2.3.1 DOAS tests: polynomial, offset, shift fit . . . 57
2.3.2 DOAS tests: Wavelength calibration windows . . . 58
2.4 Specific DOAS analysis settings . . . 60
2.4.1 UV range . . . 61
2.4.2 Visible range . . . 63
2.5 Summary of DOAS methods chapter . . . 72

3 Vertical column and profile retrieval 74
3.1 Profile retrieval methodology . . . 74
3.1.1 VCD geometric approximation . . . 74
3.1.2 Profile retrieval by inverse modelling . . . 75
3.2 General profile retrieval settings . . . 78
3.3 Assessing the retrieval quality . . . 83
3.4 A priori sensitivity tests . . . 87
3.5 Cloud filtering . . . 90
3.5.1 Cloud filtering theory . . . 90
3.5.2 Approach to cloud filtering . . . 91
3.5.3 Potential drawbacks to cloud filtering . . . 94
3.6 Profile retrieval methods: summary . . . 94

4 Intercomparison of MAX-DOAS measurements 97
4.1 TIMTAM DOAS fitting results . . . 99
4.2 Pointing accuracy comparison . . . 101
4.3 Slant column comparison . . . 103
4.4 Vertical column and profile comparison . . . 106
4.5 TIMTAM summary . . . 107

5 Urban MAX-DOAS measurements: Broadmeadows 2016-2019 109
5.1 Slant column results at Broadmeadows . . . 111
5.2 Aerosols in the urban environment . . . 113
5.3 Nitrogen oxides in the urban environment . . . 117
5.3.1 NO_2 timeseries 2016-19 . . . 117
5.3.2 Validation of NO_2 results . . . 123
5.3.3 HONO timeseries 2016-19 . . . 124
5.3.4 Discussion of potential HONO sources . . . 127
5.3.5 HONO as an OH source in Melbourne . . . 128
5.4 Formaldehyde and glyoxal at the urban-rural interface . . . 130
5.4.1 Overview of HCHO measurements 2016-2019 . . . 130
5.4.2 Overview of glyoxal results 2016-2019 . . . 134
5.4.3 Discussion of potential VOC sources . . . 138
5.4.4 Importance of HCHO in oxidation chemistry . . . 148
5.5 Broadmeadows results: summary . . . 161

6 Coastal case study: Garden Island campaign **163**
6.1 Complimentary measurements . . . 165
6.1.1 Meteorology during the campaign . . . 165
6.1.2 In-situ chemistry measurements . . . 165
6.2 MAX-DOAS measurements . . . 166
6.2.1 Differential slant columns . . . 166
6.2.2 Aerosol retrieval results . . . 170
6.2.3 NO_2 at Garden Island . . . 173
6.2.4 HCHO . . . 176
6.2.5 Iodine monoxide . . . 177
6.3 Lagrangian chemistry-trajectory modelling . . . 179
6.3.1 Introduction to CiTTyCAT . . . 179
6.3.2 WRF-Chem modelling . . . 179
6.3.3 HYSPLIT back trajectories . . . 180
6.3.4 Comparison between observations and CiTTyCAT . . . 181
6.3.5 Sensitivity studies in CiTTyCAT . . . 183
6.4 Discussion . . . 185
6.4.1 Importance of isoprene in oxidation chemistry . . . 185
6.4.2 Modelled OH production . . . 188
6.4.3 Iodine chemistry and OH . . . 188
6.4.4 A note on glyoxal . . . 189
6.5 Garden Island summary and future work . . . 190

7 Comparison and validation of formaldehyde columns **192**
7.1 Outline of measurements at Lauder . . . 193
7.1.1 Formaldehyde measurements at Lauder . . . 194
7.2 HCHO comparisons . . . 200
7.2.1 MAX-DOAS vs FTIR at Lauder . . . 200
7.2.2 MAX-DOAS vs Satellite . . . 202
7.3 HCHO validation: summary and future work . . . 208

8 Conclusion **211**

A Relating to methodology and TIMTAM chapters **215**

B Relating to Broadmeadows data analysis **218**

C Relating to Garden Island campaign **227**

List of Figures

1.1 (a) The physical vertical structure of the atmosphere, showing temperature variation throughout. (b) Vertical mixing ratio profiles of some key atmospheric gases. For example, the dominant presence of ozone in the stratosphere and water in the troposphere is evident. Figure adapted from Liou (2002). 27

1.2 Schematic diagram of the atmosphere's general circulation patterns. Figure adapted from the Australian Bureau of Meteorology website. 28

1.3 Schematic diagram of the position of the subtropical ridge, and associated broad-scale weather patterns, over Australia in summer and winter. Figure adapted from the Australian Bureau of Meteorology website. . . 29

1.4 Simplified isoprene oxidation scheme showing the major products from reaction of isoprene with OH and O_2 and secondary oxidation by HO_2 and NO radicals. Acronyms relating to highlighted molecules are explained in the text. 38

1.5 Structure of some common monoterpenes 39

1.6 Ozone mixing ratios (ppb) as a function of VOC and NO_x emission rates, showing hydrocarbon limited (right of the thick black line) and NO_x limited (left of the line) O_3 production conditions. Figure adapted from Sillman (1990) and Jacob (1999). 40

1.7 Schematic representation of the emission sources for components of the tropospheric oxidative cycle in Australia. Australia's vast marine and remote bush ecosystems provide large biogenic VOC (BVOC) sources, while the major anthropogenic VOC is agriculturally-produced methane (CH_4). Particulates and combustion products such as NO_x and carbon monoxide (CO) are natural products of bushfire in Australia, but also have anthropogenic origins in industry and transport. 43

1.8 Global distribution of formaldehyde produced from isoprene oxidation, modelled using Modis-L. This illustrates the importance of VOC oxidative chemistry in Australia. Figure from Pfister et al (2008). 44

2.1 Polar plot showing the Rayleigh scattering phase function (red dashed line), Mie scattering phase function (solid blue line, parameterised by the Henyey-Greenstein equation) and the rotational Raman scattering phase function (green dotted line). The direction of the incident light is indicated by the yellow arrow and the scattering event is at the origin. 49
2.2 Schematic showing the DOAS technique. An absorption spectrum, in intensity (I) or optical density (σ) can be separated into broadband (I'$_0$ and σ') and narrowband (D' and σ_b) components. Image adapted from Platt and Stutz (2008). 51
2.3 Absorption cross sections of molecules commonly measured using the DOAS technique. 53
2.4 Simple MAX-DOAS geometry showing the elevation angle (α) and solar zenith angle (θ) relative to the detector and the sun, respectively. Observations at low elevation angle provide long path lengths through the planetary boundary layer (PBL) while having the same path through the stratosphere. 55
2.5 Example spectra from the University of Melbourne MAX-DOAS UV and visible spectrometers. 56
2.6 Results of general QDOAS settings tests (detailed in table 2.2) for Bureau of Meteorology data, 16/02/2017: (a) Bar chart showing the magnitude of the change in residual RMS, O_4 dSCD and NO_2 dSCD for each test, relative to the standard settings. (b) Timeseries of residual RMS for each test, for the sample period on 16/02/2017. (c) Same as (b) but for O_4 dSCDs. 58
2.7 Results of QDOAS tests with different numbers of wavelength calibration bins: (a) Magnitude of the wavelength shift as a function of wavelength, for each test set. (b) Residual RMS of the DOAS fit analysis (338-370 nm) for each test set. 59
2.8 Example fits in the UV region from QDOAS, data taken from midday on 16/02/2017 using the Bureau of Meteorology MAX-DOAS at Broadmeadows. "BM" indicates the results are from the Bureau of Meteorology MAX-DOAS. "o3s" and "o3t" indicate ozone at representative stratospheric (220 K) and tropospheric (298 K) temperatures respectively. The solar zenith angle was 20.7° and the elevation angle was 3°. 61
2.9 Results of sensitivity tests to determine the appropriate fitting range for formaldehyde, using data from 04/03/2017 at Broadmeadows using the Bureau of Meteorology MAX-DOAS. All results are from the 3° elevation angle. 62
2.10 Results of sensitivity study to determine the appropriate wavelength range for fitting HONO. (b) Cross sections plotted in the HONO sensitivity study range showing overlap of cross section peaks. 63

2.11 Overlayed cross sections in the wavelength range 415-465 nm which includes the absorption bands of IO and glyoxal. 65
2.12 Results of the sensitivity studies for iodine monoxide using results from 19/04/2018 at Garden Island. The results are top: diurnal magnitude of the IO dSCD, middle: magnitude of residual RMS and bottom: IO fitting error as a percentage of the IO dSCD. (a) shows results for various fitting wavelength ranges, and (b) shows results for DOAS settings and cross section tests outlined in table 2.4. 66
2.13 (a) Results of DOAS fitting in the glyoxal range (435.5-465.5 nm) for an example day, 4/3/2017, at Broadmeadows. dSCDs for each elevation angle are plotted for NO_2 and CHOCHO, along with the residual RMS. (b) Results of DOAS tests in the 435.5-465.5 nm range, to determine the most appropriate settings for retrieval of glyoxal. For details on tests v1-v10 see table 2.4. Times are in UTC: 2 am UTC is midday local time. 69
2.14 Example spectral fits for CHOCHO, H_2O, O_4 and the Ring effect for selected DOAS glyoxal-range tests. For details on tests v1-v10 see table 2.4. Data taken from 4/3/2017 at Broadmeadows, solar zenith angle = 32° and elevation angle = 2°. 70
2.15 Results from DOAS tests using an 'instrumental cross section' in the glyoxal fitting range (435-456.5 nm). (a) Results timeseries from 4/3/2017 for (top) CHOCHO dSCD, (middle) fit error as a percentage of the dSCD and (bottom) magnitude of the residual RMS. Note that v2 refers here to standard settings with the inclusion of an instrumental cross section, not v2 as previously defined in this chapter. Times are in UTC, 2 am is midday local time. (b) Example spectral fits for CHOCHO, the instrumental cross section, H_2O, O_4 and the Ring effect. Data taken from 4/3/2017 at Broadmeadows, solar zenith angle = 32° and elevation angle = 2°. 71

3.1 Schematic diagram of the profile retrieval process. The central box indicates the core of the HEIPRO algorithm which operates on one set of differential slant columns at a time. 78
3.2 Aerosol retrieval sensitivity study for the 'fix weighting function' parameter in HEIPRO: left hand panels are retrieval results from the morning of 2/1/2018 at Lauder, NZ. Right hand panel is an example vertical profile comparison from 10:38 am local time. WF = 1 means weighting functions were recalculated, WF = 0 means they were not. Times are in local time. 80
3.3 Aerosol retrieval sensitivity study for the cross section correction (XSC) factor in HEIPRO: left hand panels are retrieval results from the morning of 2/1/2018 at Lauder, NZ. Right hand panel is an example vertical profile comparison from 10:38 am local time. 80

3.4 Aerosol retrieval sensitivity study for the cross section correction (XSC) factor in HEIPRO: left hand panels are retrieval results from the morning of 7/3/2017 at Broadmeadows, Australia. Right hand panel is an example vertical profile comparison from 12:38 pm local time. 81
3.5 Example aerosol retrievals showing (left to right) modelled ("retrieved") and observed ("measured") O_4 differential optical depths (dOD) with associated χ^2, retrieved profile with associated a priori profile and averaging kernels. (a) Example retrieval from Lauder dataset, 1 pm local time on 1/1/2018. (b) and (c) are example retrievals from the Broadmeadows dataset on 7/3/2017. 84
3.6 Example NO_2 (a-c) and HCHO (d-e) retrievals showing (left to right) modelled and measured dSCDs with associated χ^2, retrieved profile with associated a priori profile and averaging kernels. All example retrievals are from 7/3/2017 at Broadmeadows. 85
3.7 Scatterplots for formaldehyde, modelled vs measured values, for Jan-Apr 2018 (left) and Apr-Sep 2018 (right). The scatterplots are coloured by DoFs indicating the importance of the information content in assessing overall retrieval quality. 87
3.8 Results of a priori/forward model parameter tests for (a) an example aerosol extinction vertical profile (1 pm local time on 7/3/2017), left, and total aerosol optical depth over the course of the day on 7th March 2017, right; (b) an example vertical concentration profile of NO_2 and NO_2 vertical column density; (c) same as (b) but for HONO. Each colour represents the mean $\pm$ the standard deviation attributable to the particular test parameter as indicated by the legend. The ranges for each test are outlined in table 3.2. Figure adapted from Ryan et al. (2018). 89
3.9 Error attribution as a result of the a priori sensitivity studies. Bars represent the percentage of the variance explained by each sensitivity test for the retrieved vertical column amount (solid bars) and surface layer value (checked bars): (a) aerosols, (b) NO_2 and (c) HONO. 90
3.10 Example HEIPRO aerosol retrieval output from Broadmeadows at 9:55 am local time on 05/03/2017 (top row) which was a cloudy day, and 04/03/2017 (bottom row) which was a clear day. 91
3.11 (a) All daily colour index values from 1st to 12th March 2017 at Broadmeadows. (b) Histogram of normalised colour index (normalisation is with respect to the maximum CI in this case) indicating accumulation points in the CI frequency distribution. 92
3.12 Daily colour indices (CI) for a clear sky day in each month of the year 2017. Black lines indicate 5th order polynomial fits to the CI data as a function of adjusted solar zenith angle (see text for details), which are the basis of the empirical cloud filtering algorithm used in this work. . 95

3.13 Results of implementing the empirical cloud filtering algorithm in an example data period, from 2-18 March 2017. Flagged cloudy periods are indicated by compressed O_4 dSCDs (top) and colour index (CI, second from top). For CI, aerosol retrieval χ^2 and degrees of freedom for signal, as well as retrieved NO_2 vertical column density, blue indicates cloud flagged periods. 96

4.1 (a) Map of Melbourne showing the location of the Bureau of Meteorology site at Broadmeadows. The red arrow indicates the direction of measurement for the MAX-DOAS instruments involved in the TIMTAM campaign (south-south west, 220° relative to north). (b) Photo of the University of Melbourne Envimes 2D MAX-DOAS instrument at Broadmeadows (*Maps sourced from Google Maps, photo by R. Ryan*). 98
4.2 Example dSCD fits from QDOAS from 16/02/2017, solar zenith angle = 26, elevation angle = 5°, for (a) NZ, (b) UW, (c) UM and (d) BM. . . . 99
4.3 Timeseries of (a) O_4 and (b) NO_2 dSCDS, for each instrument and elevation angle, during the TIMTAM period 16/02/2017 to 22/02/2017. . 100
4.4 (a) Timeseries of the residual RMS, for each instrument and elevation angle, during the TIMTAM period 16/02/2017 to 22/02/2017. (b) Bar plot of residual RMS averages and standard deviations for each MAX-DOAS under representative clear (16th February) and cloudy (18th February) conditions. 101
4.5 Example horizon scans for each instrument, on 20th February. The left column shows horizon scans taken at 03:00 UTC (1 pm local time) while the right column shows horizon scans taken in the evening, 08:00 UTC (6 pm local time). 103
4.6 Scatter plots and linear regressions for observed horizon position (elevation angle) as a function of temperature. For the UM instrument telescope temperature is used, for the BM instrument ambient temperature is used in lieu of telescope temperature data. Note that the y-axis units are the same but the scales are different. 104
4.7 Scatter plots showing correlations between NZ measurements (x-axis) and BM, UW and UM respectively. All measurements are plotted for the period when all four instruments were running, 16-20 February 2017, with (a) showing O_4 dSCDs and (b) showing NO_2 dSCDs. 105
4.8 Timeseries results from the profile retrieval analysis, from 16-22 February for each instrument: (a) aerosol optical depth, (b) NO_2 vertical column density and (c) NO_2 volume mixing ratio in the lowest retrieval layer. . 107

5.1 Example dSCD results from DOAS analysis of Broadmeadows data in March 2017, for (top to bottom) O_4, NO_2, HONO, HCHO, CHOCHO and residual RMS. 111

5.2 (a) Timeseries of daily averaged aerosol optical depth (AOD, at 360 nm) at Broadmeadows from December 2016 to May 2019. Black points indicate raw data, gold points indicate AOD results after application of cloud filter. (b) Monthly averaged AOD over the measurement period (calculated from cloud filtered data). (c) Seasonally averaged diurnal cycle plots for AOD (calculated from cloud filtered data). Shading in (b) and (c) indicates the 95 % confidence interval 114
5.3 Monthly averaged aerosol vertical profiles at Broadmeadows for 2018. The top row shows unfiltered data, the bottom row shows cloud filtered data. 114
5.4 Polar bivariate plots of: (a) AOD at 360 nm, (b) NO_2 VMR in the lowest retrieval layer, (c) HCHO VMR in the lowest retrieval layer and (d) HONO VMR in the lowest retrieval layer, indicating the relationship between each variable and wind speed and direction. 117
5.5 (a) Timeseries of daily averaged NO_2 VCD at Broadmeadows from December 2016 to May 2019. (b) Monthly averages of NO_2 mixing ratio in the lowest retrieval layer. (c) Seasonally averaged diurnal cycle plots for NO_2 mixing ratio in the 0-200 m retrieval layer. Data in this figure is cloud filtered. 118
5.6 (a) Model/measurement comparison, (b) a priori and retrieved vertical profile and (c) averaging kernels from an example NO_2 retrieval at midday on 12/12/2017. (d) Daily NO_2 vertical profile evolution on 12/12/2017, typical of a day with high observed NO_2 at Broadmeadows. (e) Monthly averaged NO_2 vertical profiles showing annual variation in mean retrieved profiles throughout 2018. 122
5.7 Comparison of NO_2 measurements made by the MAX-DOAS at Broadmeadows (black) and average in-situ NO_2 from observations in the Melbourne metropolitan area (red). (a) Timeseries of results from December 2016 to January 2019, (b) scatterplots comparing the two datasets for each season and (c) average diurnal cycles for each dataset in each season. 124
5.8 (a) Timeseries of daily averaged HONO VCD at Broadmeadows from December 2016 to May 2019. (b) Monthly averages of HONO mixing ratio in the lowest retrieval layer. (c) Seasonally averaged diurnal cycle plots for HONO mixing ratio in the 0-200 m retrieval layer. Data in this figure is cloud filtered. 126
5.9 (a) Model/measurement comparison for one HONO vertical profile retrieval, (b) a priori and retrieved vertical profile and (c) averaging kernels from an example HONO retrieval at midday on 12/12/2017. (d) Daily HONO vertical profile evolution on 12/12/2017, typical of a day with high observed nitrous acid at Broadmeadows. (e) Monthly averaged HONO vertical profiles showing annual variation in mean retrieved profiles throughout 2018. 127

5.10 Figure adapted from Ryan et al. (2018). (a) Diurnal cycle of ground level OH radical production *P(OH)* from ozone (O_3 to $O(^1D)$) and HONO photolysis, calculated for an example day with 27 ppb surface ozone, and the HONO diurnal cycle from 7th March 2018 which peaked near midday at around 400 ppt. (b) Vertical profiles of tropospheric OH radical production from HONO photolysis, calculated using the average measured HONO vertical profile and from ozone photolysis calculated using colocated ozone sonde data averaged from January to April 2018. Points represent the mean, errorbars represent one standard deviation. (c) Measured average HONO diurnal cycle plotted with calculated photostationary state (PSS) HONO concentration and PSS including NO_2 ground conversion term (PSS inc. P_g). (d) $HONO_{unk.}$: unknown HONO production rate (measured - PSS), $HONO_D - HONO_W$: measured HONO emission rate attributable to soil processes (driest conditions - wettest conditions, see figure 5.11 and discussion in Section 3.5) and $Soil_{lit}$ representing PSS + literature HONO and NO soil emission rates. Lines represent means, shaded regions represent 95 % confidence intervals. . . 129
5.11 Figure adapted from Ryan et al. (2018). (a) HONO and (b) NO_2 diurnal cycles over the three month measurement period, divided into four soil water content (SWC) % bins. SWC data has been obtained from the Australian Water Resources Assessment Modelling System. 130
5.12 (a) Timeseries of daily averaged HCHO VCD at Broadmeadows from December 2016 to May 2019. (b) Monthly averages of HCHO mixing ratio in the lowest retrieval layer. (c) Seasonally averaged diurnal cycle plots for HCHO mixing ratio in the 0-200 m retrieval layer. Data in this figure is cloud filtered. 131
5.13 (a) Model/measurement comparison for one HCHO vertical profile retrieval, (b) a priori and retrieved vertical profile and (c) averaging kernels from an example HCHO retrieval at midday on 13/12/2017. (d) Daily HCHO vertical profile evolution on 13/12/2017, typical of a day with high observed formaldehyde at Broadmeadows. (e) Monthly averaged HCHO vertical profiles showing annual variation in mean retrieved profiles throughout 2018. 133
5.14 (a) Diurnal cycle plots for glyoxal vertical column density at Broadmeadows, broken up by season. (b) Polar bivariate plots showing the variation of glyoxal VCD with wind speed and direction, also plotted for each season. 135
5.15 Top row: example glyoxal retrievals for midday on 4/4/2017 at Broadmeadows, (a) modelled and measured CHOCHO dSCDs, (b) a priori and retrieved profiles, (c) averaging kernels. (d) Heatmap of vertical profiles across 4/4/2017, (e) heatmap of monthly averaged glyoxal vertical profiles for the year 2018. 136

5.16 Timeseries of (a) HCHO and CHOCHO monthly average VCD and (b) the glyoxal to formaldehyde ratio (R_{gf}) at Broadmeadows from December 2016 to May 2019. (c) Average diurnal cycle and (d) monthly averages of R_{gf} summarised. 137
5.17 Timeseries from an example period in summer 2018: (a) HCHO and CHOCHO daily average VCDs, (b)R_{fn} and (c) ambient air temperature. 138
5.18 Polar bivariate plots for each season at Broadmeadows, showing variation of glyoxal to formaldehyde ratio (R_{gf}) with wind speed and direction . 140
5.19 Comparison of timeseries for glyoxal (top), formaldehyde (middle) and AOD (bottom) monthly averages with the average number of fires per day in each month, recorded by the MODIS fire count algorithm. . . . 141
5.20 (a) Scatter plot showing HCHO VCD vs aerosol optical depth at Broadmeadows for 3-6 April 2017. (b) Same as (a) but for glyoxal VCD instead. (c) Same as (b) but only for the 3rd of April. (d) Maps showing fires recorded by the MODIS fire count algorithm for 3-4 April across Victoria. HYSPLIT trajectories, run 12 hours back from midday at Broadmeadows, have been superimposed over the top in blue. 143
5.21 Scatterplots showing correlation between HCHO VCD and AOD at 360 nm on some smoky days in Melbourne. (a)-(c) are are bushfire smoke days, (d)-(f) are industrial factory fire days. Raw results have been filtered for retrieval statistics (chi squared and DoFs) but not using the cloud filtering algorithm. 145
5.22 Summary of HCHO and temperature results. (a) Diurnal cycle of HCHO VMR and ambient air temperature at Broadmeadows, normalised to each other to allow comparison. (b) Monthly averages of air temperature and HCHO VMR at Broadmeadows, also normalised to each other for ease of comparison of the annual cycle. (c) Scatter plot of weekly averages of HCHO VMR and ambient temperature at Broadmeadows. 146
5.23 Seasonal scatterplots showing the relationship between VCD and surface VMR R_{fn}), i.e. HCHO VCD/NO_2 VCD vs HCHO VMR/NO_2 VMR at Broadmeadows. 150
5.24 Summary of results for the ratio of HCHO to NO_2 (R_{fn}): (a) Diurnal variation of R_{fn} shown by season. (b) Windroses (wind direction histograms) binned by four R_{fn} scenarios. 151
5.25 Scatterplots for HCHO vs NO_2 VCD daily averages, coloured by (a) the ambient air temperature and (b) average Melbourne EPA ozone mixing ratio. The solid lines indicates 1:1 (i.e. $R_{fn} = 1$), the dashed lines represent $R_{fn} = 2$ and $R_{fn} = 0.5$ respectively. 152
5.26 (a) Daily mean NO_2 mixing ratios (lowest MAX-DOAS retrieval layer) at Broadmeadows for each season, showing lower NO_2 on weekends than weekdays. (b) Daily mean O_3 mixing ratios (average of EPA sites across Melbourne metropolitan area) for each season. 153

5.27 Scatterplots showing MAX-DOAS HCHO VMR at Broadmeadows against Melbourne average EPA ozone concentration. Data is daily averages, divided up by season. 154
5.28 (a) Histogram of ozone mixing ratio (EPA average across Melbourne metropolitan area from December 2016-May 2019) when the temperature was over 30°C. (b) Same as (a) but for R_{fn} at Broadmeadows. (c) Timeseries showing the number of days with temperature exceeding 30°C in Melbourne. Data taken from ACORN-SAT long term temperature record for the city of Melbourne, through the Australian Bureau of Meteorology website. Red indicates the 1910-1998 mean and standard deviation, blue indicates the 1998-2018 average. 156
5.29 Top: timeseries showing production rate of HO_x (HO_2 + OH) for a case study period, 14-19 January 2018. pHO_x is plotted for HCHO, HONO and O_3. Middle: Ambient temperature and bottom: wind direction (blue, left y-axis) and speed (orange, right y-axis) over the same period. 157
5.30 Monthly average diurnal cycles of pHO_x from HONO, HCHO and O_3 at Broadmeadows. Top row is summer, second row autumn, third row winter and bottom row spring. 159
5.31 Example vertical profiles of pHO_x from HONO and HCHO at Broadmeadows, from 2 pm local time on the 17th (left) and 18th (right) of January 2018. Each plot is annotated with the corresponding vertically integrated pHO_x values for HONO and HCHO, which have units of $cm^{-2}s^{-1}$. 160

6.1 (a) Map showing the location of Perth and Garden Island in Western Australia. (b) Map zoomed in to the Perth region showing the location of AIRBOX (red star) on Garden Island, and proximate pollution sources Perth and Fremantle. (c) Picture of the AIRBOX mobile chemistry Laboratory at Garden Island. (d) Panoramic shot of the view west from AIRBOX out over the Indian Ocean, in the MAX-DOAS viewing direction. *Maps sourced from Google maps, photos by S. Fiddes.* 164
6.2 Timeseries of meteorological data (30 minute averages) from the automatic weather station at the Garden Island AIRBOX site. Top to bottom, variables are global radiation, air temperature, wind speed, wind direction, relative humidity and atmospheric pressure. 166
6.3 Windrose combining all wind speed and direction measurements throughout the Garden Island campaign. The radial axis represents frequency of counts (%) by wind direction. 167

6.4 Timeseries of differential slant column densities for selected elevation angles, from the Garden Island campaign: top to bottom O_4, NO_2, HCHO, CHOCHO and HONO. The black solid line indicates the detection limit calculated using the residual RMS, for the 0° elevation angle. 'UM' denotes that the University of Melbourne MAX-DOAS was used at Garden Island. . . . 168
6.5 Timeseries of halogen oxide differential slant column densities for selected elevation angles, from the Garden Island campaign: top to bottom IO, BrO, OClO. The black solid line indicates the detection limit calculated using the residual RMS, for the 0° elevation angle. 'UM' denotes that the University of Melbourne MAX-DOAS was used at Garden Island. . 169
6.6 Timeseries of vertical column densities, calculated using HEIPRO from MAX-DOAS dSCDS at Garden Island, for (a) aerosols (i.e. AOD), (b) NO_2, (c) HCHO and (d) IO. . . . 170
6.7 Example vertical profile heatmaps, output from HEIPRO MAX-DOAS retrievals at Garden Island, for (from top) aerosol extinction, NO_2 VMR, HCHO VMR, IO VMR. (a) results from 23rd April, a day with winds from the ocean sector, (b) 29th April, a day with winds from the land sector and (c) 4th May, a day with wind from the land sector bringing a large smoke plume over the measurement site. . . . 172
6.8 Three photos from the MAX-DOAS at Garden Island: (left) from 29th April, (b) from 1st May, (c) from 4th May. . . . 172
6.9 Polar bivariate plots of NO_2, HCHO and IO VMR retrieved from Garden Island MAX-DOAS data. Note that NO_2 and HCHO results are in ppb, while IO is in ppt. . . . 173
6.10 Scatterplots for NO_2 mixing ratio: (a) comparing NO_2 from UV and visible MAX-DOAS retrievals, (b) in-situ vs visible MAX-DOAS results and (c) in-situ vs UV MAX-DOAS results. (d) shows average diurnal cycles of NO_2 from in-situ, UV and visible MAX-DOAS retrievals. . . . 175
6.11 Scatterplots showing hourly averaged iodine monoxide mixing ratio vs (left) sea level at the Port of Fremantle and (right) in-situ ozone mixing ratio. . . . 178
6.12 Schematic of the CiTTyCAT model showing the key elements and loops. Figure adapted from Pugh et al. (2012). . . . 180
6.13 Two example trajectories, run 5 days back from Garden Island using the HYSPLIT model, initiated with meteorological data from the WRF model and used in turn for the CiTTyCAT modelling study. . . . 181
6.14 Timeseries comparison of Garden Island trace gas observations with CiTTyCAT (standard settings) output. In (a) the observations are in-situ ozone mixing ratio, (b) in-situ NO_2 and (c) MAX-DOAS lowest-layer retrieved formaldehyde mixing ratio. . . . 182

6.15 Bar charts showing results of CiTTyCAT sensitivity studies where the effect of each test is expressed as an average percentage difference to 'cc1', the standard model run scenario. Errorbars represent the standard deviation. Test details are outlined in table 6.1. (a) shows ozone, (b) HCHO, (c) NO_2 and (d) OH. 185
6.16 Bar charts showing results of CiTTyCAT sensitivity studies where the effect of each test is expressed as an average percentage difference to observations. Errorbars represent the standard deviation. Test details are outlined in table 6.1. (a) shows ozone, (b) HCHO, (c) NO_2 and (d) NO. 186
6.17 Timeseries of CiTTyCAT modelled mixing ratios along one example trajectory which arrived at Garden Island on 29th April (and is depicted in figure 6.13. (a) shows HCHO, (b) OH, (c) O_3 and (d) CH_4. In each case the plots show the results of sensitivity studies in which NO_x, anthropogenic VOC, isoprene and monoterpene emissions were successively turned off. 187
6.18 Timeseries of CiTTyCAT modelled hydroxyl radical production rate along one example trajectory (arriving GI 28th April, 10:00 UTC), stemming from NO_x (primarily HONO) and VOCs (biogenic and anthropogenic contributions combined). 189
6.19 (a) Timeseries of CiTTyCAT modelled glyoxal mixing ratios at the Garden Island site for the first part of the campaign, plotted for a range of sensitivity tests. (b) Timeseries over the same period of the modelled ratio between glyoxal and formaldehyde (R_fn) mixing ratios. (c) Bar chart showing the influence of sensitivity tests on glyoxal mixing ratio. Test details are outlined in table 6.1. 190

7.1 (a) Map of New Zealand showing the location of Lauder (red pin) in the South Island. (b) Map zoomed in to Central Otago showing the location of NIWA Lauder (blue star) and viewing direction of the MAX-DOAS (red arrow) towards St Bathans and the Dunstan Range. (c) Photo over the NIWA Lauder buildings, in the MAX-DOAS viewing direction, towards Mt St Bathans and the Dunstan Range (*Maps sourced from Google Maps, photo by R.Ryan*). 193
7.2 Example FTIR profile retrieval from 1 pm local time on 8th January 2018 at Lauder. The left hand panel shows a priori and retrieved HCHO profiles in the lowest 10 km, the right hand panel shows the corresponding averaging kernels. 195
7.3 Example QDOAS fits from Lauder MAX-DOAS data, 1st January 2018 at solar zenith angle 30^o and elevation angle 3^o. Top row: O_4 (338-370 nm wavelength range), HCHO (324.5-359 nm wavelength range). Bottom row: ring and residual spectra (both in the 324.5-359 nm wavelength range). 195

7.4 Comparison scatter plots for MAX-DOAS formaldehyde retrieval methods at Lauder. The x-axis in each plot indicates test 00, with standard HCHO retrieval settings. The y-axis indicates (a) test 01 designed to examine the influence of the aerosol profiles on the trace gas retrieval, and (b) test 02 which uses the a priori HCHO profile from FTIR analysis. 197
7.5 (a) An example MAX-DOAS formaldehyde retrieval from 1st January 2018 at Lauder, showing the modelled and measured values, retrieved and a priori vertical profile and averaging kernels. (b) Monthly averaged midday HCHO vertical profiles, and (c) polar bivariate plot showing the HCHO VCD as a function of wind speed and direction. All HCHO profiles in this figure retrieved using standard retrieval settings (method 00). 198
7.6 (a) Timeseries of monthly averaged formaldehyde total column measurements at Lauder from 2001-2019 measured with FTIR. Included is a cosine fit to this data highlighting the seasonal cycle. (b) Timeseries of monthly averaged formaldehyde vertical column densities from MAX-DOAS measurements at Broadmeadows (red points) and Lauder (blue squares). Cosine fits to each dataset are also plotted, along with the cosine fit from the 2001-2019 FTIR results in (a) (dashes). 199
7.7 (a) Timeseries comparison of MAX-DOAS and FTIR HCHO vertical columns (both original values and smoothed with MAX-DOAS averaging kernels) from November 2016 to January 2019. Results are daily average column amounts from measurements between 12:00 and 2:00 pm local time. (b) Scatter plot comparison of MAX-DOAS HCHO VCDs with smoothed FTIR results. (c) same as (b) but with original FTIR HCHO columns. 202
7.8 Examples of TROPOMI 0.1×0.1^o gridded output. The blue circles indicate the MAX-DOAS measurement locations. The grid lines drawn are at 1^o latitude and longitude intervals. (a) Example retrieval from the South Island of New Zealand, 24th of December 2018. (b) All New Zealand retrievals from December 2018-February 2019 averaged. (c) Example from Victoria, 14th January 2019, and (d) all Victorian retrievals from December 2018-February 2019 averaged. Note that the colour bar scale is different for each plot to emphasise the spatial patterns. 203
7.9 Timeseries comparisons for MAX-DOAS and TROPOMI. Figure titles indicate the equation describing a total least-squares linear regression fit for the two datasets. (a) Timeseries of daily averaged HCHO vertical columns at Broadmeadows from 12/12/2018 to 15/5/2019. (b) Timeseries of monthly averaged HCHO columns from Broadmeadows, May 2018-May 2019. 205

7.10 Comparison of monthly mean formaldehyde columns from TROPOMI and the MAX-DOAS at Lauder, with timeseries on the left and scatterplot of the same values on the right. (a) shows TROPOMI columns averaged 0.1^o either side of Lauder, (b) shows TROPOMI columns averaged 1^o either side of Lauder. 207
7.11 Timeseries of monthly averaged MAX-DOAS and OMI HCHO vertical columns at Broadmeadows from January 2017 to May 2019. 208

A.1 Example calibration spectra from the University of Melbourne Envimes MAX-DOAS: (a) Dark current and (b) offset spectra. 215
A.2 (a) Annotated diagram of the University of Melbourne Envimes 2D MAX-DOAS optics head, (b) the inside of the optics head, (c) the spectrometer unit 216
A.3 Lineshape functions (left) and wavelength calibrations (right) for each of the TIMTAM Envimes MAX-DOAS instruments (UV spectrometer only), calculated from mercury lamp spectra 217
A.4 Scatter plots showing correlations between NZ measurements (x-axis) and BM, UW and UM respectively, for (a) residual RMS and (b) percentage fit error (fit error/dSCD). All 5^o elevation angle results in the period 16-20 February 2017 are plotted. 217

B.1 Monthly average traffic volume on four major roads in inner Sydney, normalised to the maximum monthly traffic volume at each location, from data taken between 2010-2018. The road count locations are the Sydney Harbour Tunnel in Central Sydney, the Western Distributor at Glebe in the inner west, the Pacific Highway at Roseville in the north and the Hume Highway at Bankstown in the south-west. 218
B.2 Comparison of NO_2 diurnal cycle with aggregate traffic volume data for the Western Ring Road, Camp Road and Sydney Road. 219
B.3 Figure adapted from Ryan et al. (2018) showing (left) location of Melbourne in Australia and (right) the location of Broadmeadows relative to the Melbourne Metropolitan EPA air quality monitoring stations used for validation of MAX-DOAS NO_2 results. 219
B.4 Scatterplots showing correlation between NO_2 measured by the MAX-DOAS at Broadmeadows and in-situ NO_2 averaged across Melbourne metropolitan EPA monitoring stations. (a) shows hourly average comparison, (b) daily average comparison, (c) weekly averages, (d) monthly averages. 220
B.5 Monthly averaged averaging kernels (lowest 2 km) for trace gases retrieved at Broadmeadows, 2018 data: top NO_2, middle HCHO and bottom HONO. 221
B.6 Comparison of modelled and measured values for the four trace gases retrieved at Broadmeadows, demonstrating successful HEIPRO retrievals. 222

B.7 Methane total column mixing ratios retrieved by the TROPOMI satellite from May 2018 to April 2019. Retrievals have been re-gridded to 0.25x0.25^o resolution then averaged spatially over the state of Victoria, then temporally to produce weekly mean values. 223

C.1 Polar bivariate plots of insitu trace gas mixing ratio during the Garden Island campaign (NO_2, NO and O_3). Results taken only from daylight hours so as to be comparible with MAX-DOAS measurements. 227
C.2 Scatterplot of aerosol optical depth (AOD) vs formaldehyde VCD for 4th of May 2018 at Garden Island, a day on which a smoke plume blanketed the region. The plot title indicates the equation of the total least squares regression fit to the points. 228
C.3 Timeseries of the ratio of formaldehyde to NO_2 (R_{fn} during the Garden Island campaign. 228
C.4 Time series of ozone mixing ratios, output from CiTTyCAT for in a range of sensitivity tests. The sensitivity test details are outlined in table 6.1 in chapter 6 229

Chapter 1

Australasian atmospheric chemistry – an introduction

1.1 Opening remarks

The Earth's atmosphere holds a certain dichotomous mystique in human psyche. On the one hand, weather is undoubtedly one of most common conversation topics; we innately understand the importance of phenomena such as sunshine, cloud, rain and wind. We are quick to recognise changes in the temperature as it cycles from day to night and season to season. On the other hand, from ground level the atmosphere seems such a vast, ubiquitous and uniform vault that its predominant functions, and indeed its fragility, are often ignored or missed.

From the point of view of life on Earth, the atmosphere has two primary, indispensable functions: as a radiation filter, and as a key component in the planet's biogeochemical cycles. The fragility of these systems is evident in the atmosphere's size - almost the entire atmospheric density resides below 40 km altitude, or approximately 0.63 % of the Earth's radius. The fragility is also evident in the fine balance of chemical constituents, with recent research indicating that compositional changes on the order of parts per trillion for some gases can have significant pollution and climate consequences. It has become increasingly clear over the course of the last century that the radiation filter role cannot be ignored because human activity is disturbing its underlying fine chemical equilibrium. In particular, global attention focused on destruction of the stratospheric ozone layer by chlorofluorocarbons (Molina and Rowland, 1974), a fact which resulted in increased UV radiation penetrating to the Earth's surface.

There is growing global awareness that anthropogenic enhancement of Earth's natural greenhouse effect through fossil fuel combustion is altering the global climate. The tipping point for concern over disturbing the atmosphere's radiation balance is when the intangible influences the tangible: when climate impacts are severe enough to produce

noticeable deviations from expected weather patterns and manifest in disasters such as floods, droughts, cyclones and fires.

The role of the Earth's atmosphere in global cycles is less commonly discussed. A clear example is the water cycle, where through evaporation and precipitation the atmosphere removes and returns water to the lithosphere. Less obvious, but equally important cycling occurs for atmospheric gases far less abundant such as alkenes and alkanes emitted from plants. Anthropogenic activity is also perturbing the balance required for the oxidation mechanisms underpinning atmospheric chemical recycling, for example by emission of nitrogen oxides and associated formation of ozone, constituents hitherto highly transient in the lower atmosphere. We describe the situation where the natural atmospheric cycles systems cannot keep up with emissions as pollution, and are increasingly recognising a multitude of associated health and environmental concerns.

In a world where the atmosphere is considered so vast as to be a suitable dumping ground for greenhouse gases, nitrogen oxides and other gaseous anthropgenic waste, the role of researchers in atmospheric chemistry research must be to highlight the beauty, frailty and importance of its fine balance. It must do this by observing and seeking to understand the nature of the background atmospheric state and of the various emissions. Only then can we begin to model the atmosphere, predict future scenarios and defend appropriate social, economic and political recommendations. This thesis aims to add to the growing body of atmospheric chemistry work highlighting the importance of atmospheric oxidation chemistry, with a focus on the interplay of natural and anthropogenic emissions in the understudied Australasian region.

1.2 Structure of the atmosphere

1.2.1 Vertical structure

One of the few people to ever get an external view of the Earth, US astronaut Scott Kelly commented upon returning to Earth from space that "predominantly you just notice how thin the atmosphere is, how fragile it looks" (Yuhas, 2016). While externally thin, over time the atmosphere has developed as a robust and complex system exhibiting both large-scale uniformity and complex local-scale variability.

The vertical structure of the atmosphere is characterised by the way physical and chemical properties vary with altitude. The closest layer to the Earth's surface is the troposphere, which is characterised by dominant vertical mixing and decreasing temperature with altitude as shown in figure 1.1(a). The temperature decreases approximately linearly in the troposphere at a (dry adiabatic lapse) rate of around 7 K/km. Pressure decreases exponentially with altitude in the troposphere meaning that more than three quarters of total the mass of the atmosphere resides in the troposphere. The troposphere can be further divided into the planetary boundary layer close to ground level

and the free troposphere above. Physical mixing within the boundary layer is determined by surface interactions while convection is the dominant mixing force in the free troposphere. The top of the troposphere is marked by the tropopause, at which altitude the linear temperature decrease with height ceases. The tropopause altitude varies between approximately 8-18 km, being highest at the equator where surface solar heating and thus convective activity are at their maximum.

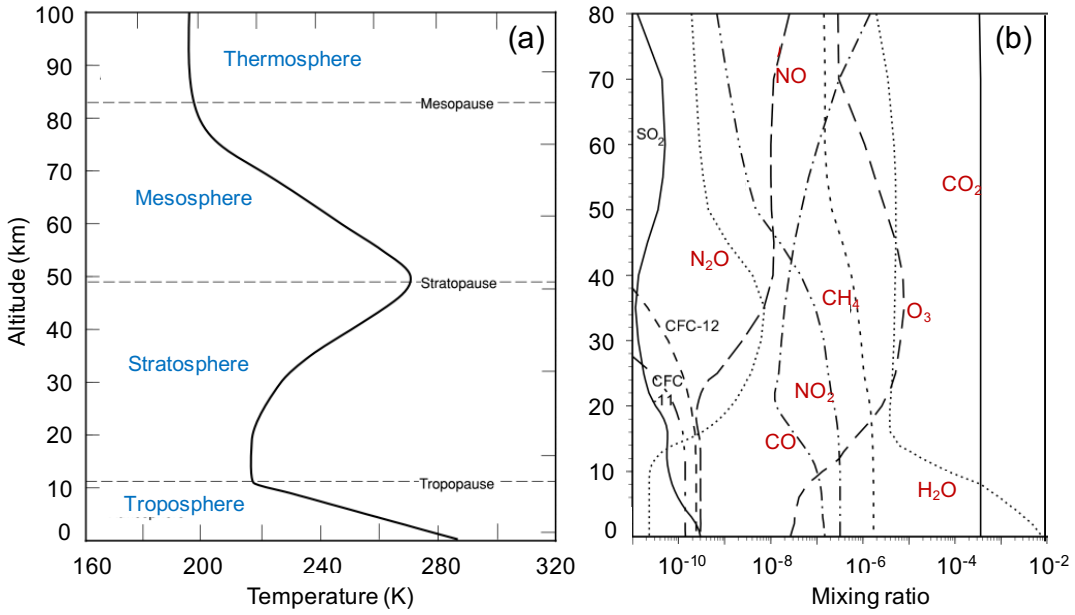

Figure 1.1: (a) The physical vertical structure of the atmosphere, showing temperature variation throughout. (b) Vertical mixing ratio profiles of some key atmospheric gases. For example, the dominant presence of ozone in the stratosphere and water in the troposphere is evident. Figure adapted from Liou (2002).

Above the tropopause lies the stratosphere, characterised by stratified (hence 'stratosphere') horizontal mixing and increasing temperature with altitude. The temperature increase is due to absorbance of ultraviolet (UV) radiation by ozone, which has peak atmospheric concentrations in the stratosphere typically between 20-40 km as shown in figure 1.1(b). The filtering of harmful UV radiation by this ozone layer is crucial for life on Earth. The stratosphere is capped by the stratopause which is is around 50 km altitude. Beyond the stratopause, temperature again decreases with altitude throughout the mesosphere due to lower ozone and decreasing pressure. The top of the mesosphere, or mesopause, is considered to be the coldest part of the atmosphere with temperatures as low as 130 K. Temperature increases with height once again in the next layer, the thermosphere, due to ionisation by UV radiation.

1.2.2 Atmospheric circulation

In addition to vertical structure, the Earth's atmosphere exhibits characteristic meridional (i.e. north-south) patterns caused dynamically by unequal distribution of solar radiation across the globe. The Earth's surface heats up much more at the equator than the poles, leading to ascending air at the equator and an overall redistribution of heat towards the poles, setting up the basis of the atmospheric general circulation depicted in figure 1.2. Ascending air at the equator creates a band of low pressure, called the intertropical convergence zone (ITCZ). Planetary rotation induces the Coriolis force, deflecting the 'trade' winds blowing towards the ITCZ to the west in each hemisphere. The rotating globe also means that the total circulation exists as three distinct cells (Hadley, Ferrel and Polar), mirrored in each hemisphere, and accompanying bands of high and low pressure where air descends and ascends respectively. It is important to note that the meridional cellular structure of convection and subsidence depicted in figure 1.2 (Figure adapted from the Australian Bureau of Meteorology: www.bom.gov.au/climate/about/australian-climate-influences). occurs within the troposphere only, and is in fact the basis of the vertical mixing defining the troposphere. The strongest convective activity at the ITCZ causes the height of the tropopause to be much higher than at the poles. In some cases, the convection can be energetic enough to 'overshoot' the tropopause and this stratospheric injection is an important mechanism by which trace gases and particulate matter can reach the upper atmosphere.

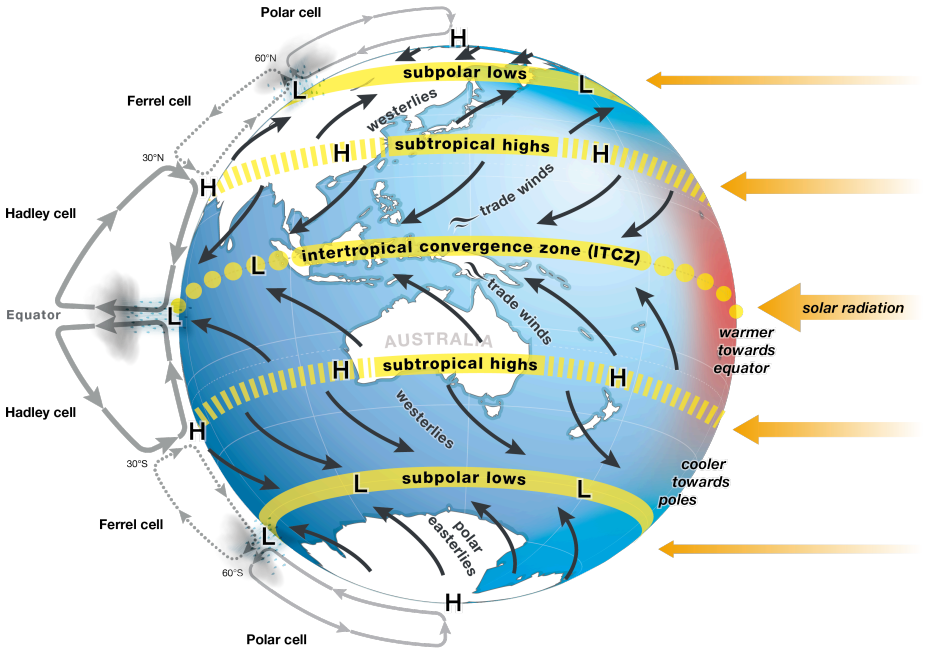

Figure 1.2: Schematic diagram of the atmosphere's general circulation patterns. Figure adapted from the Australian Bureau of Meteorology website.

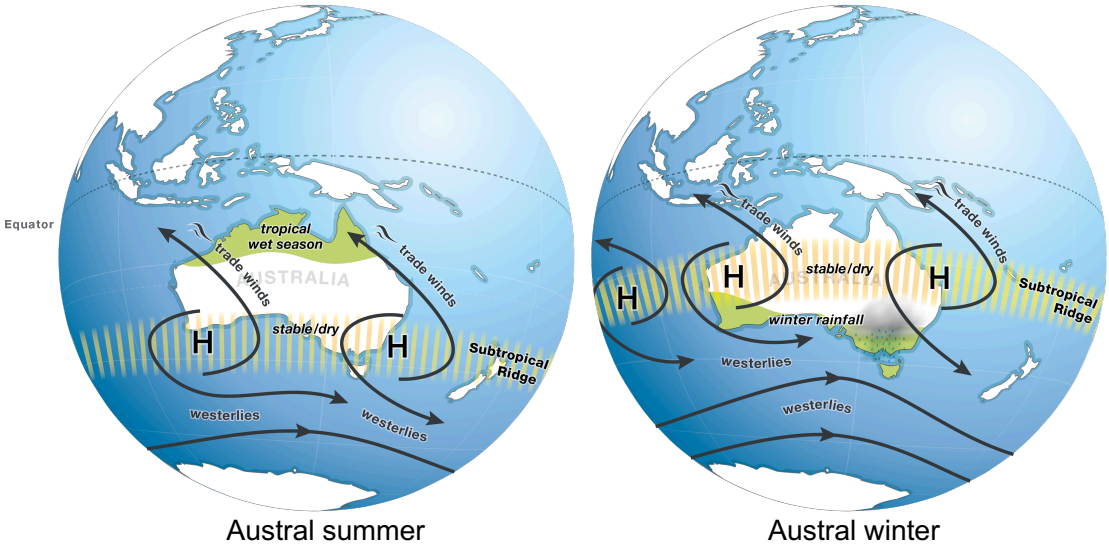

Figure 1.3: Schematic diagram of the position of the subtropical ridge, and associated broad-scale weather patterns, over Australia in summer and winter. Figure adapted from the Australian Bureau of Meteorology website.

In the northern hemisphere, the meridional pattern of high and low pressure is often interrupted in reality by the topography of large land masses. Significantly less landmass in the southern hemisphere (SH) means the prevailing large-scale weather patterns are typically uninterrupted and the subtropical high and subpolar low belts shown in figure 1.2 are maintained. The conservation of the subtropical high pressure belt (or 'ridge') creates predictability in Australasia's broadscale weather patterns. As shown in figure 1.3 (adapted from the Australian Bureau of Meteorology: www.bom.gov.au/climate/about/australian-climate-influences), in SH winter the position of the high pressure ridge is over the interior of the Australian continent. This allows westerly winds to deliver rain, associated with low pressure systems, troughs and cold fronts, to the southern parts of Australia and New Zealand. In Austral summer, the ITCZ pushes into the SH and this in turn pushes the subtropical high pressure ridge southwards so that it sits over the southern tip of the continent. Thus the midlatitude westerly winds cannot reach the continent and southern Australia experiences warm, dry summers on average, while the dipping ITCZ induces a monsoon trough which delivers significant summer rainfall to northern Australia. The typical cool, wet winters and warm, dry summers of southern Australia, often referred to as a 'Mediterranean climate', has a strong influence on seasonal patterns of atmospheric chemistry as well as meteorology.

1.3 Atmospheric composition

The gaseous chemical composition of the atmosphere is dominated by nitrogen (N_2, $\sim$ 78%), oxygen (O_2, $\sim$ 21%), argon (Ar $\sim$ 0.9%) and water vapour (H_2O, varying from 0-4% depending on location and time). The remaining species are called trace gases, the most abundant of which is carbon dioxide (CO_2, $\sim$ 0.04%). Trace gases collectively make up less than 1% of total atmospheric volume but have very important roles to play in global and regional scale atmospheric reactivity. Figure 1.1(b) shows global average mixing ratios for some atmospheric constituents. Many of the trace gas species depicted in this figure from Liou (2002) have high spatial and temporal variability, due to different sources, sinks and reactivities.

Chemical reactions or physical processes that introduce a constituent to the atmosphere are termed sources, while mechanisms that remove constituents are called sinks. Common examples of sources include combustion, biological activity (e.g. respiration), evaporation and volcanic eruptions. Sources are called primary if the constituent is emitted directly and secondary if the constituent is formed as a result of chemical reactions occurring in the atmosphere. The main sinks for atmospheric gases are chemical reactions and deposition to the Earth's surface either by direct adsorption (dry deposition) or by precipitation in the case of water soluble species (wet deposition). Determining the sources, sinks and interactions of trace gases on different scales (horizontal, vertical and temporal) is fundamental to understanding the chemical reactivity of Earth's atmosphere, and how it may change in the future.

The chemical reactivity of the atmosphere underpins its role in the Earth's recycling system: to maintain equilibrium, the atmosphere must be able to remove gases emitted to it. If the sinks do not keep up with the sources, potentially toxic chemicals can build up in the atmosphere resulting in pollution and poor air quality.

1.3.1 Aerosols

In addition to gaseous constituents, the atmosphere also plays host to a wide range of suspended solid and liquid particles, typically classified together as aerosols. Those originating directly from the Earth's surface (such as dust, sea-salt, pollen) are called primary aerosols, while those formed in the atmosphere by chemical reactions are termed secondary aerosols (Meszaros, 1999). Many secondary aerosols, such as sulfuric acid and nitric acid droplets, are formed directly from atmospheric oxidation reactions. Atmospheric aerosols range in size from tens of nanometres to hundreds of microns. Smaller particles have longest residence times in the atmosphere, larger particles are subject to deposition by gravity more rapidly.

Aerosols play several key roles in the troposphere. Firstly, they are important for their role as cloud condensation nuclei (surfaces on which water vapour condenses) which are necessary for the formation of clouds and precipitation (Meszaros, 1999). In addition to condensation, aerosol surfaces are also important host sites for heterogeneous chemical

reactions. Because aerosols have shorter atmospheric residence times with respect to deposition, reactions forming, or occurring on aerosols provide important sink pathways for many trace gases. Finally, aerosols play a significant role in atmospheric radiative forcing through scattering and absorption of light. According to the Intergovernmental Panel on Climate Change's Fifth Assessment Report (WG1, Chapter 7) "clouds and aerosols continue to contribute the largest uncertainty to estimates and interpretations of the Earth's changing energy budget" (Boucher et al., 2013). As a result, measurement and analysis techniques which provide information on the amount, type and distribution (vertical, horizontal and temporal) of aerosols all over the world continue to be vital components of atmospheric chemistry and climate research.

1.3.2 Tropospheric oxidative capacity

Defining oxidative capacity

Oxidation reactions are the primary atmospheric reactivity sink for trace gases. Since the dominance of photosynthesis and aerobic processes on Earth led to oxygen becoming a dominant atmospheric component, the atmosphere has been an oxidising environment. However, atmospheric dioxygen O_2 is not the most reactive form of oxygen in the atmosphere. Free radicals, molecules with a single unpaired electron such as the hydroxyl radical $OH^{\bullet}$, are strong oxidants and play a crucial role in overall oxidative cycle (note that in atmospheric chemistry, the 'dot' notation indicating free radical is typically neglected, i.e. $OH^{\bullet} = OH$). The total amount ('burden') of oxidising free radicals and other chemical oxidants in the atmosphere is referred to as the oxidative capacity (Prinn, 2003).

Primary oxidants

Because the work in this thesis will focus on the troposphere, the ensuing discussion will focus on tropospheric oxidative capacity. By reactivity and abundance, the most important oxidants in the troposphere are (Finlayson-Pitts and Pitts Jr, 1999):

1. **Hydroxyl radical (OH)**: OH is the primary oxidant for tropospheric methane (CH_4) and other hydrocarbons carbon monoxide (CO) and sulfourous species. The predominant source of OH is considered to be the photodissociation of ozone ($\lambda < 340$ nm) leading to the formation of singlet oxygen ($O(^1D)$):

$$O_3 + hv \longrightarrow O(^1D) + O_2 \quad \{1\}$$
$$O(^1D) + H_2O \longrightarrow 2\,OH \quad \{2\}$$

   Photolysis of nitrous acid (HONO) and hydrogen peroxide (H_2O_2) also produce OH. The importance of HONO as an OH source will be a key theme of the discussion in this thesis.

$$\mathrm{HONO} + \mathrm{hv}\,(\lambda < 400\,\mathrm{nm}) \longrightarrow \mathrm{OH} + \mathrm{NO} \quad \{3\}$$

$$\mathrm{H_2O_2} + \mathrm{hv}\,(\lambda < 370\,\mathrm{nm}) \longrightarrow 2\,\mathrm{OH} \quad \{4\}$$

As evident from these reaction schemes, the dominant OH sources are photolytic (reliant on photons, represented by "hv", for formation), meaning that OH is only an important atmospheric oxidant during the daytime.

2. **Ozone ($\mathbf{O_3}$)**: O_3 is also a strong atmospheric oxidant. About 90 % of the atmosphere's O_3 is in the stratosphere and 10 % is in the troposphere (Lelieveld and Dentener, 2000). Exchange between these layers is one source of tropospheric ozone. Another source is through reactions involving volatile organic compounds (VOCs) and the nitrogen oxides ($NO_x = NO + NO_2$):

$$\mathrm{NO_2} + h\nu \longrightarrow \mathrm{NO} + \mathrm{O} \quad \{5\}$$

$$\mathrm{O} + \mathrm{O_2} \xrightarrow{\mathrm{M}} \mathrm{O_3} \quad \{6\}$$

$$\mathrm{NO} + \mathrm{O_3} \longrightarrow \mathrm{NO_2} + \mathrm{O_2} \quad \{7\}$$

Note that [M] in this context denotes a spectator molecule facilitating the reaction, e.g. N_2 or O_2. While this cycle involves both the formation and destruction of O_3, it is a balance that can be shifted by varying the $[NO_2]/[NO]$ ratio. VOCs facilitate this through the formation of the HO_2 radical, shown below for an example VOC scheme involving methane, and then through reaction of HO_2 to form NO_2:

$$\mathrm{CH_4} + \mathrm{OH} \xrightarrow{\mathrm{O_2}} \mathrm{CH_3O_2} + \mathrm{H_2O} \quad \{8\}$$

$$\mathrm{CH_3O_2} + \mathrm{NO} \longrightarrow \mathrm{NO_2} + \mathrm{CH_3O} \quad \{9\}$$

$$\mathrm{CH_3O} + \mathrm{O_2} \longrightarrow \mathrm{HCHO} + \mathrm{HO_2} \quad \{10\}$$

$$\mathrm{HO_2} + \mathrm{NO} \longrightarrow \mathrm{NO_2} + \mathrm{OH} \quad \{11\}$$

3. **Nitrate radical ($\mathbf{NO_3}$)**: NO_3 is photolysed during the daytime, but at night in polluted atmospheres is the dominant tropospheric oxidant, when OH concentrations are low. The main tropospheric NO_3 source is:

$$\mathrm{NO_2} + \mathrm{O_3} \longrightarrow \mathrm{NO_3} + \mathrm{O_2} \quad \{12\}$$

4. **Singlet oxygen ($\mathbf{O(^1D)}$)**: In the ^1D excited state, singlet oxygen atoms can react with water as shown above, as well as oxidising hydrocarbons. It is formed predominantly through photolysis of ozone.

5. **Peroxy radicals (HO_2 + RO_2)**: HO_2 is formed from the oxidation of VOCs as shown for the example of methane above, and can also be formed from reactions which produce singlet hydrogen H or carbonyl radicals HCO. The photolysis of formaldehyde is a good example of this:

$$HCHO + hv\,(\lambda < 370\,nm) \longrightarrow H + HCO \quad \{13\}$$
$$H + O_2 \longrightarrow HO_2 \quad \{14\}$$
$$HCO + O_2 \longrightarrow HO_2 + CO \quad \{15\}$$

   When longer chain hydrocarbons are oxidised, organic analogues of HO_2, denoted by RO_2 where R signifies any hydrocarbon group, can be formed and are also strong oxidants.

6. **Hydrogen peroxide (H_2O_2)**: H_2O_2 is water soluble and hence is an important oxidant in cloud and precipitation. It is formed by recombination of peroxy radicals:

$$HO_2 + HO_2 \longrightarrow H_2O_2 + O_2 \quad \{16\}$$

1.3.3 Measuring and inferring oxidative capacity

Attempts at direct measurement of hydroxyl radical concentrations have underpinned efforts to measure atmospheric oxidation capacity. This has been achieved, for example, using UV-visible spectroscopy as OH has an absorption band at 308 nm (Prinn, 2003). This approach is very difficult however for several reasons; small and highly transient OH concentrations, the competing absorption of stratospheric ozone at this wavelength and strong Rayleigh (molecular) scattering over the long absorption pathlengths needed for this kind of spectroscopy. Alternative strategies for measuring atmospheric oxidation capacity involve inferring the concentration or production rate of oxidants from other species. Most commonly, OH is studied using methylchloroform concentrations which has well defined and documented emission sources and has OH as its primary sink (e.g. Prinn et al. (2001)).

If these methods of establishing OH concentrations are unavailable, insight into the key drivers of atmospheric oxidation chemistry can still be derived by considering the relative importance of different oxidant-producing mechanisms. For example, passive UV-visible spectrometric techniques such as differential optical absorption spectroscopy (DOAS, Platt and Stutz (2008)) routinely measure trace gases such as nitrogen dioxide, nitrous acid and formaldehyde all of which contribute to ozone and/or OH formation. Therefore DOAS is an ideal tool for inferring the different influences on oxidation chemistry, over varying spatial and temporal scales. In this work multi-axis (MAX-)DOAS, discussed in detail in the following chapter, will be used to understand the

key drivers of oxidation capacity in Australasia chiefly through OH and O_3 formation mechanisms.

1.4 Tropospheric chemistry

Considering the above broad discussion of oxidative capacity, the following section describes in greater detail the sources, sinks and interactions relevant to the key tropospheric constituents discussed in this thesis.

1.4.1 Nitrogen oxides

Nitrogen oxides are important in tropospheric chemistry because of their high reactivity, their role in tropospheric ozone cycling, reactions with volatile organic compounds and toxicity in their own right. The two predominant nitrogen oxides are nitrogen dioxide (NO_2) and nitric oxide (NO) which are often considered jointly using the term NO_x (= NO_2 + NO). NO_2 is considered to be a respiratory tract irritant and has been strongly associated with respiratory, cardiovascular and overall mortality in several multi-city studies around the world (e.g. Samoli et al. (2006), Tao et al. (2011), MacIntyre et al. (2013)). Despite uncertainty surrounding the specific mechanisms for NO_2 influencing overall mortality, including that NO_2 may be a surrogate for other co-existing pollutants (Hesterberg et al., 2009), the strength of the relationship with mortality means studying NO_2 concentrations is of primary importance in understanding air pollution.

NO_x forms from high energy processes breaking N_2 and O_2 bonds - this occurs naturally from lightning, and anthropogenically in the heat of combustion engines. Motor vehicle exhaust in urban areas is now considered to be the major global tropospheric NO_x source. Nitrogen oxides can also result from nitrogen emissions from soil and wild fires. Tropospheric NO_x concentrations range from on the order of tens of parts per trillion (ppt) in remote background conditions to to several hundred parts per billion (ppb) in polluted urban environments (Finlayson-Pitts and Pitts Jr, 1999). Through rapid industrialisation, urbanisation and increases in motor vehicle transportation it is estimated that NO_x emissions increased at an average rate of around 3 % per year between the mid 19th century and 1980 (Dignon and Hameed, 1989). More recently, studies using satellite NO_2 observations concentration have suggested that emission control measures are causing decreases in globally averaged NO_x concentration, albeit with highly regionally variable trends (e.g. Geddes et al. (2015)).

NO_x is primarily emitted as NO, followed by oxidation to NO_2 typically by ozone. Photolysis of NO_2 reforms NO, along with singlet oxygen which can go on to reform ozone (Leighton, 1961). This equilibrium, described in reactions 5-7, is catalytic in ozone and gives rise to the following photostationary state for NO_x partitioning:

$$\frac{[\mathrm{NO}]}{[\mathrm{NO_2}]} = \frac{J(\mathrm{NO_2})}{k[\mathrm{O_3}]} \tag{1.1}$$

where $J(\mathrm{NO_2})$ is the photolysis rate of $\mathrm{NO_2}$ and k is the rate constant of reaction 7, depending on temperature according to the Arrhenius law. $\mathrm{NO_x}$ partitioning is strongly spatially and temporally dependent: for example, close to direct emission sources such as factories and busy roads, NO dominates, while in lower tropospheric background air oxidation of NO means that $\mathrm{NO_2}$ dominates. During the night time, $\mathrm{NO_2}$ builds up strongly because it is not photolysed. Reaction of $\mathrm{NO_2}$ with the hydroxyl radical provides the predominant daytime sink for tropospheric $\mathrm{NO_x}$ (Finlayson-Pitts and Pitts Jr, 1999):

$$\mathrm{NO_2 + OH \xrightarrow{M} HNO_3} \qquad \{17\}$$

The reaction of $\mathrm{NO_2}$ with $\mathrm{O_3}$, which goes on to form nitrate radicals (reaction 12) also goes on to form nitric acid ($\mathrm{HNO_3}$) and is a nighttime $\mathrm{NO_x}$ sink:

$$\mathrm{NO_2 + NO_3 \longrightarrow N_2O_5} \qquad \{18\}$$

$$\mathrm{N_2O_5 + H_2O \longrightarrow 2\,HNO_3} \qquad \{19\}$$

The conversion to peroxyacetyl nitrate (PAN, $\mathrm{CH_3COO_2NO_2}$) is effectively a local $\mathrm{NO_x}$ sink but, because PAN has a long lifetime, enables preservation and transport of $\mathrm{NO_x}$ (Fischer et al., 2014):

$$\mathrm{CH_3COO_2 + NO_2 \overset{M}{\rightleftharpoons} PAN} \qquad \{20\}$$

where M is typically $\mathrm{O_2}$ or $\mathrm{N_2}$.

1.4.2 Nitrous acid

Nitrous acid (HONO), while also oxidised form of reactive nitrogen in the troposphere, is typically not considered part of the $\mathrm{NO_x}$ cycle. HONO sources include direct emission from combustion engines, the daytime homogeneous reaction of NO with OH (reaction 21) and the heterogeneous reaction between $\mathrm{NO_2}$ and water (reaction 22), occurring on wet surfaces and thought to be the main HONO source at night:

$$\mathrm{NO + OH \xrightarrow{M} HONO} \qquad \{21\}$$

$$\mathrm{2\,NO_2 + H_2O \xrightarrow{surface} HONO + HNO_3} \qquad \{22\}$$

The main sinks of nitrous acid are dry deposition, photolysis to produce OH (4) and reaction with OH:

$$\mathrm{HONO} + \mathrm{OH} \longrightarrow \mathrm{H_2O} + \mathrm{NO_2} \qquad \{23\}$$

Since reaction 23 is much slower (rate constant $1.8 \times 10^{-11} s^{-1}$) than reaction 4 (photolysis rate $J(\mathrm{HONO}) \approx 3 \times 10^{-5} s^{-1}$ around midday), photolysis is the dominant daytime sink (Sander et al., 2006). Consequently, HONO built up in the absence of photolysis at night rapidly converts with photolysis when the sun rises, with HONO concentrations typically decreasing with increasing UV radiation. While observing daytime HONO decreases from an early morning maximum, many studies have still observed higher than expected daytime HONO concentrations, indicating a missing source component peaking around the middle of the day (Li et al., 2012; Qin et al., 2009; Lee et al., 2016; Hendrick et al., 2014; Pinto et al., 2014). Some studies, in rural areas, have also reported maximum HONO mixing ratios in the middle of the day which certainly cannot be explained by the conventionally understood sources and sink mechanisms (Meusel et al., 2016; Acker et al., 2006). Because HONO can strongly influence local oxidative capacity, discussion surrounding the potential missing sources of this molecule have been a consistent research theme in atmospheric chemistry over the last decade. Hypotheses for the missing HONO source, based on both laboratory and field experiments, include heterogeneous reactions on aerosol surfaces (George et al., 2005), heterogeneous conversion of NO2 on ground surfaces (Stemmler et al., 2006; Wong et al., 2012; Lee et al., 2016), or soil-based emissions of NO and HONO (Oswald et al., 2013; Donaldson et al., 2014; Meusel et al., 2016, 2018). To test these theories, reliable and ideally long-term vertical gradient measurements of HONO and its precursors, including NO_2, are required.

1.4.3 Oxidised VOCs: formaldehyde and glyoxal

Volatile organic compounds influence tropospheric oxidation chemistry in three key ways: oxidation by OH (thereby being an important OH sink, decreasing oxidation capacity), formation of OH (e.g. by photolysis of formaldehyde) and contributing to tropospheric ozone formation. VOCs are so numerous and pathways so complicated that in field experiments, measuring key oxidised VOCs such as formaldehyde and glyoxal is a good way to understand the role of VOCs in atmospheric reactivity.

Formaldehyde (HCHO) is the simplest of the aldehydes and in laboratory conditions and high concentrations (> 0.5 ppm) is considered a highly reactive, flammable and toxic gas. In the atmosphere, concentrations are typically substantially lower than this, ranging from several hundred ppt in unpolluted marine air (Mahajan et al., 2010; Peters et al., 2012) to tens of ppb in polluted urban air (Zhu et al., 2017). Glyoxal is the simplest dicarbonyl, with formula $C_2H_2O_2$ (often written as CHOCHO). Atmospheric

mixing ratios of glyoxal are estimated to range from on the order of 0.1 ppt in remote background conditions to 20-100 ppt in some forested areas (Fu et al., 2008).

Primary sources of formaldehyde include direct emission from anthropogenic fossil fuel combustion and wildfires. HCHO is an oxidation product of numerous volatile organic compounds, hence has a wide range of secondary atmospheric sources. These VOC-oxidation sources are typically grouped into three key categories, being the oxidation of methane, isoprene and monoterpenes. Methane is a potent greenhouse gas, meaning that studying methane oxidation leading to formaldehyde production (outlined in reaction 9) has important climate change implications. Methane, deriving from a range of anthropogenic and biogenic natural gas emission sources, is considered to be the primary background HCHO source globally (Pfister et al., 2008). Isoprene (C_5H_8, see structure in figure 1.4) and monoterpene compounds (with formula $C_{10}H_{16}$, see example structures in figure 1.5) are emitted from vegetation and collectively are believed to be the dominant source of biogenic carbon to the atmosphere (Guenther et al., 2012). While methane is considered the most important OH sink in background oceanic air, over land isoprene and monoterpenes constitute the largest OH reactivity and hence these biogenic VOCs play a crucial role in determining oxidative capacity (Fuentes et al., 2000). Isoprene and monoterpenes are also thought to play a strong role in the climate system through radiative forcing by secondary formation of organic aerosols (Henze et al., 2008).

Glyoxal is considered to have few primary emission sources, with some contributions from industrial processes and biomass burning. The main atmospheric glyoxal sources are oxidation of biogenic VOCs, especially isoprene (Fu et al., 2008).

The main gas-phase chemical sinks of formaldehyde and glyoxal are photolysis and reaction by OH, restricting their atmospheric lifetime to on the order of several hours (Vlasenko et al., 2010; Fu et al., 2008). Heterogeneous uptake of glyoxal on aerosol surfaces leading to the formation of secondary organic aerosols (SOA) is an important sink of glyoxal (Li et al., 2016), with uptake to aqueous aerosols being aided by glyoxal's high solubility (Sander, 2015). The propensity of glyoxal to form aqueous SOA is complicated by factors such as increased solubility at low salt concentrations ("salting-in", Kurtén et al. (2015)) and a dependence of solubility on aerosol acidity (Shi et al., 2020).

Formaldehyde has also been associated with formation of SOA both indirectly, as a tracer of isoprene-derived SOA (Marais et al., 2016; Wang et al., 2017a) and through oxidation of HCHO to formic acid which promotes SOA formation (Jang et al., 2002; Shang et al., 2017).

The oxidation pathways of biogenic VOCs such as monoterpenes and isoprene are many and complicated, with whole textbooks, papers and theses devoted to the subject. Only a basic outline is presented here by way of introduction to understanding VOCs through formaldehyde and glyoxal as in this thesis. A simple schematic of the primary prod-

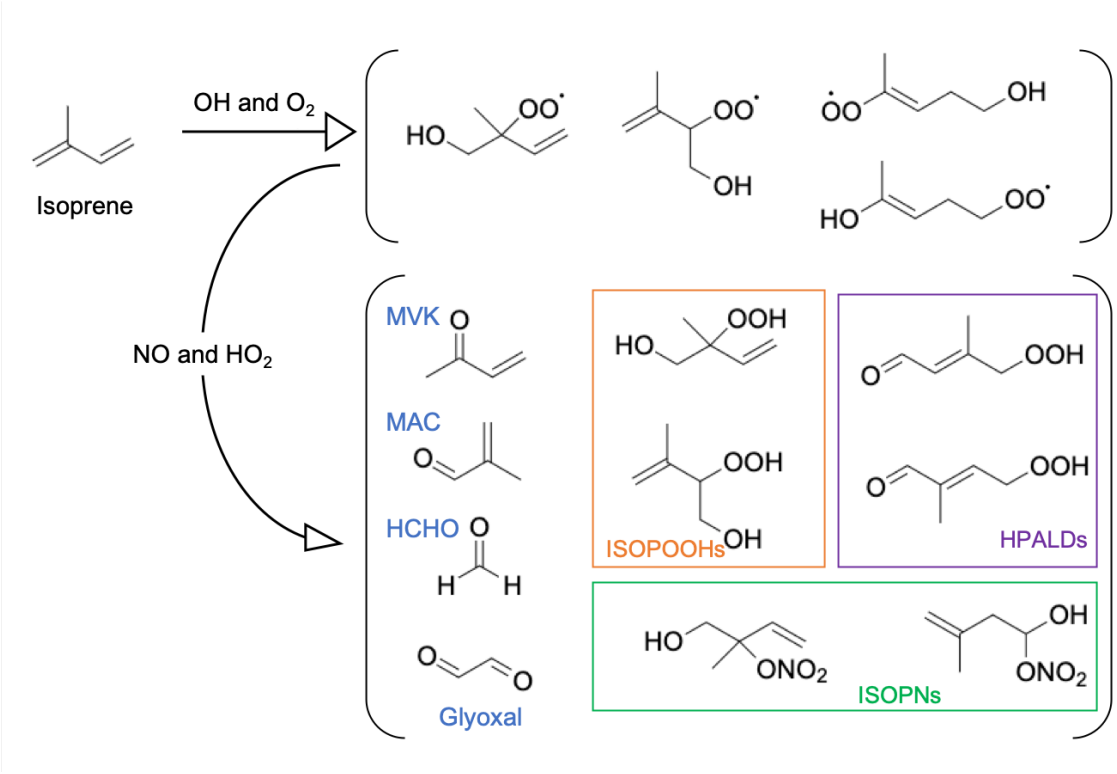

Figure 1.4: Simplified isoprene oxidation scheme showing the major products from reaction of isoprene with OH and O_2 and secondary oxidation by HO_2 and NO radicals. Acronyms relating to highlighted molecules are explained in the text.

ucts produced from oxidation of isoprene by OH and O_2 is shown in figure 1.4. OH radicals can add to either of the double bonds of isoprene, allowing subsequent addition of O_2 forming alkylperoxy radicals (examples of RO_2 briefly introduced earlier). In the second oxidation step, hydroperoxy radicals (HO_2) cause the breakdown of the RO_2 into a number of constituents including methyl vinyl ketone (MVK), methacrolein (MAC) and formaldehyde. NO can also act as an oxidant, so that the fate of oxidised VOCs in urban environments differs from those in pristine environments. For example, in remote environments with low NO_x, the production of isoprene hydroxy hydroperoxides (ISOPOOH) and isoprene hydroperoxy aldehydes (HPALDs) is favoured, while in polluted environments the production of HCHO, MAC, MVK and isoprene hydroxy nitrates (ISOPNs) is favoured. OH, RO_2, HO_2 and NO can continue to oxidise the ISOPOOHs, ISOPNs and HPALDs, and their products, and on the chains go - highlighting the complexity of the oxidation pathways for multiple-carbon chains. Both formaldehyde and glyoxal are products of the subsequent oxidation steps, hence they are considered suitable species by which to study isoprene oxidation, though the relationship is stronger in urban environments because of the dependence on the NO-oxidation pathway.

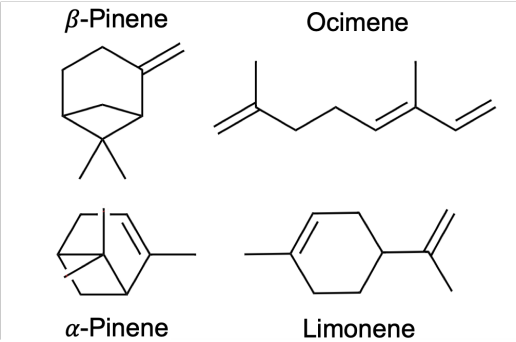

Figure 1.5: Structure of some common monoterpenes

The complex structures exhibited once the carbon chain extends to 10, as seen for some example monoterpenes in figure 1.5, give rise to a plethora of other products and reactions which also, however, often degrade to formaldehyde and glyoxal.

1.4.4 Tropospheric ozone production regimes

Through reactions with OH, the other key atmospheric oxidants and nitrogen oxides, VOCs play an important role in tropospheric ozone formation. This is achieved by production of peroxy radicals upon oxidation and photolysis of VOCs (for example reactions 9 and 14) which can shift the Leighton ratio between NO and NO_2 (equation 1.1). This is most relevant in polluted environments since NO_x emissions are predominantly anthropogenic, such as from internal combustion processes. However, varying amounts of NO_x and varying the $[NO_2]/[NO]$ ratio also has implications for OH, HO_2 and organic radical (generalised here to RO_2) sinks. Some key sink pathways for these species include:

$$2\,HO_2 \longrightarrow H_2O_2 + O_2 \quad \{24\}$$

$$HO_2 + O_3 \longrightarrow OH + 2\,O_2 \quad \{25\}$$

$$RO_2 + HO_2 \longrightarrow ROOH + O_2 \quad \{26\}$$

$$NO_2 + OH \xrightarrow{M} HNO_3 \quad \{27\}$$

Overall, it can be seen through the reaction schemes listed in this discussion that there are a number of sources, sinks and interactions between the OH/HO_2 (HO_x) cycle, the NO_x cycle, O_3 and VOCs. The determining factors for formation/destruction of ozone are the strength of NO_x and VOC sources, and the varying reactivities of molecules. As an example, OH is more reactive than HO_2. In their 1990 paper, Sillman et al. combined the reaction equations and rates in their discussion of tropospheric ozone formation in low and high NO_x conditions (Sillman et al., 1990). The findings indicate

a NO_x limited and a VOC limited regime for ozone formation as summarised in figure 1.6. In the NO_x limited case, O_3 production is independent of VOC emissions while with enough NO_x present, increasing VOC emissions lead to ozone increases (Jacob, 1999; Sillman et al., 1990).

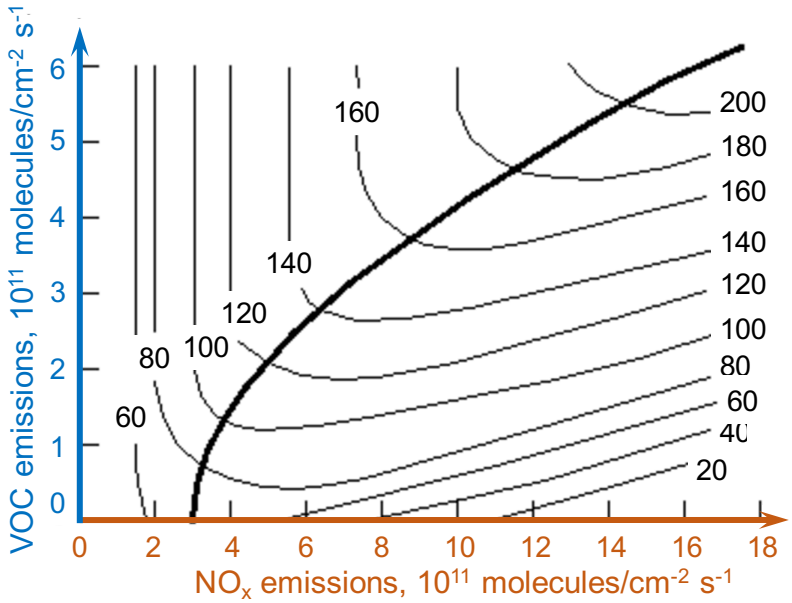

Figure 1.6: Ozone mixing ratios (ppb) as a function of VOC and NO_x emission rates, showing hydrocarbon limited (right of the thick black line) and NO_x limited (left of the line) O_3 production conditions. Figure adapted from Sillman (1990) and Jacob (1999).

The significance of this non linear relationship between O_3, NO_x and VOCs is that tropospheric ozone production is expected to be highly variable, both temporally and spatially. In polluted environments like cities, temporal patterns in NO_x are observed daily during peak traffic hours, as well as the dependence of OH production on UV radiation. Temporal variation in VOC speciation and concentration at a particular location might be seasonal, for example in regions of deciduous forest, or dependent on the local meteorology.

Irrespective of local-scale variability, modern global average tropospheric ozone levels are considered to be $\sim 30\%$ higher than pre-industrial levels (Young et al., 2013). This potentially has global consequences for the oxidative capacity of the troposphere. Modelling studies have suggested that total atmospheric oxidative capacity can be greatly impacted by perturbations in NO_x and O_3 levels, although the number of intertwined chemical and meteorological cycles makes such an analysis a daunting task (Lelieveld et al., 2004). An improved understanding of how tropospheric oxidation chemistry is varying on a local and regional scale, facilitated by long term measurements, is required to better inform these models.

1.4.5 Reactive halogen species

Reactive halogen species (RHS), comprising compounds of chlorine, bromine and iodine, play an important role in both stratospheric and tropospheric oxidation chemistry. The role of chlorine, through chlorofluorocarbons, in catalytic ozone loss in the stratosphere which was first postulated by Molina and Rowland (1974) is well known. However, halogens also react with tropospheric ozone according to the following reactions (Saiz-Lopez and von Glasow, 2012):

$$\mathrm{X} + \mathrm{O_3} \longrightarrow \mathrm{XO} + \mathrm{O_2} \quad \{28\}$$

$$\mathrm{Y} + \mathrm{O_3} \longrightarrow \mathrm{YO} + \mathrm{O_2} \quad \{29\}$$

$$\mathrm{XO} + \mathrm{YO} \longrightarrow \mathrm{X} + \mathrm{Y} + \mathrm{O_2} \quad \{30\}$$

where X is a halogen (i.e. either Cl, Br or I). At low halogen mixing ratios, reaction of halogen oxides with HO_2 can be a minor OH radical source and influences HO_x partitioning:

$$\mathrm{XO} + \mathrm{HO_2} \longrightarrow \mathrm{HOX} + \mathrm{O_2} \quad \{31\}$$

$$\mathrm{HOX} + \mathrm{hv} \longrightarrow \mathrm{X} + \mathrm{OH} \quad \{32\}$$

and in this way X can be recycled to promote further ozone loss. Halogen oxides also influence NO_x partitioning through

$$\mathrm{XO} + \mathrm{NO} \longrightarrow \mathrm{X} + \mathrm{NO_2} \quad \{33\}$$

Halogen oxides OClO, BrO and IO absorb UV radiation meaning that they can be observed using DOAS. Measurements of OClO, IO and BrO using DOAS instruments have been made in many parts of the world (see the comprehensive review of Saiz-Lopez and von Glasow (2012) and references therein), especially in polar regions, coastal areas, salt lakes and around volcanos. Key sources of RHS are thought to include concentrated saline water in polar regions (although release mechanisms are still under discussion, see review of Simpson et al. (2007)), salt release from sea-spray (e.g. Sander et al. (2003)) and, in the case of iodine, biogenic emissions from algae and exposed seaweed (Saiz-Lopez et al., 2012; Commane et al., 2011).

1.5 Research motivation

A strong understanding of atmospheric oxidation chemistry is fundamental to predicting the responses to anthropogenic change. A gap in this understanding is the influence of

local biogenic (i.e. VOCs) and NO_x emissions for overall oxidation capacity in particular regions. Ongoing measurements of ozone and methane (and/or their associated reaction products) are important for understanding how the atmosphere responds to changing amounts of these greenhouse gases. Addressing the uncertainties in our understanding of tropospheric ozone is especially important in separating the roles of ozone as a greenhouse gas at the surface from stratospheric ozone layer recovery in influencing climatic changes (Shepherd et al., 2014).

The oxidative cycles are crucial for understanding pollution and human health. Ozone and NO_2 pollution associated with industry and transport are a "major public health concern" according to the World Health Organisation, with particular significance for respiratory and cardiovascular diseases (WHO, 2006). Although NO_2 levels have fallen in parts of the US and Europe in recent times due to stricter air quality regulations, this has largely been offset on a global scale by increases in parts of Asia (Duncan et al., 2016). While ozone production levels are dependent on NO_2, the same global spatial variations are not necessarily observed because (a) ozone has a longer atmospheric lifetime and thus is capable of spreading far from its source (Doherty, 2015), and (b) dependence on VOCs means tropospheric ozone can still form in places with minimal anthropogenic NO_x pollution.

There are a number of other drivers of oxidation capacity to consider in addition to tropospheric ozone. For example, several studies have identified nitrous acid as an important, sometimes dominant, OH radical source in the boundary layer (Alicke et al., 2002, 2003; Ren et al., 2003; Elshorbany et al., 2009; Su et al., 2011). However, our understanding of the importance of HONO in driving boundary layer oxidative capacity is currently limited by (a) geographically sparse and mostly short-term observations, (b) a lack of studies directly comparing OH formation by HONO to other key sources such as O_3 and HCHO and (c) minimal vertical gradient measurements of HONO and (d) an unresolved missing daytime HONO source in many studies. In addition, our understanding of the global potential for reactive halogens such as BrO and IO to influence oxidative capacity, through ozone destruction, is limited by a lack of observations especially in the SH marine boundary layer. Resolving these issues is a key area of current research interest with potentially significant implications for understanding greenhouse gas lifetimes and air quality.

1.5.1 Australasian context

With a stark NO_x/VOC emissions contrast between urban and rural areas, Australasia provides interesting conditions for studying oxidation chemistry. Eucalyptus trees, endemic to and widespread in Australia, are known to be high isoprene and monoterpene emitters and in biogenic VOC emission models parts of Australia are therefore predicted to be emission hotspots (Winters et al., 2009; Guenther et al., 2012). Constraining these emissions has so far proven challenging in Australia, resulting in large model uncertainties: for example, global scale modelling has suggested Australia has the

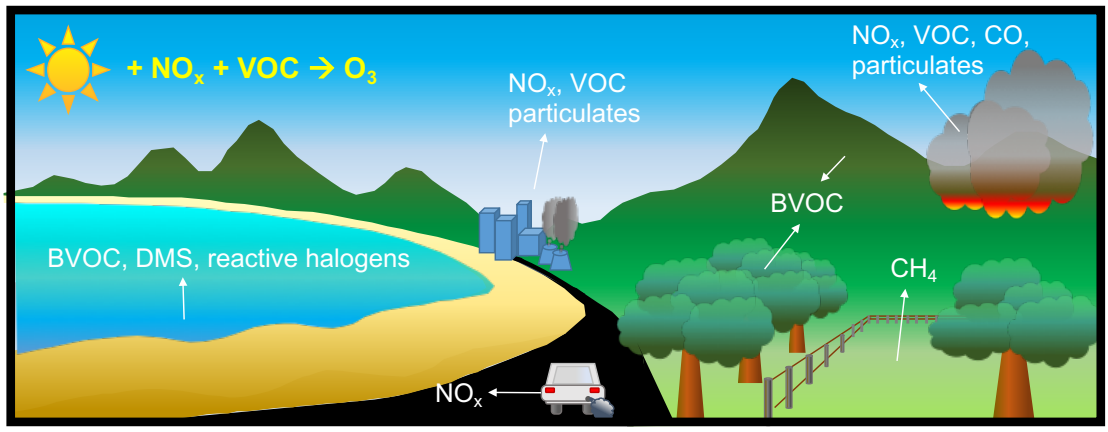

Figure 1.7: Schematic representation of the emission sources for components of the tropospheric oxidative cycle in Australia. Australia's vast marine and remote bush ecosystems provide large biogenic VOC (BVOC) sources, while the major anthropogenic VOC is agriculturally-produced methane (CH_4). Particulates and combustion products such as NO_x and carbon monoxide (CO) are natural products of bushfire in Australia, but also have anthropogenic origins in industry and transport.

highest isoprene-derived formaldehyde levels of any other continent, as shown in figure 1.8 (Pfister et al., 2008). However, regional scale models for South-Eastern Australian have been shown to underestimate HCHO levels by a factor of two (Zeng et al., 2015). Formaldehyde measurements, for example from satellites, are common proxies for biogenic VOC emissions but the accuracy of this under low NO_x conditions has not been observationally verified (Zhu et al., 2016; Wolfe et al., 2016), likely due to uncertainties in interpreting HCHO from different anthropogenic, isoprene and monoterpene sources. Emmerson et al. (2016) and Emmerson et al. (2018) highlighted this by demonstrating that the MEGAN biogenic emissions scheme, used in numerous global and regional-scale chemistry/climate models, overestimates isoprene and underestimates monoterpenes in the thickly eucalyptus-forested south-east of Australia.

Jointly studying glyoxal and formaldehyde has been proposed as a method to distinguish between VOC sources (e.g. DiGangi et al. (2012); MacDonald et al. (2012); Vrekoussis et al. (2010)), however there remains significant uncertainty in the literature as to the interpretation of the glyoxal:formaldehyde ratio (Kaiser et al., 2015). So far no studies of the glyoxal:formaldehyde ratio in the VOC hotspot of southern Australia have been reported. Long term observations and vertical gradient measurements of VOCs, and VOC oxidation products such as formaldehyde and glyoxal would be of tremendous benefit in addressing the current uncertainty in VOC emission constraints.

With global coverage and increasingly high resolution, satellite measurements using DOAS show great potential for increasing our knowledge in under-observed regions of the world, including Australia. As satellite technology develops, validation using ground-based instrumentation is required, and has been carried out using MAX-DOAS

in numerous studies (e.g. for formaldehyde: Chance et al. (2000), Thomas et al. (1998), Hoque et al. (2018b), De Smedt et al. (2015), Vigouroux et al. (2009) and OMI Lee et al. (2015) Kurosu et al. (2007). However no such validation studies have so far been carried out in the Australasian region.

There are indications from previous studies that background marine boundary layer mixing ratios of reactive halogen species such as BrO and IO are sufficient to constitute a significant global tropospheric ozone sink (e.g. Read et al. (2008), Leser et al. (2003), Großmann et al. (2013)). So far, the applicability of this theory for SH oceans is largely unknown do to a lack of observations, but surrounded by these oceans Australia is ideally placed to contribute this information.

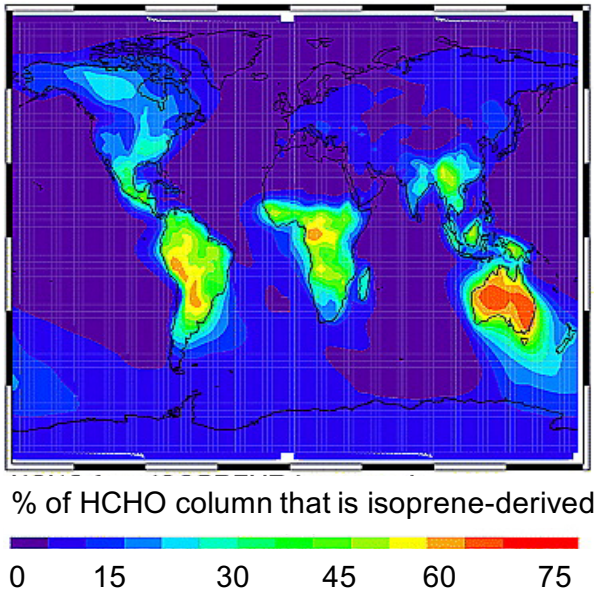

Figure 1.8: Global distribution of formaldehyde produced from isoprene oxidation, modelled using Modis-L. This illustrates the importance of VOC oxidative chemistry in Australia. Figure from Pfister et al (2008).

Despite very low population density and consequently low anthropogenic pollution in Australia's rural areas, NO_x emission in urban areas remains a problem due to public reliance on vehicle transport and minimal vehicle emissions regulation (compared, for example, to the European Union). Australia currently is ranked as the highest per capita NO_x emitter in the OECD (Organisation for Economic Co-operation and Development, 2016). Despite this, the Victorian Environmental Protection Agency (EPA) reported in 2013 that annual average annual NO_2 levels over the previous 30 years decreased from 13 ppb to below 10 ppb, despite significant population and vehicle number increases (EPA, 2013). With the Australian National Environment Protection Measure Standards annual average NO_2 concentration at 30 ppb (the World Health Organisation guideline is 21 ppb, WHO (2016)), these figures indicate that Melbourne has good

air quality as far as nitrogen oxides are concerned. On the one hand, this provides an ideal opportunity to study the oxidation chemistry relating to VOCs and nitrous acid in a low to moderately polluted urban environment. On the other hand, it could be argued that given the Victorian EPA results were taken from between 5-6 sites only, in a city nearing 5 million inhabitants, significantly more information on urban NO_2 is required.

This is poignant from an air quality point of view: epidemiological studies have demonstrated correlations between particulates and NO_2 pollution on overall mortality (Simpson et al., 2000, 2005) and cardiovascular disease (Barnett et al., 2006) in Melbourne. Air quality considerations are also likely to become more important in a warming climate, especially as increased bushfire risk pose significant new air quality threats. At the time of writing, vast tracts of forest along Australia's east coast, stretching from southern Queensland to eastern Victoria, are burning. Many towns and cities including Melbourne, Sydney and Canberra have been blanketed in thick smoke, resulting in unprecedented ozone and particulate matter pollution events (Webb and McMillan, 2020; Cushing, 2020). These events potentially represent a watershed moment in the Australian public's perception of climate change and air quality, heightening the relevance and importance of the work on Australian atmospheric chemistry in this thesis.

In addition to bushfire smoke hazards, a warming climate is likely to result in higher VOC emissions and may result in higher ozone levels, with Melbourne (Pearce et al., 2011) and especially Sydney (Utembe et al., 2018) subject to high ozone pollution episodes on hot summer days. It has been suggested in modelling studies by Utembe et al. (2018) that despite a clear correlation between VOC and ozone levels on such days, the ozone production regime is actually NO_x limited. Long term observations of the relationship between NO_x and VOCs in Australasia are required to constrain this in a useful way that can inform air quality policy and knowledge of local oxidation capacity.

Understanding of oxidation capacity over the Southern Hemisphere as a whole is greatly limited by a lack of measurements of OH and its precursors, especially compared to the more populated Northern Hemisphere. Therefore Australasia, for which minimal published reports of O_3, NO_x, HCHO, RHS exist, and none at all for HONO and glyoxal, is an excellent place to begin addressing this disparity. The Australasian region is also currently under-represented in the MAX-DOAS literature: to the best of my knowledge, no previous studies using MAX-DOAS measurements from Australia or New Zealand have been published prior to Ryan et al. (2018), the work of which forms part of this thesis. If satellite measurements are to help address the dearth of Southern Hemispheric atmospheric composition measurements then concerted validation studies in this region are required. Therefore through validation and in and of themselves, MAX-DOAS measurements of tropospheric NO_2, HCHO, glyoxal, RHS and aerosols have tremendous potential for expanding our knowledge of Australasian atmospheric chemistry.

1.6 Research aims

With the above motivations in mind, the work in this thesis is directed towards the following aims:

1. To establish the utility of MAX-DOAS measurements for the study of atmospheric chemistry in Australasia:

- Through development and harmonisation of measurement protocols and analysis methods
- Through validation using independent ground-based datasets
- Through applications to satellite validation

2. To determine the key drivers and sources of atmospheric oxidation capacity in Australia:

- Through studying key hydroxyl radical producing mechanisms and precursor sources
- These mechanisms and sources will be discussed in an urban setting (Broadmeadows, Victoria), remote background setting (Lauder, New Zealand) and coastal setting (Garden Island, Western Australia)

3. To identify the chemical sources and physical conditions associated with tropospheric ozone pollution in Australia:

- Through studying the relationship between volatile organics and nitrogen oxides on diurnal and seasonal timescales
- Through the relationship between ozone and meteorological measurements

Chapter 2

Collection and analysis of MAX-DOAS spectra

This methodology chapter is in two parts. Firstly, the background physics of solar radiation passing through the Earth's atmosphere, which underpins atmospheric spectroscopy, is introduced. This allows a thorough introduction to the differential optical absorption spectroscopy technique that is the root of the measurements discussed in this thesis. Secondly the spectroscopic collection methodology for this thesis will be outlined, including instrumental details and the optimisation tests carried out to determine appropriate spectral analysis settings for each trace gas analyte.

2.1 Background: atmospheric radiation and spectroscopy

2.1.1 Radiative transfer

Governing the large scale impacts of atmospheric chemistry on the solar radiation budget are the interactions of light and matter on a molecular scale. These interactions also provides a way to study atmospheric chemistry using spectroscopy, which is introduced here in the context of the underlying radiative transfer physics. Extinction (σ_e) due to either absorption or scattering results from the interaction of radiation with any particles, molecular sized or greater:

$$\sigma_e = \sigma_{scattering} + \sigma_{absorption} \tag{2.1}$$

In the case of elastic (Cabannes) scattering, the wavelength (λ) of the radiation is the same after as before the scattering event. Rayleigh scattering (σ_R) is a particular example of this involving particles with a smaller diameter than the incident light

wavelength of incident light. The Rayleigh scattering cross-section varies as $\sigma_R \propto \lambda^{-4}$ and the phase function $P_R(\theta)$ is given by (Platt and Stutz, 2008):

$$P_R(\Theta) = \frac{3}{4}(1 + cos^2\Theta) \tag{2.2}$$

where Θ is the scattering angle. If the size of the scattering particle and the incident light wavelength are similar, such as for the interaction of light with most atmospheric aerosols, the inelastic process is called Mie scattering. The wavelength dependence of Mie scattering is more complicated than for Rayleigh scattering because Mie theory also considers absorption. However, approximations such as the Henyey-Greenstein parameterisation can be made for the phase function (Platt and Stutz, 2008). The Henyey-Greenstein parameterisation relies on knowing the asymmetry parameter g:

$$g = \frac{1}{2}\int_0^\pi P(\Theta)\cos\Theta\sin\Theta d\Theta \tag{2.3}$$

with g ranging between possible values of -1 to 1, and is typically 0.6-0.7 for tropospheric aerosols (Platt and Stutz, 2008). The Henyey-Greenstein parameterisation for the phase function of Mie scattering is then

$$P_M(\Theta) = \frac{1 - g^2}{4\pi(1 + g^2 - 2g\cos\Theta)^{3/2}} \tag{2.4}$$

Forwards and backwards scattering directions are equally preferred in the case of Rayleigh scattering as shown in figure 2.1, while the Henyey-Greenstein equation indicates that the scattering direction depends on g. Positive values of g give preferential forward scattering, as indicated by the blue line in figure 2.1 (for $g = 0.7$).

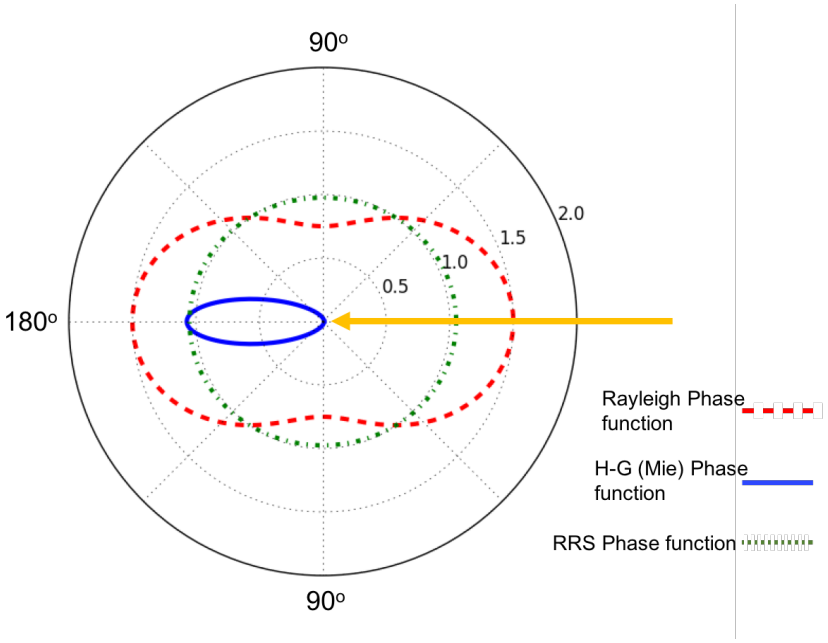

Figure 2.1: Polar plot showing the Rayleigh scattering phase function (red dashed line), Mie scattering phase function (solid blue line, parameterised by the Henyey-Greenstein equation) and the rotational Raman scattering phase function (green dotted line). The direction of the incident light is indicated by the yellow arrow and the scattering event is at the origin.

Inelastic scattering means that the wavelength of the light changes as a result of the scattering process. In the atmosphere, inelastic scattering typically results in energy being transferred from the light to the particle, resulting in an increase in the wavelength, known as a Stokes shift (Whiteman et al., 1992). *Raman scattering* is an example of inelastic scattering, causing a change in either the rotational or vibrational energy of the molecular scatterer. Cross sections for rotational Raman scattering (RRS) can be calculated for different molecules according to:

$$\sigma_{RRS} = \frac{256\pi^5}{27\lambda^4}\gamma^2.f(T,J).b(J \rightarrow J') \tag{2.5}$$

where γ is the polarizability anisotropy which is a property of each molecule, $f(T,J)$ is the fractional population of initial energy states and $b(J \rightarrow J')$ is the quantum state-dependant Placzek-Teller coefficient for a given energy transition (Chance and Spurr, 1997; van Deelen, 2007). Cross sections for Raman scattering of N_2 and O_2 are commonly calculated because these are the most abundant atmospheric molecules. The RRS phase function, which is also plotted in figure 2.1, shows uniform preference for scattering direction (Vountas et al., 1998):

$$P_{RRS}(\Theta) = \frac{3(13+\cos^2\Theta)}{40} \tag{2.6}$$

The clearest influence of RRS in atmospheric spectroscopy is the blurring of Fraunhofer lines discovered by Grainger and Ring (1962) and termed the 'Ring effect'. The primary cause of the Ring effect has been variously hypothesised as Rayleigh and/or Mie scattering and aerosol fluorescence, but is now believed to be predominantly due to rotational Raman scattering (Fish and Jones, 1995; Harrison and Kendall, 1974). In spectroscopic applications the Ring effect is usually accounted for by including a 'Ring effect' cross section as a fictitious absorber (e.g. Hönninger and Platt (2002), Wagner et al. (2004) and Frieß et al. (2006)).

Radiative transfer models (RTMs) have been written which allow simulation of atmospheric scattering and absorption at different geometries by considering the above underlying theory. Simulations computing, for example, changes in intensity of light passing through sections of the atmosphere, are computationally challenging but are crucial for interpreting the absorption spectra that form the basis of atmospheric spectroscopy.

2.1.2 Differential optical absorption spectroscopy

In addition to the scattering described in the previous section, attenuation of radiation in the atmosphere occurs due to absorption by molecules and particles. Each absorbing species has a so-called fingerprint absorption cross section, preferentially attenuating some wavelengths in the electromagnetic spectrum and not others due to the different energy transitions within the molecule. Absorption of infrared radiation, for example by carbon dioxide, results from intra-molecular bond vibrations. We will focus here on UV-visible absorption, which results from electronic transitions within molecules such as ozone and nitrogen dioxide.

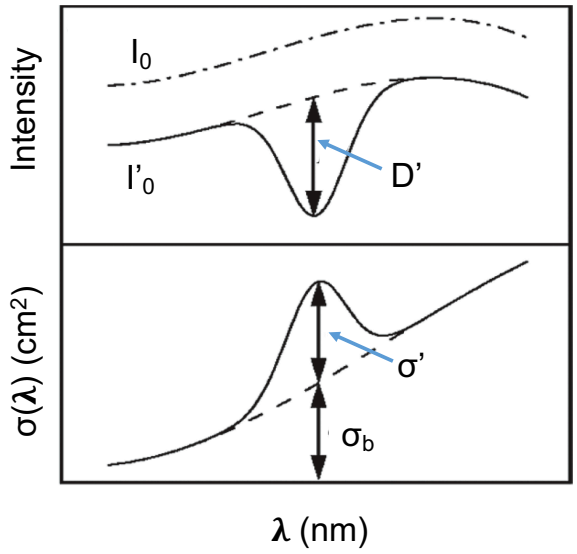

Figure 2.2: Schematic showing the DOAS technique. An absorption spectrum, in intensity (I) or optical density (σ) can be separated into broadband (I'$_0$ and σ') and narrowband (D' and σ_b) components. Image adapted from Platt and Stutz (2008).

Atmospheric spectroscopy in the UV-vis region relies on matching the fingerprint absorptions of atmospheric constituents to measured spectra of light traversing the atmosphere. As with laboratory based UV and visible spectroscopy methods, the primary theory is detailed by the Beer-Lambert Law where the intensity of light $I(\lambda)$ is given by:

$$I(\lambda) = I_0(\lambda) \exp(-\sigma(\lambda) C L) \tag{2.7}$$

$I_0(\lambda)$ is the initial light intensity, L is the light pathlength through the medium and C and $\sigma(\lambda)$ are the concentration and absorption cross section of the absorbers respectively. In an ideal laboratory experiment, all variables except the concentration are known, however in the atmosphere the number of possible scattering and absorption possibilities makes determining the light pathlength difficult. The differential optical absorption spectroscopy (DOAS) method provides a way to apply the Beer-Lambert Law to the atmosphere. It simplifies the problem by separating the broad, slowly varying (with wavelength) attenuation due to Rayleigh scattering, for example, from the sharp absorption lines of specific absorbers as shown in figure 2.2. The broadband component is designated as $I_0(\lambda) \rightarrow I_0'(\lambda)$, allowing the Beer-Lambert Law to operate on the narrowband absorption features (Platt and Stutz, 2008). Considering small photon light path segments through the atmosphere dL and writing the intensity as an integral over all possible light paths gives rise to a Beer-Lambert Law for DOAS:

$$I(\lambda) = I_0'(\lambda) \exp^{-\int(\sigma_j(\lambda_j)C(L)+\epsilon_R(\lambda,L)+\epsilon_M(\lambda,L))dL} \tag{2.8}$$

Rather than solving explicitly for concentration as in a laboratory experiment, the primary result of using the DOAS Beer-Lambert law is the slant column density given by $S = \int C(L)dL$. Slant columns for each molecule (S_i) are calculated by linearizing the Beer-Lambert law, approximating the unstructured Rayleigh and Mie scattering terms ($\epsilon_R(\lambda, L) + \epsilon_M(\lambda, L)$)) with a smooth polynomial $P(\lambda)$ and solving the resulting DOAS equation:

$$\ln I(\lambda) = \ln(I_o(\lambda) - P(\lambda) - \sum_i \sigma_i(\lambda)S_i \tag{2.9}$$

The slant column density for an atmospheric constituent is related to its vertical column density (V) by the airmass factor which is $A = S/V$. Airmass factors can be calculated for given viewing geometries by radiative transfer models, allowing vertical trace gas columns to be determined from DOAS measurements. Atmospheric trace gases commonly measured using DOAS include NO_2, HCHO, HONO, glyoxal, BrO and IO. Cross sections of these molecules in the UV-vis region of the electromagnetic spectrum are depicted in figure 2.3.

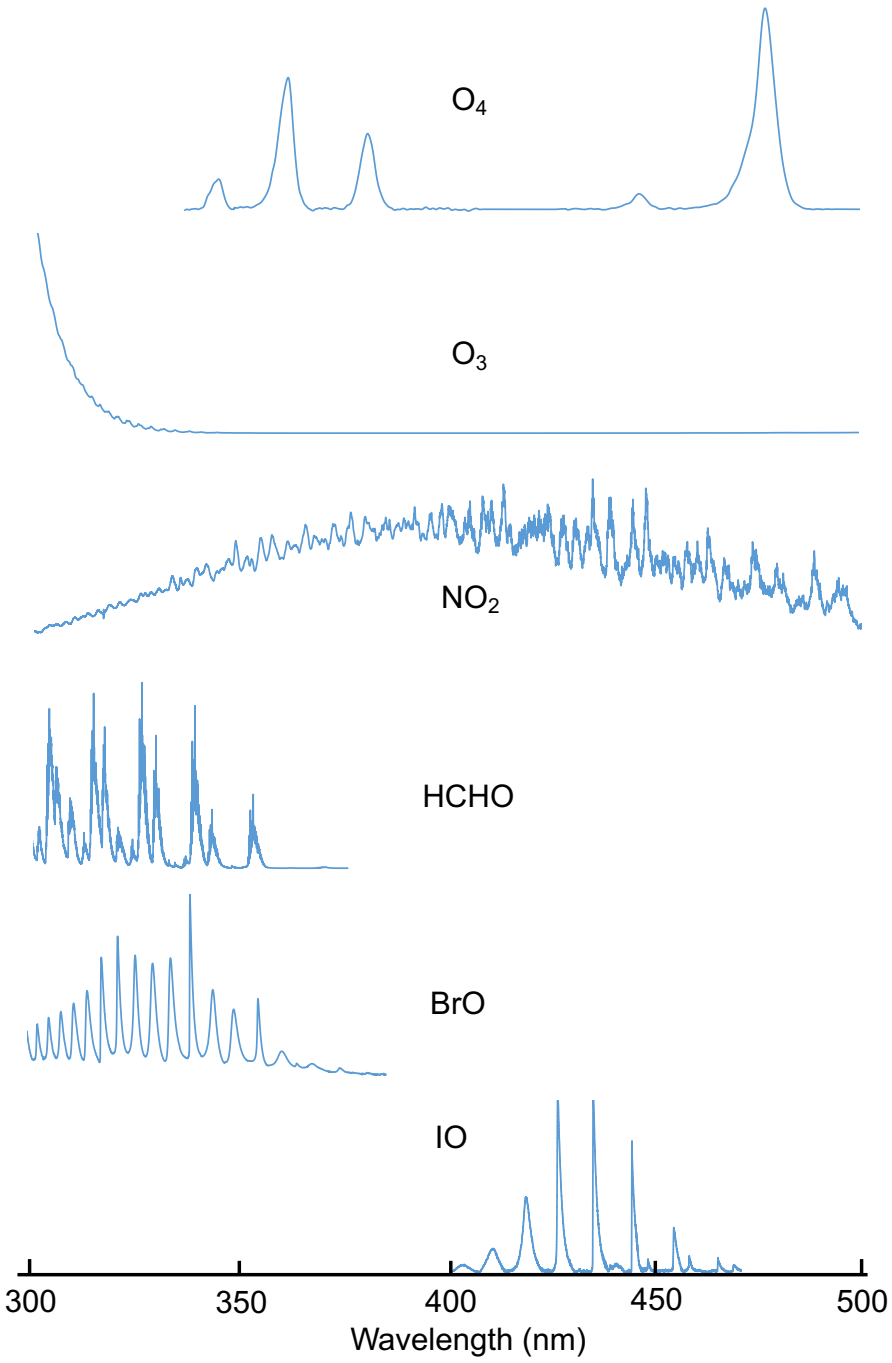

Figure 2.3: Absorption cross sections of molecules commonly measured using the DOAS technique.

DOAS has been successfully demonstrated on a wide variety of platforms, including satellites, aeroplanes, ships, towers and ground-based stations. These remote sensing

techniques, so called because they measure across a section of the atmosphere as opposed to in-situ point source techniques, can be either active if they require a synthetic light source or passive if they use natural radiation. The retrieval process is usually more straightforward for active DOAS because both light pathlengths and discrete wavelengths are well constrained. Because it does not rely on a powered light source, passive DOAS is usually cheaper to run and easier to automate. Using the Sun as a light source also allows all wavelengths of the solar spectrum, and a range of viewing geometries, to be used in the analysis. The three key angles used to define the viewing geometry in a passive DOAS setup are the solar zenith angle (θ), which is the angle of the Sun relative to the zenith, the relative azimuth angle (ζ) which is the relative compass direction between the detector and the sun and the elevation angle (α) which is the detector pointing angle relative to the horizon.

Multi-Axis (MAX-) DOAS makes use of multiple viewing geometries by collecting sets of spectra at different elevation angles. θ and α are depicted in relation to a MAX-DOAS setup in figure 2.4. According to Hönninger et al. (2004), for MAX-DOAS measurements the slant column density can be approximated as:

$$S \approx V(\frac{a}{\sin\alpha} + \frac{1-a}{\cos\theta}) \tag{2.10}$$

with a being the fraction of the vertical absorber/scatterer column V, residing below the scattering altitude. Attenuation in the lower atmosphere will enhance S by a factor of $\frac{1}{\sin\alpha}$ while an attenuation in the upper atmosphere will enhance S via the $\frac{1}{\cos\theta}$ factor. This means that measurements dependent on the solar zenith angle θ will yield information about high (i.e. stratospheric) absorbers, while measurements dependent on the elevation angle α will yield information on tropospheric absorbers. At a given solar zenith angle, light collected at a range of elevation angles will have approximately the same pathlength through the upper atmosphere, but different pathlengths (dependent on scattering) through the lower atmosphere as illustrated in figure 2.4. Therefore ratioing spectra from low elevation angles with spectra from high elevation angles (usually 90°) allows the stratospheric influence to be mostly cancelled out, meaning that the resulting differential slant column (dSCD) contains tropospheric specific information (Platt and Stutz, 2008; Hönninger and Platt, 2002). The measurement vector comprising a set of dSCDs at different elevation angles contains not just information on the total vertical trace gas column, but also the vertical distribution of the trace gas within the column (Hönninger and Platt, 2002; Hönninger et al., 2004; Platt and Stutz, 2008; Frieß et al., 2006; Wagner et al., 2004). This is the power of the MAX-DOAS technique: a passive solar spectroscopic technique which can resolve vertical profiles of UV/Vis-absorbing trace gases. In chapter 3 the steps required to retrieve vertical profile information will be described, however in the remainder of this chapter, optimisation of the procedure for calculating differential slant columns will be discussed.

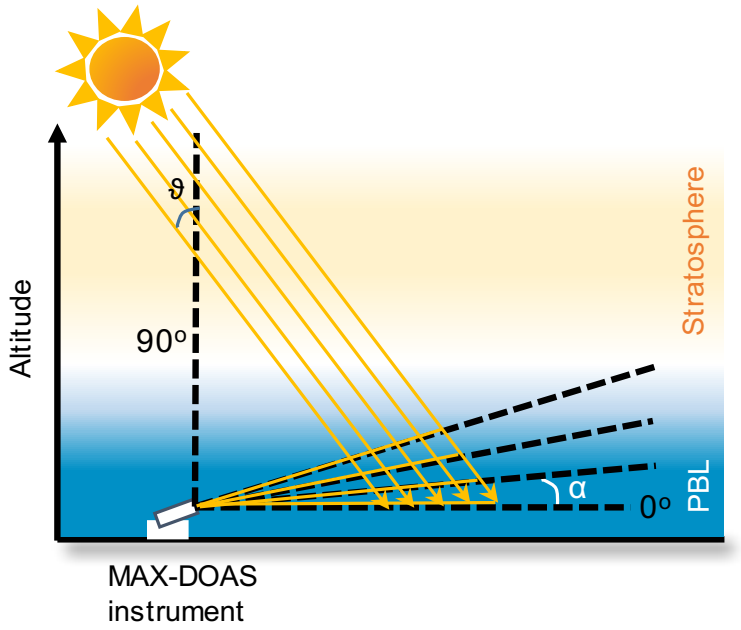

Figure 2.4: Simple MAX-DOAS geometry showing the elevation angle (α) and solar zenith angle (θ) relative to the detector and the sun, respectively. Observations at low elevation angle provide long path lengths through the planetary boundary layer (PBL) while having the same path through the stratosphere.

2.2 MAX-DOAS instrumentation

The MAX-DOAS instruments used in this work are all manufactured in Germany by Environmental Measurement Systems ("Envimes"), with the following specifications in common. The hardware consists of a scanning telescope unit, looking towards a single fixed azimuth during each campaign. The optics head connects by fibre optic and data cables to a spectrometer unit containing of temperature stablized 75 mm Avantes spectrometers for the UV (range 295-450 nm, ≈0.6 nm resolution) and visible (range 430-565 nm, ≈0.6 nm resolution) regions. The UV detectors are Hamamatsu backthinned detectors with Schott BG3 filters and 2048 pixel channels while the visible detectors are a Sony 2048L models also with 2048 channels. Example spectra from each spectrometer are shown in figure 2.5. The telescope unit contains a rotating prism and inclinometer facilitating active elevation control with quoted elevation angle accuracy $< 0.1°$. Annotated images of the University of Melbourne Envimes MAX-DOAS instrument are shown in figure A.2 in Appendix A. Commercial grade Envimes MAX-DOAS instruments have demonstrated good performance at the MAD-CAT intercomparison campaign in Mainz, Germany (Lampel et al., 2015; Wang et al., 2017b) and the CINDI-2 campaign in the Netherlands in 2016 (including the NIWA Envimes MAX-DOAS discussed in chapters 4 and 7).

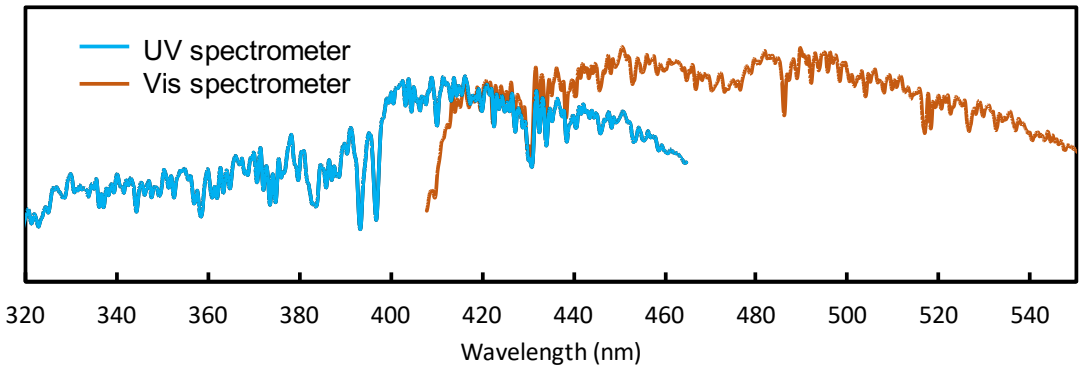

Figure 2.5: Example spectra from the University of Melbourne MAX-DOAS UV and visible spectrometers.

2.3 Measurement and calibration: general settings

The Envimes MAX-DOAS instruments were controlled using MS-DOAS, software facilitating communication between the spectrometer box and optics head. Measurement sequences can be programmed in MS-DOAS by the user allowing control of elevation angles, azimuth directions, spectral integration times and calibration routines. For each of the instruments used in this work, initial wavelength calibration polynomials were determined using emission lines from an external mercury lamp (extra wavelength calibrations were also undertaken in the spectroscopic analysis stage as discussed below). Spectra were also corrected for detector non-linearity, dark current and spectral offset using laboratory measurements. Dark current spectra were collected with 10 scans each of 30 s exposure time and offset spectra were collected with 10,000 scans each of 3 ms exposure time as recommended in the Envimes manual. Example dark current and offset spectra are shown in figure A.1 in Appendix A. Spectra were collected on a repeating program of elevation angles, typically including 90°, 30°, 20°, 10°, 5°, 3° and 2°, 1° and 0° which took between 10-15 minutes to complete depending on the exact number of angles. While the University of Melbourne instrument has capability to conduct azimuth scans too, this function was not employed throughout the work discussed in this thesis.

All spectral analysis was carried out using the QDOAS software package developed at BIRA in Brussels, Belgium. QDOAS provides an easy-to-use graphical interface and incorporates wavelength calibration, spectral convolution, Ring spectra calculation and DOAS fitting capability. The baseline settings for DOAS analysis in the UV were taken from the standardised protocol during the CINDI-2 campaign as outlined by Kreher et al. (2020). These settings are listed in table 2.1. The absorption cross sections listed in table 2.1 and shown in figure 2.3 were used in all UV analyses (wavelength fitting ranges between 300-380 nm).

DOAS parameter	Setting	Reference
O_3 xs (223 and 243 K)	Pre-orthogonalised	Serdyuchenko et al. (2014)
NO_2 xs (298 K)	-	Vandaele et al. (1998)
O_4 xs (293 K)	-	Thalman and Volkamer (2013)
HCHO xs (297 K)	-	Meller and Moortgat (2000)
BrO xs (223 K)	-	Fleischmann et al. (2004)
HONO xs (296 K)	-	Stutz et al. (2000)
Ring effect (250 K)	Calc. in QDOAS	Grainger and Ring (1962)
Polynomial	5^{th} order	-
Offset	2^{nd} order	-
WL cal.	Reference only	-
WL cal. range	320-460 nm	-
WL cal. bins	20	-
XS convolution	Offline	-
DOAS reference	Sequential	-
Shift	Ref and spec, all cross sections	

Table 2.1: Standard cross sections and DOAS settings used in this work for the UV range.

2.3.1 DOAS tests: polynomial, offset, shift fit

In order to understand in more detail the importance of individual DOAS settings, a series of simple sensitivity studies were conducted in QDOAS. In the first of these studies, the order of the DOAS polynomial and offset polynomial were varied, with the resulting residual RMS, O_4 and NO_2 dSCDs compared in each case. In subsequent tests, the utility of the 'shift fit' was investigated: this represents whether the spectrum and reference, or the cross sections, are allowed to shift with respect to each other. The baseline settings for these tests are those listed in table 2.1 using the wavelength range 338-370 nm. The modification to these settings in each test case is listed in table 2.2. Data from the Bureau of Meteorology instrument at Broadmeadows from 16/02/2017, a clear sunny day, was used in these sensitivity studies. As shown in figure 2.6, the largest increase in the residual RMS relative to the standard settings, was turning off the shift fit. The magnitude of the O_4 and NO_2 dSCDs were largely unaffected by any of the changes in DOAS polynomial or offset order, however the residual RMS tended to be higher with decreasing DOAS polynomial and offset. On the basis of these sensitivity studies, no reason was found to alter the standard settings of including shift fit for cross sections and for spectrum vs reference, 5th order DOAS polynomial and 2nd order offset term.

Test number	Modification to standard settings
338-370 t1	4th order polynomial
338-370 t2	3rd order polynomial
338-370 t3	2nd order polynomial
338-370 t4	1st order polynomial
338-370 t5	1st order offset
338-370 t6	0th order offset
338-370 t7	No offset
338-370 t8	No shift fit (Ref and Spec)
338-370 t9	No shift fit (cross sections)
338-370 t10	No shift fit at all

Table 2.2: Details of DOAS tests for polynomial, offset and shift fit, carried out in the UV region.

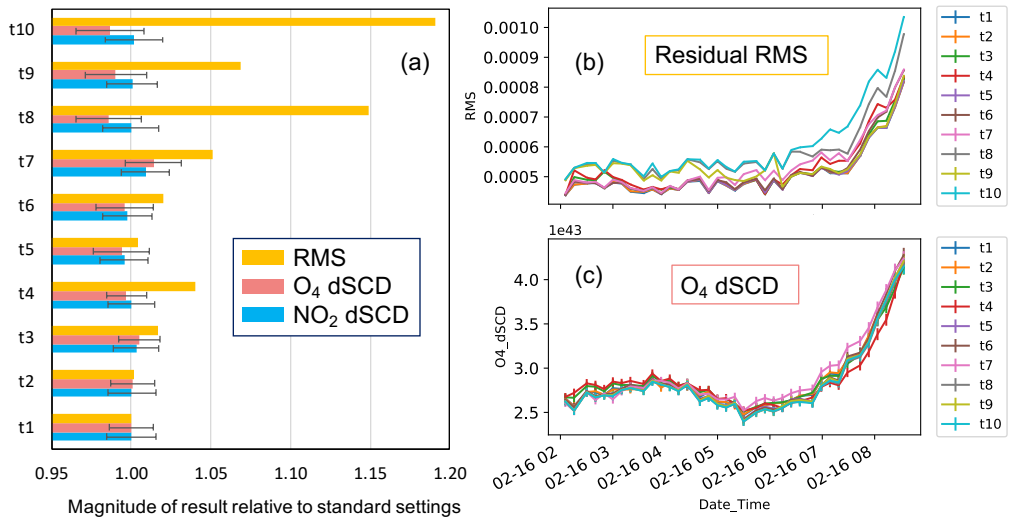

Figure 2.6: Results of general QDOAS settings tests (detailed in table 2.2) for Bureau of Meteorology data, 16/02/2017: (a) Bar chart showing the magnitude of the change in residual RMS, O_4 dSCD and NO_2 dSCD for each test, relative to the standard settings. (b) Timeseries of residual RMS for each test, for the sample period on 16/02/2017. (c) Same as (b) but for O_4 dSCDs.

2.3.2 DOAS tests: Wavelength calibration windows

Determining the wavelength calibration of the spectrometer is a key step before DOAS analysis can proceed. The initial spectrometer pixel-wavelength mapping is typically achieved by measuring reference spectral lines e.g. from a mercury emission lamp. However, depending on the wavelength range of the spectrometer there may be only a

few emission lines from which to derive the calibration, potentially introducing small inaccuracies in between the lines. Moreover, the wavelength calibration of a spectrometer may not be linear between the reference lines. These inaccuracies become important when resolving weak trace gas absorptions. To address this, additional high-resolution wavelength calibration routines can be employed for example by calibrating against the solar Fraunhofer lines. QDOAS facilitates this by dividing the spectrometer's wavelength range into a prescribed number of bins, and in each bin fitting a measured scattered light spectrum with a high-resolution solar reference spectrum. In QDOAS this can be done on every measured spectrum in turn, but this is time consuming and unnecessary if the wavelength calibration adjustment is consistent. Therefore the procedure is usually carried out on an example reference spectrum. The number of bins chosen is a trade-off between dividing the spectrum into enough segments that any systematic wavelength-dependent shift from the initial calibration is resolved, but not so many bins that spectral noise and large trace gas absorptions are interpreted as a wavelength calibration shift.

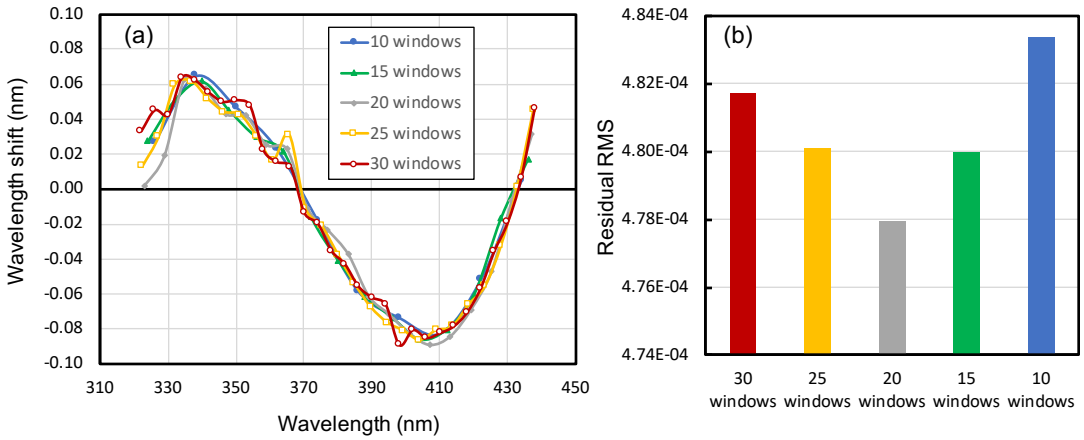

Figure 2.7: Results of QDOAS tests with different numbers of wavelength calibration bins: (a) Magnitude of the wavelength shift as a function of wavelength, for each test set. (b) Residual RMS of the DOAS fit analysis (338-370 nm) for each test set.

A simple sensitivity study was run to determine the optimal number of wavelength calibration bins, using between 10-30 bins. Figure 2.7(a) shows the calculated shift from the initial wavelength calibration (determined using mercury emission lines) as a function of wavelength, for each test number of bins. In each case the same systematic shift pattern is observed, suggesting at the outset that non-linearity makes the high-resolution calibration procedure necessary. Largest deviations in shift magnitude between the tests are observed at the UV end of the spectrum. To quantify the impact of the number of bins on the DOAS fit result, the average residual RMS for each test case, using data from the Bureau of Meteorology MAX-DOAS at Broadmeadows on a clear day (16/02/2017), was plotted in figure 2.7(b). Here the optimum value, indi-

cated by the lowest average residual RMS, is evidently 20, hence this value was taken as standard throughout the DOAS analyses in this work.

2.4 Specific DOAS analysis settings

In addition to the DOAS settings discussed above, the other key parameter is the wavelength range of the DOAS fit. Choosing a wavelength range is a trade off between encompassing the spectral bands of the trace gases of interest, and minimising the possibility of interference with other trace gas absorption features. The main trace gases considered in this work were O_4, NO_2, O_3, HCHO, HONO, CHOCHO, BrO and IO. Normalised absorption cross sections of these molecules are plotted in figure 2.3. The main absorption features for each of these molecules lie between 320 and 460 nm, so DOAS fitting throughout this thesis was concentrated in that window.

2.4.1 UV range

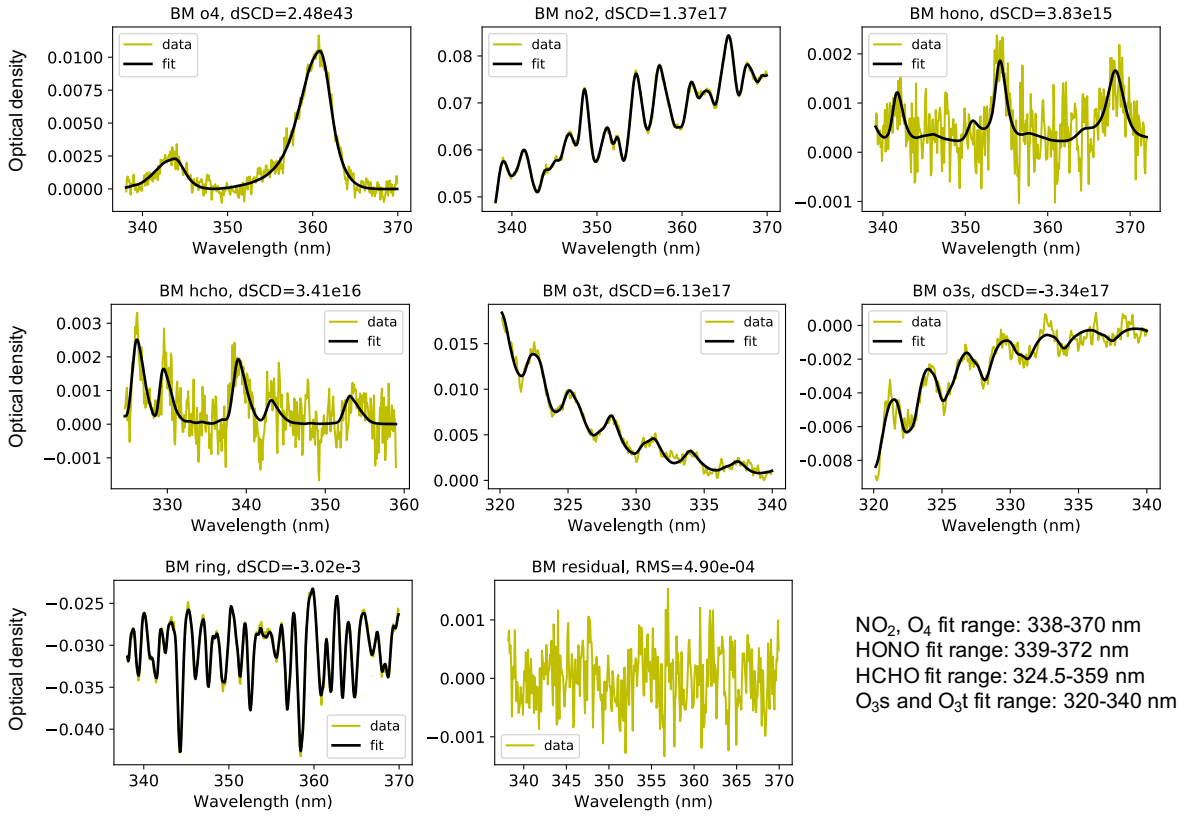

Figure 2.8: Example fits in the UV region from QDOAS, data taken from midday on 16/02/2017 using the Bureau of Meteorology MAX-DOAS at Broadmeadows. "BM" indicates the results are from the Bureau of Meteorology MAX-DOAS. "o3s" and "o3t" indicate ozone at representative stratospheric (220 K) and tropospheric (298 K) temperatures respectively. The solar zenith angle was 20.7° and the elevation angle was 3°.

O_4 and NO_2

The two main O_4 absorption features accessible to the MAX-DOAS instruments used in this work are at 361 nm (for the UV spectrometers) and 477 nm (for the visible spectrometers). Prominent absorption bands for NO_2 can be found across the range of both spectrometers. In this work the UV range was chosen for fitting O_4 and NO_2. The standard UV wavelength range recommended during CINDI-2 for fitting these is 338-370 nm (Kreher et al., 2020) and was adopted throughout the analyses in this thesis. Example fits in this window for NO_2 and O_4, along with the fit for the Ring effect and the overall residual are shown in figure 2.8.

HCHO

Strong absorption bands for formaldehyde are in theory accessible to the MAX-DOAS UV spectrometer down to 300 nm. Published examples tend to steer clear of fitting below 320 nm however due to strong ozone absorption and a higher signal to noise ratio. Most papers use a fitting range of ≈336-359 nm (e.g. Kreher et al. (2020), Heckel et al. (2005), Pinardi et al. (2013)) encompassing the three highest UV HCHO absorption features. Here a simple sensitivity study was run to determine if any benefit can be derived from including the next set of absorption bands, as in, e.g., Chan et al. (2019), Johansson et al. (2009), Wang et al. (2017e) and Franco et al. (2015). Data for this test was chosen from a warm sunny Autumn day at Broadmeadows with maximum HCHO dSCDs $\approx 7.5 \times 10^{16}$ molec.cm^{-2} at 1° elevation angle. As shown in figure 2.9, the change of wavelength range had minimal impact on the residual RMS throughout the day, and minimal impact on the magnitude of the HCHO dSCD. However despite minimal change in dSCD, the fit error was greatly reduced by using the longer wavelength range, therefore the 324.5-359.0 nm range was adopted as the standard employed for fitting formaldehyde.

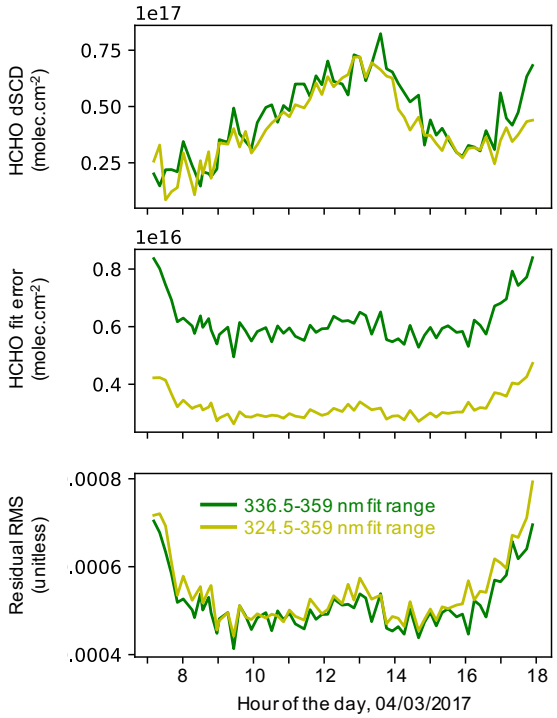

Figure 2.9: Results of sensitivity tests to determine the appropriate fitting range for formaldehyde, using data from 04/03/2017 at Broadmeadows using the Bureau of Meteorology MAX-DOAS. All results are from the 3° elevation angle.

HONO

A sensitivity study to optimise the HONO fitting wavelength range was performed using the retrieval interval mapping technique of Vogel et al. (2013) (fig. 2.10(a)) which showed that the smallest HONO fit percentage errors correspond to a wavelength range starting below 340 nm. When compared to the plot showing all cross sections fitted in the wavelength ranges in figure 2.10(b), these results show that the HONO fit error is improved by including all three of the largest HONO cross section peaks, including the 341 nm peak which overlaps strongly with formaldehyde (HCHO) and O_4 peaks. This is in line with Wang et al. (2017b) and Hendrick et al. (2014), although the fitting window 339-372 nm chosen here for HONO is shorter than used in these papers in order to minimise the overall residual RMS of the fits, while maintaining low HONO fit errors.

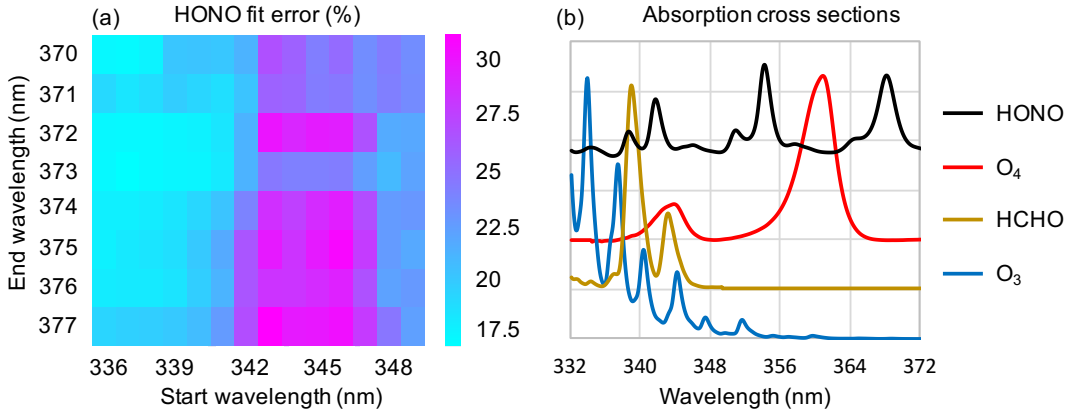

Figure 2.10: Results of sensitivity study to determine the appropriate wavelength range for fitting HONO. (b) Cross sections plotted in the HONO sensitivity study range showing overlap of cross section peaks.

2.4.2 Visible range

Glyoxal (CHOCHO) and iodine monoxide (IO) were the two main trace gases analysed in the visible wavelength range ($\lambda > 400$ nm). In general, residual structures after DOAS fitting were found to be greater for IO and glyoxal fits than the UV species discussed above. This was due to greater sensitivity of the retrieval to the accuracy of the wavelength calibration and strong absorption by water close to the main IO and CHOCHO lines. Other important factors to consider in the visible region include the influence of stratospheric NO_2 absorption (accounted for by the NO_2 cross section at 220 K, denoted by NO_{2s}), vibrational Raman scattering and the so-called 'tilt' of the Ring effect. With these in mind, some sensitivity tests were carried out to optimise the visible range fitting cross sections and settings, where the standard fit settings outlined in table 2.3 were varied.

DOAS parameter	Setting	Reference
O_3 xs (223 K)	-	Serdyuchenko et al. (2014)
NO_2 xs (220 and 298 K)	Pre-orthogonalised	Vandaele et al. (1998)
O_4 xs (293 K)	-	Thalman and Volkamer (2013)
H_2O (298 K) xs	-	Rothman et al. (2010)
CHOCHO (298 K)	-	Volkamer et al. (2005)
IO *	-	Spietz et al. (2005)
Ring effect (250 K)	Calc. in QDOAS	Grainger and Ring (1962)
Vibrational Raman (ceO2)	-	Lampel (2014)
Vibrational Raman (ceN2)	-	Lampel (2014)
Polynomial	5^{th} order	-
Offset	2^{nd} order	-
WL cal.	Reference only	-
WL cal. range	320-460 nm	-
WL cal. bins	20	-
XS convolution	Offline	-
DOAS reference	Sequential	-

Table 2.3: Standard cross sections and DOAS settings used in this work for the visible range. * IO cross section only included in IO fitting range, for spectral analysis at the coastal Garden Island campaign site.

Wavelength ranges for fitting IO and CHOCHO were first determined. DOAS fitting for iodine monoxide and glyoxal is complicated by a number of co-located absorption features, notably water (and glyoxal itself in the case of fitting for IO) as shown in the overlayed cross sections in figure 2.11. Furthermore, as noted in Lampel (2014) there is a current lack of understanding of O_4 absorption below 435 nm, e.g. Thalman and Volkamer (2013) does not include this range at all and Hermans et al. (2003), shown in figure 2.11, shows an unrealistic step feature. IO absorption features were not observed at all in spectra from Melbourne or Lauder but was detected, albeit with a weak absorption signal, during the month-long measurement campaign at Garden Island.

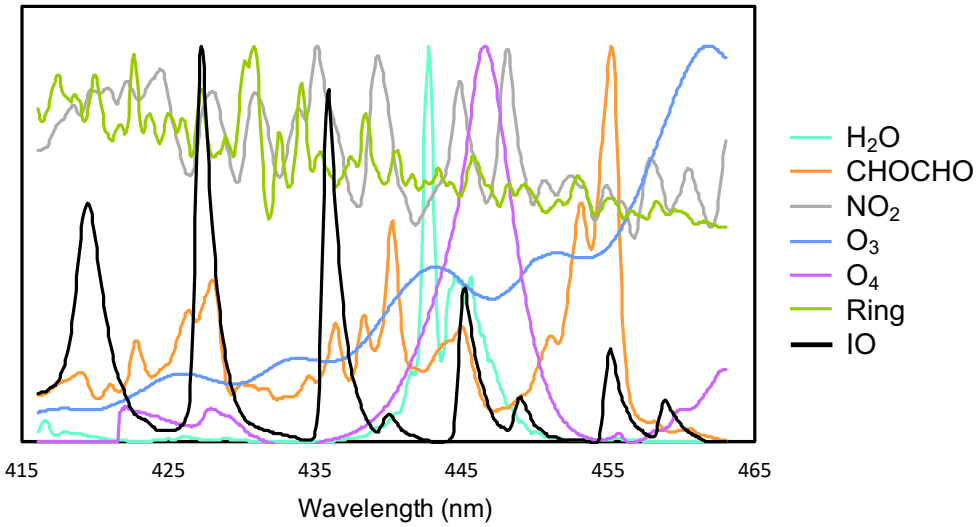

Figure 2.11: Overlayed cross sections in the wavelength range 415-465 nm which includes the absorption bands of IO and glyoxal.

For iodine monoxide, Lampel (2014) recommended a fitting range encompassing the three strongest IO bands between 416-438 nm. This was trialled alongside tests with only two absorption bands and up to all five bands as shown in 2.11. One advantage of choosing 416-438 nm is that it avoids the strong water absorption beginning at 442 nm. As shown in figure 2.12(a), this window gives low and stable fit percentage errors (IO fit error as a percentage of the dSCD) and residual RMS. In contrast, options using only two IO bands (e.g. 416-430 nm) or excluding the lowest IO bands (e.g. 425-463 nm) give large and/or highly variable fit percentage errors. Ultimately, the range chosen was 416-450 nm, encompassing four IO absorption bands and the water absorption. Compared to the 3-band fit, the residual RMS is only marginally higher by including the water absorption, while the inclusion of four IO bands gives the lowest fit percentage error.

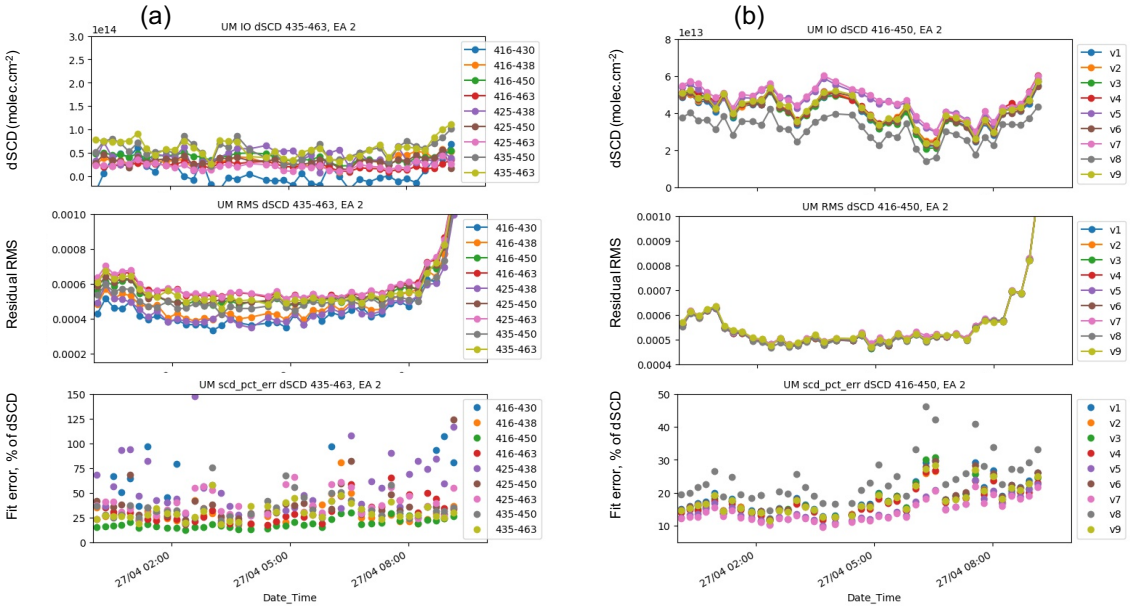

Figure 2.12: Results of the sensitivity studies for iodine monoxide using results from 19/04/2018 at Garden Island. The results are top: diurnal magnitude of the IO dSCD, middle: magnitude of residual RMS and bottom: IO fitting error as a percentage of the IO dSCD. (a) shows results for various fitting wavelength ranges, and (b) shows results for DOAS settings and cross section tests outlined in table 2.4.

For glyoxal, figure 2.11 shows that absorption bands are present in the visible region from 420 to 455 nm. However, a recent comprehensive sensitivity study carried out by Javed et al. (2019) clearly indicated more robust retrievals (lower residual RMS and lower fit errors) for wavelength ranges starting between 432-438 nm. This is likely due to the uncertainty in O_4 cross section below 435 nm. As a result, in this thesis, a wavelength range neatly encompassing the glyoxal bands above 435 nm was chosen, i.e. 435.0-456.5 nm.

With the wavelength ranges chosen, the next set of tests were to determine optimal cross sections and DOAS settings in the visible region. From the standard visible DOAS settings outlined in table 2.3, cross sections were varied across ten tests as described in table 2.4. Vibrational Raman scattering (VRS) was argued to be an important consideration in retrieving IO and CHOCHO by Lampel et al. (2015). Like rotational Raman scattering which gives rise to the filling in of Fraunhofer lines (the Ring effect, Grainger and Ring (1962)), VRS is a form of inelastic scattering which is estimated to make up around 2% of all atmospheric scattering events (Lampel, 2014). Rotational and vibrational Raman scattering lines for N_2 and O_2, the most prevalent atmospheric molecules, occur between 415 and 435 nm, coinciding with absorption features of the CHOCHO and IO cross sections (Lampel, 2014; Lampel et al., 2015).

Tests v2-v4 experimented with removing the VRS cross sections to determine if their

inclusion improves the fit results. The second additional cross section trialled was the so-called 'Ring-tilt'. This effect arises from the wavelength dependence of the amplitude of the Ring effect as highlighted by Wagner et al. (2009). Variations in Ring effect amplitude as a function of wavelength are expected to be enhanced (a) under conditions of multiple Rayleigh scattering, (b) high aerosol optical depths and cloud, and moreover (c) when using a wide fit wavelength range. While the proposed wavelength ranges for fitting glyoxal and IO here are not large, persistent residual structures were observed in the results, especially at low elevation angles, and hence a Ring tilt spectrum was tested (test v5). Further visible range tests v8-v9 examined the influence of different O_4 cross sections given the lack of cross-section agreement around the small 447 nm O_4 peak. In recent literature, considerable attention has been paid to updating UV water vapour cross sections to aid spectral evaluation of water and trace gases absorbing at similar wavelengths (Polyansky et al., 2018; Lampel et al., 2017). Previous studies using MAX-DOAS to measure glyoxal, for example, have relied upon the HITRAN (Rothman et al., 2009) or HITEMP (Rothman et al., 2010) water line lists. The HITEMP cross section was used in the standard visible settings here but in test v10 the more recent Polyansky et al. (2018) version was used.

Test number	Settings
v1	Standard settings
v2	VRS O_2 removed
v3	VRS N_2 removed
v4	both VRS removed
v5	Ring tilt removed
v6	NO_{2s} removed
v7	VRS, ring tilt and NO_{2s} all removed
v8	O_4 using Hermans xs
v9	O_4 using Greenblatt xs
v10*	H_2O using Polyansky xs

Table 2.4: Details of cross-section and DOAS setting tests in the CHOCHO and IO fitting regions. *v10 was used only in the glyoxal tests. VRS is Vibrational Raman Scattering, xs is cross section, NO_{2s} is the NO_2 cross section at 220 K representative of stratospheric NO_2.

The results of the fitting tests for IO (figure 2.12(b)) show that none of the tests made a noticeable difference at all to the residual RMS. However, differences were apparent in the retrieved dSCD amount and the fitting error, expressed here as a percentage of the total IO dSCD. Clearly the largest percentage fit error and the lowest dSCD were found using the Hermans O_4 cross section. The fit percentage error plot also shows that the original Thalman and Volkamer O_4 cross section is preferable to the one from Greenblatt. Removal of the N_2 VRS cross section had a negative impact on the fit percentage error. The most significant improvement on the original settings was found to be removing the Ring tilt cross section, for which tests (v5 and v7) the highest

IO dSCD and lowest fit percentage error were found. Hence it is concluded that the persistent residual structure cannot be explained by variations in Ring effect amplitude across the short wavelength range used for analysing IO, and, moreover, inclusion of this effect when not appropriate can cause cross-sensitivities with the Ring cross section that are detrimental to the retrieval. From these sensitivity study results, fitting for IO proceeded using the original standard DOAS visible range settings, with the exclusion of the Ring tilt parameter.

The sensitivity study results in the glyoxal fitting range (figure 2.13(b)) are different in a number of ways. Firstly, it is clear that the different tests have a greater impact on residual RMS in this shorter wavelength range, than for the IO window. Secondly, given that this window cuts out the region of highest uncertainty in O_4 cross section below 435 nm, the test results with alternative O_4 cross sections are also different. Here we see that using the Thalman and Volkamer cross section and the Hermans cross section produces very similar dSCD and residual RMS, although the fit error is typically much higher when using the Hermans cross section. The Greenblatt cross section results in consistently high dSCD, low fit percentage error and low residual RMS. This result is analysed in more detail in figure 2.14 where for test v9, the Greenblatt cross section results in a negative O_4 dSCD whereas the Hermans version (v8) and Thalman and Volkamer (all other tests) produce positive dSCD. Since a negative dSCD implies more of the trace gas in the reference spectrum, the result for the Greenblatt spectrum seems physically implausible (a) because O_4 decreases with height in the atmosphere with the square of atmospheric pressure and it is difficult to imagine how there could be more in the zenith reference spectrum than the 2° elevation spectrum, and (b) the reference, in any case, is the same for all tests. Therefore it is concluded that while the results using the Greenblatt O_4 cross section seem promising, they cannot be trusted, and the original Thalman and Volkamer cross section was retained for the glyoxal analysis.

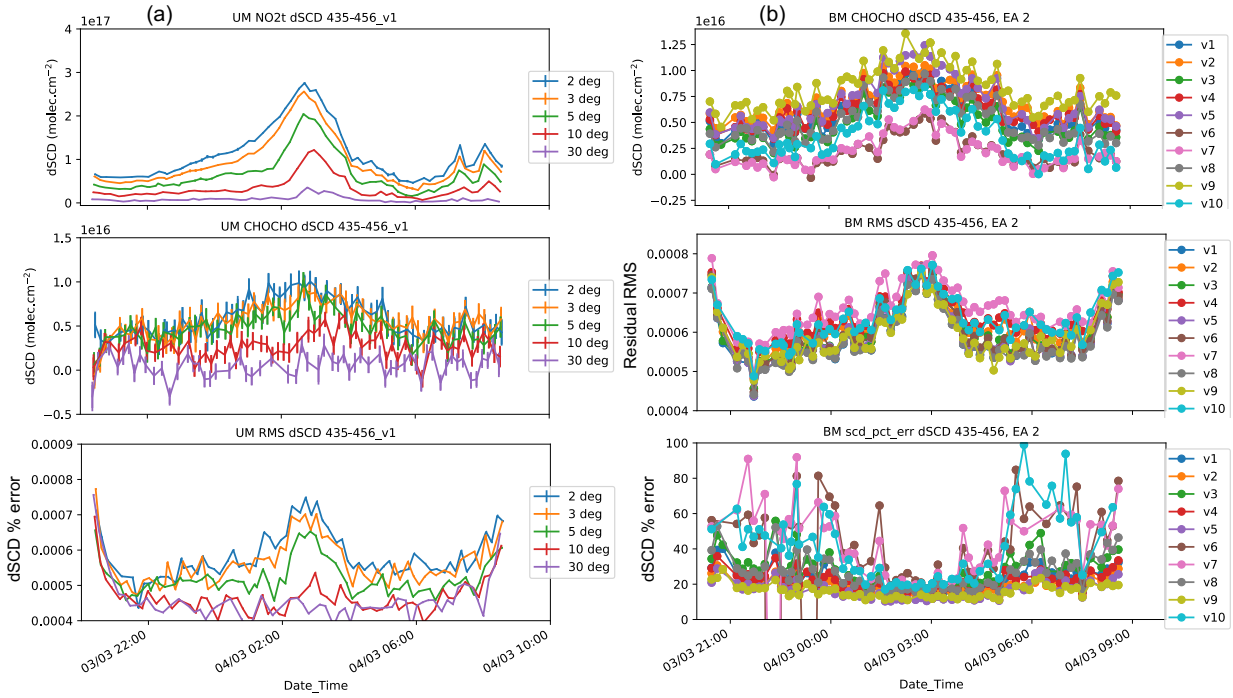

Figure 2.13: (a) Results of DOAS fitting in the glyoxal range (435.5-465.5 nm) for an example day, 4/3/2017, at Broadmeadows. dSCDs for each elevation angle are plotted for NO_2 and CHOCHO, along with the residual RMS. (b) Results of DOAS tests in the 435.5-465.5 nm range, to determine the most appropriate settings for retrieval of glyoxal. For details on tests v1-v10 see table 2.4. Times are in UTC: 2 am UTC is midday local time.

Similarly to the IO tests, removing the N_2 VRS spectrum was found to be detrimental to the retrieval results, more so than the O_2 VRS removal. The removal of both VRS spectra and the Ring tilt (v6) was found to cause large spikes in fit error, which seemingly can be mostly attributed to the importance of the N_2 VRS since the N_2 inelastic scattering lines (vibrational and rotational Raman) are concentrated inside the chosen glyoxal wavelength range. Interestingly, one of the clearest results from the CHOCHO sensitivity study was that the updated Polyansky water cross section led to significantly higher dSCD fit errors, especially at high solar zenith angles. This result accords with Behrens et al. (2019) who also found no improvement in fit results when using the Polyansky et al. (2018) water vapour cross section instead of the HITEMP linelist. Examining the example fits in figure 2.14, it appears that the source of the enchanced CHOCHO fit error in the case of using the Polyansky et al. (2018) water spectrum are on the 'shoulders' of the water vapour peak (i.e. 440 and 444-445 nm) where enhanced residual structure is evident.

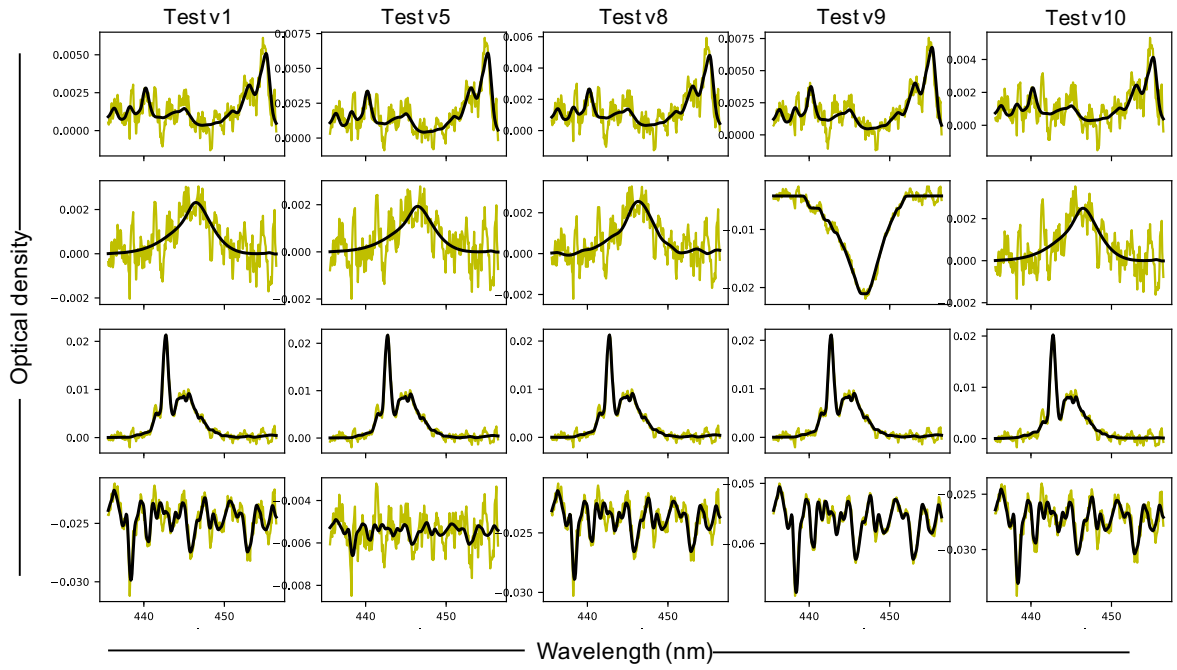

Figure 2.14: Example spectral fits for CHOCHO, H_2O, O_4 and the Ring effect for selected DOAS glyoxal-range tests. For details on tests v1-v10 see table 2.4. Data taken from 4/3/2017 at Broadmeadows, solar zenith angle = 32° and elevation angle = 2°.

Since the Ring tilt spectrum was found to negatively impact the retrieval in the longer IO fit range, it was not surprising to find the same in the shorter CHOCHO range. However, pursuing this result further by examining the spectral fits in figure 2.14 shows the curious outcome that removing the Ring tilt term greatly weakens the strength of the Ring fit itself. Since when the Ring tilt term is removed, the overall residual RMS is barely different but the CHOCHO dSCD is increased, it is implied that the reduction in Ring signal is effectively transferred to the CHOCHO dSCD. This raises the possibility of cross-correlation of the Ring effect and CHOCHO cross section which should be explored more thoroughly in future work.

In the IO and CHOCHO wavelength ranges discussed, more than in the UV wavelength ranges, residual RMS was found to exhibit elevation angle dependence. This is shown for example on 4/3/2017 at Broadmeadows (figure 2.13(a)) where, especially in the middle of the day, there is clearly enhanced residual RMS at low solar zenith angles, which decreases as elevation angle increases. Over the course of glyoxal retrievals at Broadmeadows, such examples frequently correlated temporally with NO_2 and CHOCHO peaks. As seen in figure 2.13(b) the midday residual RMS spike on this day was not remedied by any of the cross sectional tests. This suggests that underlying problems with the retrieval remain. These problems could relate to poor wavelength calibration, and to explore this, sensitivity tests were carried out to determine the optimum number of wavelength calibration bins in the QDOAS procedure, as described

above for the UV region. However, in the visible range, no consistent optimum value was found ('optimum' values varied between 10 and 20). These factors combined make it difficult to interpret the magnitude of IO and CHOCHO dSCDs with confidence in these wavelength ranges, as found in previous studies. Such uncertainties have previously been, loosely speaking, overcome by the introduction of a phantom 'instrumental' cross section to the DOAS analysis (e.g. Behrens et al. (2019)).

The efficacy of this method was examined for Broadmeadows data by taking an example day (once again 4/3/2017) and averaging the residuals spectrum from all elevation angles, and all solar zenith angles $< 70^o$, using the 'residuals' saving tool in QDOAS. This produced an instrumental function which could be included as a pseudo absorber in the QDOAS analysis. As shown in figure 2.15(a), not surprisingly, including the average residual structure in the fit considerably reduces the calculated residual RMS across the course of the chosen day in question. The bulk of the residual structure averaged across the day presumably comes from the middle of the day because when the instrumental function is used the midday spike in RMS is removed. The CHOCHO dSCD decreased slightly using this cross section while the fit error was mostly unchanged.

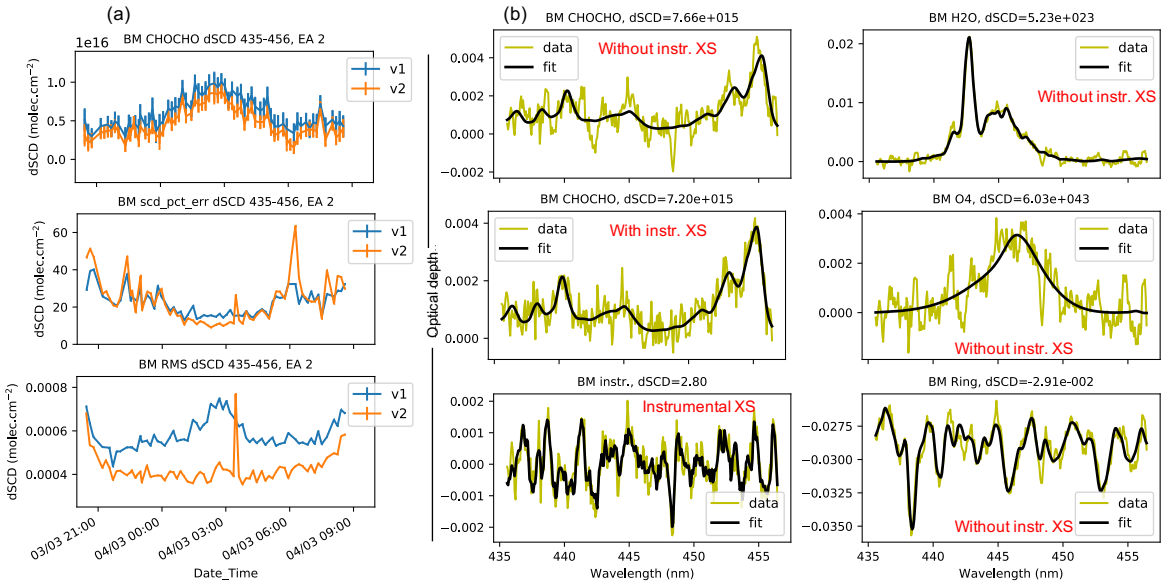

Figure 2.15: Results from DOAS tests using an 'instrumental cross section' in the glyoxal fitting range (435-456.5 nm). (a) Results timeseries from 4/3/2017 for (top) CHOCHO dSCD, (middle) fit error as a percentage of the dSCD and (bottom) magnitude of the residual RMS. Note that v2 refers here to standard settings with the inclusion of an instrumental cross section, not v2 as previously defined in this chapter. Times are in UTC, 2 am is midday local time. (b) Example spectral fits for CHOCHO, the instrumental cross section, H_2O, O_4 and the Ring effect. Data taken from 4/3/2017 at Broadmeadows, solar zenith angle = 32° and elevation angle = 2°.

Considering the example fits in figure 2.15(b), the instrumental cross section itself fits strongly with optical density between -0.02 and 0.02. The absorption 'features' of this cross section removed from the glyoxal fit produce a cleaner, more convincing result across the wavelength range, although the value of the CHOCHO dSCD calculated is slightly lower. Some elements of the instrumental cross section appear to relate to the shoulders of the water vapour peak as discussed above, while on the available evidence the residual RMS peaks cannot be assigned to problems with the O_4 cross section. Rather, the instrumental function bears most resemblance to the Ring spectrum, indicating (a) remaining wavelength calibration problems using Fraunhofer lines in QDOAS or (b) remaining unresolved inelastic scattering processes. While the inclusion of this phantom absorber cross section clearly improves the fit residual, it is difficult to interpret the dSCDs for trace gases such as CHOCHO without fully understanding the source of the removed residual structure. Further work is necessary, especially examining different approaches for calculating Ring (and other inelastic scattering processes) cross sections, before this avenue can be pursued further.

2.5 Summary of DOAS methods chapter

In this chapter, the physics underpinning atmospheric spectroscopy and DOAS in particular was presented. Following from this, a range of sensitivity tests were presented which aimed to optimise the settings and parameters of the DOAS analysis in this thesis.

Key outcomes of this chapter include the demonstration of lower fitting errors using the longer 324.5-359 nm wavelength range rather than 336-359 for formaldehyde. Nitrous acid was found to best be retrieved between 339-372 nm and iodine monoxide between 416-450 nm incorporating four strong absorption bands. No reason was found to alter literature recommended fitting windows for other trace gases examined. Sensitivity tests suggested the number of wavelength calibration bins in the QDOAS routine was important to overall residual RMS, with 20 bins found to be optimal. No clear optimum number of bins was found in the visible region. An examination of the cross sections in the visible region showed the importance of including vibrational raman scattering especially for N_2, suggested that the HITEMP water lines perform better in IO and glyoxaly retrievals than the updated Polyansky et al. (2018) cross section, and demonstrated that the Thalman and Volkamer (2013) O_4 gives most stable retrieval results for IO. The inclusion of a 'Ring tilt' cross section reduced dSCDs and increased dSCD errors for both glyoxal and IO, but enhanced the Ring fit itself suggesting there may be some cross-correlation between the Ring tilt, IO and CHOCHO cross sections that should be explored more thoroughly in future work.

In summary, these DOAS tests demonstrate that convincing spectral retrievals of O_4, NO_2, HCHO, HONO, CHOCHO and IO can be achieved from the Australasian datasets, providing the slant columns which are foundation of the MAX-DOAS results discussed

throughout this thesis. In the following methodology chapter, the retrieval of vertical columns and profiles from these differential slant columns will be discussed.

Chapter 3

Vertical column and profile retrieval

This chapter focuses the methodology of retrieving vertical trace gas columns and concentration profiles from MAX-DOAS differential slant column measurements. The first part of this chapter deals with the background theory of the inversion technique for trace gas and aerosol profile retrieval. The second part outlines a series of optimisation experiments designed to elicit the best retrieval settings and to understand uncertainties inherent to the process. Finally, methods for data filtering and quality control are discussed, including the development of a cloud filtering algorithm.

3.1 Profile retrieval methodology

The differential optical absorption spectroscopy approach outlined in the previous chapter yields differential slant column densities (dSCDs) for the trace gases of interest. In order to solve for the more useful quantities of vertical column density and trace gas concentration from MAX-DOAS dSCD measurements, the Beer-Lambert law requires information on the atmospheric light path. In MAX-DOAS retrievals, this information is typically obtained in two steps. Firstly, the atmospheric light path depends on the amount of scattering which depends in turn on the vertical distribution of aerosols in the atmosphere. Secondly, using this aerosol distribution, the atmospheric light path is determined implicitly for use in the DOAS version of the Beer-Lambert law by calculating airmass factors (AMFs) which relate the slant column to the vertical column.

3.1.1 VCD geometric approximation

The simplest approach to calculating trace gas vertical columns relies on assuming that photons reaching the detector have only been scattered once, above the absorbing trace

gas layer. In this case, the vertical column density can be expressed in simple relation to the elevation angle geometry (Li et al., 2012):

$$VCD_{geom} = \frac{dSCD}{dAMF} = \frac{dSCD}{(1/\sin(\alpha)) - 1} \tag{3.1}$$

This 'geometric approximation' uses the differential airmass factor (dAMF) which is the difference between AMF at 90° and AMF for a lower elevation angle α. In practice, the probability of the single-scattering assumption is much more likely for high values of α so dSCDs above 20° are usually used in VCD_{geom} calculations. This approach has been used to calculate VCDs from MAX-DOAS results in several papers (e.g. Hönninger and Platt (2002); Leser et al. (2003); Javed et al. (2019); Khokhar et al. (2016)). However, the geometric approach is highly limited, firstly because the single scattering approximation is invalid in the UV and in cases of high aerosol optical depth (Li et al., 2012) and secondly because only information on the vertical column, not vertical distribution, is retrieved.

3.1.2 Profile retrieval by inverse modelling

Significantly more robust retrieval methods have been developed which rely on inverse modelling and allow estimation of trace gas vertical profiles. Instead of assuming a single-scattering case above a certain altitude, information on the vertical distribution and optical properties of atmospheric aerosols can be determined from measurements of the oxygen collision complex O_4 (Frieß et al., 2006; Irie et al., 2008; Ortega et al., 2016; Vlemmix et al., 2015; Wagner et al., 2004; Wang et al., 2016, 2015; Heckel et al., 2005). O_4 has a well defined vertical profile which is proportional to the square of the dioxygen concentration. (Wagner et al., 2004). The inverse modelling strategy is to find a solution for the trace gas vertical profile $\mathbf{x}$ by minimising the difference between modeled and measured dSCDs ($\mathbf{y}$). This is achieved by iteratively varying the input trace gas parameters until best agreement is found, for example using the optimal estimation method (Rodgers, 1990, 2000; Frieß et al., 2006; Wagner et al., 2004). The agreement is quantified by the cost function χ^2:

$$\chi^2 = (\mathbf{y} - \mathbf{F}(\mathbf{x}))^T {\mathbf{S}_\epsilon}^{-1} (\mathbf{y} - \mathbf{F}(\mathbf{x})) + (\mathbf{x} - \mathbf{x_a})^T {\mathbf{S_a}}^{-1} (\mathbf{x} - \mathbf{x}_a) \tag{3.2}$$

where $\mathbf{F}$ represents the forward model (in this case a radiative transfer model). $\mathbf{x}_a$ is a priori information which must be provided to constrain the inversion algorithm because the problem is ill-conditioned due to both the limited vertical sensitivity of the MAX-DOAS technique and the retrieval of an atmospheric profile containing more layers than dSCDs in the measurement vector. $\mathbf{S}_\epsilon$ is the measurement error covariance matrix, the diagonal elements of which are the square of the measurement errors.$\mathbf{S_a}$ is the error covariance matrix of the a priori vector, the diagonal elements of which are the squares

of the a priori errors and the non-diagonal elements of which are the correlation length (set to 0.5 km) between retrieval layers which constrains the smoothness of the vertical profile $\mathbf{x}_a$ (Frieß et al., 2006). In the case of aerosol retrievals, the measurement vector $\mathbf{y}$ contains differential optical depths of O_4 at different elevation angles. In the case of trace gas retrievals, $\mathbf{y}$ is the set of trace gas dSCDs at the different viewing geometries. In the MAX-DOAS literature, several algorithms have been described which use optimal estimation to retrieve trace gas and aerosol vertical columns and from MAX-DOAS measurements. A review and intercomparison of these algorithms is contained in Frieß et al. (2016). For the MAX-DOAS measurements in this thesis, the HEIPRO algorithm, developed at Heidelberg University in Germany, was used. HEIPRO uses SCIATRAN as the radiative transfer model (Rozanov et al., 2002, 2014). HEIPRO is described in detail in Yilmaz (2012), Zielcke (2015) and Frieß et al. (2006), so only a brief overview of the algorithm is given here.

For linear cases, the modelled state vector can be simply written as $\mathbf{F}(\mathbf{x}) = \mathbf{K}\mathbf{x}$ where $\mathbf{K}$ is the weighting function matrix which quantifies the sensitivity of the measurements to perturbations in the aerosol distribution. This allows the cost function to be solved, for an optimal state vector $\hat{\mathbf{x}}$, as follows:

$$\nabla_x \chi^2(\hat{\mathbf{x}}) = 0 \tag{3.3}$$

$$\nabla_x \mathbf{F}(\hat{\mathbf{x}})^{\mathbf{T}} {\mathbf{S}_\epsilon}^{-1}(\mathbf{K}\hat{\mathbf{x}} - \mathbf{y}) + {\mathbf{S_a}}^{-1}(\mathbf{x} - \mathbf{x}_a) = 0 \tag{3.4}$$

and with $\mathbf{F}(\mathbf{x}) = \mathbf{K}\mathbf{x}$ and therefore $\nabla_x \mathbf{F}(\mathbf{x}) = \mathbf{K}$,

$$\mathbf{K}^T {\mathbf{S}_\epsilon}^{-1}(\mathbf{K}\hat{\mathbf{x}} - \mathbf{y}) + {\mathbf{S_a}}^{-1}(\mathbf{x} - \mathbf{x}_a) = 0 \tag{3.5}$$

which can be solved analytically for $\hat{\mathbf{x}}$. Although the trace gas retrieval in theory presents an example of a linear inversion, in order to avoid unrealistic negative values HEIPRO transforms $\mathbf{x}$ into a safe state (i.e. a logarithmic transform) and this results in a nonlinear problem. In this case, equation 3.3 must be solved using an iterative scheme. The approach in HEIPRO is based on the Gauss-Newton method as follows:

$$\mathbf{x}_{i+1} = \mathbf{x}_i - [\nabla_x \mathbf{g}(\mathbf{x}_i)]^{-1} \mathbf{g}(\mathbf{x}_i) \tag{3.6}$$

where

$$\mathbf{g}(\mathbf{x}) = \frac{1}{2} \nabla_x \chi^2(\mathbf{x}) \tag{3.7}$$

and

$$\nabla_x \mathbf{g}(\mathbf{x}) = \mathbf{H} = \nabla_x \mathbf{K}^T {\mathbf{S}_\epsilon}^{-1} [\mathbf{F}(\mathbf{x}) - \mathbf{y} + \mathbf{K}^T {\mathbf{S}_\epsilon}^{-1} \mathbf{K} + {\mathbf{S_a}}^{-1}] \tag{3.8}$$

In HEIPRO, the Gauss-Newton is modified using the Levenberg-Marquardt method which is more stable in converges faster, as described in Frieß et al. (2006) and Platt and Stutz (2008). An approximation is made:

$$\mathbf{H}_{LM} \approx \mathbf{H} + \gamma \mathbf{S_a}^{-1} = (1+\gamma)\mathbf{S_a}^{-1} + \mathbf{K}^T \mathbf{S_\epsilon}^{-1} \mathbf{K} \tag{3.9}$$

which results in the following iteration scheme for the Levenberg-Marquardt method:

$$\mathbf{x}_{i+1} = \mathbf{x}_i + [(1+\gamma_i)\mathbf{S_a}^{-1} + \mathbf{K_i}^T \mathbf{S_\epsilon}^{-1} \mathbf{K_i}]^{-1} (\mathbf{K_i}^T \mathbf{S_\epsilon}^{-1} [\mathbf{y} - \mathbf{F}(\mathbf{x}_i)] - \mathbf{S_a}^{-1} [\mathbf{x}_i - \mathbf{x}_a]) \tag{3.10}$$

There are two key retrieval sensitivity terms in addition to the weighting functions. Firstly, the gain function represents the sensitivity of the inversion result to the measurements. It is given by:

$$\mathbf{G} = \frac{\partial \hat{\mathbf{x}}}{\partial \mathbf{y}} = (\mathbf{S_a}^{-1} + \mathbf{K}^T \mathbf{S_a}^{-1} K)^{-1} \mathbf{K}^T \mathbf{S_a}^{-1} \tag{3.11}$$

Secondly, the averaging kernels represent the sensitivity of the retrieved profile to the true atmospheric profile, which is:

$$\mathbf{A} = \frac{\partial \hat{\mathbf{x}}}{\partial \mathbf{x}} = \mathbf{G}\mathbf{K} = (\mathbf{S_a}^{-1} + \mathbf{K}^T \mathbf{S_a}^{-1} K)^{-1} \mathbf{K}^T \mathbf{S_a}^{-1} K \tag{3.12}$$

Therefore the retrieved trace gas or aerosol profile is the true profile, smoothed by $\mathbf{A}$:

$$\hat{\mathbf{x}} = \mathbf{x}_a + \mathbf{A}(\mathbf{x} - \mathbf{x}_a) \tag{3.13}$$

The information content can be quantified by the degrees of freedom for signal (DOFs), which is the trace of the averaging kernel matrix. In an ideal retrieval, the averaging kernel pertaining to each retrieval altitude would peak at that altitude, with a value of 1. However, because (in this case) 20-layered profiles are retrieved from measurement vectors containing much less than 20 pieces of information, the problem is ill-posed and the DoFs is much less than 20. Due to the high sensitivity of low elevation angle dSCDs to the lower troposphere, where light path lengths are longest and trace gas concentrations are usually largest, the sensitivity of MAX-DOAS retrievals is almost always weighted strongly to the lowest 1-2 km of the retrieval.

The value of χ^2 can be used as a metric for analysing the retrieval; it is the key metric of the iteration scheme, quantifying the the agreement between modelled and measured values as a result of the inversion. Put simply, 'high' χ^2 indicates that the inversion has not converged and therefore the retrieval is unsuccessful, 'low' χ^2 indicates good convergence and a successful inversion outcome.

3.2 General profile retrieval settings

The aerosol retrieval from O_4 dSCDs itself provides useful information i.e. aerosol optical depth and extinction profiles. It is also necessary as input information to the trace gas retrieval, hence the overall HEIPRO algorithm is in two steps, shown as a flowchart in figure 3.1. In addition to the basic elements necessary for profile retrieval shown in the flowchart (dSCDs and a priori information), the HEIPRO algorithm has a wide range of settings controlling, among other things, the iteration parameters, cross sections, implementation of errors, representation of viewing geometry, times and dates. These settings are controlled using an input text file in HEIPRO ("retrieval.inp"). In this section, descriptions of some of these settings, and justification for the choices implemented here, are briefly outlined. A summary of HEIPRO retrieval settings is presented in table 3.1.

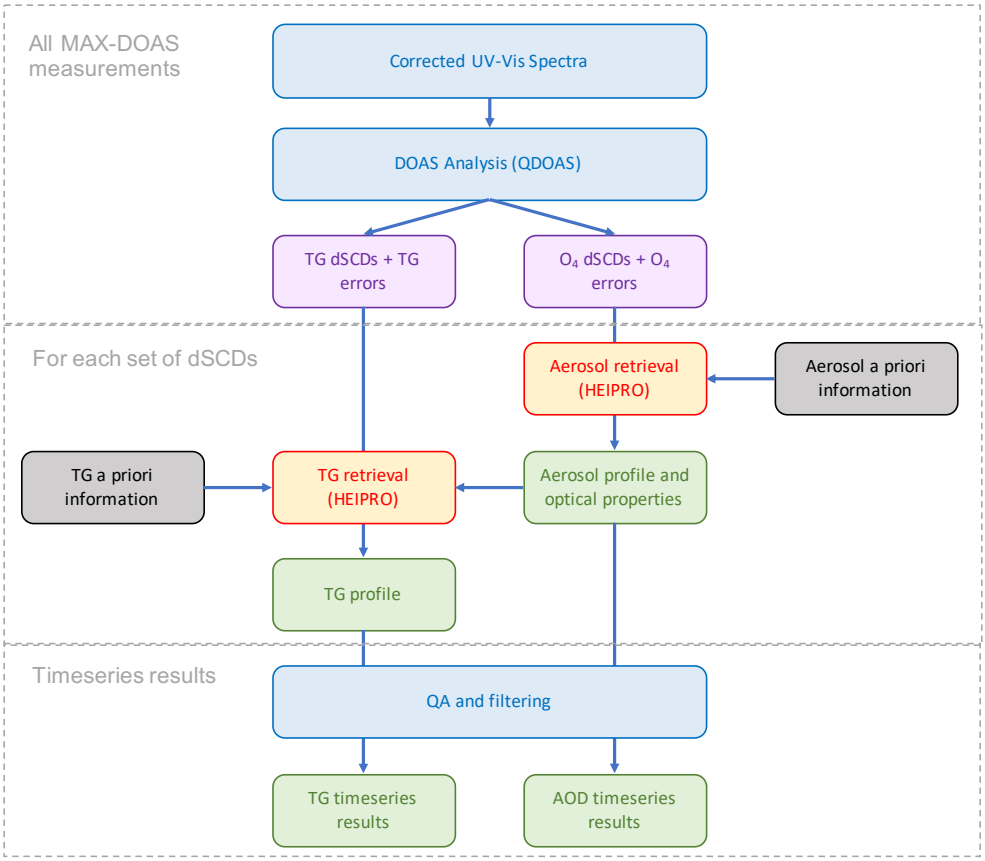

Figure 3.1: Schematic diagram of the profile retrieval process. The central box indicates the core of the HEIPRO algorithm which operates on one set of differential slant columns at a time.

Campaign specific settings

The initial part of the HEIPRO input file contains campaign specific information such as instrument height, details on the DOAS method used (i.e. sequential referencing or single reference), the azimuth viewing direction, the dates and times of the desired retrieval period and information on the input file structure. Importantly, the time settings also define the measurement vector; a time window must be specified (in minutes) in which all slant columns found contribute to the measurement vector. The standard operating procedure included between 8 and 10 elevation angles, including 90° which was sometimes duplicated. Each scan typically had exposure times around 1 minute, but up to 2 minutes at high solar zenith angles. Therefore for most retrievals in this work a time interval of 10-15 minutes was chosen to define the measurement vector.

Settings for controlling the retrieval strategy

The retrieval wavelength for each species was first determined. For O_4, HONO and glyoxal this was determined by choosing the wavelength of maximum absorption in the relevant wavelength fitting range (see chapter 2). For the remaining species the retrieval wavelength was the median wavelength of the fitting window. All retrieval wavelengths are listed in table 3.1.

All trace gas and aerosol retrievals were run using a 20-layer altitude grid at 200 m resolution, from 0-4 km. This was specified in HEIPRO using the centre altitudes of each layer (i.e. layer centres were 0.1 km, 0.3 km, ... 3.9 km).

The trace gas and aerosol retrievals were always run with 'safe-state' on, to prevent unphysical retrievals. The option to use the retrieved profile as a priori for the next sequence was always turned off, meaning that the a priori was always independent of the measurements. Sensitivity tests by Zielcke (2015) showed that there was no advantage to re-calculating the weighting functions for each iteration in the case of low and medium aerosol extinction cases (extinction less than 1), as expected for the majority of the time in Australia and New Zealand. This was tested in an example aerosol retrieval from Lauder data taken on 2nd January 2018, as shown in figure 3.2, where the same retrieval scenario was run with and without fixed weighting functions. In the timeseries plots, no significant advantage in terms of χ^2 is found. The DoFs is higher in general for the fixed weighting function case, but oscillates between 1.5 and 2 between retrievals. In the particular profile example from 10:38 am local time on this day, the DoFs are the same in each case, but the fixed weighting function case has retrieved a two-peaked aerosol profile which is highly unlikely given no accompanying sensitivity improvement at the altitude of the second peak. No significant difference was found in the retrieved AOD in each case. Hence no advantage was found in including the weighting function recalculation step.

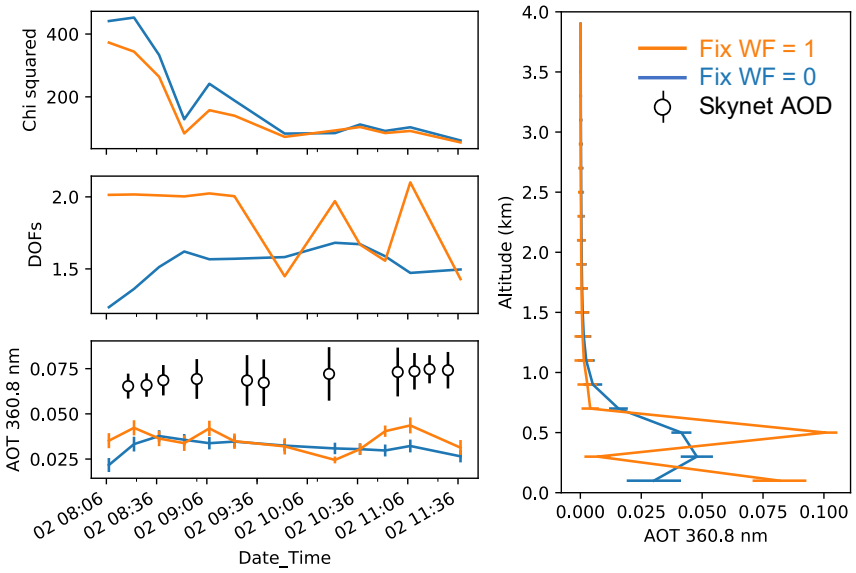

Figure 3.2: Aerosol retrieval sensitivity study for the 'fix weighting function' parameter in HEIPRO: left hand panels are retrieval results from the morning of 2/1/2018 at Lauder, NZ. Right hand panel is an example vertical profile comparison from 10:38 am local time. WF = 1 means weighting functions were recalculated, WF = 0 means they were not. Times are in local time.

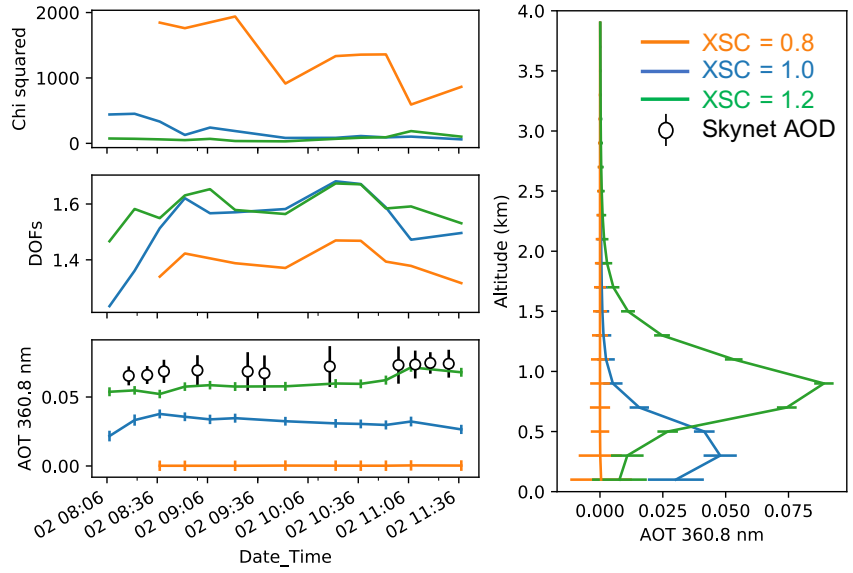

Figure 3.3: Aerosol retrieval sensitivity study for the cross section correction (XSC) factor in HEIPRO: left hand panels are retrieval results from the morning of 2/1/2018 at Lauder, NZ. Right hand panel is an example vertical profile comparison from 10:38 am local time.

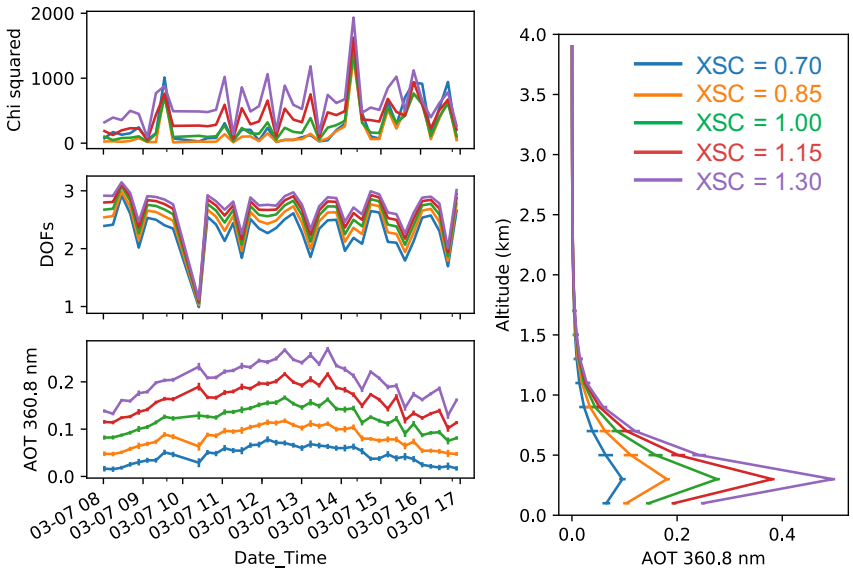

Figure 3.4: Aerosol retrieval sensitivity study for the cross section correction (XSC) factor in HEIPRO: left hand panels are retrieval results from the morning of 7/3/2017 at Broadmeadows, Australia. Right hand panel is an example vertical profile comparison from 12:38 pm local time.

There has been some recent debate in the MAX-DOAS literature about the need to apply a correction factor to the O_4 dSCDs section in the profile retrieval, in order to match the RTM simulations. For example, Clémer et al. (2010), Vlemmix et al. (2011), Wagner et al. (2009) and Irie et al. (2011) all found correction factors around 0.75 - 0.80 were approriate. However, Frieß et al. (2016), Ortega et al. (2016) and Spinei et al. (2015) argue that such a correction factor should not be necessary. In the HEIPRO algorithm, the application of a correction factor can be tested in a reverse experiment, by correcting the O_4 cross section used to model the dSCDs. Two case studies were examined here, one with moderate AOD in Melbourne, one with low AOD at Lauder, New Zealand. Different outcomes are observed in each test case. In the Lauder example in figure 3.3, a cross section correction factor (XSC) of 0.8 clearly has a detrimental impact on the retrieval χ^2 and DoFs compared to XSC of 1.0 and 1.2. XSC of 1.2 brings the HEIPRO-retrieved AOD values closely into line with co-measured Skynet AOD results. This is consistent with Clémer et al. (2010) and the other studies showing measured O_4 dSCDs are about 20 % higher than the RTM simulations. However, the increase in AOD in this case, as shown in the profile plot in figure 3.3, comes from the retrieval of an elevated aerosol layer (around 1 km altitude) but with no accompanying improvement in sensitivity at this altitude. Therefore the confidence in the promising AOD result is low.

In direct contrast to the Lauder example, the Melbourne case study (figure 3.4) shows XSC greater than 1.0 gives highest χ^2. XSC of 1.0, 0.85 and 0.70 show very little

variation in χ^2 or DoFs. Also in contrast to the Lauder results, this particular Melbourne example shows no variation in profile shape, only in magnitude of consistent 400 m altitude peak. Overall, these tests showed no consistent or compelling evidence for the application of a correction factor to the O_4 cross section or dSCDs. As a result, a XSC value of 1.0 was used throughout the work in this thesis, consistent with the recommendations for HEIPRO in Frieß et al. (2016) and Yilmaz (2012).

Settings for SCIATRAN and other input files

HEIPRO automatically passes a number of parameters from its own input file to the SCIATRAN radiative transfer model input files. One key parameter which is not passed is the measurement latitude and longitude, which was manually updated for each retrieval location in the SCIATRAN control file. In addition, cross sections used in the DOAS fitting were supplied to SCIATRAN (instead of the pre-existing cross section files with the SCIATRAN package, where they were different) to ensure consistency of trace gas cross sections throughout the analyses.

Temperature and pressure profiles are necessary for calculating the expected O_4 vertical distribution. These were supplied to HEIPRO via standard atmospheric monthly profiles. The available options for latitudes relevant to this work were standard atmospheric profiles at 45°S and 35°S for Lauder and Melbourne/Perth respectively. While ideally, locally measured temperature and pressure profiles, e.g. from a radiosonde, would provide a better constraint on the O_4 distribution, Frieß et al. (2006) estimated that error margins only in the range of 3-4 % and 0.2-1 % for AOD and surface aerosol extinction respectively could be expected for errors of 10 hPa in the pressure profile.

To constrain the aerosol distribution in the upper atmosphere, aerosol profiles from the Stratospheric Aerosol and Gas Experiment (II) (e.g. Thomason et al. (1997)) were used. To constrain aerosol optical properties in the troposphere, data from the Aerosol Robotic Network (AERONET), https://aeronet.gsfc.nasa.gov) from Canberra was used in the case of Melbourne retrievals since this was the closest available single scattering albedo (SSA) and asymmetry parameter (Asy) data. For the Lauder retrievals, no proximate AERONET data was available in the right time period, so the standard HEIPRO settings of SSA = 0.89 and Asy = 0.68 were used (note these values are specific to the 360.8 nm O_4 retrieval. The chosen SSA value was consistent with Skynet data at Lauder, which over the period 2015-2018 had a mean of 0.895 ± 0.078. The chosen value of Asy was consistent with AERONET measurements at Dunedin on the east coast of New Zealand's south island between 2006-2009.

Settings for controlling the iteration

Remaining settings for controlling the iteration are listed in table 3.1.

Parameter	Retrieval species	Setting used
Retrieval wavelength	Aerosol (O_4)	360.8 nm
" "	NO_2	365.4 nm
" "	HONO	354.3 nm
" "	HCHO	338.9
" "	CHOCHO	455.0 nm
" "	IO	433.0 nm
Time interval	All	10-15 min, campaign specific
Retrieval grid	All	0-4 km, 200 m spacing
Safe state	All	On
Recalculate weighting functions	All	Off
Use relative intensity	Aerosol (O_4)	Off
XS correction factor	Aerosol (O_4)	0
Starting Gamma	All	1000
Maximum Gamma	All	1×10^8
Number of iteration runs	Aerosol (O_4)	2
Number of iteration runs	All trace gases	1
Adaptive a priori	All	Off
Iterative a priori	All	Off
A priori profile shape	All	Exponential
A priori ground extinction	Aerosol (O_4)	0.06 km^{-1}
" "	NO_2	5 ppb
" "	HONO	0.2 ppb
" "	HCHO	2 ppb
" "	CHOCHO	0.5 ppb
" "	IO	2 ppt
A priori scale height	All	1 km
A priori relative error	All	1.0
A priori correlation length	All	0.5 km

Table 3.1: Details of the key HEIPRO retrieval settings.

3.3 Assessing the retrieval quality

Four key parameters were used to assess the quality of each individual profile retrieval and to 'filter' the final trace gas and aerosol results. They were the χ^2, the degrees of freedom for signal, the retrieval errors and the cloud filtering index. The cloud filtering procedure will be discussed in detail at the end of this chapter. Largest retrieval errors were dealt with post-retrieval simply by filtering for results where the error on the vertical column was greater than the vertical column itself.

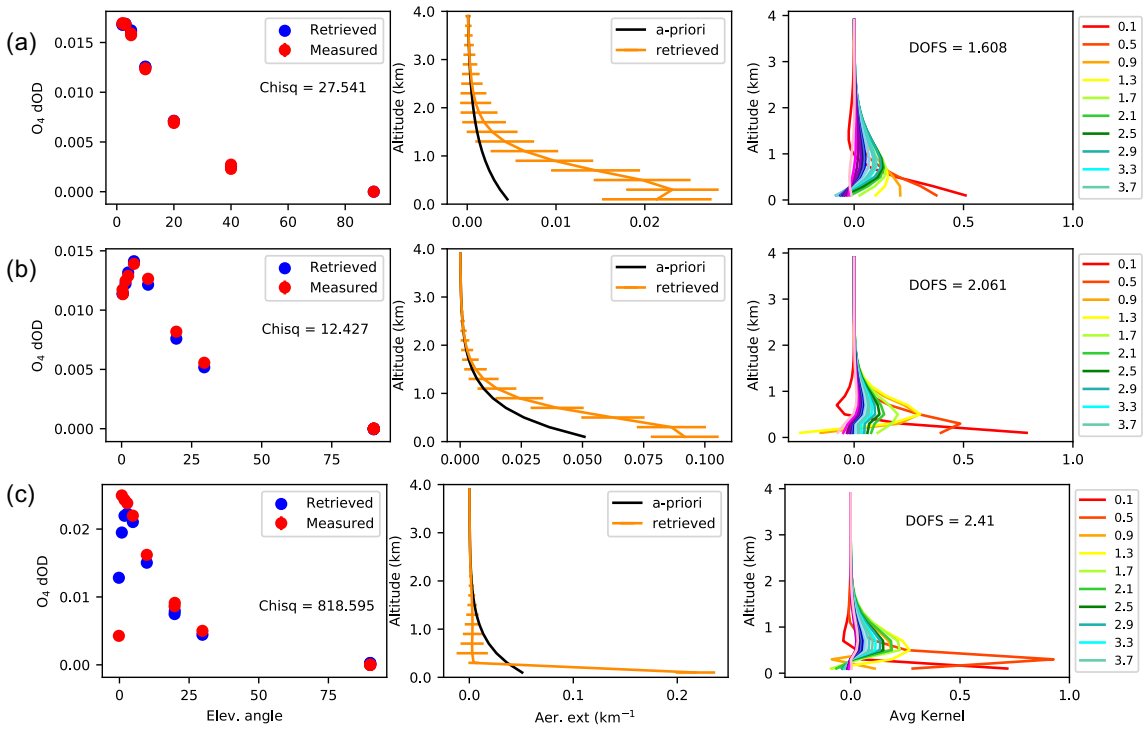

Figure 3.5: Example aerosol retrievals showing (left to right) modelled ("retrieved") and observed ("measured") O_4 differential optical depths (dOD) with associated χ^2, retrieved profile with associated a priori profile and averaging kernels. (a) Example retrieval from Lauder dataset, 1 pm local time on 1/1/2018. (b) and (c) are example retrievals from the Broadmeadows dataset on 7/3/2017.

Establishing what value of χ^2 constitutes adequate convergence is an important step in assessing overall retrieval quality, addressed here by inspection. For the aerosol retrieval, plotting the modelled and measured O_4 differential optical depths together shows whether the measurements have been well modelled by the RTM. For example figures 3.5(a) (a Lauder example with low aerosol extinction and minimal information content) and (b) (a Melbourne example with moderate aerosol extinction and information content) show that modelled and measured dODs plot on top of each other within the errorbars. Figure 3.5(c) appears to show a high aerosol extinction case, however for low elevation angles the modelled and measured values do not match: the inversion has not satisfactorily converged. Aerosol retrievals with χ^2 less than 100, as in figures 3.5(a) and (c), were generally found to have good agreement between modelled and measured dOD and therefore results with with χ^2 greater than 100 were filtered out.

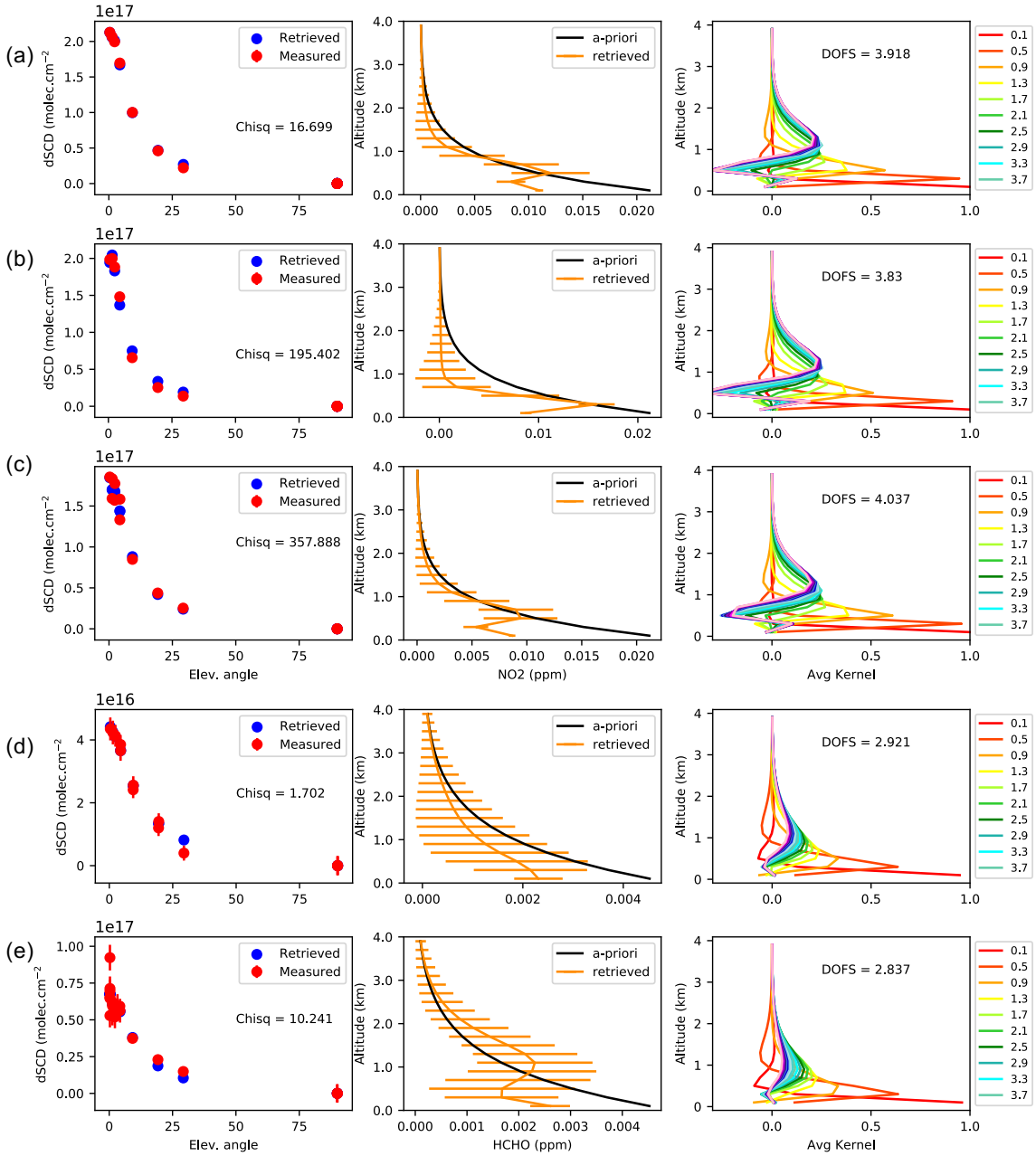

Figure 3.6: Example NO_2 (a-c) and HCHO (d-e) retrievals showing (left to right) modelled and measured dSCDs with associated χ^2, retrieved profile with associated a priori profile and averaging kernels. All example retrievals are from 7/3/2017 at Broadmeadows.

Figure 3.6(a-c) show three example NO_2 retrievals from Broadmeadows. Because NO_2 is a strong absorber and dSCDs were often of the order 10^{17} molecules.cm^{-2}, the threshold χ^2 for successful retrievals was higher than for O_4 and the more weakly absorbing trace gases. For example, the inversion pictured in figure 3.6(a) has converged very well with

χ^2 of 17, but the inversion shown in figure 3.6(b) also appears to have modelled the measured dSCDs well and has χ^2 195. In contrast, low elevation angle dSCDs in figure 3.6(c) are modelled much too high, with χ^2 being of 360. On this evidence, χ^2 filter of 200 was applied to the NO_2 measurements. For formaldehyde and the other weakly absorbing trace gases (nitrous acid and glyoxal), successful retrievals were found to have χ^2 less than 10 as shown for example in figure 3.6(d), while cases that had not converged (especially with low elevation angle results poorly modelled, such as figure 3.6(e)) had χ^2 greater than 10. Therefore for HCHO, CHOCHO and HONO, a χ^2 filter of 10 was applied post-retrieval.

The information content of the retrieval was also considered in assessing the quality of the final retrieval results. As indicated in the averaging kernel plots for example aerosol retrievals at Lauder (figure 3.5(a)) and Broadmeadows (3.5(b)), the information content was generally higher for Broadmeadows than Lauder. A key reason for this is that the Broadmeadows site sits atop a hill and thus elevation angles down to 0° are possible, allowing much greater sensitivity in the lower retrieval layers. At Lauder, mountain ranges surrounding the site mean only angles 2° and greater can be used. The observed DoFs for aerosol and trace gas retrievals in this work were generally between 1.2 and 4. Retrievals with DoFs less than 1 were filtered out. Intuitively, this is because such retrievals contained less than one independent piece of information and hence no advantage was gained going through the inversion as opposed to using the geometric approximation. Graphically, this is demonstrated for HCHO retrievals at Broadmeadows in figure 3.7, which shows that modelled and measured values are very well simulated (with correlation $R^2 > 0.98$ and slope around 1 between January and April, with very few instances of DoFs < 1.5. In winter however, with lower light levels, significant deviations from unity are observed and they consistently have DoFs < 1. Therefore, the instances of low information content coincided with the periods of lowest χ^2, justifying the filtering out of retrievals with DoFs below 1. Deviations from modelled vs measured unity were similarly observed for all other trace gases when the information content was very low.

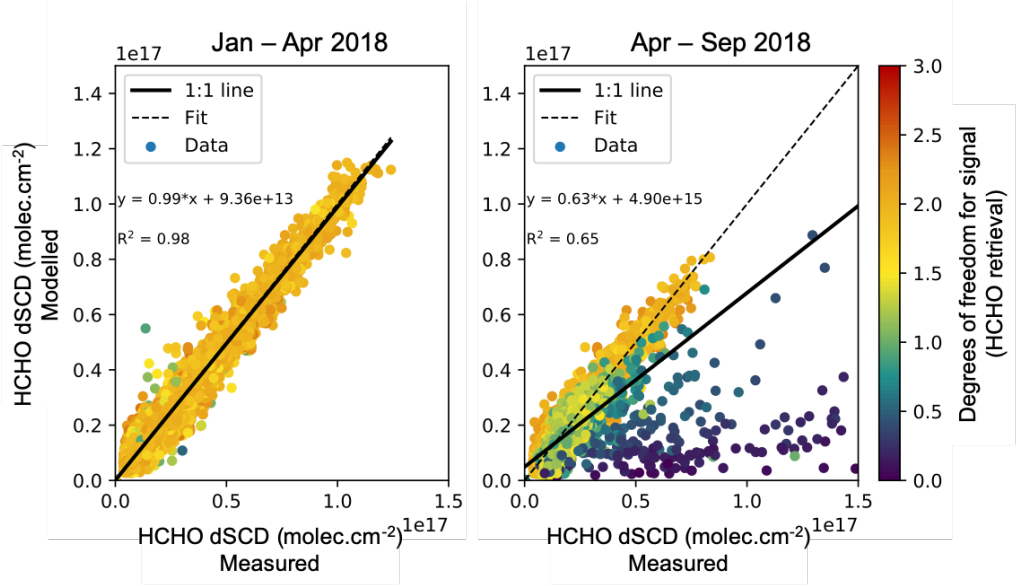

Figure 3.7: Scatterplots for formaldehyde, modelled vs measured values, for Jan-Apr 2018 (left) and Apr-Sep 2018 (right). The scatterplots are coloured by DoFs indicating the importance of the information content in assessing overall retrieval quality.

3.4 A priori sensitivity tests

As identified in the earlier inversion theory, the retrieval process minimises the difference between modelled and measured dSCDs (or dODs) and also between an a priori atmospheric state vector and the true atmospheric state. Defining an appropriate a priori state vector, which is effectively an initial guess of the trace gas or aerosol profile, is crucial to a successful inversion especially for MAX-DOAS measurements which have limited sensitivity at high altitudes. The shape of a priori profiles for MAX-DOAS retrievals are often described by 'linearly decreasing below a characteristic altitude' or 'exponentially decreasing', reflecting the typical scenario whereby aerosol extinction and trace gas concentration increase with decreasing altitude. Throughout this work, exponentially decreasing a priori profile shapes were used which are characterised by scale height below which most of the trace gas concentration resides, and a surface concentration (or aerosol extinction). The uncertainty assigned to the a priori profile, $\mathbf{S_a}$ in equation 3.2, also plays an important role in the inversion, determining how much weighting is given to the a priori profile vs the measurement vector.

One approach to understanding the role of a priori profiles is to simulate an atmospheric state and associated dSCDs using an RTM, then retrieve the profile using the inversion algorithm, allowing a comparison with "truth". This approach is useful for optimising the a priori parameters for the true scenario simulated. Sensitivity studies using this method were carried out by Zielcke (2015), testing the influence of a priori scale height, ground extinction(concentration) and relative error. Zielcke (2015) found that aerosol

a priori surface extinction values of 0.2 km^{-1} allowed profiles for high and low aerosol load to be retrieved successfully. They found the main concern choosing the scale height parameter was that low values (< 0.5 km) led to the inversion constraining all the aerosols to the surface layers. A priori parameters for the trace gas retrieval were tested in Zielcke (2015) using bromine monoxide (BrO), for which minimal dependence was found on the final for varying surface BrO mixing ratio. Similar to the aerosol retrieval, a scale height of 1 km was chosen to avoid constraining the profile to the surface layer, while also preventing the retrieval from using the a priori to assign BrO at high altitudes. Optimum values for the a priori relative error across low, medium and high aerosol load scenarios (and BrO examples) were 0.1-0.5 (i.e. AP uncertainty set to 100-500 % of the AP value at all levels).

Retrieval	A priori parameter	Range
Aerosol, NO_2, HONO	Relative error	0.1-2.0
Aerosol, NO_2, HONO	Scale height (km)	0.2-1.2
Aerosol	Surface extinction (km^{-1})	0.02-0.12
Aerosol	Asymmetry parameter.	0.66-0.75
Aerosol	Single scat. albedo	0.7-1.0
Aerosol, NO_2, HONO	Elevation angle corr.	0 ± 0.5
Aerosol	Ground albedo	0.02-0.2
NO_2, HONO	Aerosol params.	All aerosol tests
NO_2	Surface VMR (ppb)	0.5-10
HONO	Surface VMR (ppb)	0.1-0.4

Table 3.2: Details of the a priori sensitivity studies in Ryan et al. (2018), for aerosol, NO_2 and HONO retrievals.

Another sensitivity study approach is to vary each parameter within realistic bounds to constrain the uncertainty due to choice of a priori profile. The tests results from Zielcke (2015) provided a starting point such sensitivity studies in this work, which were published in Ryan et al. (2018). Details of the a priori tests, which were run on data from three sunny days at Broadmeadows, are listed in table 3.2. Figure 3.8(a) shows an example aerosol profile and AOD timeseries from 7/3/2017 at Broadmeadows, with shaded regions indicating the uncertainty on the profile and daily AOD due to each sensitivity test. In the profile plot, the largest uncertainty in the surface extinction is clearly the elevation angle offset, highlighting the importance of well calibrated pointing accuracy (i.e. within 0.5°). The a priori scale height has the largest influence on the upper part of the profile (60% of the total profile error above 500 m), and therefore also the largest overall impact on the AOD timeseries. This is expected since the inherent higher sensitivity of the retrievals to the measurements at low altitudes, means the a priori profile more strongly constrains the retrieval at high altitudes. Below 500m, the influence of the shape parameters is much less significant at 10%, while the optical

properties (yellow and green colours), especially the asymmetry parameter are more a substantial contribution (12%) to the profile error. The role of the surface albedo term is found here to be negligible, in contrast to the test results in Zielcke (2015). All other tested parameters played only a minor role in the overall uncertainty.

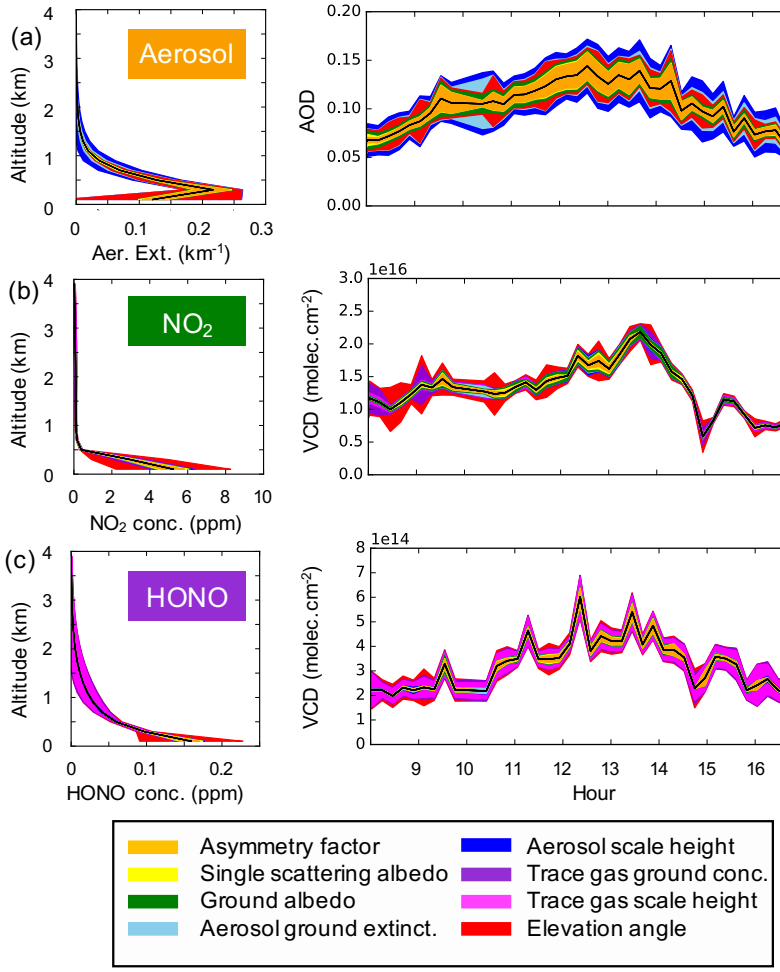

Figure 3.8: Results of a priori/forward model parameter tests for (a) an example aerosol extinction vertical profile (1 pm local time on 7/3/2017), left, and total aerosol optical depth over the course of the day on 7th March 2017, right; (b) an example vertical concentration profile of NO_2 and NO_2 vertical column density; (c) same as (b) but for HONO. Each colour represents the mean $\pm$ the standard deviation attributable to the particular test parameter as indicated by the legend. The ranges for each test are outlined in table 3.2. Figure adapted from Ryan et al. (2018).

Figure 3.8(b) and (c) show the same as (a) but for NO_2 and HONO retrievals. In addition to the trace gas a priori parameters, the uncertainty due to carry-over from the aerosol retrieval was also tested and found to be small overall. As with the aerosol results, the elevation correction term is dominant source of surface level uncertainty,

while upper level profile uncertainty is influenced by the 'shape parameters', surface VMR and scale height. The percentage contributions of each parameter to the overall vertical column and surface value are shown in figure 3.9. A priori scale height is the most significant contributor to shape parameter uncertainty for aerosols and HONO total column, each at around 50 % of the total a priori error. In contrast, the surface VMR and the aerosol scale height are the largest shape parameter influences on NO_2 VCD and surface VMR. The aerosol ground extinction and optical property parameters have a negligible influence on any of the retrieval values. Importantly, the influence of the aerosol carry-over and trace gas a priori parameters on the NO_2 and HONO profiles were found to be only around 10 % of the magnitude of the smoothing and noise errors, suggesting that within the measurement uncertainty the trace gas retrievals are independent of all a priori choices (Ryan et al., 2018).

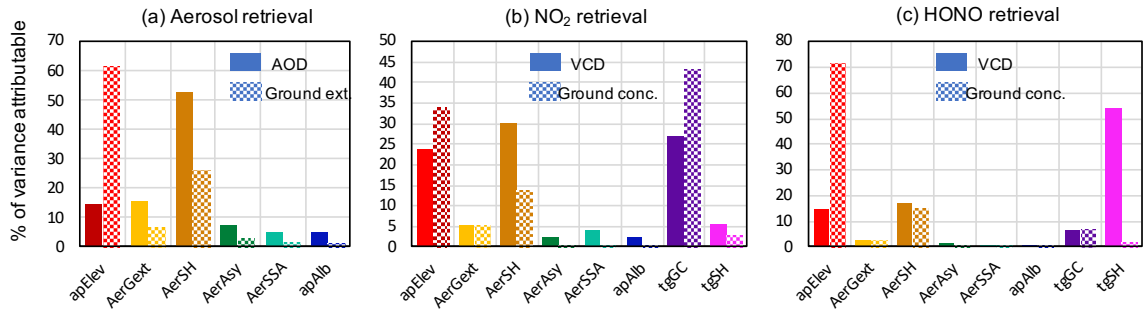

Figure 3.9: Error attribution as a result of the a priori sensitivity studies. Bars represent the percentage of the variance explained by each sensitivity test for the retrieved vertical column amount (solid bars) and surface layer value (checked bars): (a) aerosols, (b) NO_2 and (c) HONO.

3.5 Cloud filtering

3.5.1 Cloud filtering theory

Because O_4 concentration is a function of pressure rather than surface emissions or other chemistry, variations in O_4 dSCD (such as the lack of dSCD separation for different elevation angles on the 5th of March in figure 5.1) can be attributed to light path changes rather than concentration changes. Clouds are one of the strongest influences on light path in the atmosphere.

Radiative transfer models (RTMs) used in profile retrieval algorithms, such as SCIATRAN in HEIPRO as in this work, typically include multiple atmospheric scattering. This allows vertical 'scattering', or aerosol profiles, to be retrieved. The RTMs usually assume a cloud-free atmosphere because clouds add scattering events which are difficult to model. This is especially the case for patchy cloud periods because the MAX-DOAS may observe light scattered from cloud in some elevation angles but not

others. Furthermore clouds are usually at altitude, above the region of highest sensitivity for MAX-DOAS measurements. This is evident in the example HEIPRO aerosol retrieval outputs shown in figure 3.10. On the 4th of March 2017, a clear day, HEIPRO models the O_4 optical density (OD) well as indicated by the overlap of red and black modelled and measured points. The averaging kernels indicate high sensitivity in the lowest km of the retrieval grid. In contrast, on the 5th of March which was cloudy, the O_4 OD is not well modelled with a χ^2 four times higher than the day before, the averaging kernels indicate minimal sensitivity even in the lowest retrieval layers. The extinction profile peaks five times higher than the clear day example and at around 1 km altitude, which could be consistent with cloud, but the lack of sensitivity and poor model/measurement match make this result difficult to be confident of. As a result, cloudy periods are usually screened from MAX-DOAS timeseries results (Wagner et al., 2016; Gielen et al., 2014). Identifying cloudy periods then need to be identified, this can be facilitated by external co-located measurements for example using a LIDAR (Hoque et al., 2018a) or sun-photometer (Benavent et al., 2019). Given that the MAX-DOAS measures solar intensity too, and in the absence of such co-located information, cloud identification for the Broadmeadows dataset was facilitated by the MAX-DOAS measurements themselves.

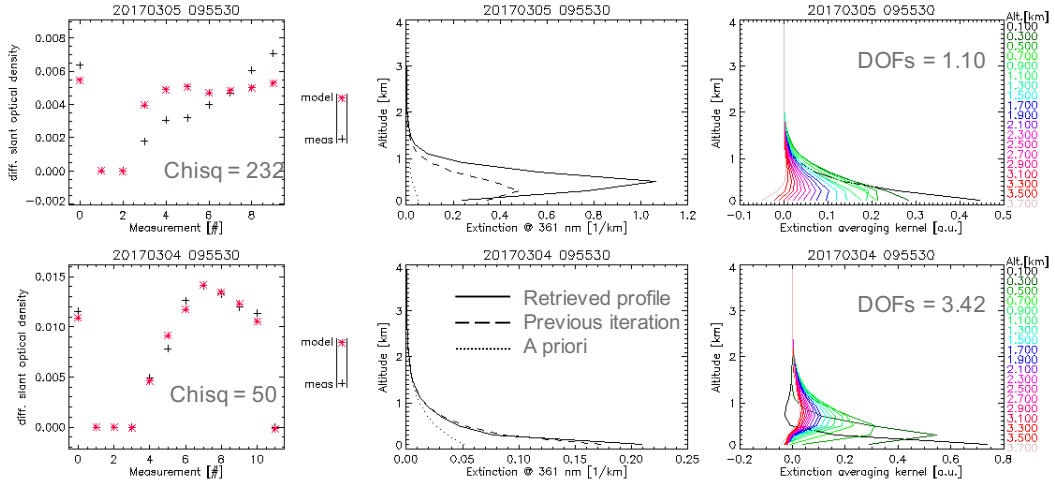

Figure 3.10: Example HEIPRO aerosol retrieval output from Broadmeadows at 9:55 am local time on 05/03/2017 (top row) which was a cloudy day, and 04/03/2017 (bottom row) which was a clear day.

3.5.2 Approach to cloud filtering

Some discussion of cloud-identification using MAX-DOAS measurements exists in the literature already. Gielen et al. (2014), Wagner et al. (2014) and Wagner et al. (2016) suggested the colour index as the primary tool for identifying sky conditions, alongside variation in overall spectral intensity and O_4 absorption. The colour index (CI) is defined simply as the ratio of two spectral intensities. The wavelengths chosen for

each of the intensities are decided by the largest spectral contrast possible for the particular instrument's specifications, and avoiding strong spectral features (such as O_4 or H_2O lines) Gielen et al. (2014). Wagner et al. (2014) and Gielen et al. (2014) suggested $CI = I_{\approx 320nm}/I_{\approx 440nm}$ however in Wagner et al. (2016) it was argued that $CI = I_{330nm}/I_{390nm}$ was more appropriate as (a) 330 nm is less effected by O_3 absorption than 320 nm, and (b) variability of surface albedo is lower for 390 nm than 440 nm. Hence in this work $CI = I_{330nm}/I_{390nm}$ was chosen. It is expected that when the sky is clear, the 'blue' side of the CI ratio is strong hence CI is high, while when the sky is cloudy the CI is low as the 'white' side of the ratio dominates.

Figure 3.11(a) shows diurnal variation in colour index at Broadmeadows from 1st-12th March 2017, calculated for the 30° elevation angle. Wagner et al. (2014) and Gielen et al. (2014) used zenith observations to calculate CI, arguing that temporal cloud variation is lowest for the 90° elevation. On the other hand, the 30° elevation gives a more representative picture of the sky conditions 'seen' by the lower elevation angles, which provide the key lower-atmospheric sensitivity of the MAX-DOAS technique, while still having low temporal cloud variability. Hence the 30° elevation angle results were used for CI in this work.

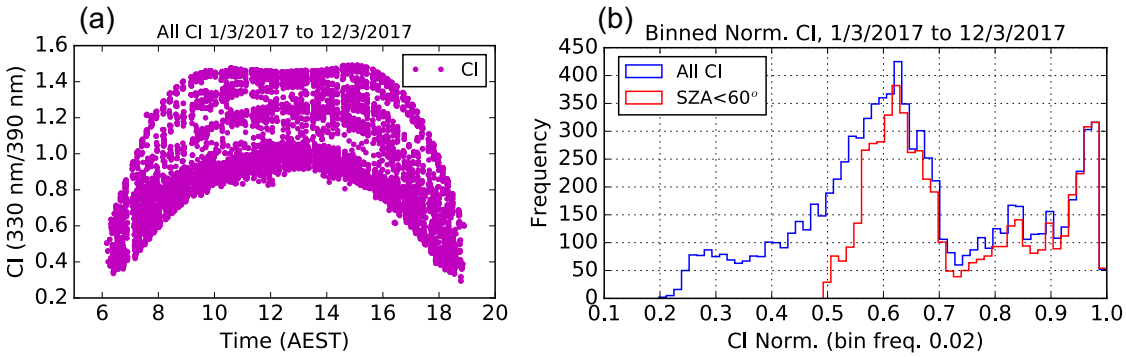

Figure 3.11: (a) All daily colour index values from 1st to 12th March 2017 at Broadmeadows. (b) Histogram of normalised colour index (normalisation is with respect to the maximum CI in this case) indicating accumulation points in the CI frequency distribution.

Wagner et al. (2014) and Gielen et al. (2014) suggest comparing measured CI with simulated CI at the same measurement geometry in order to identify clouds. This requires a calibration of the simulated calibration, proposed by Wagner et al. (2016). This relied on finding the accumulation point in the frequency distribution of the minimum CI, for SZA $< 60^o$, because the minimum CI was found to be SZA-independent below 60°, and less influenced by AOD variation than the maximum CI. However as shown in Figure 3.11(a), for SZA $< 60^o$ in Melbourne (i.e. between 7 am and 4 pm in this case) the minimum CI is not independent of SZA. An accumulation peak is found at the left hand end of the frequency distribution of normalised (to the maximum) CI for SZA $< 60^o$ shown in figure 3.11(b), as in Wagner et al. (2016). However, the full width half

maximum of the frequency distribution peak is about four times greater for this dataset than in Wagner et al. (2016), indicating that no consistent minimum exists that could be used as the calibration value and hence the method cannot be applied here.

As a result, a simple empirical approach was taken to cloud filtering the Broadmeadows dataset. Rather than comparison of measured and modelled CI, measured CI was compared to measured CI from known (observed) clear sky days. CI thresholds were determined by fitting a 5th order polynomial to measured CI from clear days as a function of solar zenith angle (adjusted so that sunrise SZA was -90° and sunset SZA was +90°). This has the advantages of being very simple to implement, self-calibrating and accounting for SZA/solar azimuth dependence of the CI at the given location. Downsides to this approach include a lack of specificity in terms of cloud type compared to the classification algorithms of Wagner et al. (2014) and Gielen et al. (2014) and the requirement of needing totally cloud-free days to produce threshold CI values. Fortunately, there was at least one cloud free day in each month of 2017 at Broadmeadows facilitating the calculation of threshold polynomials for each month as shown in figure 3.12.

A 'cloudy sky' flag was raised if the measured CI at a given (adjusted) solar zenith angle was less than 10% of the monthly threshold clear sky CI. In the absence of a co-located sky camera or other potential cloud-validation methods, the somewhat arbitrary figure of 10% was chosen by inspecting the resulting filtering on daily CI and daily O_4 dSCDs as shown in the top two panels of figure 3.13. A characteristic U-shaped diurnal pattern for O_4 dSCDs, with well separated results between low and high elevation angles, is expected under clear-sky conditions (e.g. Frieß et al. (2006); Wagner et al. (2014); Gielen et al. (2014)) as evident on 4th, 7th and 8th March. On those days, the cloud filtering algorithm does not remove any data points. On cloudy days the O_4 dSCDs are expected decrease overall and to 'collapse' with respect to elevation angle separation. This is evident on the morning of the 3rd, and throughout the 11th and 12th of March and accordingly, the cloud filter comes into effect.

It is expected that the retrieval algorithm might perform poorly under cloudy conditions as was the case for the example in figure 3.10, exhibiting telltale metrics such as high measured vs model χ^2 and low degrees of freedom for signal (DOFs). Figure 3.13 shows the influence of cloud filtering on these statistcs, for the HEIPRO aerosol retrieval, from 1-12th March 2017. In some cases, e.g. 11th and 15th of March, it is clear that the cloud filtering removes examples of low DOFs and high χ^2. In other periods, such as 14th March, the cloud filter removes periods with unremarkable χ^2 and DOFs while on other occasions throughout this time anomalously high χ^2 and low DOFs are untouched by the filter. This suggests (a) that the aerosol retrieval is robust to some unknown extent in the presence of cloud, and (b) there are other factors contributing to poor retrieval statistics such as high dSCD errors or individual retrieval sets without enough dSCD measurements.

The last panel in figure 3.13 shows that there was no significant impact of cloud filtering

on NO_2 vertical column amount, encouragingly suggesting that the trace gas retrieval is robust in the presence of clouds. Surprisingly though, the same was true for retrieved aerosol optical depth, with cloud filtering not preferentially removing high AOD values. This implies that the effect of clouds on the aerosol profiling is to redistribute the retrieved scattering rather than simply increase it (see for example the profile comparison in figure 3.10). Hence even while the retrieved column amount may not be significantly impacted by clouds, the vertical distribution is highly uncertain.

3.5.3 Potential drawbacks to cloud filtering

There are a few limitations to the cloud filtering method employed here. Firstly, the imposition of a filter based on a value of 10 % difference from the threshold colour index is empirical only and somewhat arbitrary. It also does not differentiate between different cloud conditions such as broken cloud, high cloud and foggy conditions as more complicated flagging algorithms might. In addition the cloud filter may remove data of interest where thick aerosol or smoke layers, rather than cloud, influence the colour index.

3.6 Profile retrieval methods: summary

In this chapter the background theory for vertical column and profile retrieval from MAX-DOAS slant columns has been presented. Throughout this thesis vertical profiling has been carried out using the optimal estimation method through the HEIPRO algorithm. Following especially the recommendations of Frieß et al. (2006), Wagner et al. (2004), Zielcke (2015) on the use of HEIPRO, along with a range of sensitivity studies, the choices of retrieval parameters have been outlined in detail. Key results from this chapter include optimisation of, and uncertainty estimates from, aerosol and trace gas a priori parameters. In particular, trace gas retrievals were found to have minimal dependence on carry-over aerosol retrieval uncertainty. This chapter also outlines the quality control factors considered when presenting results in the rest of the thesis. Threshold values for filtering by chi-squared and information content were empirically determined from retrieval examples. Finally, an empirical cloud-filtering algorithm based on clear-sky colour index measurements was developed and demonstrated. Ultimately, the outcome of the methodology chapters, this and the previous, is confidence in the ability to retrieve results from MAX-DOAS spectra in Australasia using optimised DOAS and profile retrieval methods.

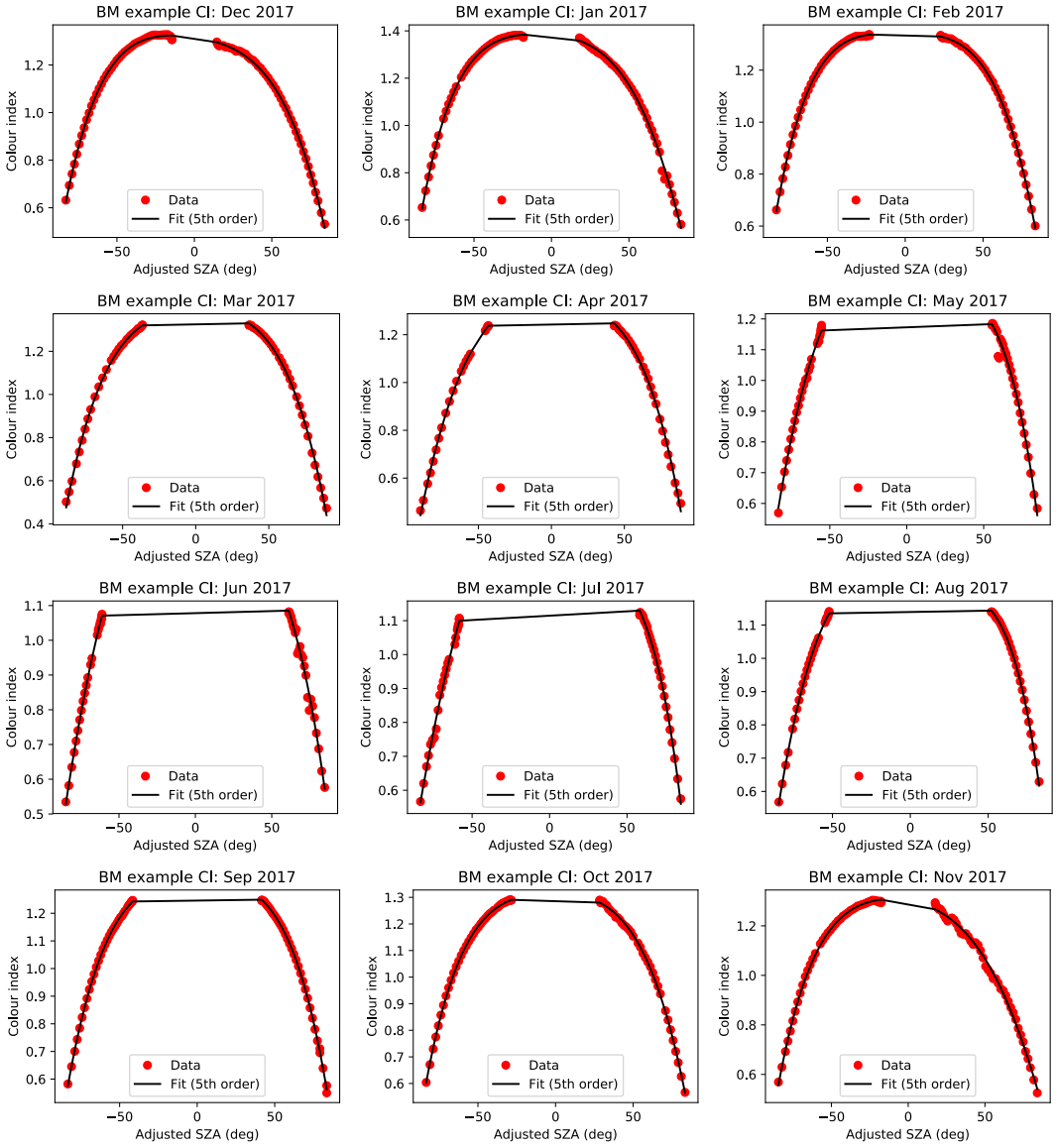

Figure 3.12: Daily colour indices (CI) for a clear sky day in each month of the year 2017. Black lines indicate 5th order polynomial fits to the CI data as a function of adjusted solar zenith angle (see text for details), which are the basis of the empirical cloud filtering algorithm used in this work.

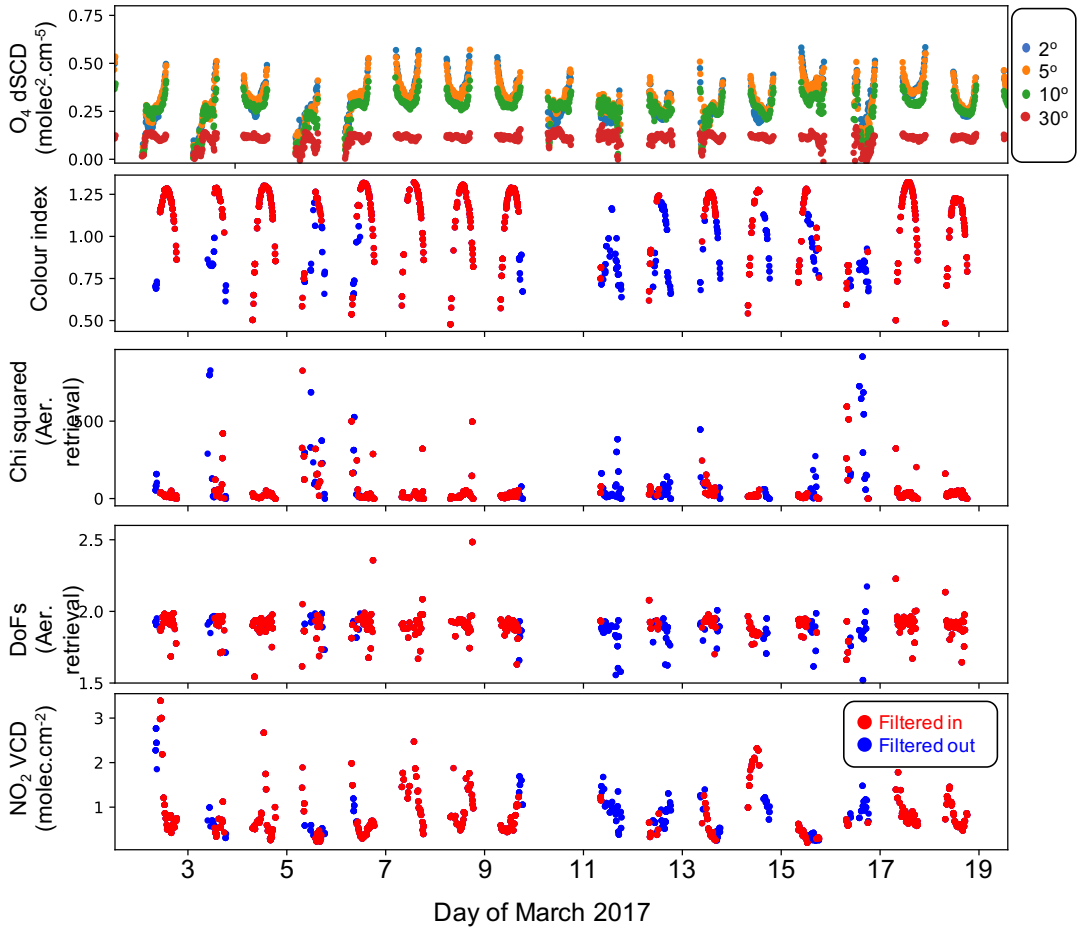

Figure 3.13: Results of implementing the empirical cloud filtering algorithm in an example data period, from 2-18 March 2017. Flagged cloudy periods are indicated by compressed O_4 dSCDs (top) and colour index (CI, second from top). For CI, aerosol retrieval χ^2 and degrees of freedom for signal, as well as retrieved NO_2 vertical column density, blue indicates cloud flagged periods.

Chapter 4

Intercomparison of MAX-DOAS measurements

The Trans-Tasman Inter-comparison of MAX-DOAS Trace gas and Aerosols in Melbourne (TIMTAM) was held at the Bureau of Meteorology (BOM) training site in Broadmeadows (lat. -37.691°, lon. 144.947°, elevation 110 m ASL), a northern suburb of Melbourne. The location of the BOM facility is shown in figure 4.1. The measurement period ran from the 16th of February to the 7th of April 2017. Envimes MAX-DOAS instruments from four institutions participated: BOM (the host institution), the University of Melbourne (UM), the University of Wollongong (UW) and the New Zealand National Institute of Water and Atmosphere Research (NIWA).

All four instruments were mounted on a laboratory roof and oriented to a south-westerly viewing angle (220°). Measurements were synchronised using a daily measurement schedule, facilitating an accurate temporal comparison between the measurements, an approach adapted from the CINDI-2 campaign held at Cabauw in the Netherlands in September 2016 (Kreher et al., 2020). The aim of the work was to compare instrument performance in retrieving differential slant columns of O_4 and NO_2.

Note: throughout the figures and discussion in this chapter the data from each instrument is referred to by a two letter label; UM (University of Melbourne), UW (University of Wollongong), BM (Bureau of Meteorology) and NZ (NIWA New Zealand).

The aim of the TIMTAM campaign was to evaluate the performance of the Envimes instruments used in Australia and New Zealand against one another. In particular, since the NZ MAX-DOAS had demonstrated good performance in the second Cabauw Intercomparison of Nitrogen Dioxide Measuring Instruments campaign (CINDI-2) (Kreher et al., 2020) in the Netherlands four months before TIMTAM, the UW, UM and BM instruments could be evaluated against one known to be conforming to international standards. Intercomparison exercises in the MAX-DOAS field, including 'MAD-CAT' in Mainz 2013 (e.g. Roscoe et al. (2010); Wang et al. (2017b)), CINDI-1 (e.g. Pinardi

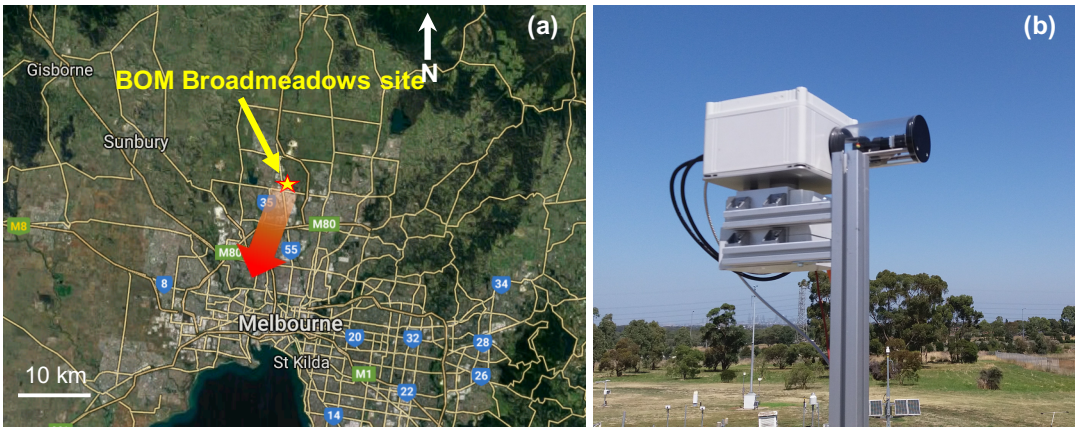

Figure 4.1: (a) Map of Melbourne showing the location of the Bureau of Meteorology site at Broadmeadows. The red arrow indicates the direction of measurement for the MAX-DOAS instruments involved in the TIMTAM campaign (south-south west, 220° relative to north). (b) Photo of the University of Melbourne Envimes 2D MAX-DOAS instrument at Broadmeadows (*Maps sourced from Google Maps, photo by R. Ryan*).

et al. (2013); Frieß et al. (2016)) and CINDI-2 have proven very useful for establishing measurement and analysis guidelines as well as identifying problems and solutions for those making or using MAX-DOAS observations. Therefore it was hoped TIMTAM could help establish some guidelines for MAX-DOAS in Australasia, and identify any problems before deployment of instruments to other field campaigns.

Initial measurement and analysis guidelines for TIMTAM were based on the CINDI-2 protocol, with some key differences. While CINDI-2 adopted a semi-blind approach to ensure an impartial assessment of performance, the presence of only four instruments at Broadmeadows meant that this was impractical for TIMTAM. Secondly, TIMTAM was a very short comparison period, with all four instruments operating simultaneously for only seven days. Nevertheless this period allowed the collection of sufficient spectra, under a range of atmospheric conditions, to perform useful comparative analyses.

Spectra were collected simultaneously at elevation angles 3°, 5°, 10°, 20°, 30° and 90° using a timing scheme to ensure measurements would be directly comparable. Each institution separately measured dark current and offset spectra for their spectrometers which were subtracted from each spectrum using custom-written Python code which transformed the spectra into files readable by QDOAS. Each group also measured mercury lamp spectra which allowed the calculation of wavelength calibration polynomials and spectral lineshape functions (see Appendix A).

4.1 TIMTAM DOAS fitting results

For this work, UV spectra were analysed in QDOAS using the CINDI-2 recommended settings for NO_2 and O_4 (link here to methods chapter). All cross sections were convolved with the respective spectrometer's lineshape using the QDOAS convolution tool, and Ring spectra were calculated for each instrument using the QDOAS Ring tool supplied with lineshape and wavelength calibration information. Figure 4.2 shows example NO_2 and O_4 fits, as well as the residual, from simultaneous 5^o elevation angle measurements shortly after midday on 16/02/2017. While all four instruments clearly observe NO_2 and O_4, resulting slant columns and residuals are different for each instrument despite apparently measuring the same air mass at the same time. For example, UW produces a strong O_4 fit and a moderate NO_2 fit; UM the opposite. All instruments exhibited minimal residual structure, with the root mean squared (RMS) of the residual for each $< 4.5 \times 10^{-4}$.

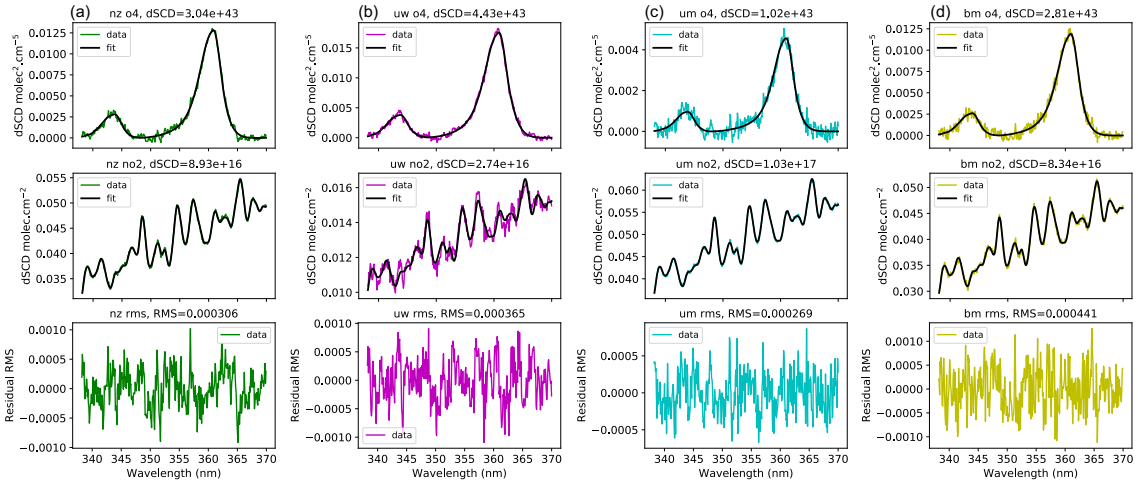

Figure 4.2: Example dSCD fits from QDOAS from 16/02/2017, solar zenith angle = 26, elevation angle = 5°, for (a) NZ, (b) UW, (c) UM and (d) BM.

Figures 4.3(a) and 4.3(b) show timeseries throughout the TIMTAM period for O_4 and NO_2 respectively. It should be noted that during the middle of the day on 20th February, UW and UM stopped measuring in order to run a pointing accuracy calibration (discussed in detail below), and UM stopped completely thereafter for maintenance. During this time periods of clear sky (16th, 17th afternoon, 21st and 22nd February) were highlighted by characteristic U-shaped O_4 dSCD diurnal profiles and clear separation between dSCDs of different elevation angles. The 16th and 21st of February saw strong NO_2 dSCDs, independent of deviations from the expected O_4 pattern, suggesting the observed NO_2 dSCD was due to elevated NO_2 concentrations rather than light path effects. During simultaneous measurement periods, the temporal trend for these characteristic clear/cloudy sky and NO_2 incursion events were well captured by all four instruments although dSCD magnitudes varied.

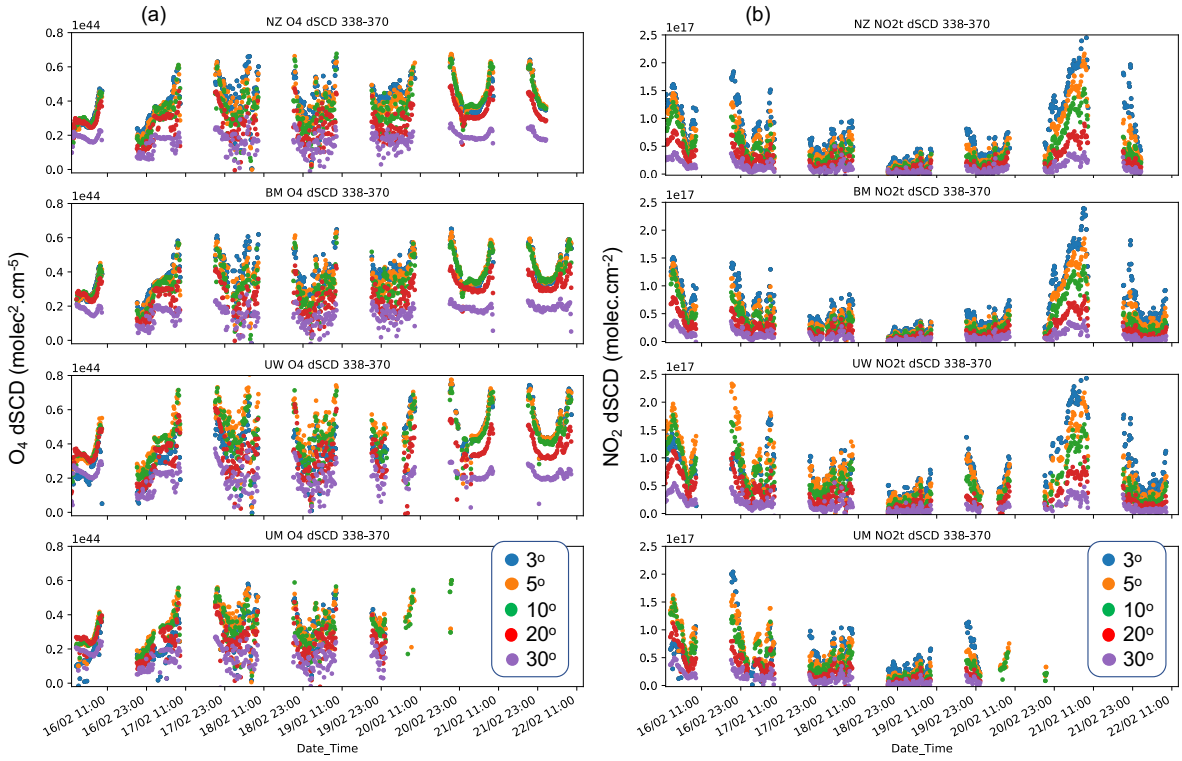

Figure 4.3: Timeseries of (a) O_4 and (b) NO_2 dSCDS, for each instrument and elevation angle, during the TIMTAM period 16/02/2017 to 22/02/2017.

Timeseries for the residual RMS are plotted in figure 4.4(a). Immediately notable is the higher RMS for the UW and UM 3^o elevation angle (EA) in the early part of TIMTAM. This was as a result of pointing accuracy problems which are discussed below. Considering elevation angles $> 3^o$, the median BM RMS is consistently $\approx 1\times10^{-4}$ higher than the other four instruments. Since the BM slit function and wavelength calibration polynomials were almost identical to the other three instruments (see appendix A) the RMS discrepancy was likely due to problems with the dark current and offset correction. Nevertheless BM, along with the other instruments, typically exhibited RMS $< 5 \times 10^{-4}$ in line with expectations. The temporal trend in RMS is consistent between instruments, i.e. RMS is highest in the early morning and late afternoon when the sun traverses the longest light path through the lower troposphere.

Ideally the residual RMS should be independent of the elevation angle. This was tested, again considering EA$> 3^o$, by examining the standard deviation of all residual RMS values two representative days. As shown in figure 4.4(b) the standard deviations (errorbars) for each instrument are much less than the mean residual RMS, under both clear (16th February) and cloudy (18th February) conditions, suggesting there is no residual bias either toward low or high elevation angles.

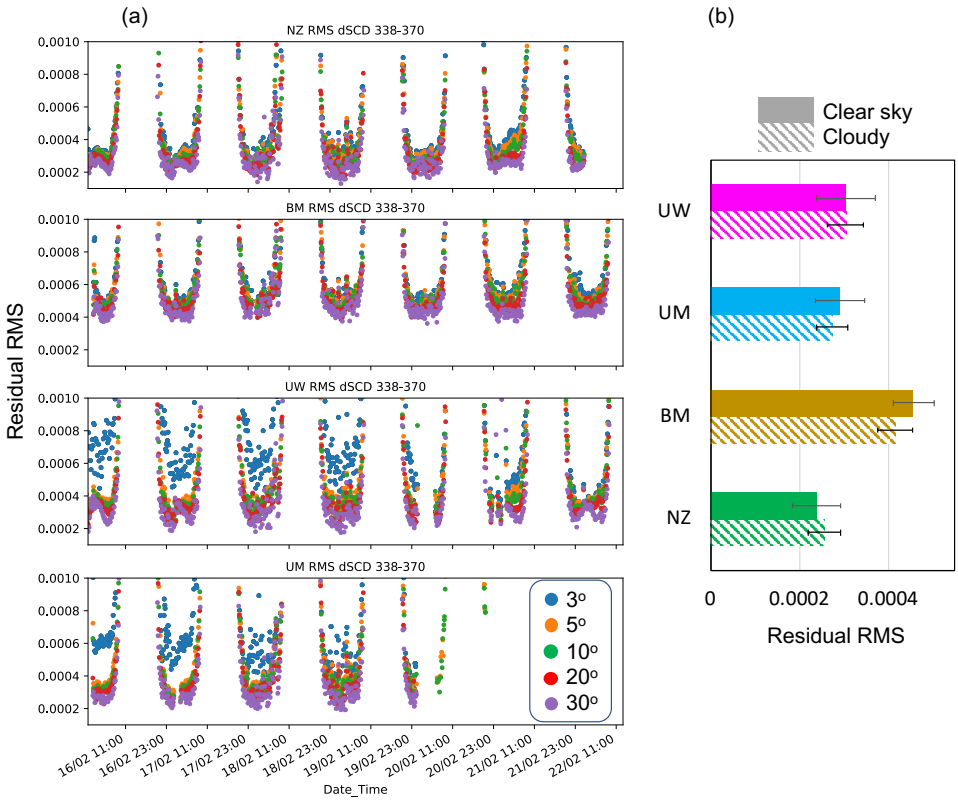

Figure 4.4: (a) Timeseries of the residual RMS, for each instrument and elevation angle, during the TIMTAM period 16/02/2017 to 22/02/2017. (b) Bar plot of residual RMS averages and standard deviations for each MAX-DOAS under representative clear (16th February) and cloudy (18th February) conditions.

4.2 Pointing accuracy comparison

The MAX-DOAS technique relies on precise knowledge of the viewing geometry in order to retrieve vertical profile information. The largest uncertainty in the viewing geometry is usually the telescope elevation angle and, as discussed in section 3.4 of chapter 3, errors in pointing accuracy can result in large errors in retrieved profile. This is fairly straightforward to calibrate in a laboratory setting by, for example, scanning over an illuminated slit at a known height and distance from the MAX-DOAS optics. In the field however, calibration of elevation angle accuracy can be more difficult. For one, laboratory style setups can be impractical in the field, and also it is necessary to check the calibration under field conditions including variable temperature and light. Donner et al. (2020) outlined three field methods for pointing accuracy calibration: using a lamp at a known height and distance, scanning over a painted white stripe, and so-called horizon scans. The horizon scans method was employed at Broadmeadows for checking the pointing accuracy of each of the TIMTAM instruments.

Horizon scans involve measuring intensity at a range of elevation angles either side of the horizon point. The horizon typically exhibits a rapid intensity jump, therefore the horizon point is identified as the elevation angle corresponding to the maximum intensity gradient. This method relies on a consistent, unobstructed view of the horizon and is best suited to clear-sky conditions because low clouds can also cause confusing sharp intensity gradients or blurring of the horizon.

During TIMTAM, the measurement location was elevated, on a hill looking towards the south-west and also on top of a laboratory roof. The horizon to the south-west was approximately 1 km away but treed, making calculation of the expected horizon position in terms of MAX-DOAS viewing angle difficult. Therefore calibration of the UM, BM and UW pointing accuracy was only possible using horizon scans by using the NZ instrument as a standard, given its demonstrated pointing accuracy during CINDI-2. The horizon was determined to be at -1.7^o elevation angle according to the NZ instrument. Figure 4.5 shows example horizon scans for each instrument from 20th February, a clear day. In these examples, the elevation angle has been adjusted by the determined horizon position of -1.7^o to clearly assess the variation of the observed horizon position with the horizon denoted as 0^o. Throughout the TIMTAM period, as with the horizon scans shown for 20th February, the NZ instrument showed a variation in the horizon position of less than 0.2^o consistent with its good performance at CINDI-2. However, none of the other instruments performed satisfactorily. UW consistently pointed $\approx 2.6^o$ too high. Given that this was a consistent effect, it could be accounted for with a simple constant elevation angle offset in the post-processing.

In contrast, the UM and BM instruments were found to have variable 'horizon positions', as shown in figure 4.5 where the horizon was reported to be higher in the middle of the day than at the end of the day. This was subsequently attributed to a temperature sensitive component in the MAX-DOAS optics heads. The variability of the elevation angle offset makes it much more difficult to apply to post-processing than a constant offset. The magnitude of the correction required for each instrument was determined by a simple linear regression between reported horizon position and temperature as shown in figure 4.6. In the case of UM, the telescope temperature was used in calculating the regression because the temperature sensitive component was in the telescope. A strong linear relationship with $R^2 \approx 0.8$ was found. The BM instrument did not record telescope temperature so ambient temperature was used instead. Because the telescope temperature is not simply a function of ambient temperature but also other meteorological variables such as humidity and light intensity, the relationship between BM's horizon position and ambient temperature is not so strong, with $R^2 \approx 0.5$. It should be noted that the temperature sensitivity of the UM instrument was more severe than BM, hence the greater variation in elevation angle observed for UM in figure 4.6. The linear polynomials generated here were used to correct the UM instrument's elevation angles during the TIMTAM analysis, and the BM data throughout the work described in this thesis.

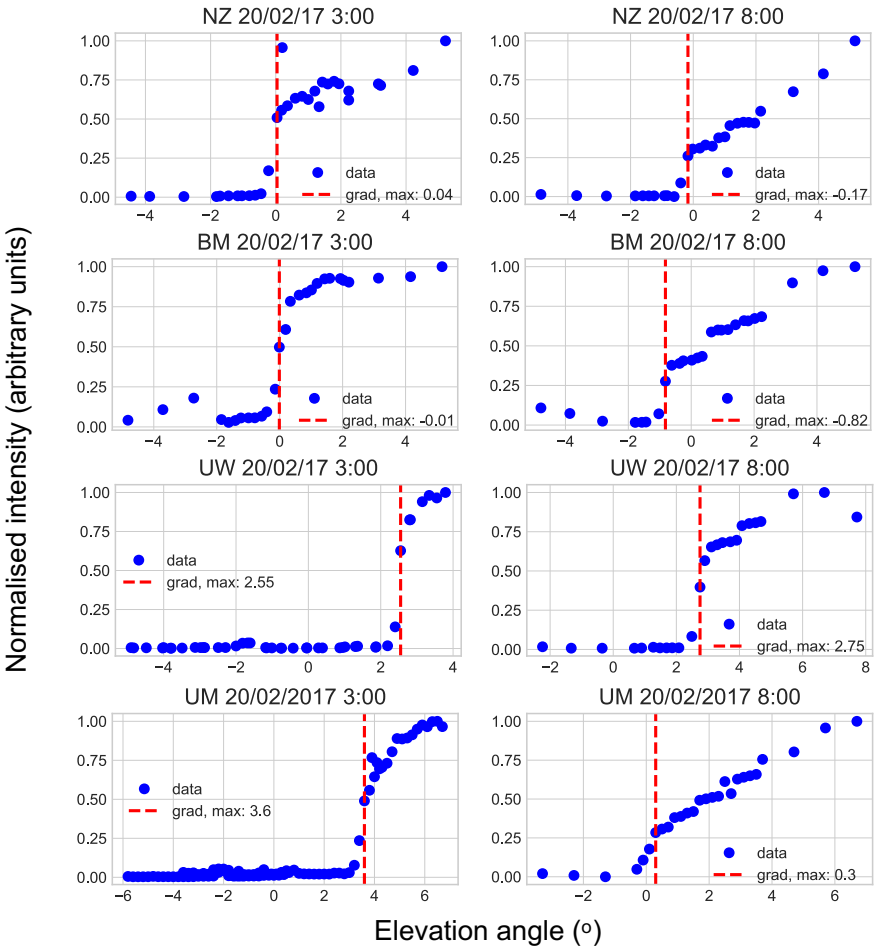

Figure 4.5: Example horizon scans for each instrument, on 20th February. The left column shows horizon scans taken at 03:00 UTC (1 pm local time) while the right column shows horizon scans taken in the evening, 08:00 UTC (6 pm local time).

4.3 Slant column comparison

CINDI campaign analysis work suggested temporal correlations as an appropriate method for assessing the performance of MAX-DOAS instruments relative to a standard. The key criteria for consideration are the linear regression statistics from fits to the scatter-plots, namely the offset, slope and correlation coefficient. In CINDI-2 the correlation criterion was represented as the root mean squared error. The NIWA MAX-DOAS was chosen as the reference standard. Scatterplots and linear regression fits for BM, UW and UM vs NZ are shown in figure 4.7. Slant columns from all elevation angles are included in this analysis, but filtered for residual RMS $< 1 \times 10^{-3}$ and restricted to the period 16-20 February when all four spectrometers were measuring simultaneously. UM and UW show much greater scatter than BM and are typically higher than NZ, i.e. above the 1:1 line, likely because they were the two instruments with most severe

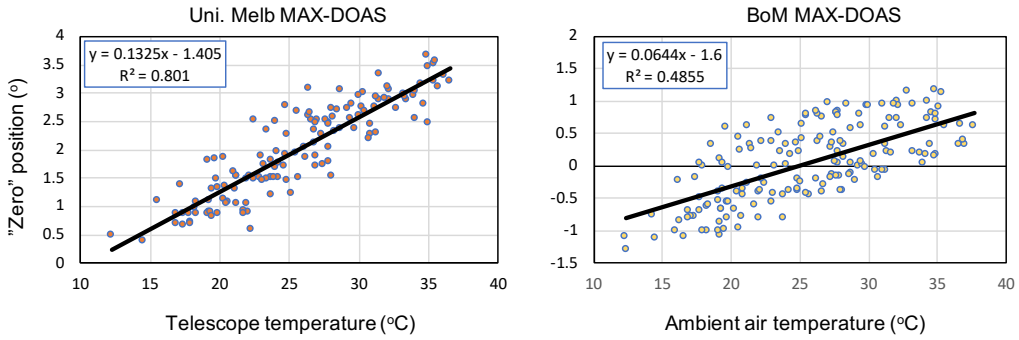

Figure 4.6: Scatter plots and linear regressions for observed horizon position (elevation angle) as a function of temperature. For the UM instrument telescope temperature is used, for the BM instrument ambient temperature is used in lieu of telescope temperature data. Note that the y-axis units are the same but the scales are different.

pointing inaccuracies. The higher dSCDs are more apparent in the low elevation angles (see breakdown of scatterplots for 5^o and 30^o EAs in Appendix A). After 20th February the UW instrument software included an elevation angle correction which improved the correlation between it and NZ, almost to parity in the case of NO_2 dSCDs.

Instrument	**Slope O_4**	**Offset O_4**	**RMSE O_4**	**Slope NO_2**	**Offset NO_2**	**RMSE NO_2**
CINDI-2 guideline	1 ± 0.06	0.8×10^{42}	4.0×10^{42}	1 ± 0.06	1.5×10^{15}	8.0×10^{15}
BM	0.93	1.4×10^{41}	2.2×10^{42}	0.94	4.8×10^{14}	2.5×10^{15}
UM	0.9	6.9×10^{41}	4.4×10^{42}	1.24	1.4×10^{15}	7.1×10^{15}
UW	1.15	9.4×10^{41}	4.8×10^{42}	1.42	5.6×10^{14}	5.9×10^{15}
UW*	1.12	1.0×10^{42}	4.7×10^{42}	1.04	1.4×10^{14}	5.4×10^{15}

Table 4.1: Statistical summary for TIMTAM comparing the performance of BM, UM and UW against NZ, presented with the CINDI-2 guideline statistical criteria. * denotes results following elevation angle correction for UW. Note that for clarity the absolute value of the offset is quoted.

The statistical results of the linear regression analysis are summarised in table 4.1 alongside the guideline CINDI-2 criteria for O_4 and NO_2 UV retrievals. It should be noted that in CINDI-2, 30 minute dSCD averages were considered. In TIMTAM, this was not done in order to maximise datapoints in the comparison. Furthermore, while the NZ MAX-DOAS performed within the performance criteria at CINDI-2, it was not the highest performing instrument. For both these reasons the comparison provided here should serve only as a rough guide. Seen in this light, the results are very encouraging: BM falls within the criteria on all points except for an O_4 slope too low by 0.01. Seemingly the dSCD comparison for these strong absorbers was not substantially affected by BM's higher residual RMS or the elevation angle inaccuracy.

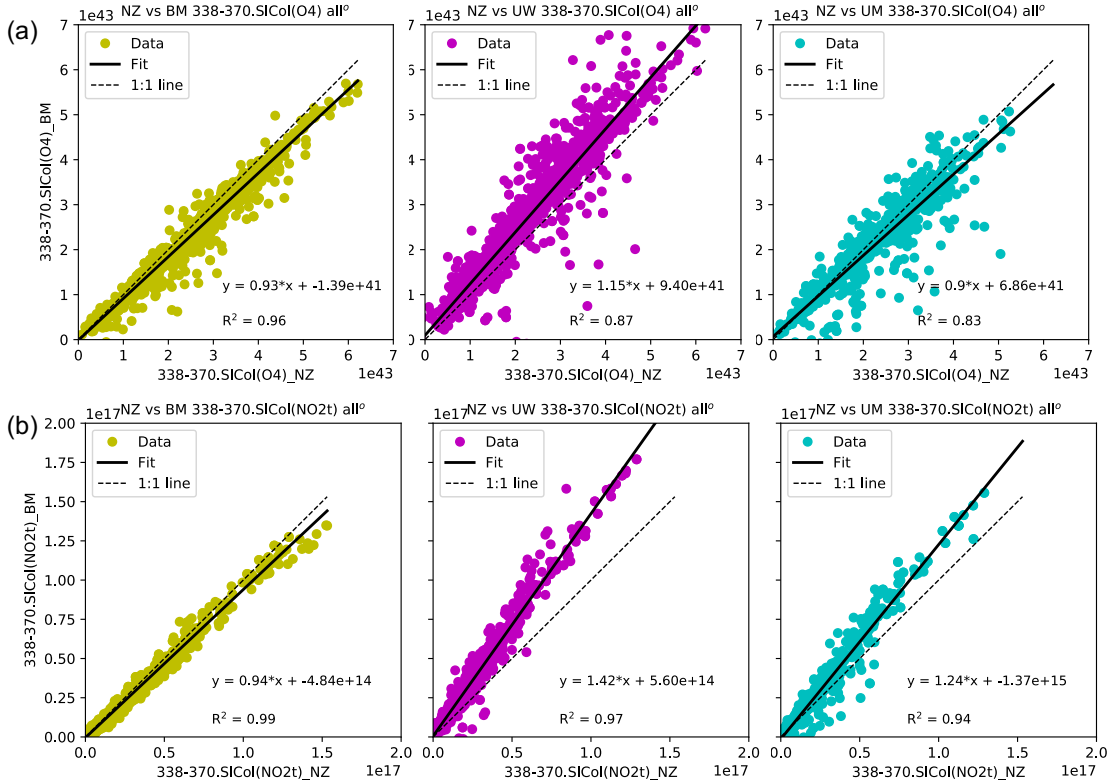

Figure 4.7: Scatter plots showing correlations between NZ measurements (x-axis) and BM, UW and UM respectively. All measurements are plotted for the period when all four instruments were running, 16-20 February 2017, with (a) showing O_4 dSCDs and (b) showing NO_2 dSCDs.

In order to examine a weaker absorber, in a separate test (not shown) NZ and BM HONO dSCDs were also studied using a linear regression. Given the (expected) low HONO concentrations and the fact it is a weak absorber, greater scatter was expected and this was reflected in an R^2 of 0.74. However a slope close to unity (1.01) suggests that BM is indeed performing at a very comparable level to NZ.

Pre-correction, UW was the worst performing instrument of the three, but this was greatly improved, almost to parity with NZ in the case of NO_2, after the elevation angle offset was corrected. UM performs within 20% of the guidelines on all points, which is perhaps surprisingly good given the severity of the elevation angle pointing problems. The improvement demonstrated for UW upon elevation angle correction boded well for UM, for which the elevation was appropriately corrected in subsequent campaigns.

Similar scatterplots were made to compare the residual RMS and percentage error (100×(Fit error/dSCD)) between NZ and each of BM, UM and UW. This data is shown in Appendix A. For UM and UW, most values lay close to the 1:1 line, with

low percentage errors ($< 2\%$ for O_4 retrievals) and residual RMS ($< 4 \times 10^{-3}$). The remaining few datapoints at higher error values showed more scatter and were likely due to increased scattering at high solar zenith angles.

Another useful exercise from a comparison campaign such as TIMTAM is to evaluate the results from simultaneous measurements as a guide to instrumental uncertainty. To study this, data from 21st and 22nd February was chosen, from NZ (the TIMTAM standard), BM (shown to perform well compared to NZ) and UW (shown to perform well compared to NZ in this period). The instrumental uncertainty (E_{IU}) was estimated as the standard deviation of the three simultaneous dSCD results, and compared to the quoted fit error in QDOAS. For O_4 between 21 and 22 February the mean O_4 dSCD was 4.44×10^{43}, the average fit error was 4.54×10^{41} and the average E_{IU} was 4.25×10^{42}. This implies up to a 10% uncertainty on O_4 dSCDs due simply to instrumental differences. For NO_2 in the same time period, the mean dSCD was 7.03×10^{16}, the mean fit error was 9.34×10^{15} and the average E_{IU} was a little lower than this, 6.77×10^{15}. Therefore for NO_2, similar to O_4, a 10% uncertainty due to choice of instrument may be expected. This is useful information which may be used as input to the inversion scheme in the profile retrieval stage.

4.4 Vertical column and profile comparison

The HEIPRO retrieval algorithm was used to calculate vertical columns and profiles for aerosol extinction (from O_4 dSCDs) and NO_2. Settings for the retrievals were as described in chapter 3. Elevation angles were corrected for the UW, UM and BM instruments as described in section 4.2. Timeseries plots for retrieval results including aerosol optical depth (AOD), NO_2 vertical column density (VCD) and volume mixing ratio (VMR) in the 0-200 m retrieval layer, are shown in figure 4.8. Overall, comparison of retrieval results is severely hampered by the need for elevation angle corrections, the short time period of TIMTAM and the fact that four of the seven days were mostly cloudy. The retrieved AOD is highest, but also most highly variable from 17-20 February which were mostly cloudy days. During the sunny days, the four instruments generally retrieved very similar AOD. R^2 correlation coefficients for UM, BM and UW AOD compared to NZ AOD range between 0.73 and 0.94 for the whole period, including cloudy times.

Figure 4.8(b) shows that NO_2 VCD retrievals are very consistent between the instruments, with R^2 correlation coefficients for UM, BM and UW compared to NZ greater than 0.88 in each case. This suggests that the trace gas vertical column retrieval deals well with cloudy periods, and is largely independent of the retrieved AOD. In contrast, the vertical distribution of the total trace gas column is influenced more strongly by cloud and probably also by elevation angle corrections, as demonstrated by the comparison of NO_2 VMRs in figure 4.8(c). While the general trend of surface VMRs is well captured each day by each instrument, the R^2 correlation coefficients for NZ vs

Figure 4.8: Timeseries results from the profile retrieval analysis, from 16-22 February for each instrument: (a) aerosol optical depth, (b) NO_2 vertical column density and (c) NO_2 volume mixing ratio in the lowest retrieval layer.

the rest range from 0.48 to 0.77. The UW MAX-DOAS showed the lowest correlation, because it had a consistent 2.6^o elevation angle offset applied, reducing the amount of low elevation angles available to the retrieval.

4.5 TIMTAM summary

In summary, the TIMTAM campaign was a worthwhile exercise which brought the Australasian MAX-DOAS community together in Melbourne for one week. Despite the short period of simultaneous measurements, TIMTAM was able to achieve its main goals. Firstly, the collaboration allowed harmonisation of spectral collection and analysis routines. This was achieved by building on the framework provided by the CINDI-1 and CINDI-2 campaigns. Secondly, some major instrumental problems were detected, most notably the pointing inaccuracy of the BM, UM and UW optics. Through studying the residual RMS the importance of accurate dark current, offset, wavelength calibration and lineshape determination was highlighted. In the absence of a dedicated modelling study and in lieu of longer-running "standard" instruments, the NZ MAX-DOAS provided a robust reference against which to test the Australian instruments' performance. On all measures, BM performed very comparably with NZ. UM and UW

were hampered by elevation pointing problems but UW was able to be corrected during TIMTAM, whereupon significant improvement was observed. During the 21st and 22nd February, simultaneous dSCD results from the three highest performing instruments (NZ, BM and corrected UW) were used to estimate instrumental uncertainty, found to be in the order of 10% for both NO_2 and O_4. This work represents the first attempt at a comparison and validation study for MAX-DOAS instruments in Australasia and provides the groundwork validation for further analysis using these instruments in subsequent measurement campaigns.

Chapter 5

Urban MAX-DOAS measurements: Broadmeadows 2016-2019

This chapter presents two and a half years of MAX-DOAS measurements from the Bureau of Meteorology's Broadmeadows facility. Results from 21 December 2016 until 15 May 2019, including the TIMTAM campaign period, were used to construct timeseries' of aerosol, O_4 and NO_2, nitrous acid, formaldehyde and glyoxal results. The results in this chapter are entirely from the Bureau of Meteorology instrument, described in chapter 4. This chapter places the timeseries results for MAX-DOAS measurements in Melbourne in the context of air quality measurements in different places around the world. The high versatility of the MAX-DOAS technique is highlighted for each species: in addition to timeseries, vertical profiles, diurnal cycles and seasonal cycles are presented. Alongside co-located atmospheric composition and meteorological measurements these results allow a thorough discussion of the potential sources, contribution to oxidative capacity and air quality implications of NO_2, HONO, HCHO and glyoxal.

The chapter is organised as follows: DOAS dSCD results from the BOM MAX-DOAS are first presented as background to the ensuing discussion of vertical column and mixing ratio results. Aerosol optical depth and NO_2 results are then discussed in an air quality context including a review of how pollution in Melbourne compares with previous measurements in other cities. HONO measurements are then presented including a discussion of potential sources and the role of HONO as an OH radical source. The final section deals with volatile organics, through measurements of HCHO and glyoxal, again including detailed analysis of potential precursors and influence on oxidation chemistry. In particular the influence of HCHO on OH and O_3 production are explored.

The south-westerly viewing direction of the MAX-DOAS at Broadmeadows looks over one of Melbourne's main arterial motorways (the Western Ring Road) and, further to the south, the northern suburbs and central city as shown in figure 4.1. Being close

to the Western Ring Road, the MAX-DOAS is ideally placed to measure the resulting traffic pollution plumes. Being on the northern fringes of the Melbourne metropolitan area, the instrument is well placed to study the interaction of rural and urban air masses given the appropriate prevailing meteorology.

Co-located useful measurements at Broadmeadows include in-situ meteorological data, twice weekly Dobson spectrophotometer ozone column measurements and weekly ozone sondes. Intermittent solar radiation measurements are also made on site, with more frequent observations at Melbourne Airport 9 km to the west. By combining the MAX-DOAS results with these co-located measurements and other ancillary datasets, a comprehensive analysis of the key drivers of tropospheric oxidation chemistry and air quality in Melbourne is provided in this chapter. Aerosol optical depth and nitrogen dioxide results are presented which highlight the capability of the MAX-DOAS technique to provide both a broad overview of key air quality influences in Melbourne, and specific spatiotemporal analysis of traffic pollution plumes. Validation of NO_2 results with Environment Protection Agency data confirms that the Broadmeadows MAX-DOAS results are quantitatively sensible, as well as qualitatively sensible within our understanding of the expected pollution sources and sinks, including patterns on daily and seasonal timescales. Using nitrous acid, formaldehyde and glyoxal results we detail for the first time in Melbourne the competing roles of nitrogen oxides and organic compounds in ozone and hydroxyl radical production, which define the budget of atmospheric oxidants.

5.1 Slant column results at Broadmeadows

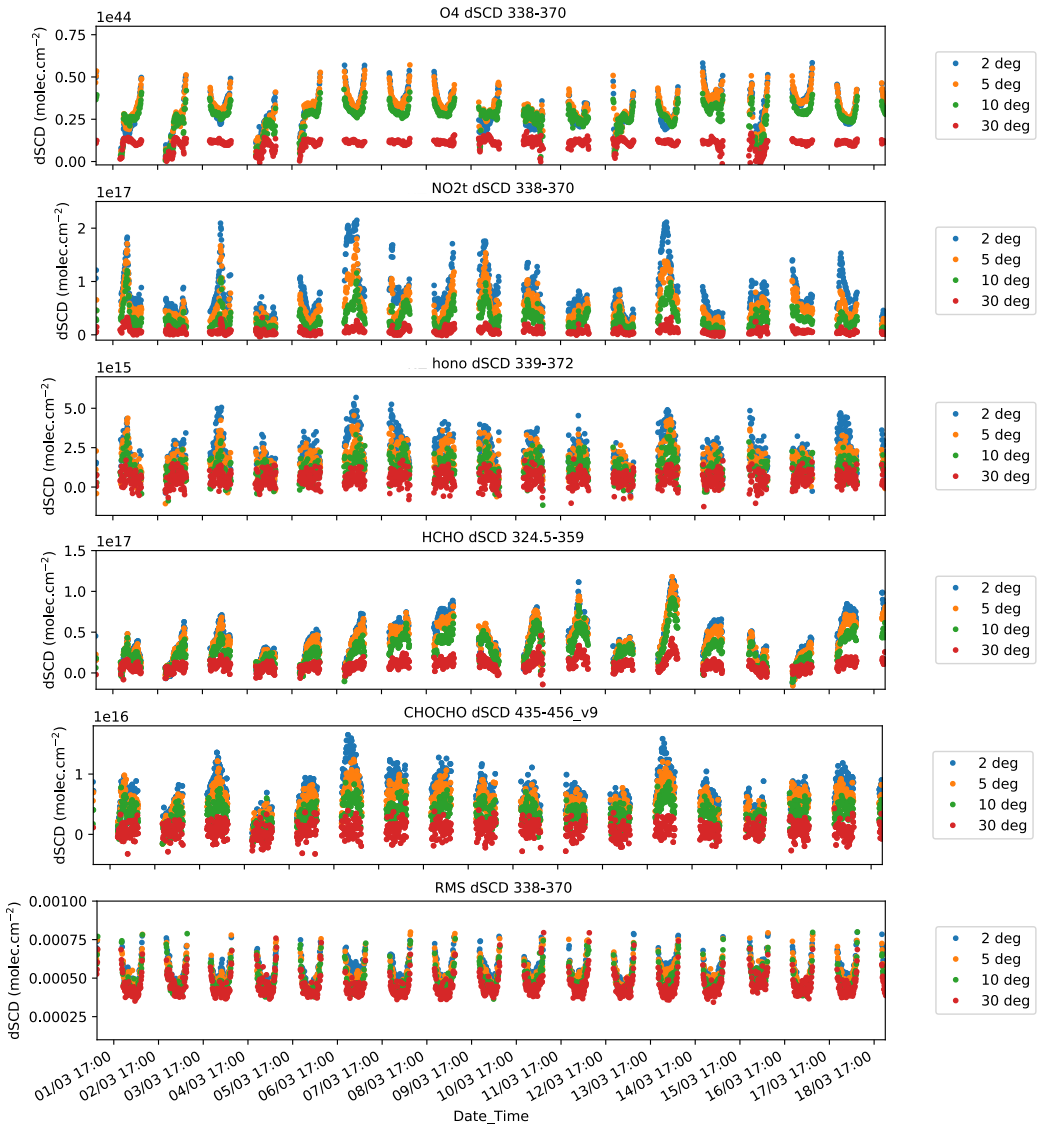

Figure 5.1: Example dSCD results from DOAS analysis of Broadmeadows data in March 2017, for (top to bottom) O_4, NO_2, HONO, HCHO, CHOCHO and residual RMS.

Differential slant column densities (dSCDs) for a range of target trace gases were retrieved using QDOAS for all UV spectra collected at Broadmeadows. The analysis settings used in QDOAS for each trace gas are described in detail in Chapter 2. Example dSCD results coloured by elevation angle (EA) for 1-18 March 2017 are shown in figure 5.1 for O_4, NO_2, HONO, HCHO and CHOCHO, alongside the residual RMS. For plot clarity, only the 2°, 5°, 10° and 30° EAs are shown. The strongest two UV absorbers of these, O_4 and NO_2 were fitted using the 338-370 nm wavelength range

and consistently gave convincing DOAS fits. Good spectral fits for a trace gas are, at a qualitative first glance, indicated by clear separation between the dSCDs at different EAs, typically with the highest dSCD at the lowest EA. This is expected because (a) the target trace gases mostly (but not always!) have highest concentrations at the ground level, and (b) because the tropospheric light path is longest at lowest elevation angle. In figure 5.1, the 7th of March provides a nice example of EA separation of dSCDs for each of the trace gases plotted. Moreover, peaks in NO_2 and HONO dSCD do not correspond with spikes or dips in O_4 dSCD (this is more evident for HCHO on the 9th rather than the 7th of March) implying that the dSCD increase is due to increasing trace gas concentration rather than changing light path. Strong spectral detection with clear EA separation of dSCDs was common for HCHO, CHOCHO and HONO, but less frequent than for O_4 and NO_2 because of their weaker UV absorbtion, and because of their larger relative variation in abundance. The dSCD ranges observed for each trace gas are broadly consistent with the ranges reported from MAX-DOAS slant column comparison exercises in Europe (e.g. Roscoe et al. (2010); Pinardi et al. (2013); Wang et al. (2017c) although it is worth noting that few prior MAX-DOAS dSCDs have been reported from the southern hemisphere.

Value	NO_2	HONO	HCHO	CHOCHO
XS max.	8.39×10^{-19}	5.21×10^{-19}	1.32×10^{-19}	1.05×10^{-18}
2° mean DL	1.32×10^{15}	2.09×10^{15}	8.38×10^{15}	9.61×10^{14}
2° mean dSCD	6.44×10^{16}	2.19×10^{15}	3.35×10^{16}	5.33×10^{15}
30° mean DL	1.12×10^{15}	1.93×10^{15}	6.77×10^{15}	7.91×10^{14}
30° mean dSCD	7.99×10^{15}	1.06×10^{15}	1.17×10^{16}	3.57×10^{14}

Table 5.1: Analysis of average dSCDs and detection limits (DL) for NO_2, HONO and HCHO over the course of the Broadmeadows measurement period. XS max. = maximum of the absorption cross section (units of cm^2). Detection limits and dSCDs are in units of molecules.cm^{-2}. See text for details of how DL dSCDs are calculated.

Spectral detection limits can give further evidence of clear detection for each trace gas. The detection limit for DOAS spectral analysis is approximated as the minimum detectable optical density, determined by dividing the root mean squared of the residual (residual RMS) by the maximum of the cross section for the trace gas, in the wavelength range considered (Sinreich et al., 2010). For a conservative detection limit estimate, a value of twice the residual RMS is typically used (Sinreich et al., 2010; Behrens et al., 2019). Results of analysing the detection limits for the Broadmeadows dataset are shown for NO_2, HONO and HCHO in table 5.1. In this table, 'XS max' refers the maximum value of each cross section in the relevant fitting wavelength range, and $2\times$ the residual RMS for each measurement has been used to calculate the minimum detectable optical density. For each molecule, both the residual RMS in the fit range and dSCD are typically higher for low elevation angles, and for the example given (2°

elev.) the average dSCD is greater than the average calculated detection limit. For higher elevation angles such as 30° as shown, the detection limits are lower owing to lower residual RMS. In the case of HCHO, 30° dSCDs are usually much higher than the detection limit in summer months and on or below the detection limit during winter. Mean HONO and glyoxal 30° dSCDs are lower than the calculated DL (they sit around the DL if considering 1×RMS rather than 2×RMS), potentially due both to strong vertical trace gas gradients and their weak absorption cross sections.

5.2 Aerosols in the urban environment

The aerosol extinction vertical profile results for Broadmeadows, calculated from O_4 dSCDs, are presented here. As well as supplying light path and scattering details necessary for the subsequent trace gas retrievals, the aerosol results can give information on particulate pollution at this urban location which is important for air quality and human health, and is also important in the context of the overall atmospheric oxidation chemistry discussion in this chapter. Vertically integrated extinction profiles give the aerosol optical depth (AOD) which is a measure of atmospheric visibility at a particular wavelength. The aerosol retrieval calculations used a wavelength of 360 nm and henceforth in this chapter, unless otherwise specified, AOD refers to the optical depth at this wavelength. AOD results have been summarised for the 2016-2019 Broadmeadows dataset in figure 5.2. Considering firstly daily averages of AOD over the measurement period, the timeseries in figure 5.2(a) shows the AOD is quite variable from day to day, with a maximal range 0.06-0.5 and overall average of 0.078±0.051. Points in black are the raw data averaged daily, whereas the gold points are the cloud filtered data that has been averaged daily. The cloud filtering procedure removes the majority of instances with retrieved AOD > 0.2. Moreover, the cloud filtering procedure has a pronounced effect on the average monthly aerosol vertical profile shapes as shown in figure 5.3: the cloud filtering reduces instances of elevated aerosol layers being retrieved. This suggests both that the cloud filtering procedure is indeed filtering out cloud (evidenced by the removal of elevated layers) and that without the cloud filtering procedure, cloudy events would effectively be misclassified as elevated aerosol layers with high AOD.

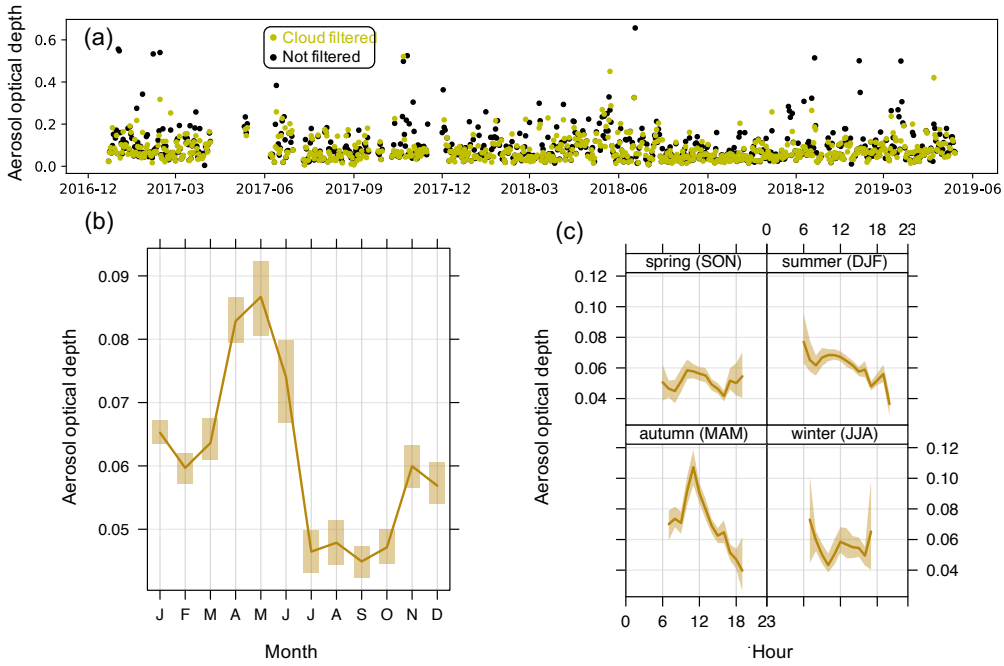

Figure 5.2: (a) Timeseries of daily averaged aerosol optical depth (AOD, at 360 nm) at Broadmeadows from December 2016 to May 2019. Black points indicate raw data, gold points indicate AOD results after application of cloud filter. (b) Monthly averaged AOD over the measurement period (calculated from cloud filtered data). (c) Seasonally averaged diurnal cycle plots for AOD (calculated from cloud filtered data). Shading in (b) and (c) indicates the 95 % confidence interval

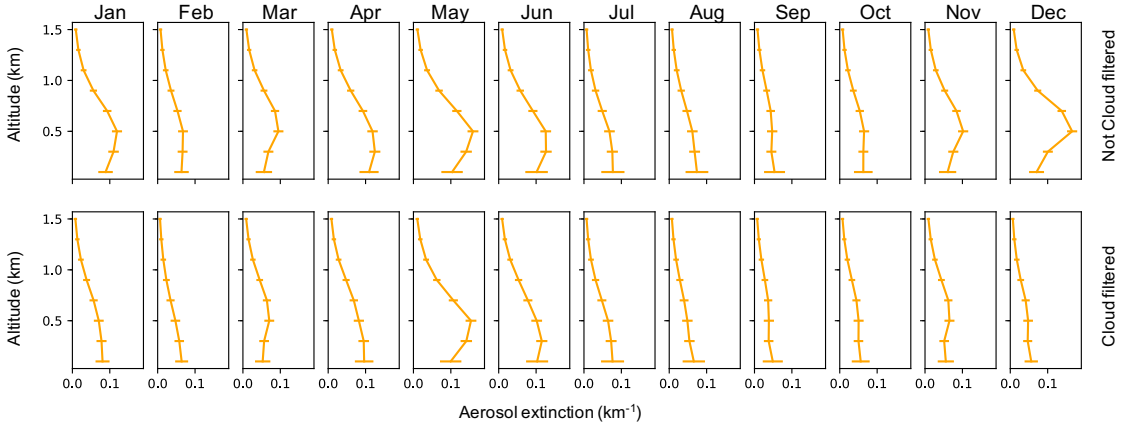

Figure 5.3: Monthly averaged aerosol vertical profiles at Broadmeadows for 2018. The top row shows unfiltered data, the bottom row shows cloud filtered data.

The ranges for AOD found reveal that the atmosphere in Melbourne is quite clean with respect to aerosol pollution, relative to other cities around the world. For example, from

MAX-DOAS measurements in Madrid, Spain, from March to September 2015 Wang et al. (2016) found monthly average AOD (at 360 nm) between 0.1 and 0.2 whereas monthly averages in Melbourne (see figure 5.2(b)) are always less than 0.09. From five years of MAX-DOAS measurements in Hong Kong Chan et al. (2018) found an average AOD (at 477 nm) of 0.58 compared to Melbourne's 2.5 year average of 0.078. In a more extremely polluted example, Hendrick et al. (2014) found monthly AOD (360 nm) averages ranging between 0.2 and 3.0 across four years of MAX-DOAS measurements in Xianghe and Beijing, China.

The plot of monthly averaged AOD in Melbourne (5.2(b)) shows a pronounced annual cycle which peaks above 0.07 in April - June, drops to a minimum below 0.05 in July - October and is around 0.06 between November and February. There are a range of potential physical and chemical drivers of this annual cycle. For example, high aerosols may be expected in summer in South-Eastern Australia generally, due to smoke from wildfires. The same might be expected in Autumn months due to controlled fuel reduction burns which are held after the summer heat abates, and are often take place in bushland close to the urban fringes. If biomass burning smoke was a major contributor to the higher summer and autumn AOD, it would most likely come from the proximate rural and forested areas to the north and east of Broadmeadows. However the polar bivariate plot in figure 5.4(a) of AOD as a function of wind speed and direction suggests that there is no clear source direction in summer at all, rather a ubiqutous background AOD around 0.06 regardless of the wind. In autumn, the highest AOD occurs during periods of low windspeed. The former is consistent with either localised aerosol production from nearby roadways, or slow build up of pollutants (e.g. from stagnant bushfire smoke under stable atmospheric conditions). The latter is consistent with aerosol sources in the industry-heavy south-western suburbs of Melbourne. It is notable that in winter, the source direction implied by the polar bivariate plot is entirely from the industrial south-west. The fact that high AOD episodes from the north and east appear to be switched off in the coldest part of the year lends some weight to the theory that temperature, biogenic or smoke related aerosols contribute to the observed AOD at other times of the year.

Meteorological factors could also contribute to the observed AOD. Reactions which promote secondary aerosol formation would be expected to proceed faster at higher temperatures. On the other hand, higher temperatures leading to strong surface heating promote greater boundary layer growth in warmer compared to cooler months. This has the effect of diluting the concentration of aerosols in the lowest MAX-DOAS retrieval layers, the region of highest sensitivity. These competing effects may help to explain the AOD diurnal variation, plotted as seasonal averages in figure 5.2(c). In spring, summer and autumn, AOD peaks in the mid morning before mostly declining throughout the rest of the day. The morning increase could correspond to traffic with the main traffic peak expected around 7-9 am whereas the peak AOD is somewhat later between 10-11 am. The morning increase could also suggest a temperature or photolytic link although if so, it is unclear why the peak AOD in autumn ($\approx$0.11) is so much higher than spring

and summer (≈0.06-0.07).

Synoptic scale meteorology may also influence aerosol amounts. Using self-organising maps to determine the most common synoptic types in Melbourne, Pearce et al. (2011) increases of up to 40 % in PM10 concentrations (particles less than 10 μm) were associated with large scale high pressure systems centred over Melbourne. The reason for this may simply be that under highly stable conditions, aerosol pollution is able to build up without being blown away. According to NCEP/NCAR reanalysis data (1979-2000, sourced from BOM Climate Data Online), the months with highest occurence of high pressure systems in Melbourne are April, May and June which correspond to the highest observed AOD at Broadmeadows.

Therefore on the available evidence, local traffic as well as industry in Melbourne's south-west seem to be consistent sources of AOD observed at Broadmeadows. In warmer months these are supplemented by AOD sources in other regions potentially related to biomass burning and biogenic secondary aerosol formation. In addition to considering aerosol sources, the high AOD observed in the period April-June could be partly explained by increased atmospheric stability in these months.

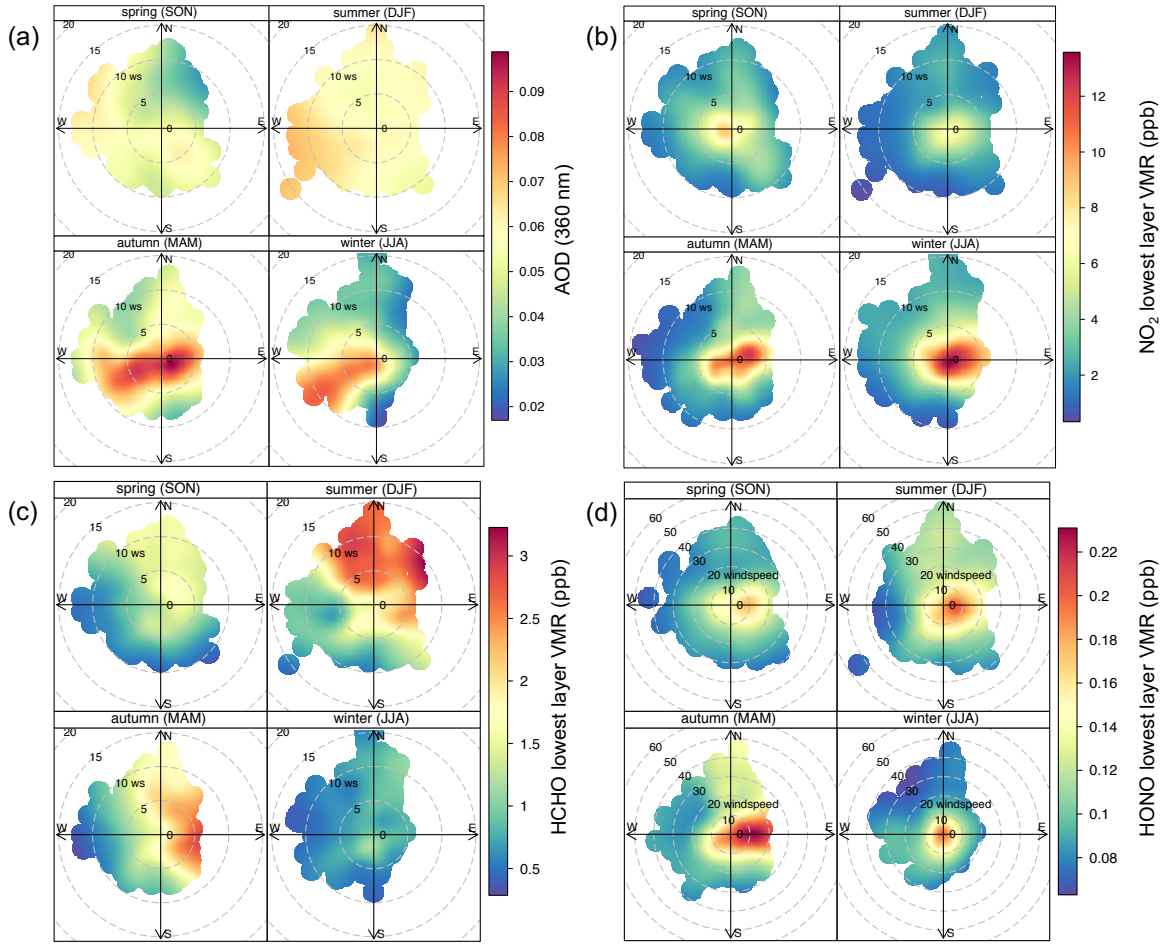

Figure 5.4: Polar bivariate plots of: (a) AOD at 360 nm, (b) NO_2 VMR in the lowest retrieval layer, (c) HCHO VMR in the lowest retrieval layer and (d) HONO VMR in the lowest retrieval layer, indicating the relationship between each variable and wind speed and direction.

5.3 Nitrogen oxides in the urban environment

5.3.1 NO_2 timeseries 2016-19

Nitrogen dioxide (NO_2), the primary nitrogen oxide measured with the MAX-DOAS at Broadmeadows, was retrieved consistently throughout the measurement period as shown by the timeseries of NO_2 daily averaged VCD in figure 5.5(a). Throughout the entire campaign, daily average NO_2 VCD ranged from 1.63×10^{15} molecules.cm^{-2} to 4.31×10^{16} molecules.cm^{-2}, with a mean of 7.59×10^{15} molecules.cm^{-2}. This corresponded to daily averaged volume mixing ratios in the 0-200 m retrieval layer (henceforth termed the 'surface VMR') ranging from 0.59 ppb to 32.29 ppb with overall mean

of 6.08 ppb. These retrieved NO_2 values are well higher than the calculated detection limits for VCD and surface VMR which are 7.75×10^{13} molecules.cm^{-2} and 95 ppt respectively. These detection limits have been calculated using the method outlined in Peters et al. (2012):

$$DL_{VCD} = \frac{2 \times R_{avg}}{XS_{max} \times A - 1} \tag{5.1}$$

$$DL_{VMR}(ppb) = 1 \times 10^9 \frac{DL_{VCD} k_b T}{hP} \tag{5.2}$$

where R_{avg} is the average residual RMS (4.5×10^{-4}), XS_{max} is the maximum value of the cross section (see table 5.1), A is the airmass factor taken here as 15 for low elevation angles, k_b is the Boltzmann constant, T is the temperature (taken as 300 K), P is the pressure (taken as 1000 hPa) and h is a mixing layer height of 1 km. While fixed values of T, P and h are not realistic for all measurement conditions, considering twice the optical depth of the residual RMS as the minimum detectable is a generous compensation, hence, the detection limits quoted are considered to be conservative estimates.

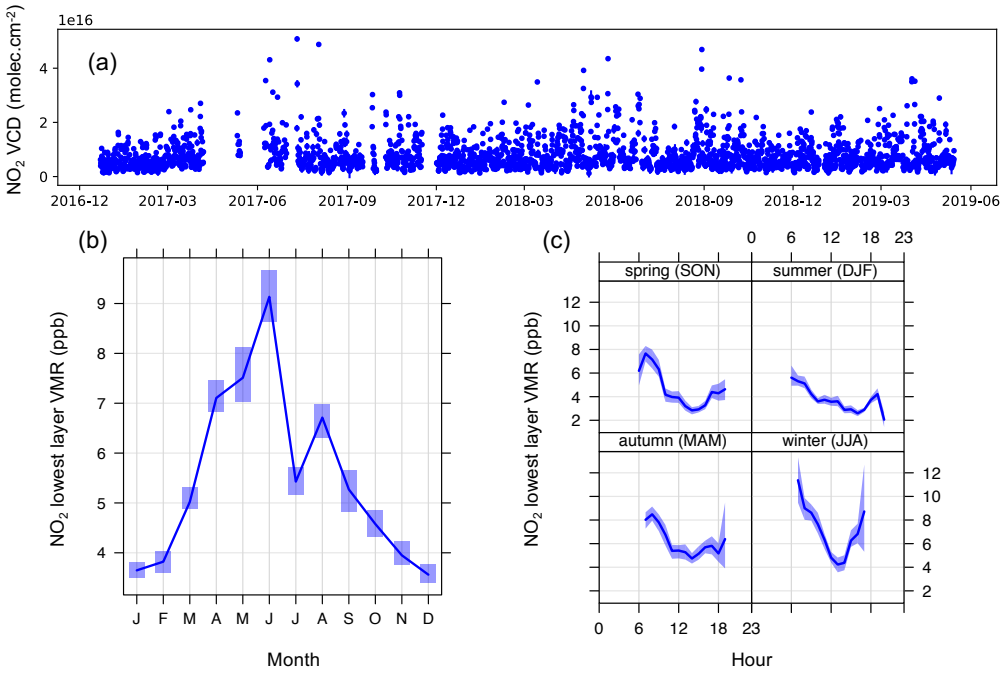

Figure 5.5: (a) Timeseries of daily averaged NO_2 VCD at Broadmeadows from December 2016 to May 2019. (b) Monthly averages of NO_2 mixing ratio in the lowest retrieval layer. (c) Seasonally averaged diurnal cycle plots for NO_2 mixing ratio in the 0-200 m retrieval layer. Data in this figure is cloud filtered.

Only twice in the measurement period did the average daily NO_2 concentration at Broadmeadows exceed 30 ppb. Australia's National Environment Protection Measure annual average NO_2 standard is currently set at 30 ppb (and the WHO annual average guideline is 21 ppb, WHO (2016)), indicating that even adjacent to arterial motorways Melbourne sits comfortably inside the guideline for NO_2. The Broadmeadows results generally sit below the range of urban NO_2 concentrations in other cities around the world. For example, throughout several major Israeli cities, Boersma et al. (2009) found a range of monthly-averaged NO_2 mixing ratios (from in situ measurements) between 5-15 ppb, peaking in the Israeli winter months. A report on European NO_x trends by Carslaw et al. (2011) showed that annual average roadside NO_2 concentrations at a majority of monitoring sites across western Europe exceeded 18 ppb in 2008. Updated results for London suggested that in 2015 roadside NO_x pollution in that city was largely unchanged from 2008 values (Carslaw et al., 2016).The values for NO_2 observed in Melbourne certainly fall well short of the most polluted cities in the world, such as Beijing and Xianghe, China, where Hendrick et al. (2006) reported monthly a monthly average NO_2 range of between 5 and 30 ppb (2013-2017 data), New Delhi in India where daily average NO_2 concentrations regularly exceed 45 ppb (2017 data) (Mishra et al., 2016), and Hong Kong where monthly average NO_2 levels are around 50 ppb (Zhu et al., 2018).

In contrast, the annual average NO_2 measured by the MAX-DOAS at the Broadmeadows roadside site between 2016-19, and as reported by the Victorian EPA between 2008-17, is around 9 ppb. NO_2 monthly averages measured by the MAX-DOAS at Broadmeadows range between 3 and 9 ppb as shown in figure 5.5(b). It is anticipated that at Broadmeadows the predominant source of nitrogen oxides will be road transport emissions from proximate road corridors, and this is confirmed by plotting the NO_2 surface VMR as a function of wind speed and direction throughout the measurement period (figure 5.4(b)). Here the highest NO_2 concentrations are found to occur for low wind speed, independent of wind direction or season, indicating highly localised sources.

A clear seasonal cycle is evident in figure 5.5(b) with surface VMR that is a maximum in winter and minimum in summer. The dip in July which is inconsistent with this trend is due to (a) a sampling bias caused by a large number of cloudy days in July 2018 and (b) July was found to have, on average, the highest windspeed of any month at Broadmeadows, conditions which do not enable build up of surface NO_2. To interpret the observed seasonal variation it would be useful to know if vehicle emissions are expected to vary throughout the year. Monthly averaged traffic data was not available for Victoria so instead, monthly traffic data from Sydney (2010-2018) was analysed (see figure B.1 in Appendix B). For four major road corridors in inner Sydney a general trend was evident: minimum traffic volume occurred in December and January, presumably due to most people taking their summer holidays. For the rest of the year traffic volume was fairly constant with a slight decrease at each location in July and August, possibly due this time to winter holidays. In taking the large assumption that traffic patterns

in Sydney and Melbourne are comparable, there is nothing in these results to suggest that emissions can explain the observed winter NO_2 peak.

A counterargument to this is provided by recent studies demonstrating the significant temperature dependence of NO_x emissions from diesel vehicles. For example Grange et al. (2019) found, in a study across the United Kingdom, that diesel NO_x emissions increased at a rate of 0.36 grams per kilogram of diesel, for every degree of temperature decrease. Assuming the same relationship holds for Australian diesel vehicles, where the daytime average monthly temperature difference between the warmest (January) and coldest (July) months at Broadmeadows is $24.1 - 11.4 = 12.7^oC$, this would imply diesel NO_x emissions could be 4.6 times higher in winter than summer. The NO_2 seasonal cycle observed at Broadmeadows shows that the maximum monthly NO_2 is only 2.5 times higher than the minimum. The 2019 Motor Vehicle Census, carried out by the Australian Bureau of Statistics, reported that diesel vehicles made up 24.6 % of Australia's total fleet, up from 18.2 % at the time of the 2014 Census (https://www.abs.gov.au/ausstats). Therefore, with potentially a quarter of the cars subject to an ambient temperature-dependent emission regime, it seems plausible that this effect may be increasingly contributing to the observed NO_2 seasonal cycle. In addition to emissions considerations, the winter NO_2 maximum will also be due to a combination of chemical and physical processes. Firstly, the ambient meteorology plays a key role in the partitioning of NO_x between NO_2 and NO. Considering a simplified photochemical steady-state equilibrium where O_3 is the primary atmospheric oxidant, the reactions governing the interaction of NO_x and ozone are:

$$NO_2 + h\nu \longrightarrow NO + O(^3P) \quad \{34\}$$

$$O(^3P) + O_2 + M \longrightarrow O_3 + M \quad \{35\}$$

$$NO + O_3 \longrightarrow NO_2 + O_2 \quad \{36\}$$

with the key rates governing the kinetics of the system being the NO_2 photolysis rate J_{NO_2}, and the rate constant k_1 for the reaction NO + O_3. The NO_x partitioning, according to this system, is therefore given by (Leighton, 1961):

$$\frac{[NO_2]}{[NO]} = [O_3]\frac{k_1}{J_{NO_2}} \quad (5.3)$$

Since J_{NO_2} depends on solar radiation, and k_1 depends on temperature, both of which are a minimum in winter, it follows that the formation of NO_2 from NO is less favourable in winter than in summer. This accords with the findings of Van Der A et al. (2008) over polluted parts of Europe, Asia, North America and South Africa. Interestingly, the observed seasonal cycle in Melbourne with maximum in winter does not agree with Van Der A et al. (2008) who estimated, from satellite measurements, that the

maximum seasonal NO_2 over Victoria should be in late summer or early Autumn. This finding presumably relates to a perception that, on a global scale, Australia is largely unpolluted and that nitrogen oxide production is therefore dominated by lightning and biomass burning, both of which would have summer maxima. In addition to temperature and sunlight partitioning effects, greater boundary layer heights in summer due to strong surface heating will lead to dilution of the NO_2 retrieved from using MAX-DOAS technique in the 0-200 m layer, a further instrument-specific reason why a winter time NO_2 maximum might be expected.

The NO_2 diurnal cycle at Broadmeadows, plotted as an average for each season, is shown in figure 5.5(c). The broad pattern for the NO_2 diurnal cycle is consistent with a morning peak followed by a decrease throughout the day until a second, afternoon, increase. Throughout all seasons, the average midday NO_2 concentration is fairly constant at around 4 ppb. Largest seasonal variations are observed in the peak values, which in each case occur corresponding with the morning rush hour period between 6 and 9 am local time. The timing of this rush hour peak is consistent with peak morning traffic volume along the Western Ring Road, Camp Road and Sydney Road corridors (see comparison of NO_2 diurnal cycle with Broadmeadows traffic volume data, figure B.2 in Appendix B). The afternoon traffic volume peak is between 3 and 5 pm local time. This timing is captured in the measured NO_2 cycle too, although a greater discrepancy between morning and afternoon peak magnitude is apparent in summer than in winter. This is an indicator that boundary layer heights are a strong constraint on the observed NO_2 because the dilution effect will be much weaker in winter, allowing the afternoon NO_2 to be observed more readily than in summer.

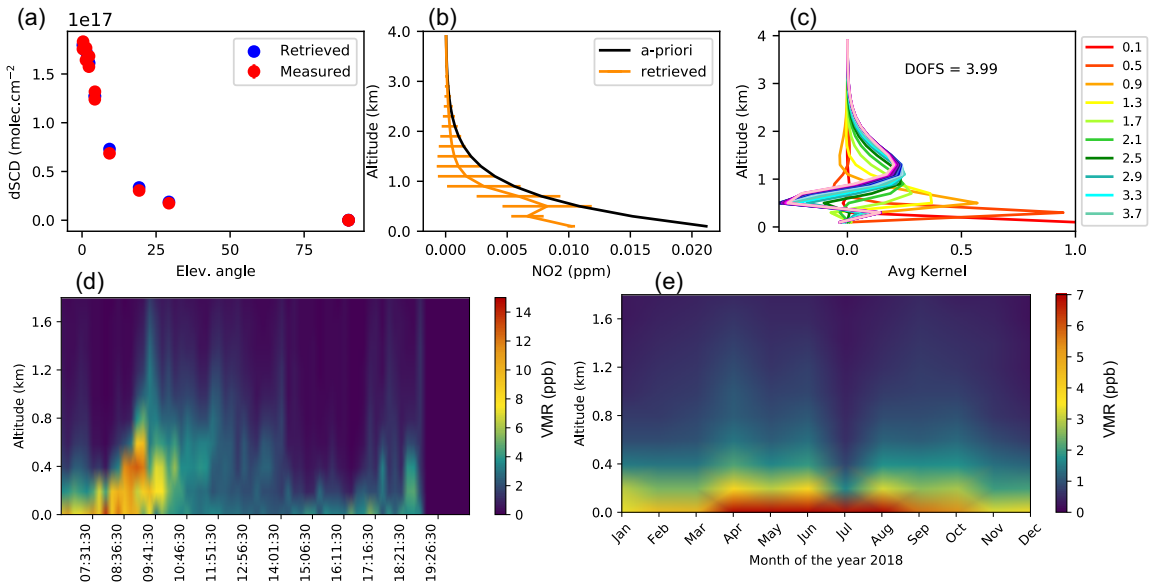

Figure 5.6: (a) Model/measurement comparison, (b) a priori and retrieved vertical profile and (c) averaging kernels from an example NO_2 retrieval at midday on 12/12/2017. (d) Daily NO_2 vertical profile evolution on 12/12/2017, typical of a day with high observed NO_2 at Broadmeadows. (e) Monthly averaged NO_2 vertical profiles showing annual variation in mean retrieved profiles throughout 2018.

A summary of the vertical distribution results for NO_2 at Broadmeadows is shown in figure 5.6. In general throughout the measurement period NO_2 dSCDs measurements were well modelled by HEIPRO (see, e.g., figure 5.6(a)) with overall R^2 correlation coefficient and slope for modelled vs measured values each 0.99 (figure B.6(a) in Appendix B). The averaging kernels for the NO_2 retrieval consistently indicated good information content for MAX-DOAS results with tpyically > 3.5 degrees of freedom. Sensitivity was highest in the lowest kilometer of the retrieval grid and almost zero above 2 km as indicated in the example from an exemplary retrieval on 12th December 2018, in figure 5.6(c). For this day, the vertical NO_2 distribution evolving across the course of the day is plotted as a colormap (figure 5.6(d)), typical of daily NO_2 vertical profiles throughout a day when high NO_2 (i.e. higher than an 8 ppb maximum) was observed. On the 12th of December 2018, conditions were clear and sunny with a light south-westerly breeze. Here, the morning traffic rush produces significant NO_2, with levels at 10 ppb, concentrated at the ground level, before the plume expands in the evolving boundary layer to approximately 600 m by 10 am local time. At this point, the NO_2 in the plume remains at this altitude but decreases to about 4 ppb presumably by virtue of decreasing emissions and increased photolytic destruction. On this day, in increase in NO_2 with the evening traffic rush was observed across the 0-500 m range, but with maximum concentrations at half the morning due to (a) higher windspeeds on this afternoon blowing the plume away, and summertime dilution and photolytic destruction reducing the amount of NO_2 observed in the afternoon. Taken in conjunction with me-

teorological information, figure 5.6(d) demonstrates the complexity of spatiotemporal analysis facilitated by the MAX-DOAS technique for studying trace gas distributions and plume evolution.

In addition to individual spatiotemporal plume analysis, the average vertical structure of traffic NO_2 plumes can be studied by considering the monthly mean vertical profiles as shown for 2018 in figure 5.6(e). While it appears that for diurnal patterns the influence of changing bounday layer heights can be discerned, as discussed for the diurnal cycles in figure 5.5(c) and the individual plume analysis in figure 5.6(d), this effect is smoothed out in the monthly averages. There is no evidence of more elevated plumes in summer, for example, when boundary layer heights would be expected to be larger. Rather, 5.6(e) suggests that the NO_2 vertical structure is very consistent across the course of the year, with the majority of the plume contained below 500 m.

5.3.2 Validation of NO_2 results

Comparison with Victorian EPA measurements

Air quality monitoring is carried out at a range of sites across the Melbourne Metropolitan area by the Victorian Environment Protection Agency (EPA). While there are no EPA sites immediately proximate to Broadmeadows, these measurements provide the only opportunity for validation of the MAX-DOAS results at Broadmeadows with in-situ NO_2 data. For the comparison, the mean NO_2 concentration from four sites was taken: Altona North in Melbourne's south-west, Footscray west of the city, Alphington in the inner north and Dandenong in the far eastern suburbs. These locations are shown on a map with Broadmeadows in figure B.3 in appendix B. As seen timeseries comparison in figure 5.7, the average EPA value and the MAX-DOAS are generally in very good agreement. EPA averaged values are typically 1-2 ppb higher than the Broadmeadows MAX-DOAS which may be explained by the fact that the EPA monitors are in-situ instruments whereas the MAX-DOAS 'surface VMR' is of course averaged over the lowest 200 m of the troposphere. In the timeseries, the seasonal trend of higher NO_2 in winter than summer is clearly captured by both datasets.

A simple linear regression analysis has been carried out using the average of hourly reported EPA values across the four sites, and hourly averaged MAX-DOAS results as shown by season in figure 5.7(b). The correlation between methods is strongest in winter and autumn with $R^2 = 0.56$ and $R^2 = 0.39$ respectively, compared to $R^2 = 0.28$ and $R^2 = 0.31$ respectively for spring and summer. In each scatterplot, the slope of the regression is less than 1 (between 0.65 and 0.80) suggesting that, contrary to what would be expected from the observed offset in the timeseries, the MAX-DOAS measures higher NO_2. It seems that the regression is skewed by the extreme cases: when high NO_2 is observed, the MAX-DOAS sees more than the EPA average, and vice versa for the low end of the range. This view is confirmed by considering the overall correlation for hourly and daily averages (gradients equal 0.80 and 0.75 respectively, see figure B.4

in appendix B) compared to weekly and monthly averages (gradient = 1.1 in each case). In other words, when the extremes are smoothed by weekly and monthly averaging, the overall bias towards higher EPA NO_2 is present in the regression too. It is very plausible that the MAX-DOAS is higher than the EPA in cases of highest NO_2 at Broadmeadows because it is site-specific, whereas co-incident extreme values in the EPA monitoring network will be smoothed out by averaging over four disparate sites.

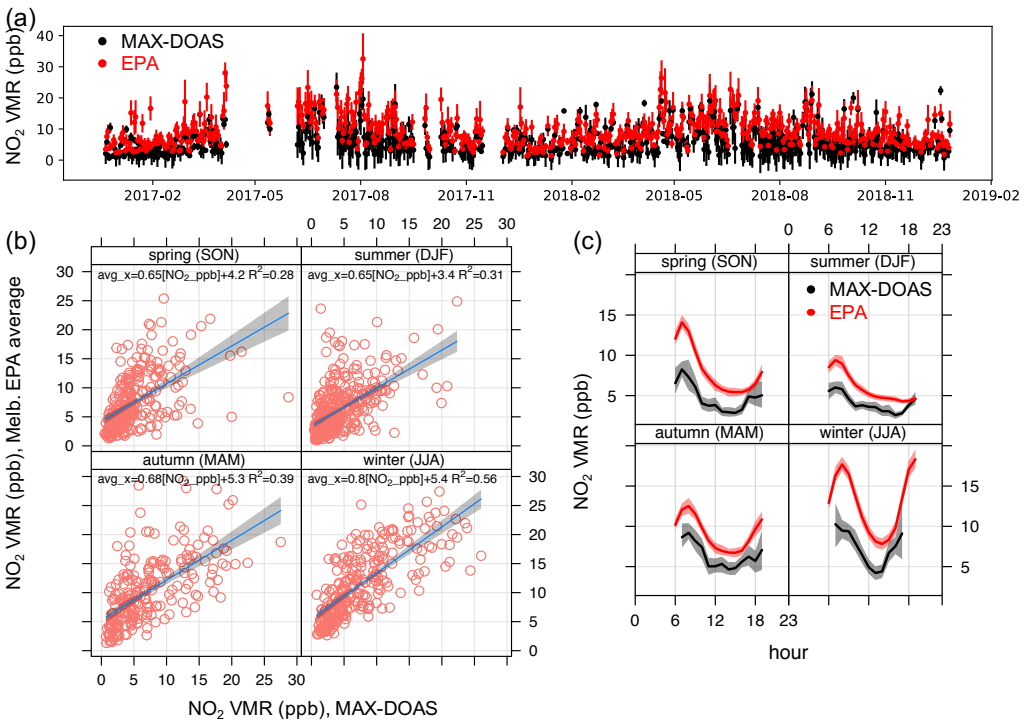

Figure 5.7: Comparison of NO_2 measurements made by the MAX-DOAS at Broadmeadows (black) and average in-situ NO_2 from observations in the Melbourne metropolitan area (red). (a) Timeseries of results from December 2016 to January 2019, (b) scatterplots comparing the two datasets for each season and (c) average diurnal cycles for each dataset in each season.

The average diurnal cycles reported by the MAX-DOAS at Broadmeadows and the EPA measurements across Melbourne has been compared in figure 5.7(c). While once again an offset is apparent, with EPA results higher than the MAX-DOAS over long term averages, the shape of the diurnal cycles in each season align nicely between datasets.

5.3.3 HONO timeseries 2016-19

The second nitrogen oxide species measured with the MAX-DOAS at Broadmeadows was nitrous acid (HONO). HONO was detected at Broadmeadows throughout the measurement period as shown in the timeseries in figure 5.8(a), with daily average vertical

column densities ranging from below the calculated detection limit of 1.12×10^{14}, to and 7.42×10^{14} molecules.cm^{-2} with a mean of 1.89×10^{14} molecules.cm^{-2}. This corresponded to daily average HONO surface VMR ranging from below 45 ppt, the calculated detection limit, to 820 ppt, with a mean value across all measurements of 120 ppt. The diurnal cycle of HONO measured at Broadmeadows, averaged over the whole measurement period, suggests that on average, HONO is at a maximum in the middle of the day between 10 am and 1 pm local time. The average surface mixing ratio during these times across the campaign was 0.14 ppb. This is comparable with midday of HONO levels observed in many urban locations around the world including Paris, France (Michoud et al. (2014), 0.1 ppb), Houston, USA (Wong et al. (2012), 0.1 ppb), Rome, Italy (Acker et al. (2006), 0.2 ppb) and Beijing, China (Hendrick et al. (2014), 0.2 ppb). HONO has also been observed at considerably higher average midday concentrations, for example 0.8 ppb in Hong Kong (Xu et al., 2015) and even up to 1.7 ppb in Santiago, Chile (Elshorbany et al., 2009). A summary of these and other campaigns reporting HONO levels in urban locations is provided in table B.1 in Appendix B. A pronounced seasonal cycle is evident in figure 5.8(b), with monthly averaged HONO greater than 0.1 ppb in the warmest months (November through to April) and between 0.1 and 0.08 ppb in the cooler months (May through to October). Broadly speaking this seasonal cycle with a seasonal maximum is the opposite of NO_2.

Nitrous acid has received considerable attention in recent literature primarily because in numerous measurement campaigns, higher daytime HONO concentrations have been observed than can be explained by the standard source/sink chemical mechanisms (e.g. Lee et al. (2016); Acker and Möller (2007); Kleffmann (2007); Wong et al. (2012); Huang et al. (2017); Neuman et al. (2016); Li et al. (2012); Qin et al. (2009); Hendrick et al. (2014); Pinto et al. (2014)). This implies a hitherto unknown, and strong, daytime HONO source and hence, through photolysis, a strong daytime hydroxyl radical source. Therefore the diurnal cycle observed in Melbourne for spring through to autumn, with HONO consistently peaking in the middle of the day (figure 5.8(c)), is particularly interesting. In the studies listed, which were conducted in urban areas, HONO during daylight hours typically peaked close to sunrise and, despite higher than expected daytime concentrations, decreased across the course of the day. In contrast, during spring, summer and autumn at Broadmeadows the HONO mixing ratio measured rises from an early morning minimum to a maximum approximately one hour before solar noon. Previously such daytime maxima in the HONO diurnal cycle have only been observed in rural locations for example at a mountain site in Germany (Acker et al., 2006), a forested site in Michigan USA (Zhou et al., 2011), and in rural Cyprus (Meusel et al., 2016). In each case however, the maximum HONO VMR observed was less than the overall midday average in Melbourne, at 110 ppt, 70 pptv and 100 pptv respectively. Therefore the diurnal maximum HONO measured here is unusual for an urban environment and supports the presence of a strong daytime source.

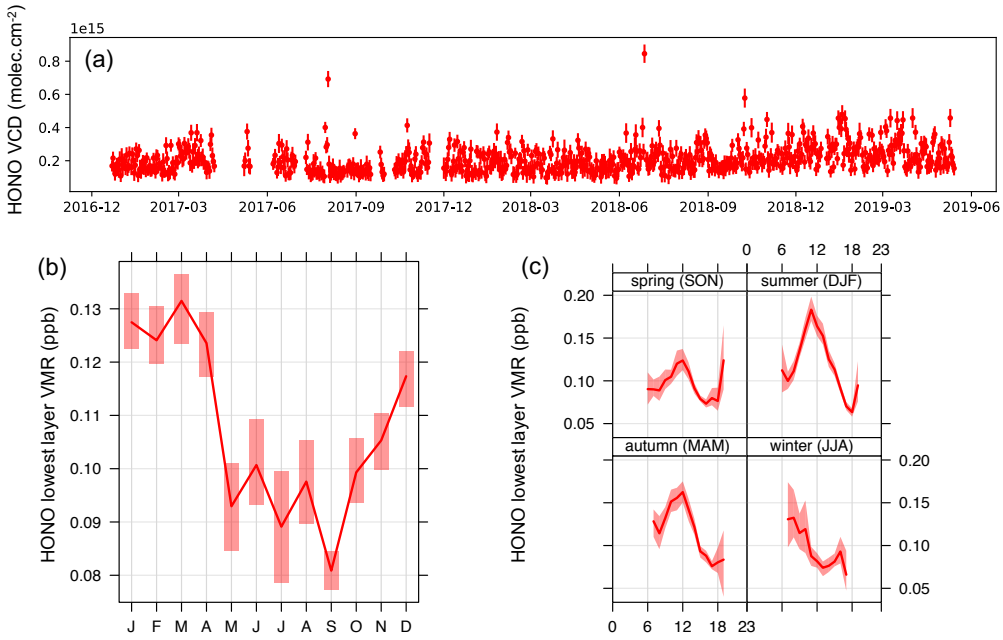

Figure 5.8: (a) Timeseries of daily averaged HONO VCD at Broadmeadows from December 2016 to May 2019. (b) Monthly averages of HONO mixing ratio in the lowest retrieval layer. (c) Seasonally averaged diurnal cycle plots for HONO mixing ratio in the 0-200 m retrieval layer. Data in this figure is cloud filtered.

In the seasonal polar bivariate plots (figure 5.4(d) the highest HONO concentrations correlate with low windspeed throughout the year, in a similar pattern to NO_2, implying that the source is highly localised and not dependent on long range transport. The vertical profiles of HONO retrieved at Broadmeadows, as shown in the example daily profile in figure 5.9(d) and the monthly average vertical profiles in figure 5.9(e), consistently reveal a strong vertical gradient with HONO VMRs >0.1 ppb almost exclusively contained within the lowest 400 m. The averaging kernels for the HONO retrieval (see example in figure 5.9(c)) show that there is in fact very little measurement sensitivity above this level. The fact that the maximum HONO is in the middle of the day, and that it is evident in spring, summer and autumn but not in winter, suggests that light or temperature could be drivers of the observed HONO. However, considering the dataset either as a whole or broken up by season, no significant correlation was found for surface HONO concentration vs global radiation (measured 9 km away at Melbourne Airport) or ambient temperature (measured at the Broadmeadows site) - R^2 values were always less than 0.1. Therefore while the diurnal and seasonal variations in HONO potentially signify some relationships with solar radiation and temperature, the magnitude of HONO concentrations on any given day are likely complicated functions of these and many other variables.

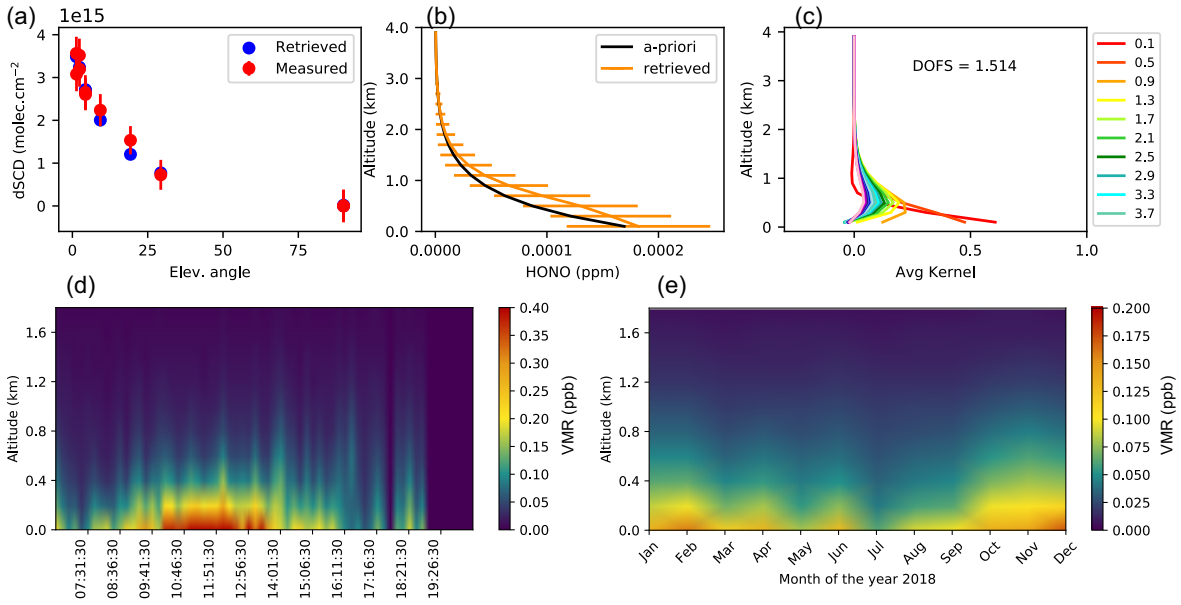

Figure 5.9: (a) Model/measurement comparison for one HONO vertical profile retrieval, (b) a priori and retrieved vertical profile and (c) averaging kernels from an example HONO retrieval at midday on 12/12/2017. (d) Daily HONO vertical profile evolution on 12/12/2017, typical of a day with high observed nitrous acid at Broadmeadows. (e) Monthly averaged HONO vertical profiles showing annual variation in mean retrieved profiles throughout 2018.

5.3.4 Discussion of potential HONO sources

In order to examine in greater detail potential HONO sources in Melbourne when large HONO concentrations exist a subset of the overall dataset from summer and autumn 2017 was examined, as presented in Ryan et al. (2018).

Previous studies concluded that direct emission of HONO from combustion engines could be identified by the ratio of HONO:NO_2 being greater than 0.01 (Wojtal et al., 2011; Hendrick et al., 2014; Qin and Mitchell, 2009; Elshorbany et al., 2009). At Broadmeadows, the HONO/NO_2 ratio measured by the MAX-DOAS was consistently < 0.01 implying that direct emissions cannot explain the observed HONO. Ryan et al. (2018) also concluded that the photostationary steady state chemistry underpinned by reactions involving OH, NO and HONO was insufficient to explain the high midday concentrations of HONO observed at this location. This is illustrated in figure 5.10(c). The same figure also shows that despite a strong correlation observed between NO_2 and HONO concentrations, heterogeneous conversion of NO_2 to HONO on the ground or wet surfaces, as hypothesised by Stemmler et al. (2006), Lee et al. (2016) and Wong et al. (2012), were insufficient at the observed NO_2 concentrations to explain all the mid-day HONO. No significant correlation was found between measured AOD and HONO suggesting that heterogeneous chemistry on aerosol surfaces (George et al., 2005) was also not a key HONO producing mechanism here.

Therefore Ryan et al. (2018) inferred the presence of an 'unknown HONO source', with a consistent diurnal profile qualitatively matching that found in several previous papers (e.g. Lee et al. (2016); Acker and Möller (2007); Kleffmann (2007); Wong et al. (2012); Huang et al. (2017); Neuman et al. (2016); Li et al. (2012); Qin et al. (2009); Hendrick et al. (2014); Pinto et al. (2014)). In the sample period, the midday HONO mixing ratio was found in Ryan et al. (2018) to be responsive to soil moisture content, using data extracted from the Australian Water Resources Assessment Modelling System (Hafeez et al., 2015), as shown by the diurnal cycle plots in figure 5.11. It is worth noting that the same decrease of HONO midday concentrations with increasing soil moisture is observed across the entire 2016-2019 HONO dataset at Broadmeadows. Using this information and the HONO and NO emission rates from soil-based bacteria found by Meusel et al. (2018), as shown in figure 5.10(d) Ryan et al. (2018) argued that soil emissions could plausibly explain the missing HONO source at Broadmeadows. This hypothesis is supported by both laboratory (e.g. Donaldson et al., 2013, 2014; Oswald et al., 2013) and field (e.g. Meusel et al., 2016, 2018) experiments showing soil emissions to be an important HONO source in other parts of the world.

5.3.5 HONO as an OH source in Melbourne

The key implication of the HONO observed at Broadmeadows for oxidation chemistry is that, through photolysis, HONO is a strong source of OH radicals. To quantify the significance of HONO as an OH source, Ryan et al. (2018) calculated the OH production rate from HONO and compared it to that from ozone according to:

$$P(\mathrm{OH})_{\mathrm{O_3}} = 2 \times f \times J(\mathrm{O}\,(^1\mathrm{D})) \times [\mathrm{O_3}] \tag{5.4}$$

$$P(\mathrm{OH})_{\mathrm{HONO}} = J(\mathrm{HONO}) \times [\mathrm{HONO}] \tag{5.5}$$

In equation 5.4, f is the fraction of $\mathrm{O}^1\mathrm{D}$ reacting with water vapour to form OH (Finlayson-Pitts and Pitts Jr, 1999). The ozone concentration $[\mathrm{O_3}]$ in ppb were taken from EPA results averaged EPA across the four measurements sites in the Melbourne metropolitan area, and [HONO] was the surface mixing ratio calculated by the MAX-DOAS retrieval. The photolysis rates $J(\mathrm{O}\,(^1\mathrm{D}))$ and $J(\mathrm{HONO})$ were simulated using the TUV radiation model (Madronich and Flocke, 1999) for 7/3/2017, a sunny day with a midday HONO concentration 400 ppt and Melbourne EPA average $\mathrm{O_3}$ surface concentration 27 ppb. Further details of the OH production calculations are contained in Ryan et al. (2018). As shown in figure 5.10(a), the pOH results suggest that on days with such high HONO levels, it acts as a clearly dominant OH source over ozone photolysis, consistent with results for surface OH production rates in other urban areas (e.g. Ren et al. (2003); Elshorbany et al. (2009)). To extend this work by exploiting the vertical profiling capability of the MAX-DOAS technique, Ryan et al. (2018) went on to show that although HONO can dominate the surface OH production its strong vertical

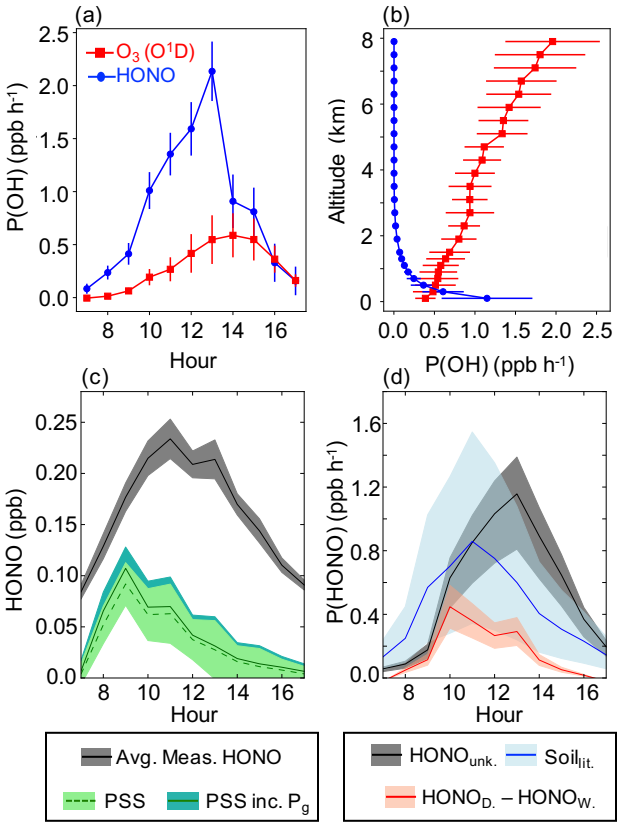

Figure 5.10: Figure adapted from Ryan et al. (2018). (a) Diurnal cycle of ground level OH radical production *P(OH)* from ozone (O_3 to $O(^1D)$) and HONO photolysis, calculated for an example day with 27 ppb surface ozone, and the HONO diurnal cycle from 7th March 2018 which peaked near midday at around 400 ppt. (b) Vertical profiles of tropospheric OH radical production from HONO photolysis, calculated using the average measured HONO vertical profile and from ozone photolysis calculated using colocated ozone sonde data averaged from January to April 2018. Points represent the mean, errorbars represent one standard deviation. (c) Measured average HONO diurnal cycle plotted with calculated photostationary state (PSS) HONO concentration and PSS including NO_2 ground conversion term (PSS inc. P_g). (d) $HONO_{unk.}$: unknown HONO production rate (measured - PSS), $HONO_D - HONO_W$: measured HONO emission rate attributable to soil processes (driest conditions - wettest conditions, see figure 5.11 and discussion in Section 3.5) and $Soil_{lit}$ representing PSS + literature HONO and NO soil emission rates. Lines represent means, shaded regions represent 95 % confidence intervals.

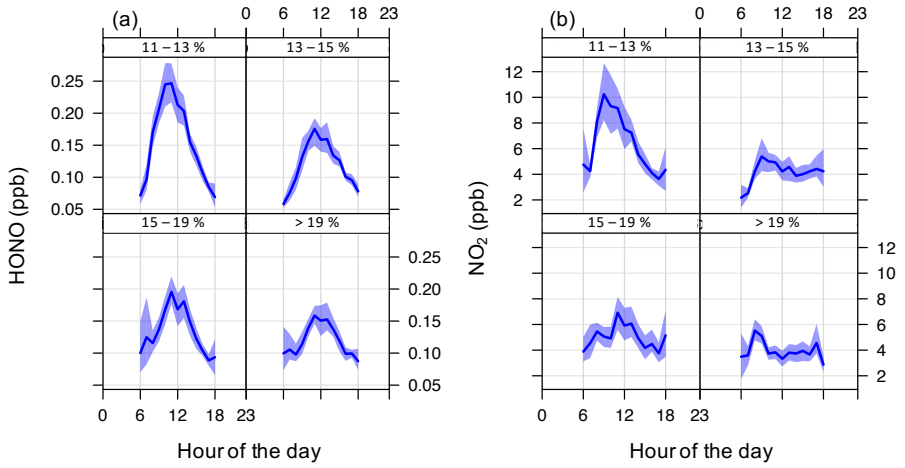

Figure 5.11: Figure adapted from Ryan et al. (2018). (a) HONO and (b) NO_2 diurnal cycles over the three month measurement period, divided into four soil water content (SWC) % bins. SWC data has been obtained from the Australian Water Resources Assessment Modelling System.

concentration gradient means that its influence on OH production drops quickly below that of O_3 photolysis above the boundary layer (fig 5.10(b)).

5.4 Formaldehyde and glyoxal at the urban-rural interface

5.4.1 Overview of HCHO measurements 2016-2019

In addition to nitrogen oxides, formaldehyde (HCHO) and glyoxal (CHOCHO) measurements at Broadmeadows give an insight into Melbourne's overall atmospheric oxidation chemistry by providing information on volatile organic compounds (VOCs).

The timeseries of HCHO measurements at Broadmeadows in figure 5.12(a), shows that vertical column densities ranged from 1.7×10^{15} to 2.4×10^{16} molecules.cm^{-2} with a clear increase in HCHO in summer months. Therefore HCHO was observed throughout the measurement period above the calculated detection limit of 4.9×10^{14} molecules.cm^{-2}, and corresponding approximate surface VMR detection limit of 0.5 ppb, calculated using the method described in the NO_2 discussion above. The mean HCHO VCD throughout the measurement period was 5.8×10^{15} molecules.cm^{-2} which corresponded to a mean surface mixing ratio of 1.59 ppb. Examining recently published studies where atmospheric formaldehyde mixing ratios have been measured in long term campaigns reveals a wide range of results, reflecting at the outset the complexity of factors governing VOC emissions and chemistry (see compiled results from literature examples in table B.2 in Appendix B). The range of observed HCHO values at Broadmeadows are

lower than other studies in urban areas, especially the many recent reports in Chinese cities where average HCHO VMR across all seasons is between 2.7 and 4.8 ppb, compared to 1.6 ppb here (Lui et al., 2017; Yang et al., 2019; Guo et al., 2014, 2016). The mean HCHO VMR at Broadmeadows sits higher than recently reported values in rural areas such as the Valderejo national park in Spain (de Blas et al., 2019), Schneefernerhaus in the German Alps (Leuchner et al., 2016) and Lauder, New Zealand (discussed in detail in the next chapter). However, the range of monthly average VMRs of 2-8 ppb at a rural site in Thailand (Hoque et al., 2018a) was higher than the monthly average range in Melbourne (0.8-1.9 ppb), potentially due to differences in both vegetation and biomass burning emissions.

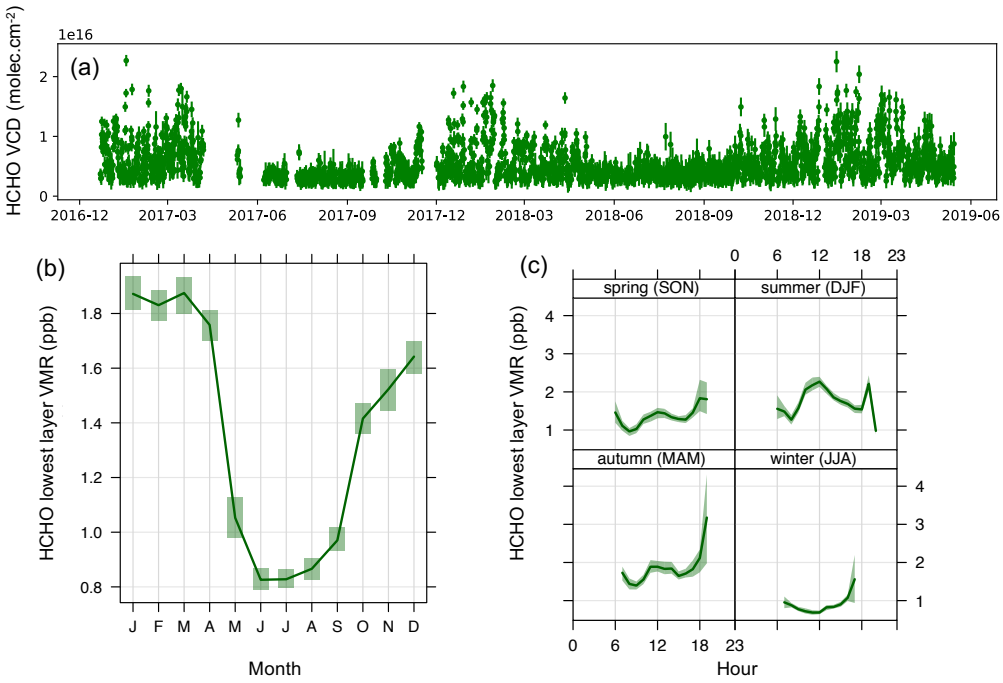

Figure 5.12: (a) Timeseries of daily averaged HCHO VCD at Broadmeadows from December 2016 to May 2019. (b) Monthly averages of HCHO mixing ratio in the lowest retrieval layer. (c) Seasonally averaged diurnal cycle plots for HCHO mixing ratio in the 0-200 m retrieval layer. Data in this figure is cloud filtered.

Of the reported studies in table B.2 from locations with four distinct seasons (i.e. not tropical), all except Madrid, Spain (Benavent et al., 2019), showed HCHO maxima in summer in agreement with the Broadmeadows results. In figure 5.12(b), three distinct regimes are apparent in the monthly average HCHO surface concentrations: maximum VMRs (>1.7 ppb) occur between January and April, decreasing rapidly to minimum values (<1.2 ppb) between May and September before increasing again (between 1.4 and 1.7 ppb) from October to December. Qualitatively, this seasonal cycle correlates with HONO and anticorrelates with NO_2, and as with the nitrogen oxides hints at the

broad importance of solar radiation and temperature in driving chemical composition. In fact, the annual average cycle of ambient temperature at Broadmeadows was found to correlate strongly with HCHO surface mixing ratio - a more thorough quantitative investigation of this correlation will follow in discussing potential HCHO sources below.

There are, to date, only a handful of ground-based formaldehyde measurements reported in the literature from Australia. In November-December 1993, measurements at the Cape Grim Baseline Air Pollution Station in Tasmania revealed a clear HCHO diurnal cycle in clean, marine air consistent with background photochemical production (Ayers et al., 1997). The average background diurnal cycle had a maximum value of 0.4 ppb in the middle of the day, and a minimum value of 0.3 ppb overnight, considerably lower than the average diurnal cycle values in Melbourne, as expected given the background vs environments. Measurements of formaldehyde vertical columns have been made using Fourier transform infrared spectroscopy (FTIR) at Wollongong, south of Sydney in New South Wales since 1996, as presented in Zeng et al. (2015) and Lieschke et al. (2019). Across all measurements between 1996 and 2015, Lieschke et al. (2019) reported a seasonal cycle that was, qualitatively, very similar to that at Broadmeadows. However, the value of the VCDs was greater in Wollongong with maximum monthly average around 2.4×10^{16} molecules.cm^{-2} ($\approx 3.4\times$ greater than Broadmeadows) and minimum monthly average around 6.0×10^{15} molecules.cm^{-2} ($\approx 1.9\times$ greater than Broadmeadows). The difference in HCHO VCD amount could be partially explained by the fact that the FTIR retrieval method used calculates vertical columns to 12 km (Jones et al., 2009) rather than 4 km as for the MAX-DOAS, but is also likely a function of Wollongong's location, surrounded by large forested areas.

Studies using global chemical transport simulations give an indication of the expected HCHO seasonal cycle in Australia. In one such study, Pfister et al. (2008) used the MOZART-4 model to examine regional variations in, among other things, the contribution of isoprene to formaldehyde production. The average seasonal cycle reported therein over the Australian region matches qualitatively and quantitatively well with the observed seasonal cycle in Melbourne. In another example, Zeng et al. (2015) modelled HCHO using a range of global chemical transport models and VOC emission schemes and compared the results with FTIR column measurements at Wollongong. The ensemble mean of these simulations replicated the seasonal cycle pattern of the Wollongong and Melbourne MAX-DOAS results but significantly underestimated the magnitude of the Wollongong VCDs, by almost a factor of two in summer. It was concluded by the authors that the models were likely missing important HCHO sources, related to large uncertainties in biogenic VOC emissions. This finding was echoed with some specificity in Emmerson et al. (2016) and Emmerson et al. (2018) where it was shown that in the MEGAN biogenic emissions scheme isoprene was overestimated and monoterpenes underestimated for south-east Australian forests.

Unlike NO_2, there are no in-situ formaldehyde measurements in Victoria that could be

used for validation of the MAX-DOAS results, and hence the similarity of the Wollongong HCHO seasonal cycle seasonal cycle and associated model runs presented in Zeng et al. (2015) and Lieschke et al. (2019) give the strongest available evidence that the Broadmeadows MAX-DOAS is reporting sensible HCHO results. The average diurnal cycle of HCHO in Melbourne is distinctly different to the nitrogen oxide species discussed above, with a notable 'W' shape: peaks early in the morning, in the middle of the day and at the end of the day. This suggests a range of competing influences on HCHO formation. When viewed by season (figure 5.12(c)), the trimodal pattern is interrupted in winter by the loss of the midday peak. This suggests that there are processes forming HCHO which are dependent on light/temperature and are present in the lighter/warmer months - and ubiquitous processes which are not dependent on light/temperature.

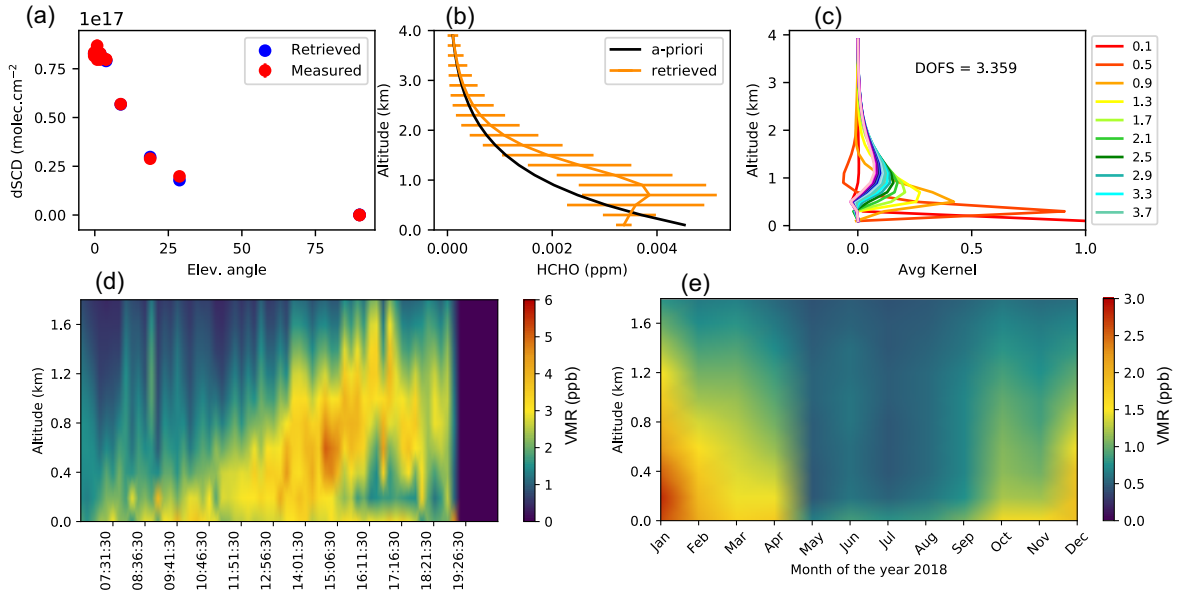

Figure 5.13: (a) Model/measurement comparison for one HCHO vertical profile retrieval, (b) a priori and retrieved vertical profile and (c) averaging kernels from an example HCHO retrieval at midday on 13/12/2017. (d) Daily HCHO vertical profile evolution on 13/12/2017, typical of a day with high observed formaldehyde at Broadmeadows. (e) Monthly averaged HCHO vertical profiles showing annual variation in mean retrieved profiles throughout 2018.

Another factor distinguishing HCHO from the nitrogen oxide results at Broadmeadows is the vertical distributions. Whereas HONO and NO_2 were found, on average, to have very strong vertical gradients with most of the trace gas in the lowest 500 m of the atmosphere, HCHO plumes were often observed at higher altitudes as shown, for example, on 13/12/2017 in figure 5.13(d). An example individual retrieval from this day, with HCHO mixing ratios exceeding 2 ppb up to 1.6 km, is shown in figures 5.13(a-c), demonstrating that good agreement between modelled and measured values, and good

averaging kernels with DoFs >3.3, were achieved for such retrievals. Furthermore, in contrast to the nitrogen oxides, the average vertical distribution of HCHO was found to vary throughout the year: not only were HCHO surface mixing ratios much higher in summer, but HCHO plumes extended to much higher altitudes (i.e. >1 km) on average between December and April as shown in figure 5.13(e).

5.4.2 Overview of glyoxal results 2016-2019

Glyoxal (CHOCHO) vertical columns were also retrieved at Broadmeadows and can give additional insight into volatile organic compounds in Melbourne. Across the whole measurement period, glyoxal VCDs ranged from 1.17×10^{14} to 3.87×10^{14}, with a mean of 4.65×10^{14} molec.cm^{-2}. As with formaldehyde, glyoxal was therefore observed above the detection limit (8.84×10^{13} molec.cm^{-2}) throughout the campaign. Note that this detection limit has been calculated using an average residual RMS of 6.5×10^{-4} rather than 4.5×10^{-4} for the other molecules, due to the persistent higher residual structure in the DOAS fitting range for glyoxal. This range for CHOCHO VCD lies within previous MAX-DOAS observations in both urban (e.g. Madrid, Spain Benavent et al. (2019)) and rural (e.g. Pearl River Delta region in China Li et al. (2013) and Phimai, Thailand Hoque et al. (2018a)). The average diurnal profile of glyoxal VCDs, shown for each season in figure 5.14(a), was consistent across the year in the mornings, increasing steeply from an early morning minimum to a maximum around the middle of the day. This implies temperature or light-driven processes may be responsible for morning CHOCHO formation. Autumn shows the highest average midday value, followed by an afternoon decrease as expected from a temperature-driven or photolytic process, but in other seasons the afternoon VCD plateaus, then decreases again overnight. This suggests different sink processes may be in play at different times of year. The polar bivariate plots in figure 5.14(b) show that highest CHOCHO VCD is expected for low windspeeds, similar to the nitrogen oxides. Because the sinks (OH oxidation and photolysis) and lifetimes for CHOCHO and HCHO are similar (Kaiser et al., 2015), the polar bivariate plots for HCHO and CHOCHO can be compared; there is no similarity either in directionality or summertime maximum suggesting that the predominant sources of CHOCHO and HCHO at this location are different.

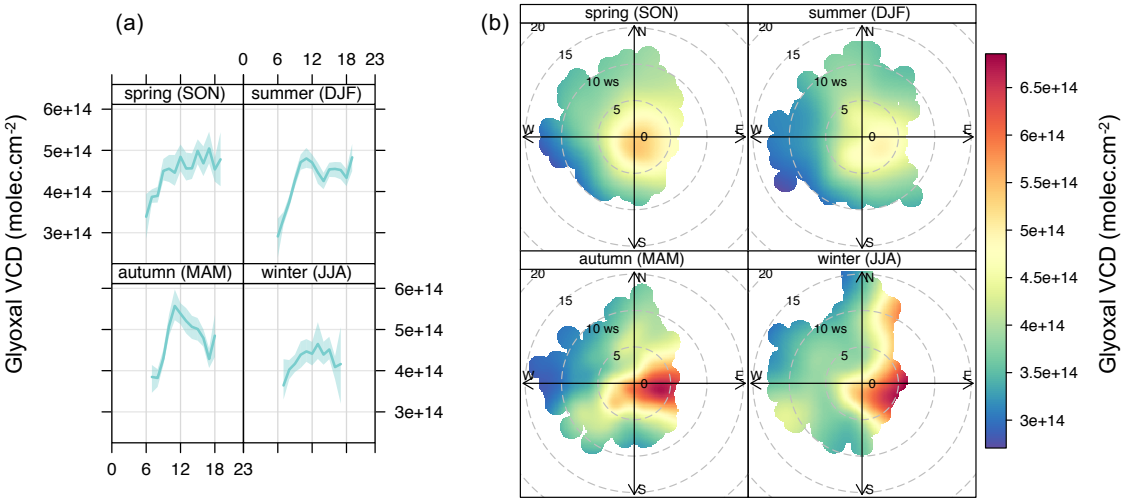

Figure 5.14: (a) Diurnal cycle plots for glyoxal vertical column density at Broadmeadows, broken up by season. (b) Polar bivariate plots showing the variation of glyoxal VCD with wind speed and direction, also plotted for each season.

The vertical profile retrieval for glyoxal at Broadmeadows is demonstrated in figure 5.15. The individual retrieval set shown in (a)-(c) is typical for the the campaign, with modelled and measured values well matched and the profile uncertainty less than 100 % of the retrieved surface mixing ratio. However, glyoxal was the most challenging molecule to retrieve chiefly because of higher residual RMS and dSCD errors at the DOAS stage compared to other trace gases, despite extensive optimisation tests, as discussed in the methods section. This led to a higher measurement covariance error matrix in the profile retrieval stage and consequently, higher profile retrieval errors than for HONO, HCHO and NO_2. For example, considering monthly average vertical profiles across the campaign period, the total uncertainty at all profile levels for all months was greater than 100 % for all layers. Shallow vertical gradients were often retrieved for CHOCHO as shown in the heatmap of monthly averaged vertical profiles in figure 5.15(e), similar to HCHO although with different seasonal trends. However, the averaging kernels showed that sensitivity above the lowest retrieval layer was minimal (see example averaging kernel in figure 5.15(c) and monthly average averaging kernels in figure B.5 in Appendix B). In light of these limitations, the ensuing discussion of CHOCHO focuses on the retrieved column amount, rather than the vertical distributions and surface mixing ratio values.

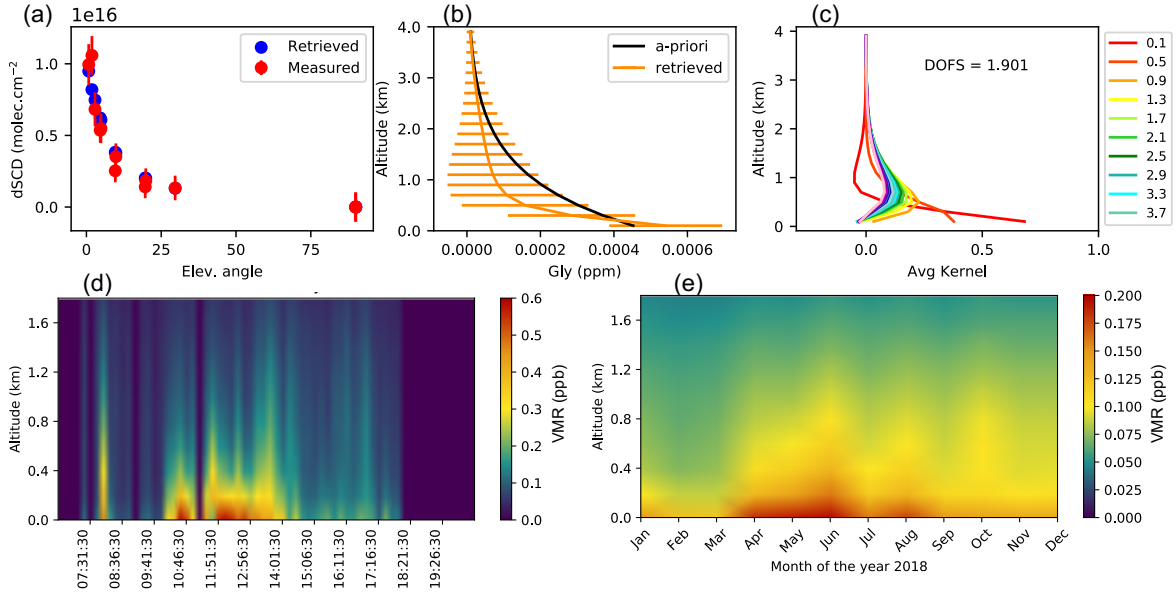

Figure 5.15: Top row: example glyoxal retrievals for midday on 4/4/2017 at Broadmeadows, (a) modelled and measured CHOCHO dSCDs, (b) a priori and retrieved profiles, (c) averaging kernels. (d) Heatmap of vertical profiles across 4/4/2017, (e) heatmap of monthly averaged glyoxal vertical profiles for the year 2018.

The comparative seasonality of HCHO and CHOCHO VCDs is examined further in figure 5.16, where the timeseries shows that the five highest monthly average CHOCHO VCDs all occur in either April or September. This 'bimodal' seasonal distribution does not match the co-measured HCHO, nor either of the measured nitrogen oxides, but qualitatively better resembles the seasonal cycle of aerosol optical depth (see figure 5.2). Across the measurement campaign, the minimum monthly average HCHO VCD is less than half of the maximum while for glyoxal the minimum is only a quarter less than the maximum. Hence, qualitative variations in the ratio between HCHO and CHOCHO VCDs are driven predominantly by HCHO while qualitative (i.e. timing of the seasonality) is driven by both VOCs. This ratio, known as R_{gf} and discussed in the literature as an indicator of VOC speciation because of the similarity of HCHO and CHOCHO lifetimes (Kaiser et al., 2015), varies between monthly averages peaking in winter and spring at around 0.15, with minima in autumn and summer around 0.05 shown in figure 5.16(b). There are a wide range of values reported for R_{gf} in the literature, from 0.02 to 0.4 in different locations (see Kaiser et al. (2015) and references therein) and therefore the values calculated for Melbourne are reasonable. The seasonal cycle of R_{gf} with a winter maximum could imply that R_{gf} increases with increasing NO_x, which could suggest that anthropogenic emissions enhance R_{gf} as suggested by Li et al. (2014). The evidence of the seasonal cycle is supported by the average diurnal cycle (figure 5.16(c)) which shows that R_{gf} peaks in the morning, consistent with the timing of the NO_2 diurnal cycle discussed above.

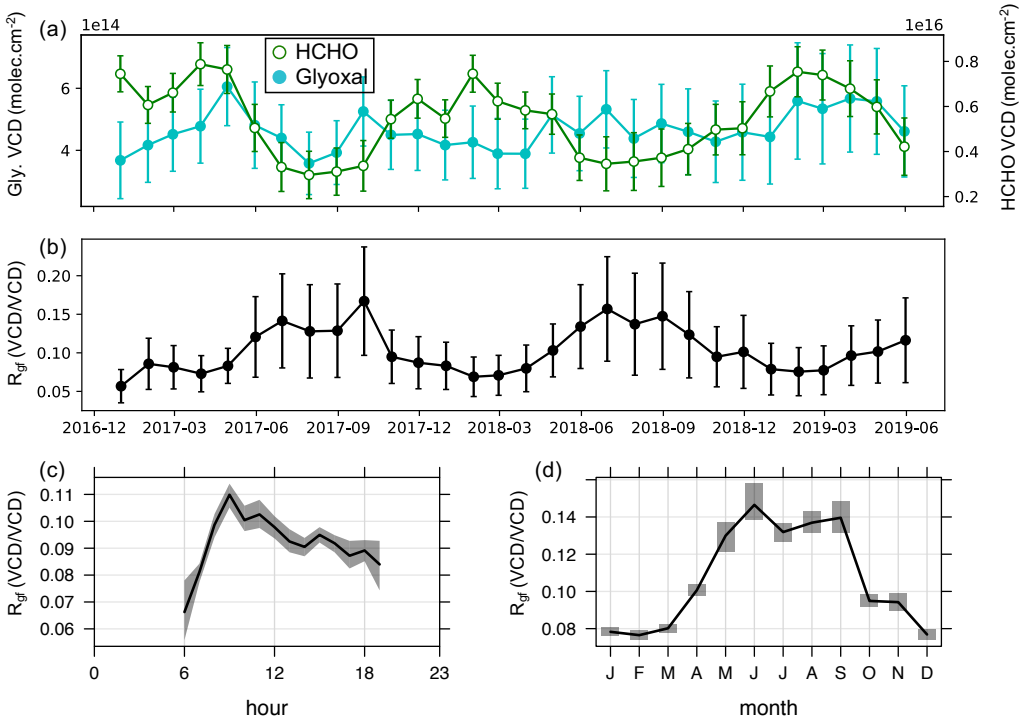

Figure 5.16: Timeseries of (a) HCHO and CHOCHO monthly average VCD and (b) the glyoxal to formaldehyde ratio (R_{gf}) at Broadmeadows from December 2016 to May 2019. (c) Average diurnal cycle and (d) monthly averages of R_{gf} summarised.

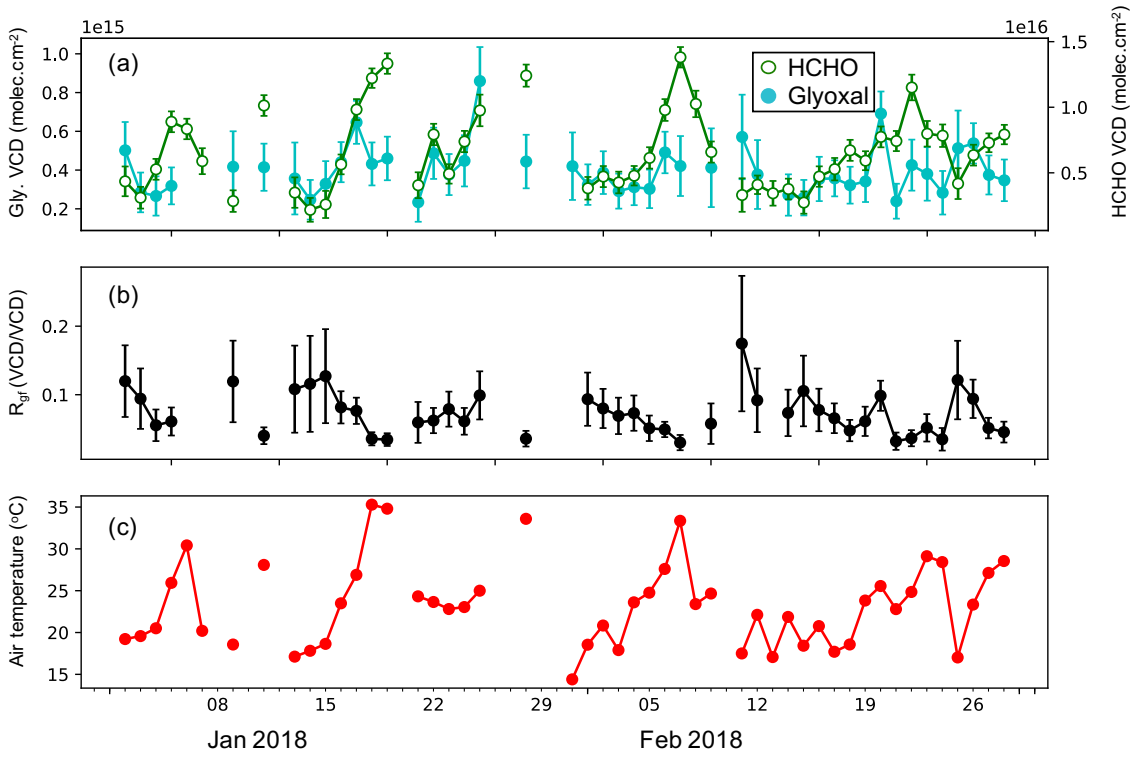

Figure 5.17: Timeseries from an example period in summer 2018: (a) HCHO and CHOCHO daily average VCDs, (b)R_{fn} and (c) ambient air temperature.

5.4.3 Discussion of potential VOC sources

Methane oxidation as a HCHO source

The first important VOC precursor to consider is methane. Methane will not contribute directly to glyoxal formation because glyoxal is a dicarbonyl - but methane oxidation is estimated to be responsible for around 48 % of atmospheric formaldehyde production globally (Pfister et al., 2008). The process is driven photolytically because the primary oxidant is the hydroxyl radical. For example, in clean atmospheric conditions production of HCHO from methane oxidation may proceed as follows:

$$CH_4 + OH \longrightarrow CH_3 + O_2 \quad \{37\}$$
$$CH_3 + O_2 + M \longrightarrow CH_3O_2 + M \quad \{38\}$$
$$CH_3O_2 + HO_2 \longrightarrow CH_3OOH + O_2 \quad \{39\}$$
$$CH_3OOH + hv \longrightarrow CH_3O + OH \quad \{40\}$$
$$CH_3O + O_2 \longrightarrow HCHO + HO_2 \quad \{41\}$$

This mechanism is also relevant in urban, anthropogenically polluted conditions because

CH_3O_2 may react with NO, rather than HO_2, to produce CH_3O. The observed seasonal cycle of HCHO peaks strongly in summer, in contrast to the expected seasonal cycle for methane, according to modelling studies of Australia's CH_4 budget, which peaks in winter months (Fraser et al., 2011; Loh et al., 2015). The modelled winter CH_4 maximum is supported in Fraser et al. (2011) by flask samples at remote locations Cape Ferguson (Queensland) and Cape Grim (Tasmania), and by GOSAT satellite retrievals and FTIR column measurements in the city of Wollongong in Parker et al. (2011). In the absence of in-situ methane measurements for the Melbourne region, the TROPOMI satellite CH_4 product over Victoria was examined for the currently available data (May 2018-April 2019, see figure B.7 in Appendix B). July 2018 has the highest CH_4 column amount but apart from this period, within the uncertainty, the values show little variation. Hydroxyl radicals are expected to be at a maximum in summer however due to its photolytic production, explaining the modelled winter CH_4 maximum and meaning that CH_4 oxidation would be expected to occur more in summer.

In the absence of actinic flux or $J(O^1D)$ measurements, the contribution of methane oxidation to observed HCHO in Melbourne cannot be quantified. However, it can be inferred from the polar bivariate plots of HCHO surface VMR in figure 5.4 that CH_4 is not the dominant summertime HCHO source. The lifetime of methane (on the order of years) is vastly longer than isoprene (order of hours) meaning that if methane oxidation was the dominant HCHO source, no difference should be observed in HCHO concentration with varying windspeed and direction. Instead, the HCHO polar bivariate plot, especially in summer, shows highest HCHO from the north and east which resembles the distribution of forests (isoprene sources) near Melbourne as will be discussed in greater detail in following sections. This discussion accords with the modelling study of Pfister et al. (2008) who estimated methane oxidation to account for approximately 20 % of HCHO formation in summer across Australia compared to isoprene oxidation approximately 80 %.

Potential anthropogenic VOC sources

Oxidation of non-methane volatile organics (NMVOCs) and direct emission make up the remainder of the global formaldehyde budget. Pfister et al. (2008) estimate that direct emission comprises, on average, only about 0.4 % of the total atmospheric formaldehyde burden, although this may vary regionally depending on local industry and biomass burning. Melbourne is a large city with significant industry and road transport emissions, however anthropogenic VOCs are considered to play only a minor role in formaldehyde production at Broadmeadows for two main reasons. Firstly, if primary or secondary emissions from vehicles were producing significant formaldehyde then a strong relationship would be expected between NO_2 and HCHO. However, the average diurnal cycles and seasonal cycles and temperature dependence of the NO_2 and HCHO results are completely different. Secondly, the polar bivariate plots of HCHO varying with wind speed and direction (figure 5.4) show that the highest formaldehyde concentration coincides with winds from the north and east, i.e. not the direction of the

the city centre or major industrial areas, nor localised to the surrounding road corridors as observed for NO_2.

The polar bivariate plots for glyoxal and NO_2 are, however, much more similar suggesting that glyoxal may have more localised, and therefore anthropogenic, sources than formaldehyde. This observation does not imply that glyoxal and NO_2 are emitted from the same source; no clear relationship was found between CHOCHO and NO_2 in time timeseries results and in any case, direct vehicular emissions of glyoxal are expected to be minimal (Volkamer et al., 2005). Similarly, no clear relationship was found between glyoxal and formaldehyde vertical columns in the long term timeseries, apart from the observation that the ratio between the two exhibits a marked seasonal cycle. However, some periods in the timeseries were identified which showed similarities in daily variation of HCHO and CHOCHO, except for the hottest days. Throughout January and February 2018 as illustrated in figure 5.17, the variation in daily average CHOCHO and HCHO VCDs matched on several occasions such as 14-18 and 21-25 January while the daily maximum temperature remained below 30°C. Each sequence of matching VCDs and accompanying $R_{gf} > 0.1$ was ended by a day where the maximum temperature exceeded 30°C, the R_{gf} dropped below 0.1, the HCHO VCD rose sharply and the CHOCHO VCD remained largely unchanged. The dependence of HCHO on temperature is is a strong indicator of biogenic influence, as will be discussed in greater detail below. In contrast, the consistency of glyoxal VCDs to temperature variations suggests that background VOCs in the urban environment play a more significant role in CHOCHO formation than for HCHO.

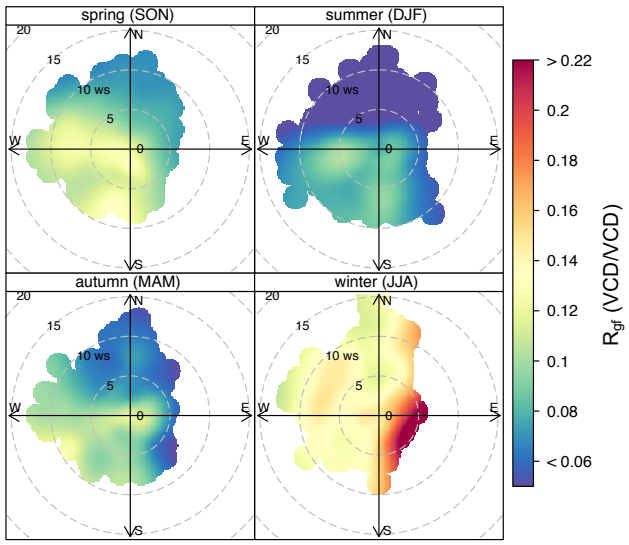

Figure 5.18: Polar bivariate plots for each season at Broadmeadows, showing variation of glyoxal to formaldehyde ratio (R_{gf}) with wind speed and direction

The glyoxal to formaldehyde ratio has previously been proposed as a diagnostic tool for

disentangling the anthropogenic and biogenic contributions to VOC emissions. However as summarised in Kaiser et al. (2015) there are directly contradictory results in the literature, for different measurement locations and techniques, as to what magnitudes and trends of R_{gf} signify increasing anthropogenic influence. Nevertheless, the R_{gf} may still be a useful local indicator of different VOC airmass characteristics. As illustrated in figure 5.18, in winter time formaldehyde levels are very low promoting a high R_{gf} for all wind speeds and directions in the polar bivariate plot. For spring summer and autumn R_{gf} is typically < 0.1 when the wind comes from the mostly rural north and north-east sectors, while R_{gf} is typically > 0.1 under the lowest wind speed conditions or when the wind comes from the more industrial south and south-westerly sectors. This implies that there is a local difference between R_{gf} in airmasses of anthropgenic and biogenic origin and that R_{gf} increases with increasing anthropogenic influence, matching the earlier observation of R_{gf} seasonal and diurnal cycles being qualitatively similar to NO_2.

In summary, these MAX-DOAS measurements highlight qualitatively the capacity of the MAX-DOAS technique to provide important information on broad VOC speciation in Melbourne. To extend this work in a more quantitative manner, significant further work, including a speciated study of anthropogenic VOC emissions in Melbourne, is required to quantify the role of anthropogenic VOC emissions to the mix of CHOCHO and HCHO measured here.

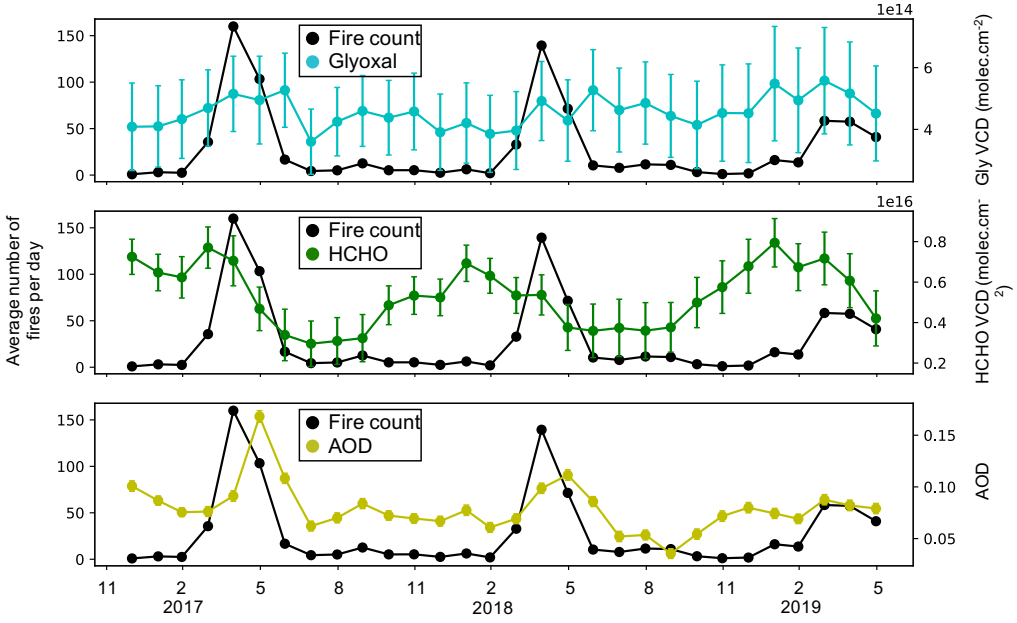

Figure 5.19: Comparison of timeseries for glyoxal (top), formaldehyde (middle) and AOD (bottom) monthly averages with the average number of fires per day in each month, recorded by the MODIS fire count algorithm.

Biomass burning as a VOC source

Biomass burning has previously been shown to be a major VOC source in Australia (e.g. Paton-Walsh et al. (2004, 2005, 2010)) and therefore must be considered alongside the other potential sources at Broadmeadows. In addition, formaldehyde and glyoxal have been identified as key products of biomass burning observed in MAX-DOAS studies in other parts the world (Hoque et al., 2018a,b). The MODIS Howe fire count product derived from satellite observations has been used in this section to understand the potential contribution of smoke plumes to the VOCs observed. The natural bushfire season is at its most severe in the middle of summer across southern Australia when temperatures are highest and the forest driest, as confirmed by the fact that fire radiative power peaks in January (from MODIS fire count, not shown). However, the highest number of fire events actually occurs in Autumn, due to post-fire season fuel-reduction burning by regulatory authorities. The average number of fire events per day across Victoria in each month is plotted alongside the glyoxal and formaldehyde VCDs, as well as AOD measured by the MAX-DOAS, in figure 5.19. The maximum fire count in autumn is qualitatively similar to the seasonal pattern of glyoxal VCDs and AOD, although the peak AOD occurs in May rather than April. Note that because the MAX-DOAS was not operational between 8-30 April 2017, the April 2017 trace gas and AOD monthly averages are likely under-represented. The relationship between HCHO and temperature will be discussed more thoroughly in the following section, however it is worth noting here that the only month in which the temperature and HCHO seasonal cycles do not align is April, suggesting that controlled burning smoke plumes may be sustaining the formaldehyde level in Melbourne beyond its typical summer maximum. The indication of biomass burning being a signficant contributor to aerosol optical depth in the Melbourne metropolitan area is in line with Keywood et al. (2015) who found particulate matter metrics and aerosol scattering coefficients during smokey periods in Melbourne were a factor of 10 higher than normal.

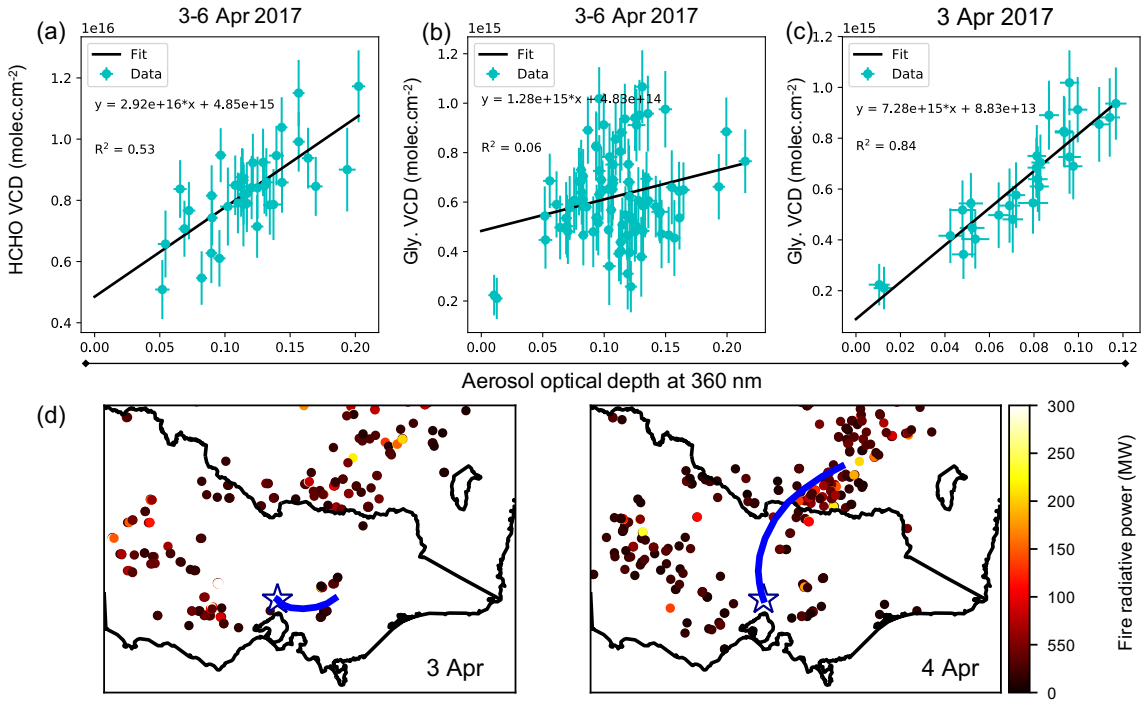

Figure 5.20: (a) Scatter plot showing HCHO VCD vs aerosol optical depth at Broadmeadows for 3-6 April 2017. (b) Same as (a) but for glyoxal VCD instead. (c) Same as (b) but only for the 3rd of April. (d) Maps showing fires recorded by the MODIS fire count algorithm for 3-4 April across Victoria. HYSPLIT trajectories, run 12 hours back from midday at Broadmeadows, have been superimposed over the top in blue.

Previous work on atmospheric chemistry in Australian bushfire smoke by Paton-Walsh et al. (2004) and Paton-Walsh et al. (2005) found that aerosol optical depth and formaldehyde VCD were linearly related during smoke plume episodes and they suggested that this could enable VOC emissions from fires to be inferred from AOD retrievals. These results were obtained using fourier transform infrared spectroscopy for the formaldehyde measurements, and visible spectral irradiance (500 nm) for the AOD measurements. Here, HCHO VCDs and AOD at 360 nm calculated by the MAX-DOAS have been compared for days on which bushfire smoke plumes impacted the Melbourne metropolitan area. One such event was an extended period from 3-6 April 2017, detailed in figure 5.20. On the 3rd of April, smoke from planned fuel-reduction burns in the Yarra and Dandenong ranges to the east of Melbourne blanketed the suburbs in a thick smoke haze. On 4-6 April, the winds turned northerly, bringing smoke from fuel-reduction burns in the Hume region of north-eastern Victoria and southern New South Wales. Across this entire period, HCHO and AOD were found to correlate moderately with an R^2 of 0.53 and slope of 2.92×10^{16} (figure 5.20(a)). This slope is between those reported in Paton-Walsh et al. (2005) (2.5×10^{16}) and Paton-Walsh et al. (2004) (3.3×10^{16}) for AOD vs HCHO in smoke plumes around Wollongong and Sydney, a very

encouraging result bearing in mind the different wavelengths of the AOD retrieval and the different HCHO measurement technique. This result serves two purposes, namely (a) validating the approach suggested by Paton-Walsh et al. (2004) and Paton-Walsh et al. (2005) for different fire scenarios and using a different (and only one) measurement technique. Secondly, this result confirms that bushfire smoke plumes contribute to the budget of formaldehyde observed in the Broadmeadows dataset. In the same time period, AOD and glyoxal did not correlate at all (figure 5.20(b)) although it is worth noting that, considering only the first day of the event with the most proximate fires, glyoxal and AOD did correlate strongly with R^2 =0.84 and slope of 7.28×10^{15} (figure 5.20(c)). Therefore it is suggested that the relationship between CHOCHO and AOD may be able to provide information on bushfire smoke processes for different timescales and/or plume ages to the established relationship between HCHO and AOD, a hypothesis deserving more sustained attention in future work.

In each of the years of the measurement campaign detailed here, an event of bushfire smoke blanketing the Melbourne suburbs was observed to produce a linear relationship between AOD and HCHO as shown in figures 5.21(a-c). The slopes of these regressions varied from 2.92×10^{16} for 3-6 April 2017 as discussed above, to 3.37×10^{16} for the 9-10 March 2019 event, again close to the slope values reported in Paton-Walsh et al. (2004) and Paton-Walsh et al. (2005). In figures 5.21(d-e), scatterplots for AOD vs HCHO VCD are shown for three industrial fire events occuring in the northern and western suburbs of Melbourne, with smoke plumes that passed over Broadmeadows. Moderate linear relationships exist between the two variables in each case, with R^2 around 0.5. The slopes exhibit a wider range than for the biomass burning examples, between 2.26 and 3.85×10^{16}, perhaps reflecting the different chemical compositions of the industrial waste burning in each case. This result highlights the potential for the methodology suggested by Paton-Walsh et al. (2004) and Paton-Walsh et al. (2005) for inferring VOC emissions from AOD measurements during biomass burning events, to be applied also to other types of fires.

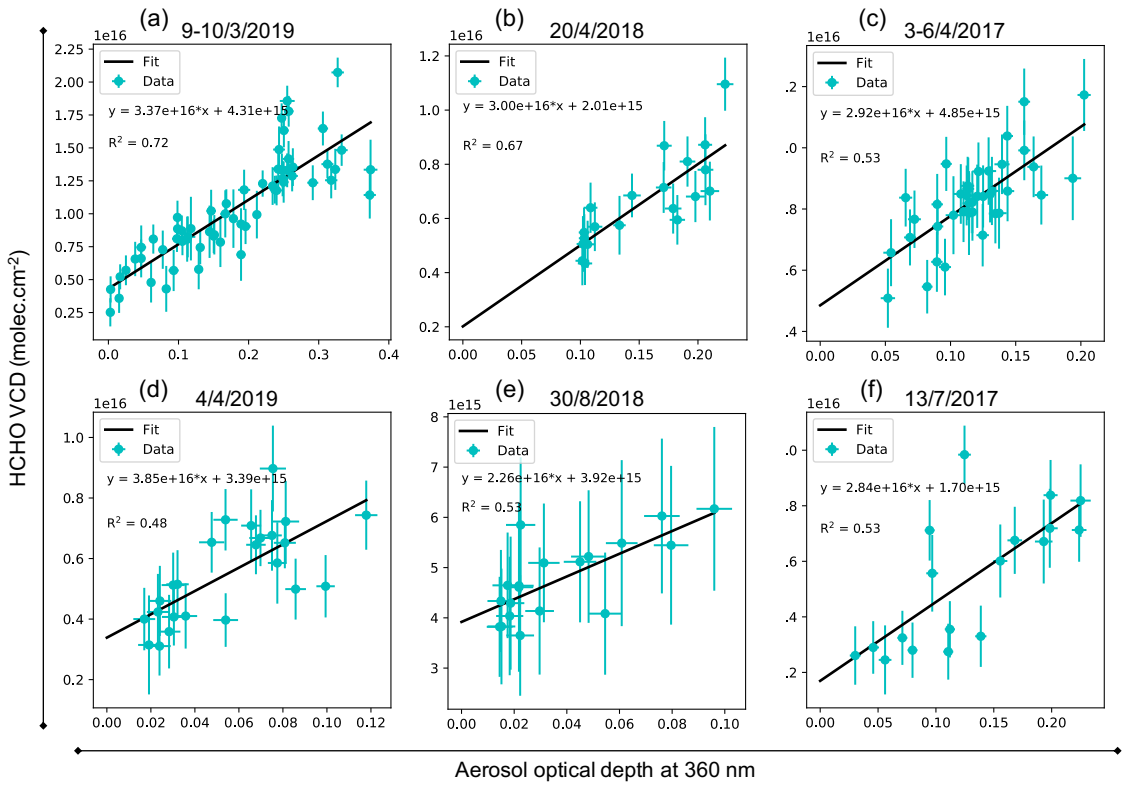

Figure 5.21: Scatterplots showing correlation between HCHO VCD and AOD at 360 nm on some smoky days in Melbourne. (a)-(c) are are bushfire smoke days, (d)-(f) are industrial factory fire days. Raw results have been filtered for retrieval statistics (chi squared and DoFs) but not using the cloud filtering algorithm.

Biogenic VOC emissions

There is strong evidence that biogenic VOC (bVOC) emissions play a key role in Australia's atmospheric composition and, in particular, formaldehyde production. Using global chemical transport models coupled with the MEGAN model for VOCs, Pfister et al. (2008) estimate that oxidation of isoprene, the most abundant bVOC in terms of direct emissions, contributed up to 80% of the HCHO budget over the Australian continent. This figure was higher than anywhere else in the world due to Australia's endemic vegetation, especially eucalypt trees, being noted high emitters of isoprene and monoterpenes. Monoterpenes is the name given to the group of alkenes with formula $C_{10}H_{16}$ which comprise the second most abundant bVOC emissions. Broadmeadows, on the northern fringe of Melbourne's suburbs, has large regions dominated by eucalypt forests in between rural and semi-urban landscapes, about 35 km away to the north west, north east and east. In addition, Melbourne is widely regarded as a 'green city' with large expanses of parkland, along with ubiquitous street and garden trees - in summary, there is significant proximate vegetation which may contribute to isoprene and monoterpene emissions. The polar bivariate plots for formaldehyde in figure

5.4(d) show that highest surface VMRs, which occur in summer, coincide with wind directions from the rural north and east sectors, consistent with the directions of the forested areas. There are two possible and not mutually exclusive, interpretations of this result: (a) formaldehyde formed in rural areas is being transported directly to the city, or (b) other strong drivers of formaldehyde production correlate with wind from these directions.

Option (a) can be explored by looking at the wind speed, as well as direction dependence. The main daytime sink of HCHO is photolysis which restricts the HCHO lifetime to around four hours (Fried et al., 1997) - enough time, in winds of 10 ms^{-1} for transport of around 150 km. Considering summer, the highest HCHO concentrations occur from the north and north east sectors almost irrespective of wind speed, suggesting that both transport and related meteorological factors are relevant to the Broadmeadows observations.

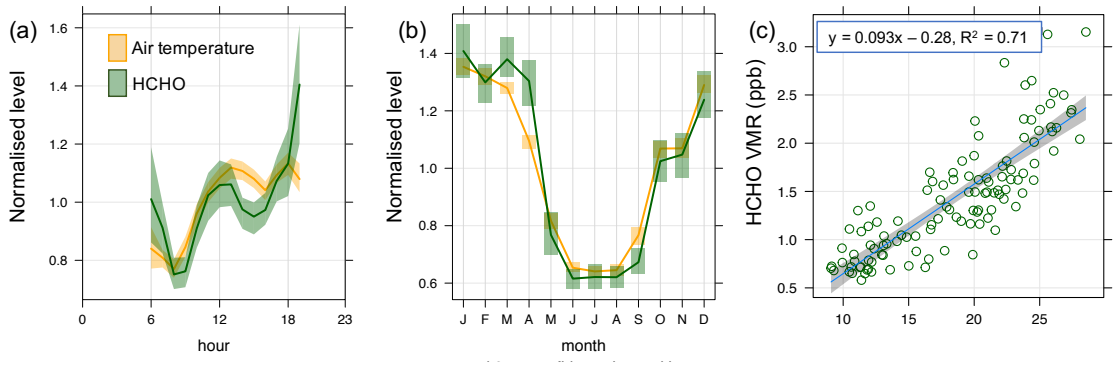

Figure 5.22: Summary of HCHO and temperature results. (a) Diurnal cycle of HCHO VMR and ambient air temperature at Broadmeadows, normalised to each other to allow comparison. (b) Monthly averages of air temperature and HCHO VMR at Broadmeadows, also normalised to each other for ease of comparison of the annual cycle. (c) Scatter plot of weekly averages of HCHO VMR and ambient temperature at Broadmeadows.

Option (b) is important because northerly winds (from the interior of the Australian continent) in Melbourne in spring - autumn are almost invariably associated with warmer weather than winds from the south (off Bass Strait and the Southern Ocean). bVOC emissions from vegetation are well known to be temperature dependent. Examples of the relationship between ambient temperature and isoprene emissions and formaldehyde VCDs are given in several studies of satellite-retrieved HCHO over the south-eastern United States (Palmer et al., 2006; Duncan et al., 2009; Zhu et al., 2014). Duncan et al. (2009) reported a linear relationship during summer months, with slope of 1.5×10^{15} and R^2 of 0.59. This slope is more than twice as steep as the relationship found in Melbourne, where the summer-time slope linear regression slope is calculated to be 4.9×10^{14}. However, Palmer et al. (2006) and Zhu et al.

(2014) found that the relationship was best fit exponentially, for example in Zhu et al. (2014) ten day averaged OMI HCHO VCDs in summer over Texas were summarised by $ln(V_{HCHO}) = 2.62 + 0.11T$, $R^2 = 0.64$. They found that focusing on the urban centre of Houston, the fit was poor with $R^2 < 0.1$ and theorised that the difference in temperature dependence could be explained by isoprene oxidation dominating the background, and anthropogenic emissions dominating the urban formaldehyde source budgets. Using ten day averages of Melbourne summer data an exponential relationship was also found to be appropriate and, moreover, an almost identical slope was found for the regression: $ln(V_{HCHO}) = 5.8 + 0.10T$ with $R^2 = 0.89$. The exponential fit is essentially as good as the linear fit ($R^2 = 0.90$) for the same time averaged period at Broadmeadows. It is interesting to note that neither the slopes or R^2 values of the regressions in spring, summer and autumn are changed for the Melbourne data when considering wind from the south implying that bVOC oxidation may consistently be the dominant HCHO source in Melbourne.

The fact that almost identical slopes were determined in Melbourne as for Texas is evidence that the same underlying temperature-dependent processes are driving HCHO production in each location. Despite the focus on isoprene thus far in the discussion, it but is one of many biogenic VOCs potentially contributing to HCHO and glyoxal formation in Australia. In attempting to reconcile modelled VOC emission processes with VOC observations, Emmerson et al. (2016) and Emmerson et al. (2018) suggested that the MEGAN model may overestimate isoprene emission factors from eucalyptus forests and underestimate monoterpene emissions. Monoterpene emissions have previously been shown to have a strong exponential temperature dependence (Guenther et al., 2012; He et al., 2000) and it would therefore be difficult to distinguish its role in HCHO formation from isoprene on the evidence available in this study. The ratio between glyoxal and formaldehyde has been proposed as an indicator not only of biogenic vs anthropogenic VOC contributions, but also of isoprene to monoterpene contributions to the biogenic component (Chan Miller et al., 2014; Kaiser et al., 2015). For example, Kaiser et al. (2015) found that the highest R_{gf} in the south-eastern US (> 0.04) was in an area dominated by a tree known to release monoterpenes and not isoprene. Hence the conclusion was drawn, in line with the OMI satellite observations of Chan Miller et al. (2014), that monoterpenes are a key driver of R_{gf}. Applying the same metric to the Melbourne measurements, where the seasonal cycle suggests R_{gf} is on average greater than 0.04 (in fact greater than 0.08, see figure 5.16(d)) in all months, monoterpenes must consistently be a dominant component of the bVOCs in Melbourne. Rather than formation of glyoxal from monoterpenes driving variations in R_{gf} however, the temperature dependence of HCHO and lack thereof for CHOCHO, leads to the conclusion that HCHO formation from isoprene is the key driver of variations in R_{gf}.

Between options (a) and (b) to explain the strong dependence of HCHO mixing ratio on northerly and easterly winds lies an intermediate pathway: transport of temperature-dependent formaldehyde precursors (i.e. bVOCs) which undergo oxidation in the urban environment. This pathway arises because bVOC oxidation is dependent on NO_x levels.

For example, Zhu et al. (2017) found that HCHO levels due to isoprene oxidation are enhanced by between 10 and 30 % across the United States because of ambient NO_x pollution. Wolfe et al. (2016) examined HCHO production rates from isoprene oxidation, under different NO_x regimes, and concluded two likely mechanisms for NO_x influence: OH production and peroxy radical branching ratios. This can be summarised through the reaction schemes:

$$NO + HO_2 \longrightarrow NO_2 + OH \quad \{42\}$$

$$VOC + OH \longrightarrow RO_2 \quad \{43\}$$

$$VOC + (O_3 \,/\, h\nu) \longrightarrow RO_2 \quad \{44\}$$

$$RO_2 + (NO, HO_2, RO_2, \text{isomerization}) \longrightarrow \alpha \cdot HCHO \quad \{45\}$$

from which the production rate of HCHO can be expressed as a function of the production rate of RO_2 radicals: $P(HCHO) = \alpha.P(RO_2)$ (Wolfe et al., 2016). Both terms in this equation are influenced by NO_x, hence the important role for NO_x in HCHO formation from isoprene. Therefore the formaldehyde measured at Broadmeadows, on the urban fringe and next to major roadways, may be enhanced above the 'background rural' formaldehyde levels. Because urban fringe locations like Broadmeadows will be one of the first large NO_x pools encountered by bVOCs transported on hot, north-wind days, the formaldehyde levels may even be enhanced at this urban-rural interface over the rest of the city.

5.4.4 Importance of HCHO in oxidation chemistry

The presence of VOCs, along with nitrogen oxides, in an urban environment has implications for the overall oxidation chemistry. Firstly, NO_x and VOCs are crucial to formation and destruction pathways of ozone. The MAX-DOAS formaldehyde and NO_2 measurements can be used as proxies for studying the local influence of NO_x and VOCs on ozone pollution conditions. Secondly, similarly to nitrous acid, photolysis of formaldehyde produces OH radicals and OH production from HCHO and HONO can therefore be compared using the MAX-DOAS measurements at Broadmeadows.

Links between formaldehyde and ozone

Studying ozone formation as a function of nitrogen oxide and volatile organic levels is of benefit for two key reasons. Firstly, considering ozone as a key atmospheric oxidant, it is important to understand the conditions under which NO_x or VOCs drive atmospheric oxidation capacity in Australia, in light of Australia's expected high bVOC levels and strong but isolated NO_x pollution sources. Secondly, considering tropospheric ozone as a toxic pollutant, examining formation conditions will help determine which emission reduction strategies will best curb photochemical smog.

Numerous studies in the early 1990s addressed the question of ozone production in NO_x-limited and NO_x-saturated environments (e.g. Sillman et al. (1990); Sillman (1995); Kleinman (1994)), primarily with the aim of helping regulators implement appropriate ozone-mitigation strategies. Following on from this work, Martin et al. (2004) and Duncan et al. (2010) demonstrated that the transition between NO_x-limited and NO_x-saturated ozone production (pO_3) regimes could be estimated using the ratio of formaldehyde to NO_2 column measurements (R_{fn}) from satellite retrievals. NO_x-saturated (and VOC-limited) conditions, in which reducing VOC emissions would has the greatest impact on reducing pO_3, were identified for $R_{fn} < 1$. NO_x-limited conditions, where reducing NO_x reduces pO_3 but reducing VOCs has no impact, were identitied for $R_{fn} > 2$. For R_{fn} between 1 and 2, the so-called 'transition zone', reduction of both NO_x and VOC emissions would curb ozone production. In order to use R_{fn} as an indicator of ozone production regimes, HCHO must be assumed to be a reliable proxy for VOC reactivity. In recent work, using box model simulations for Seoul, South Korea, Souri et al. (2020) found a tight correlation between HCHO mixing ratios and VOC reactivity for HCHO below approximately 7 ppb. Here we examine the relationship between R_{fn} and ozone surface mixing ratios using daily average HCHO VCDs for which the corresponding surface mixing ratios were all less than 6 ppb implying that these HCHO measurements can be considered good proxies for VOC reactivity. Souri et al. (2020) also found that the designation of ozone production regimes as being VOC-limited for $R_{fn} < 1$ and NO_x-limited for $R_{fn} > 2$, was valid for formaldehyde mixing ratios < 10 ppb, therefore applicable to this work too. Ideally, in future work, box modelling simulations incorporating local speciated VOC and NO_x mixtures, would be useful to quantify ozone production regimes for Australia. In the absence of certainty in current model estimates of VOC speciation in south-eastern Australia (as described in Emmerson et al. (2016) and Emmerson et al. (2018)) this has not been carried out and the designation of R_{fn} in Duncan et al. (2010) has been used to guide likely ozone production regimes.

Previously, R_{fn} has been applied by using total column measurements to understand surface ozone production and the question arises whether the total column R_{fn} is reflective of surface conditions. This was addressed in a global-scale modelling study by Jin et al. (2017) who found that while trends (e.g. seasonal variation) in column R_{fn} generally matched surface R_{fn}, the magnitudes were different arising from the different vertical distributions of HCHO and NO_2. They found the need for a correction factor to convert total column to surface R_{fn} which varied seasonally and spatially. The vertical profiles calculated by the MAX-DOAS technique give a way to observationally constrain the differences between column and surface R_{fn}.

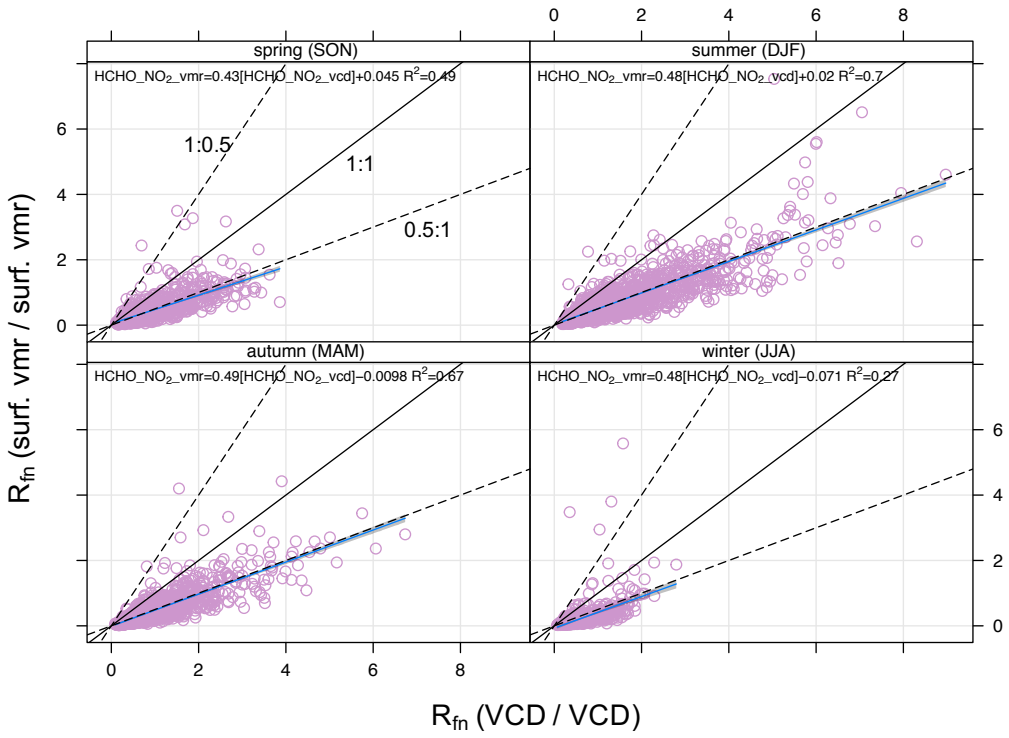

Figure 5.23: Seasonal scatterplots showing the relationship between VCD and surface VMR (R_{fn}), i.e. HCHO VCD/NO_2 VCD vs HCHO VMR/NO_2 VMR at Broadmeadows.

R_{fn} calculated using the MAX-DOAS results at Broadmeadows were as high as 9 for the VCD ratio and 7 for the VMR ratio as shown in figure 5.23. In all seasons, these scatterplots show a clear bias towards the VCD R_{fn}, with slope between 0.43 and 0.49. In other words the column-to-surface correction factor using these results is consistently between 2 and 2.3. In their global modelling study, Jin et al. (2017) calculate a conversion factor for surface-to-column R_{fn} between 1 and 2 during summer months across North America, Europe and East Asia, from global modelling studies. The Melbourne results are therefore higher than these but within the quoted uncertainty. In any case direct comparison of the conversion factors is problematic because of the different techniques (model vs measurement). In addition, the ratio of VCD to surface R_{fn} is expected to vary from location to location due to differing vertical gradients of formaldehyde and NO_2 in different places. This highlights the importance of ground-based and vertically resolved measurements to understanding the relationship between column and surface concentration ratios, and the associated limitations in using column ratios to understand pollution and chemistry at the surface.

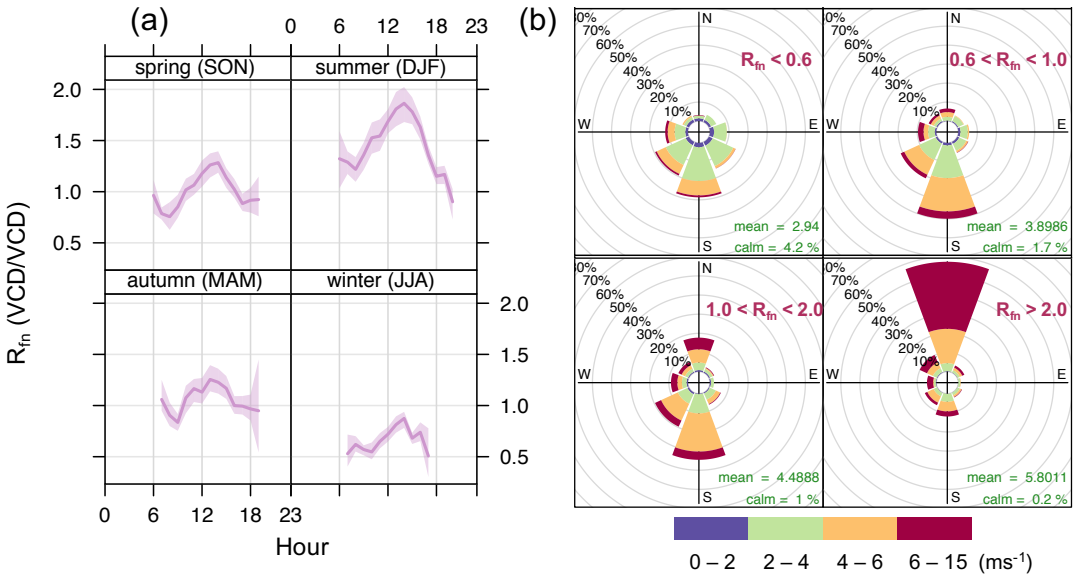

Figure 5.24: Summary of results for the ratio of HCHO to NO_2 (R_{fn}): (a) Diurnal variation of R_{fn} shown by season. (b) Windroses (wind direction histograms) binned by four R_{fn} scenarios.

To study pO_3 regimes in Melbourne, column R_{fn} will be used in the following discussion to be consistent with literature definitions of NO_x- and VOC-limited conditions. The diurnal cycle of R_{fn} has a fairly consistent general shape in each season, as shown in figure 5.24(a), with a maximum around midday. In winter, the average diurnal R_{fn} stays below 1, and thus VOC-limited, throughout the day. In spring and autumn, the midday diurnal cycle peaks in the transition zone between 1 and 2. In summer, the average midday peak is close to 2, close to NO_x-limited conditions. The values of VCD R_{fn} in figure 5.23 show that the threshold for NO_x-limited conditions of 2 is exceeded often at Broadmeadows in spring, summer and autumn, although almost never in winter. The windroses in figure 5.24(b), which are binned by R_{fn}, give an indication of some specific meteorological conditions under which this occurs. When R_{fn} is less than one (top two panels), more than 50% of the time the wind is from the southerly sector. In the transition zone for $1 < R_{fn} < 2$, contributions from both south (dominant sector) and north are observed. However, when NO_x-limited conditions occur ($R_{fn} > 2$), around 70 % of the time the wind is northerly and at speeds greater than 4 ms^{-1}. This is consistent with our earlier understanding of strong HCHO formation under conditions of high temperature weather and northerly winds. The temperature relationship is clear when considering the scatter plot of HCHO VCD vs NO_2 VCD in figure 5.25(a) which is coloured by temperature; a clear gradient is seen where high ambient temperatures predominantly relate to R_{fn} in the transition zone or NO_x-limited pO_3 conditions. The relationship between R_{fn} and temperature could be described by an exponential function with moderate correlation coefficient ($R^2 = 0.4$ in summer), and an equation

of $ln(R_{fn}) = 0.08T - 2$ indicating that the temperature-dependent HCHO formation processes discussed earlier are driving the R_{fn} value especially in summer.

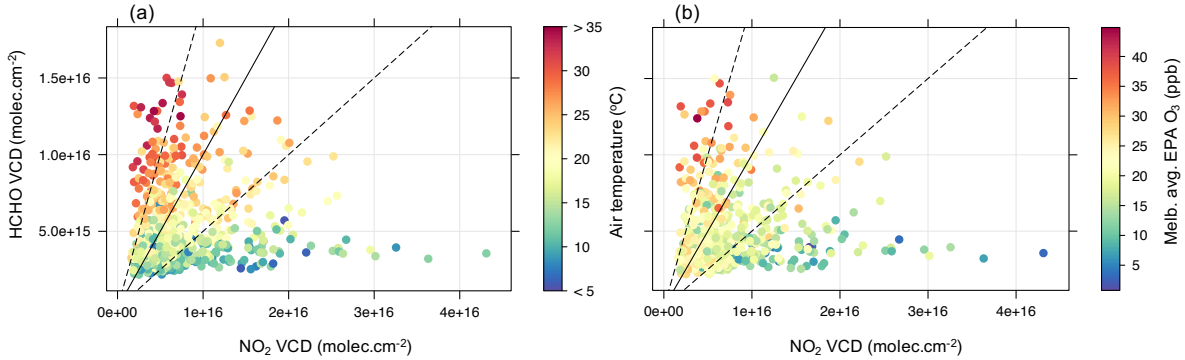

Figure 5.25: Scatterplots for HCHO vs NO_2 VCD daily averages, coloured by (a) the ambient air temperature and (b) average Melbourne EPA ozone mixing ratio. The solid lines indicates 1:1 (i.e. $R_{fn} = 1$), the dashed lines represent $R_{fn} = 2$ and $R_{fn} = 0.5$ respectively.

Figure 5.25(b) shows the same as (a) but coloured instead by the ozone concentration, which is the average across all EPA monitoring sites in the Melbourne metropolitan area as described for NO_2 earlier. The results are striking: almost all instances of daily average O_3 exceeding 35 ppb coincide with $R_{fn} > 1$ at Broadmeadows. During the whole measurement period, the World Health Organisation (WHO) guideline for of O_3 mixing ratio of 50 ppb (8 hour averages) was exceeded 18 times in Melbourne and 17 of these events showed $R_{fn} > 1$, 11 of these $R_{fn} > 2$. This accords with previous work to understand pO_3 in Australian cities by Linfoot et al. (2005) who found that the majority of ozone standards exeedances in Sydney between 1998 and 2003 occurred in NO_x-limited conditions.

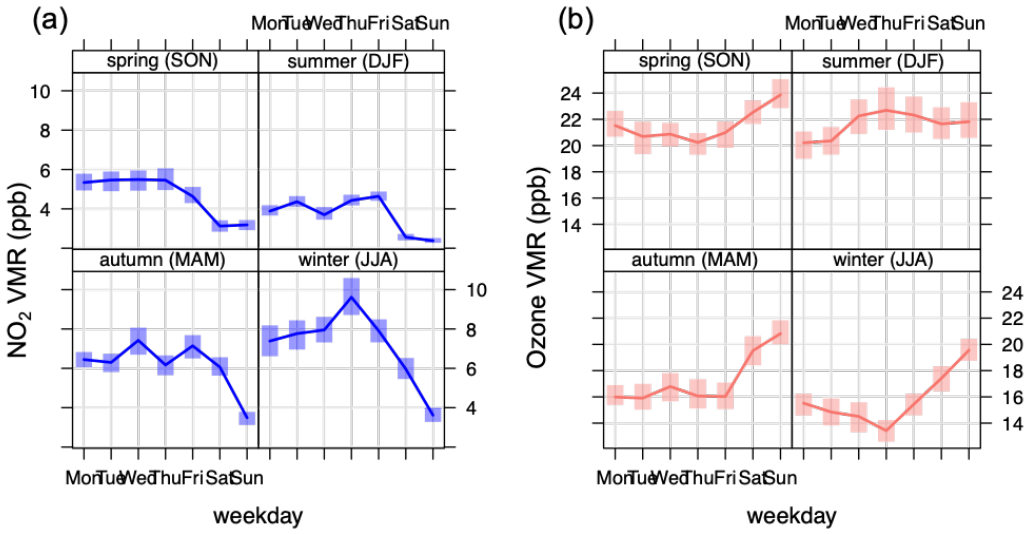

Figure 5.26: (a) Daily mean NO_2 mixing ratios (lowest MAX-DOAS retrieval layer) at Broadmeadows for each season, showing lower NO_2 on weekends than weekdays. (b) Daily mean O_3 mixing ratios (average of EPA sites across Melbourne metropolitan area) for each season.

To test whether lower NO_x may indeed lead to lower ozone concentrations under NO_x-limited conditions, the "weekend effect" of nitrogen oxides can be exploited. Lower nitrogen oxides at Broadmeadows on weekends are evident in figure 5.26 in all seasons. In Autumn, Winter and Spring, there is an accompanying reverse weekend effect on ozone concentrations because removal of NO_x reduces NO-titration of ozone. In summer, the decrease in NO_x on the weekend still exists, and therefore the reduced ozone titration pathway should still hold – but a weekend ozone increase is not observed. This suppression of the ozone weekend effect suggests that the ozone production is sensitive to NO_x as implied by the HCHO:NO_2 ratio. This accords with findings in Baidar et al. (2015) who showed a suppression of the ozone weekend effect in support of NO_x-limited ozone production in summer.

It can be argued that high temperatures and corresponding high HCHO levels are driving not only the ozone production regime, but may be driving ozone concentrations too. This suggestion is backed up by a linear relationship with moderate correlation observed for HCHO surface mixing ratio and average O_3 concentration in summer as shown in figure 5.27. The slope of the regression in summer was 0.094. This slope is of a similar magnitude to previous reports; it is higher than found in essentially free tropospheric air at Mt Cimone (slope = 0.079) in Italy (Fischer et al., 2003) and lower than found urban Milan (slope = 0.11) with significant HCHO contributions attributed to both anthropogenic and biogenic VOCs (Jiménez et al., 2000). Leuchner et al. (2016) found summertime correlations between HCHO and O_3 with much less steep slopes (between 0.02 and 0.04) at a German rural mountainside site, although they

noted a wintertime inversion of the relationship as seen in also in figure figure 5.27. This was attributed to a more significant role of direct anthropogenic HCHO emissions in winter compared to summer. Two important conclusions can be offered from these results: (a) it is likely that biogenic VOCs are a dominant driver of oxidative chemistry through ozone formation in Melbourne, especially on hot summer days and (b) the worst instances of photochemical ozone pollution in Melbourne occur when the production regime tends to NO_x-limited. This is good news for the reduction of high ozone episodes in Melbourne; biogenic VOC emissions cannot be controlled, but anthropgenic NO_x emissions can through regulation and thus there are significant improvements that can be made to overall air quality in Melbourne by reducing NO_x.

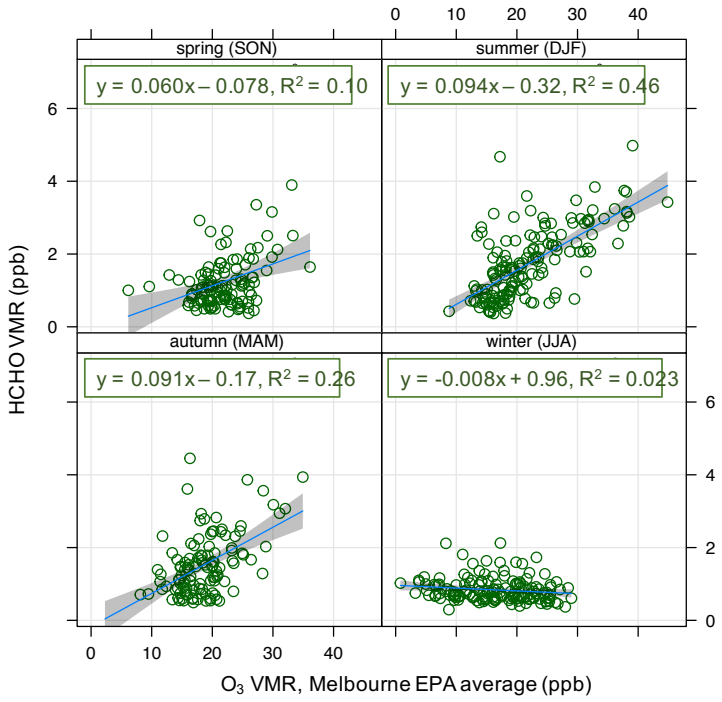

Figure 5.27: Scatterplots showing MAX-DOAS HCHO VMR at Broadmeadows against Melbourne average EPA ozone concentration. Data is daily averages, divided up by season.

The implication of biogenic VOCs being critical to high ozone episodes in Australia is in line with the findings of the study of ozone on hot summer days in Sydney by Utembe et al. (2018). For example, their modelling work showed that instances of high ozone on hot days was removed if biogenic VOC emissions were omitted from the simulation. Given that removing the bVOCs is not practical in a real-world experiment, a good follow up question to Utembe et al. (2018) would be to check whether the instances of high O_3 is removed by lowering NO_x instead, as predicted by the finding of NO_x-limited nature of such events. Additionally the omnipresent temperature dependence highlights that climate change is an important consideration; if high biogenic emissions occur on

the hottest days and are related to photochemical smog production at current NO_x levels, then in a warming world one must expect the number of ozone pollution events to also increase. Because the ozone production is mostly NO_x limited at temperatures greater than 30°C, the risk of hotter days heightens the imperative for stringent NO_x regulations to curb high ozone episodes.

It has been shown that anthropogenic climate change has already increased the frequency of high temperature events in Australia (Lewis and Karoly, 2013; Lewis and King, 2015). To assess what this means for ozone pollution episodes on hot days in Melbourne, a histogram of ozone concentration in Melbourne when the temperature exceeds 30°C has been plotted in figure 5.28(a). This suggests that when the temperature is over 30°C, there is a greater than 50% chance of ozone concentration exceeding 40 ppb (one hour average value). Using the ACORN-SAT temperature record (Trewin, 2012) which is available through the Australian Bureau of Meteorology's website, the number of days in Melbourne with temperature exceeding 30°C since 1910 has been shown in figure 5.28(c). Between 1910 and 1998 (also between 1910-2000, and 1970-2000) the average number of days with temperature over 30°C was 26. Between 1998 and 2018, this average was 31 - five days more per year on which high ozone episodes were likely. Therefore it is concluded that, based on temperature alone, high ozone episodes are of increasing concern in Melbourne. However, the histogram of R_{fn} for conditions $> 30^o$C in figure 5.28(b) shows that more than three quarters of the time $R_{fn} > 2$, confirming that most of the hot-day high ozone events could be curtailed by the introduction of NO_x emission measures.

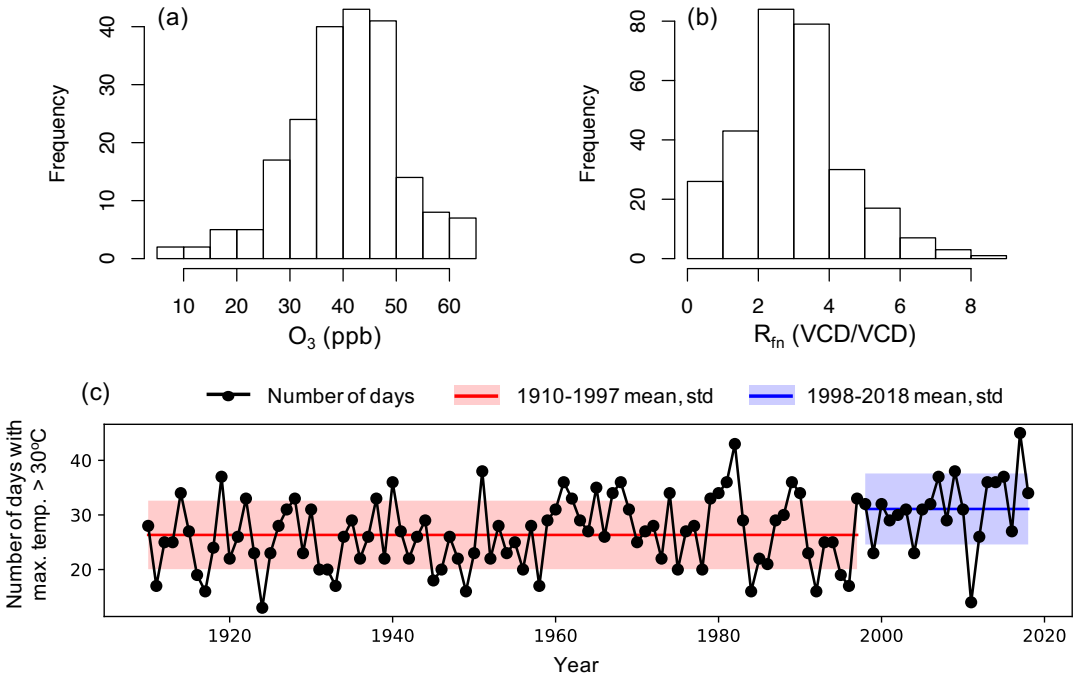

Figure 5.28: (a) Histogram of ozone mixing ratio (EPA average across Melbourne metropolitan area from December 2016-May 2019) when the temperature was over 30°C. (b) Same as (a) but for R_{fn} at Broadmeadows. (c) Timeseries showing the number of days with temperature exceeding 30°C in Melbourne. Data taken from ACORN-SAT long term temperature record for the city of Melbourne, through the Australian Bureau of Meteorology website. Red indicates the 1910-1998 mean and standard deviation, blue indicates the 1998-2018 average.

HO_x radical production

Formaldehyde is an important species in the overall HO_x cycle because it photolyses to form HO_2 and OH radicals:

$$\mathrm{HCHO} + h\nu \xrightarrow{J(\mathrm{HCHO}_{rad})} \mathrm{HCO} + \mathrm{H} \quad \{46\}$$

$$\mathrm{H} + \mathrm{O_2} + \mathrm{M} \longrightarrow \mathrm{HO_2} \quad \{47\}$$

$$\mathrm{HCO} + \mathrm{O_2} \longrightarrow \mathrm{HO_2} + \mathrm{CO} \quad \{48\}$$

$$\mathrm{HO_2} + \mathrm{NO} \longrightarrow \mathrm{OH} + \mathrm{NO_2} \quad \{49\}$$

The HO_2 formed by HCHO photolysis can produce hydroxyl radicals in the presence of NO as shown in this reaction scheme, a process relevant for the Broadmeadows location. Therefore, in this section, HCHO is considered alongside HONO and ozone as a local HO_x producer.

In order to compare HO_x from HCHO, HONO and O_3, photolysis rates ($J(O^1D)$, $J(\text{HCHO}_{rad})$ and $J(\text{HONO})$) were calculated using the TUV model, assuming clear sky conditions, as described in section 5.3.5 and in Ryan et al. (2018). A case study comparison period is illustrated in figure 5.29 from 14-19 January 2018. During this time, daily maximum temperatures rose from 19°C on the 14th to 41°C on the 19th and, as expected from the earlier discussion, the amount of HCHO also increased considerably. The highest HONO levels coincided with the lowest wind speeds on the morning of the 16th and 17th, with the maximum HONO mixing ratio being 0.34 ppb. This resulted in maximum OH production rates due to HONO ($pHO_x(\text{HONO})$) $> 1 \times 10^7$ molecules.cm^{-3}s^{-1}. In comparison, pHO_x(HCHO) and $pHO_x(O_3)$ were very similar to each other, were less variable overall but increased each day that the temperature increased from maximum values around 5×10^6 molecules.cm^{-3}.s^{-1} on the 16th to around 9×10^6 molecules.cm^{-3}.s^{-1} on the 19th. These values of pHO_x due to HONO, HCHO and O_3 are of the same order as observations in other parts of the world both in urban (e.g. Alicke et al. (2002); Ren et al. (2003); Lin et al. (2012)) and rural (e.g. Acker et al. (2006); Kleffmann et al. (2005)) environments. On the 17th, HONO photolysis contributed approx. 53 % of the total OH produced, while O_3 and HCHO contribute 18 and 29 % respectively. With much more HCHO production, and the HONO unable to build up on the 19th due to stronger winds, HCHO becomes the dominant HCHO producer at 39 %, followed by O_3 at 35 % and HONO at 26 %.

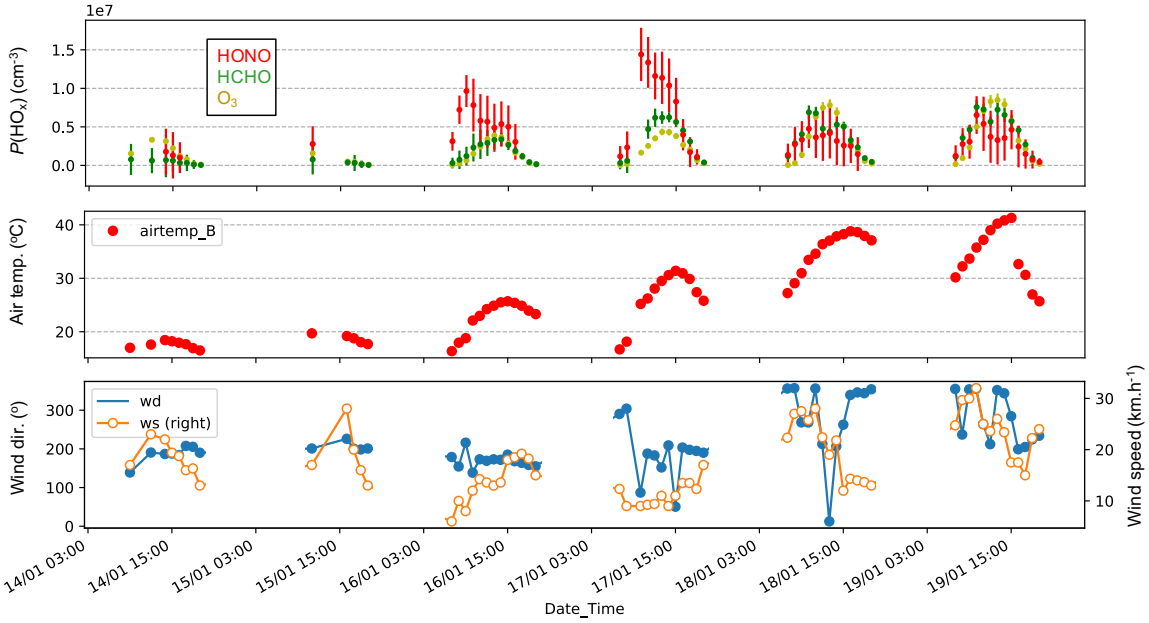

Figure 5.29: Top: timeseries showing production rate of HO_x (HO_2 + OH) for a case study period, 14-19 January 2018. pHO_x is plotted for HCHO, HONO and O_3. Middle: Ambient temperature and bottom: wind direction (blue, left y-axis) and speed (orange, right y-axis) over the same period.

To gauge the relative importance of these HO_x production mechanisms beyond these case study examples, average monthly surface pHO_x values for HONO, HCHO and O_3 have been estimated. To do this, the average diurnal cycle of each trace gas and their respective J values (calculated using the TUV model) have been used. The results, shown in figure 5.30, have been arranged in rows by season and show that the highest pHO_x for all species occurs in summer. This is expected of course because J values depend on solar radiation. These average values indicate that pHO_x is dominated by HONO photolysis in all seasons, with highest percentage contributions (60-70 %) from April through to August. HONO contributes a minimum of around 45 % in December and January and otherwise sits around 50 %. Formaldehyde photolysis contributes around 25 % to pHO_x in the warmest months (December-March), and between 15-20 % during the cooler months. The contributions of HCHO and O_3 are commensurate for most months, except December where the contribution from O_3 dominates. HONO is especially dominant in the morning, with average pHO_x from HCHO and O_3 much closer to HONO during the afternoon.

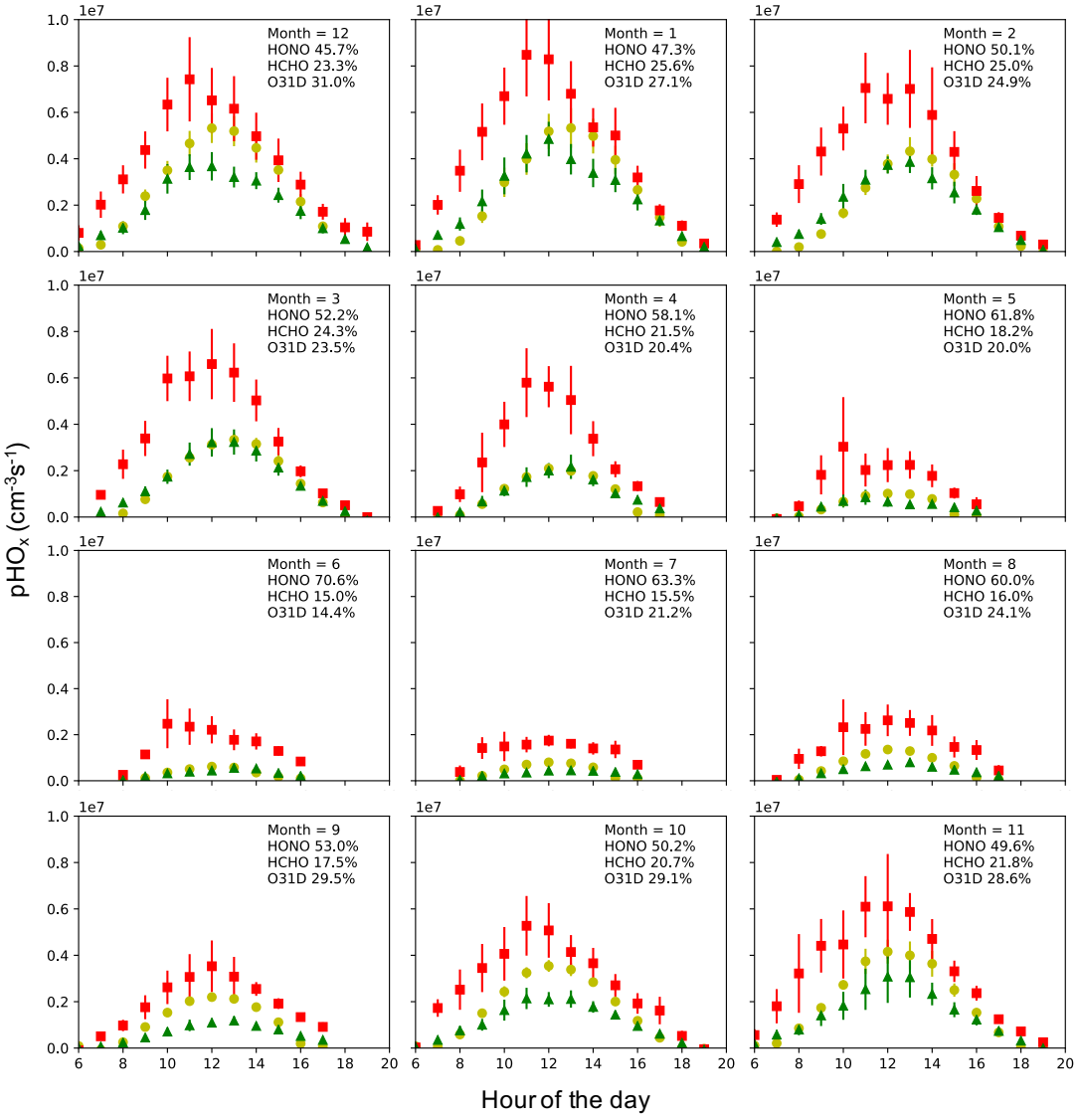

Figure 5.30: Monthly average diurnal cycles of pHO_x from HONO, HCHO and O_3 at Broadmeadows. Top row is summer, second row autumn, third row winter and bottom row spring.

There are some important caveats to this analysis. Firstly, the ozone concentrations used to calculate pHO_x are the average of EPA in-situ ozone monitors around the Melbourne CBD and so direct comparison with results at the specific Broadmeadows location must be treated with caution. Secondly, a third key OH radical production mechanism, namely ozonolysis of alkenes, is not considered here due to a lack of speciated VOC measurements in Melbourne. This mechanism has previously been found to contribute in the order of 10 % to total OH production (Alicke et al., 2002; Kleffmann et al., 2005), and given the prevalence of HCHO suggests significant VOC abundance, alkenes are likely to play a role here also. The third caveat is that more precise OH

production results could be calculated using measured photolysis (i.e. measured actinic flux) rates rather than modelled values. Finally, this comparison considers only surface values of trace gas concentration, however, the MAX-DOAS vertical profile results can give some indication of pHO_x at higher altitudes for HCHO and HONO.

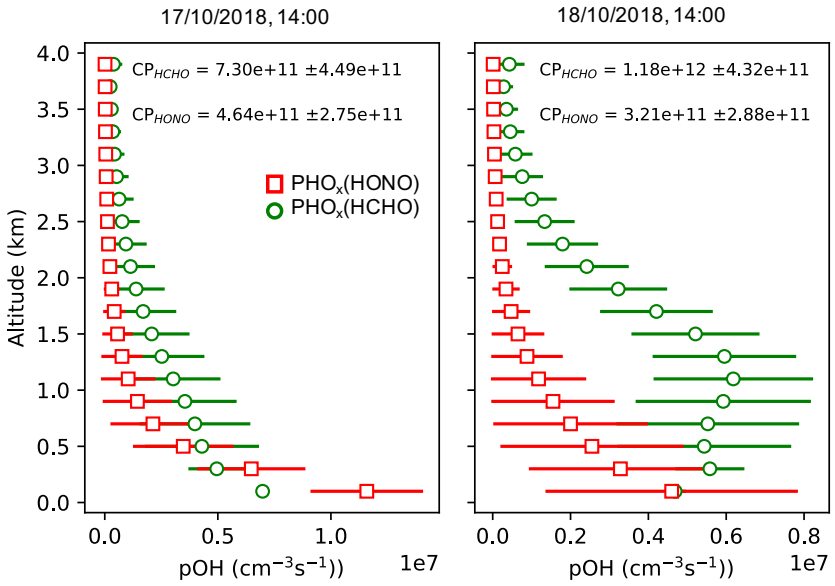

Figure 5.31: Example vertical profiles of pHO_x from HONO and HCHO at Broadmeadows, from 2 pm local time on the 17th (left) and 18th (right) of January 2018. Each plot is annotated with the corresponding vertically integrated pHO_x values for HONO and HCHO, which have units of $cm^{-2}s^{-1}$.

Calculating pHO_x for HONO and HCHO in the same way as before, using J values calculated by the TUV model at each altitude, results in vertical pHO_x distributions as shown in figure 5.31. For this analysis, we return to two of the case study days in January 2018 (see timeseries in figure 5.29). It was observed earlier that the average vertical profile distributions for HONO and HCHO were markedly different in summer, with HONO exhibiting a much stronger vertical gradient. In both plots in figure 5.31, this strong vertical gradient is also reflected in the pHO_x. The left hand plot is from 14:00 local time on the 17th, showing that in the lowest retrieval layer HONO photolysis dominates HCHO by a factor of two as main HO_x source, matching the timeseries in figure 5.29. Above the 500 m retrieval layer however, the contribution of HONO drops off much more rapidly than HCHO. Within the error bars, the vertically integrated "column" pHO_x for HCHO and HONO are similar. In the right hand panel of figure 5.31, taken from 14:00 local time on the 18th, the surface pHO_x values are the same again matching the timeseries. However, as indicated in the previous discussions of HCHO vertical profiles, on hot days such as this the HCHO is often observed in a plume extending above 1-1.5 km altitude. This is reflected in the pHO_x for HCHO in

this example which remains above 4×10^6 molecules.cm^{-3}.s^{-1} at 1.5 km while pHO_x for HONO has reduced to zero. In this example, the column pHO_x is a factor of four higher for HCHO than HONO. These results highlight the importance of vertical trace gas distributions in the overall picture of atmospheric oxidation chemistry, and the utility of the MAX-DOAS technique to provide such insight. This work suggests that considering purely the surface diurnal cycles or timeseries of HCHO and HONO gives undersells the importance of HCHO photolysis as a lower tropospheric HO_x source at Broadmeadows.

5.5 Broadmeadows results: summary

In this chapter, a two and a half year long dataset of MAX-DOAS measurements at Broadmeadows has been presented, providing information on aerosol optical depth, nitrogen dioxide, nitrous acid, formaldehyde and glyoxal. Collectively and alongside supplementary data, these species give a picture of the key sources and drivers of tropospheric oxidation chemistry and air quality at Broadmeadows.

The potential sources of each species were examined predominantly by analysing the measured trace gas concentrations alongside meteorological information. It was concluded that for most of the year, the aerosol optical depth observed at Broadmeadows can be explained by emissions from the industrial south-western suburbs of Melbourne. In isolated events, especially in summer and autumn, smoke plumes from biomass burning outside the city can transport significant aerosol pollution to the metropolitan area. The NO_2 measured at this location was dominated by traffic emissions from the adjacent road corridors, and much higher in winter than summer. Despite the proximity to the highways NO_2 pollution was not found in exceedance of the Australian NEPM standards. Nitrous acid was found in substantial concentrations in the middle of the day, which could not be explained by the standard HONO formation mechanisms involving NO_2, NO and OH. The observed midday HONO levels show a dependence on soil moisture content and it is therefore hypothesised that soil-based emissions could explain missing source of HONO at Broadmeadows. Formaldehyde was detected in much higher concentrations in summer than winter, with an exponential temperature dependence. Therefore oxidation of biogenic VOCs was identified as the most likely VOC precursor for HCHO formation. Glyoxal was also measured at Broadmeadows with little seasonal variation, although maximum concentrations in Autumn may be related to VOCs associated with fuel-reduction biomass burning. The consistently high ratio of glyoxal to formaldehyde (around 10 %) suggest that monoterpenes make up a consistently high proportion of the biogenic VOCs in Melbourne.

The drivers of air quality and oxidation chemistry were analysed using photolysis rate equations and by calculating characteristic ratios of tropospheric constituents. Photolysis of HONO was found to be the largest single contributor to boundary layer hydroxyl radical production at Broadmeadows, contributing on average between 45-50 % of OH

production in all months. Photolysis of HCHO and O_3 were significant contributors in summer, and on the hottest and windiest summer days the HCHO was present at sufficient levels to overtake HONO as the primary surface OH source. Using the vertical profiling capability of the MAX-DOAS technique it was shown that while HONO typically dominates the OH production close to the surface, HCHO and O_3 are likely dominant at higher altitudes. Finally, the broad VOC and nitrogen oxide drivers of ozone smog formation were considered using the ratio of HCHO:NO_2. These results indicate that ozone production conditions are usually VOC-limited at Broadmeadows due to the NO_x from the nearby highways. However, on hot summer days when significant levels of both HCHO and ozone are often observed, the ozone production regime tends toward NO_x-limited. This means that NO_x control measures would be effective at reducing high ozone episodes on hot days, a fact made all the more imperative by the likelihood of increased extreme temperature events in the future.

Chapter 6

Coastal case study: Garden Island campaign

Between 19th April and 15th May 2018 an intensive field campaign was held at Garden Island, Western Australia (lat. -32.189°, lon. 115.667°, elevation 5 m ASL), to study local atmospheric chemistry and aerosol properties. The campaign was funded by, and held on the land of, the Australian Government's Defence Science and Technology Group (DSTG). The following describes the key results of the measurement campaign pertaining to air quality and oxidation chemistry in this complex coastal environment. The first part of this chapter describes the meteorological, trace gas and aerosol time-series results, including MAX-DOAS vertical profiles, from the month-long campaign. The second part of this chapter discusses and interprets the competing influences on air quality and oxidation chemistry at Garden Island with the aid of Lagrangian chemistry-back trajectory modelling.

The primary research groups involved in the Garden Island campaign were the University of Melbourne's AIRBOX (Atmospheric Integrated Research facility for Boundaries and Oxidative eXperiments, airbox.earthsci.unimelb.edu.au) mobile chemistry laboratory, and DSTG. Garden Island (GI, see figure 6.1) is a thin 10 km long island running approximately parallel to, and about 8 km from, the coast of Western Australia. The position of AIRBOX on GI was approximately 30 km south west of the Perth's metropolitan centre. This location provides several characteristic airmass sectors experienced at the measurement site: background marine air from the Indian Ocean to the west, background continental air from the south east and urban/industrial polluted air from the east and north-east. Because GI and the nearby suburb of Kwinana are home to an Australian Naval base, oil refinery and chemical manufacturing plant and proximate to the busy port of Fremantle, shipping and industry was expected to supply a practically ubiquitous NO_x emission source.

AIRBOX, an atmospheric chemistry laboratory housed inside a 6.1 m × 2.4 m shipping

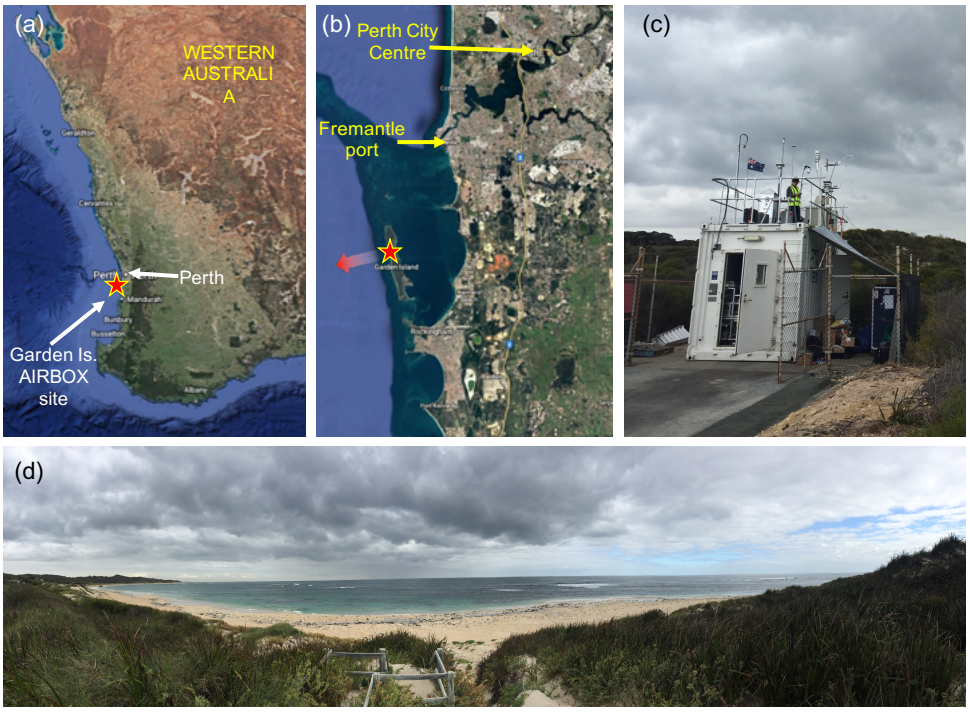

Figure 6.1: (a) Map showing the location of Perth and Garden Island in Western Australia. (b) Map zoomed in to the Perth region showing the location of AIRBOX (red star) on Garden Island, and proximate pollution sources Perth and Fremantle. (c) Picture of the AIRBOX mobile chemistry Laboratory at Garden Island. (d) Panoramic shot of the view west from AIRBOX out over the Indian Ocean, in the MAX-DOAS viewing direction. *Maps sourced from Google maps, photos by S. Fiddes.*

container, hosted a large number of instruments for characterising aerosol properties at Garden Island. These included particle counters, particle sizing instruments, mass spectrometers, a black carbon counter, a nephelometer, micro-pulse lidar and hi-volume sampler. Radon measurements were made to monitor the 'over-land' component of air-masses reaching the measurement location. In addition, in-situ meteorology, O_3 and NO_2 measurements were conducted and aerosol optical thickness was calculated from a nearby DSTG sun photometer. This campaign, including the MAX-DOAS measurements made with the University of Melbourne's instrument, therefore constituted a measurement-rich, if temporally short, snapshot of the local atmospheric chemistry and physics.

6.1 Complimentary measurements

6.1.1 Meteorology during the campaign

Data from an automatic weather station ('LUFFT WS800 UMB' weather sensor by Thomson Environmental Systems) provided meteorological data which is useful context for the aerosol and atmospheric chemistry measurements at Garden Island. A variety of weather conditions were experienced during the campaign, typical of autumn in this location. A timeseries of meteorological observations for the duration of the campaign is shown in figure 6.2. Daily maximum temperatures ranged between 20-30°C and minimum temperatures between 12-20°C. Highest temperatures typically occurred during periods of easterly winds (from the interior of the continent) and high pressure, associated with synoptic scale systems. On other days, such as the 3rd, 7th and 8th of May, the local scale sea-breeze process is evident with winds shifting from east/south-easterly to west/south-westerly around the middle of the day.

The wind data throughout the Garden Island campaign is summarised by the windrose in figure 6.3. This shows two dominant wind patterns throughout the measurement period. Approximately 20% of the time wind came from the south-west, and this sector was dominated by wind speeds > 6 ms^{-1}. The most dominant wind direction was the easterly sector, accounting for over 30 % of measurements and dominated by low wind speeds < 4 ms^{-1}. These two dominant sectors provide ideal comparison points for atmospheric aerosols and chemistry of oceanic and urban/continental origin respectively.

A notable feature of Autumn in southern Australia is biomass burning related to both wildfire and controlled fuel reduction events. During the Garden Island campaign period, 17 separate fire and/or smoke events were reported in the Perth region by the Western Australian Department of Fire and Emergency Services. Most of these reports were due to controlled fuel reduction burns. Smoke from these events was evident, both visibly and in the measured trace gas and aerosol data at Garden Island on several days and will be discussed in further detail below.

6.1.2 In-situ chemistry measurements

Oxides of nitrogen were measured using an in-situ analyser (ThermoFisher 42i-TL NOx analyser, drawing 7.5 litres of air per minute, logging 1 minute averages) located in AIRBOX throughout the campaign. An in-situ ozone monitor was also employed (ThermoFisher O_3 monitor, also drawing 7.5 litres per minute and logging 1 minute averages). Both instruments were operated by the University of Wollongong. This dataset is referred to throughout the discussion in this chapter. Polar bivariate plots of the (daytime) relationship between these species and wind are shown in figure C.1 in Appendix C.

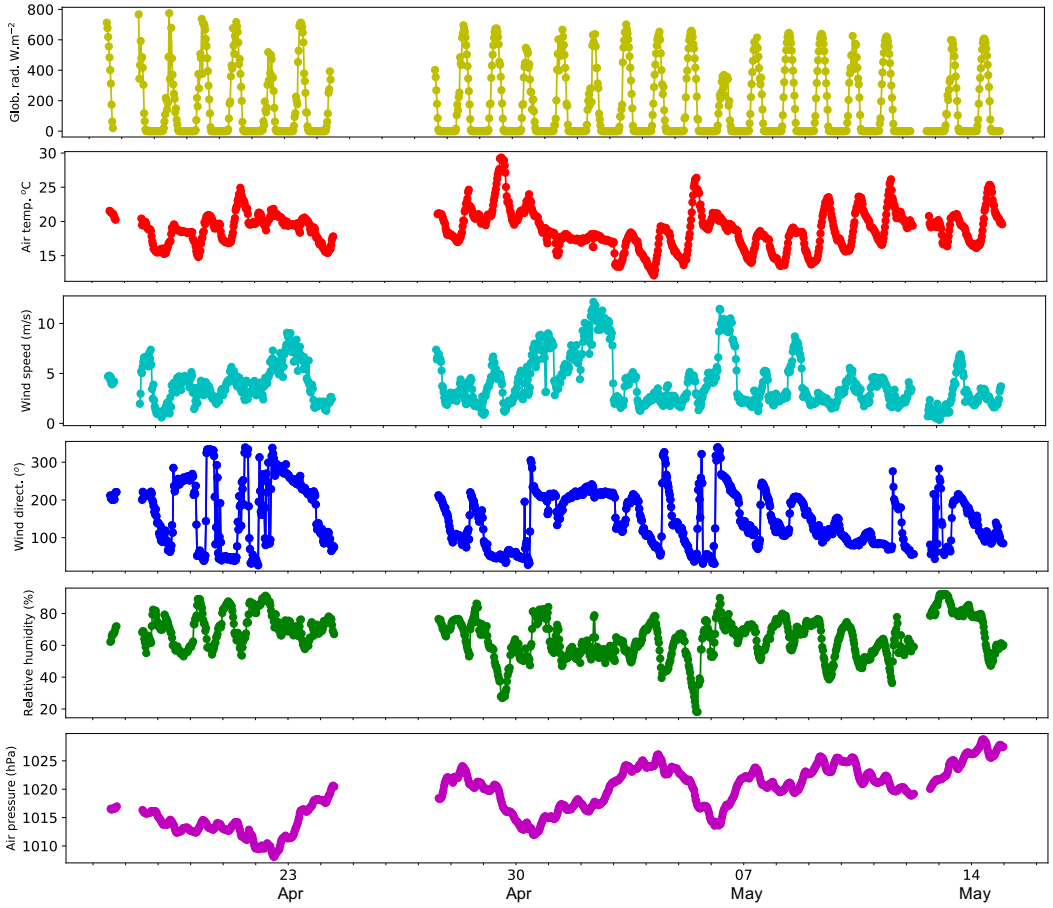

Figure 6.2: Timeseries of meteorological data (30 minute averages) from the automatic weather station at the Garden Island AIRBOX site. Top to bottom, variables are global radiation, air temperature, wind speed, wind direction, relative humidity and atmospheric pressure.

6.2 MAX-DOAS measurements

The MAX-DOAS instrument at Garden Island was mounted on the roof of the AIRBOX container with a view looking over the Indian Ocean to the west, as shown in figure 6.1(d). Differential slant columns for various trace gases were retrieved from the MAX-DOAS spectra in QDOAS in the same manner described in chapter 2, followed by inversion to vertical columns and profiles using HEIPRO as described in chapter 3. The following outlines the key results from the MAX-DOAS measurements.

6.2.1 Differential slant columns

Differential slant columns (dSCDs) for the GI campaign period are presented in figures 6.4 and 6.5. The detection limit for each species (shown as the black line in each plot)

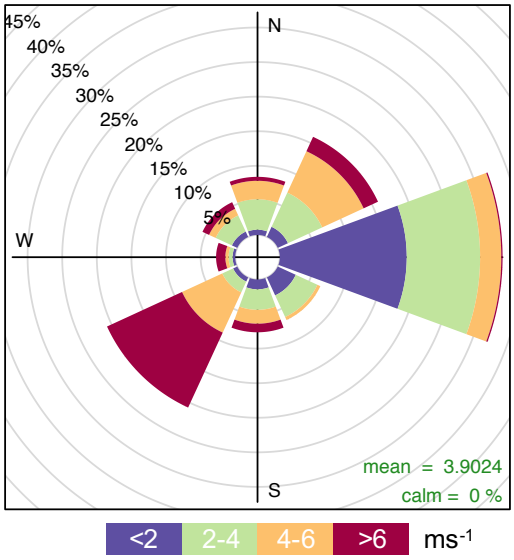

Figure 6.3: Windrose combining all wind speed and direction measurements throughout the Garden Island campaign. The radial axis represents frequency of counts (%) by wind direction.

has been calculated for the 0° elevation angle using the residual RMS and the trace gas absorption cross section maximum, as described in chapter 5. The timeseries plots show that O_4, NO_2 and HCHO dSCDs were consistently above the detection limit throughout the campaign, hence, these species were further analysed to produce vertical columns in HEIPRO. Spectral fits for glyoxal were seen at Garden Island exceeding 1×10^{16} molecules/cm^{-2}, however residual RMS values at the blue end of the spectrum used for glyoxal retrieval were much higher (around 9×10^{-4}) than for the O_4, NO_2 and HCHO retrieval windows (around 4×10^{-4}). This placed the majority of CHOCHO dSCDs below the detection limit. In addition, no separation of dSCDs from different elevation angles was observed, implying no clear vertical gradient and as a result glyoxal was not pursued further for Garden Island. Except for two small events (11th and 15th of May) nitrous acid dSCDs were below the detection limit and exhibited no variation with elevation angle. Therefore HONO was also not analysed further in the Garden Island analysis process.

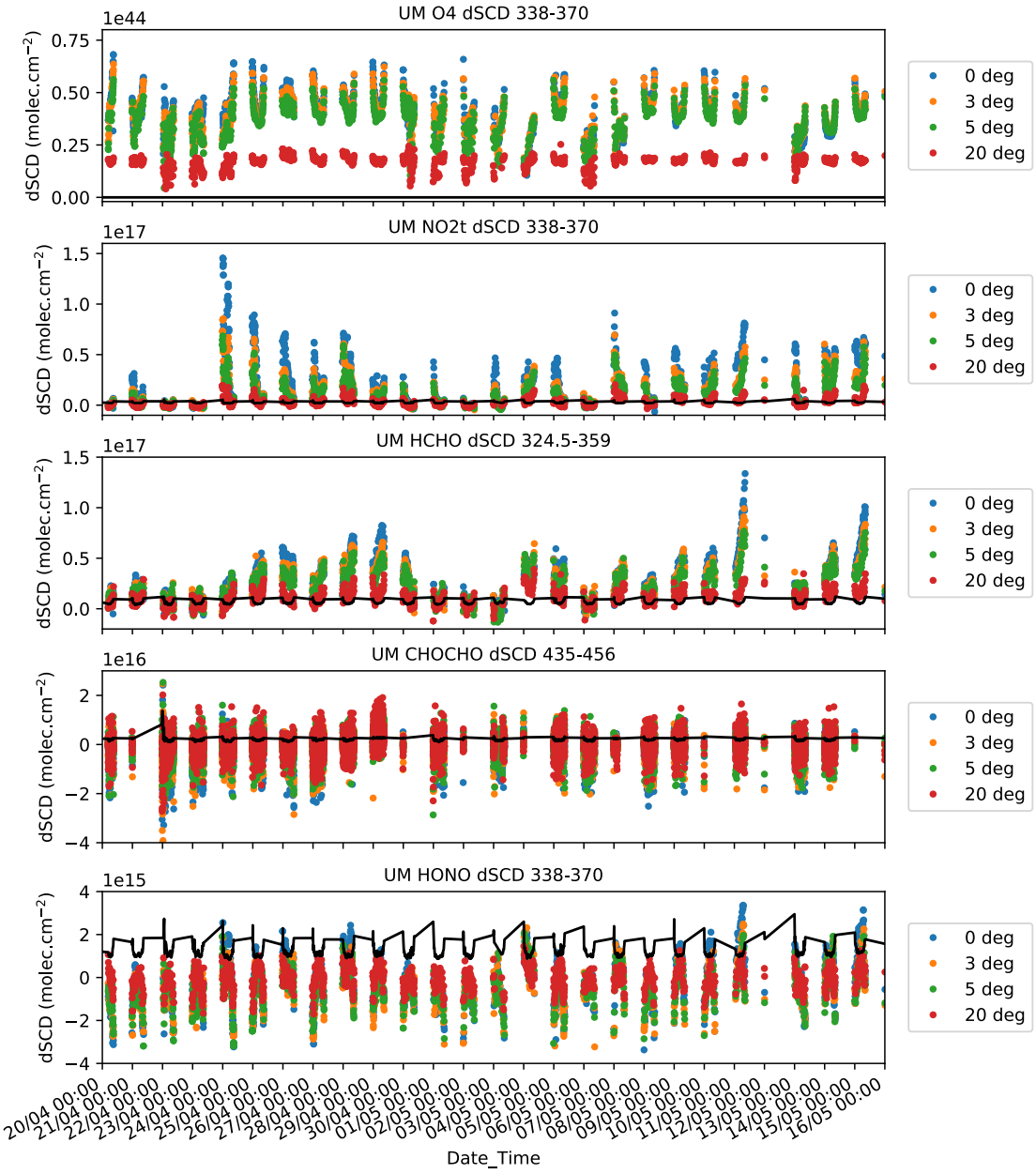

Figure 6.4: Timeseries of differential slant column densities for selected elevation angles, from the Garden Island campaign: top to bottom O_4, NO_2, HCHO, CHOCHO and HONO. The black solid line indicates the detection limit calculated using the residual RMS, for the 0° elevation angle. 'UM' denotes that the University of Melbourne MAX-DOAS was used at Garden Island.

Given the coastal location of the measurement site, in addition to the molecules discussed in the previous chapters halogen oxides were also considered at Garden Island. As shown in the top panel of figure 6.5, iodine monoxide (IO) 0° and 3° dSCDs were

frequently observed above the 0° detection limit. It is important to note that the higher elevation angle dSCDs were also frequently observed above their respective detection limits (which vary because residual RMS is slightly different for each elevation angle) but these detection limit lines are excluded from the plots for clarity. The low elevation angle slant columns for IO reached 7×10^{13} molecules.cm^{-2}, siginifantly higher than previous papers in which IO was successfully retrieved from MAX-DOAS measurements, for example in the Western Pacific Ocean by Großmann et al. (2013). Therefore the analysis of IO was pursued further in this work. In contrast, bromine monoxide (BrO) and chlorine dioxide (OClO), the other atmospheric halogen oxides accessible to UV-Vis spectroscopy, were not observed in the Garden Island spectra.

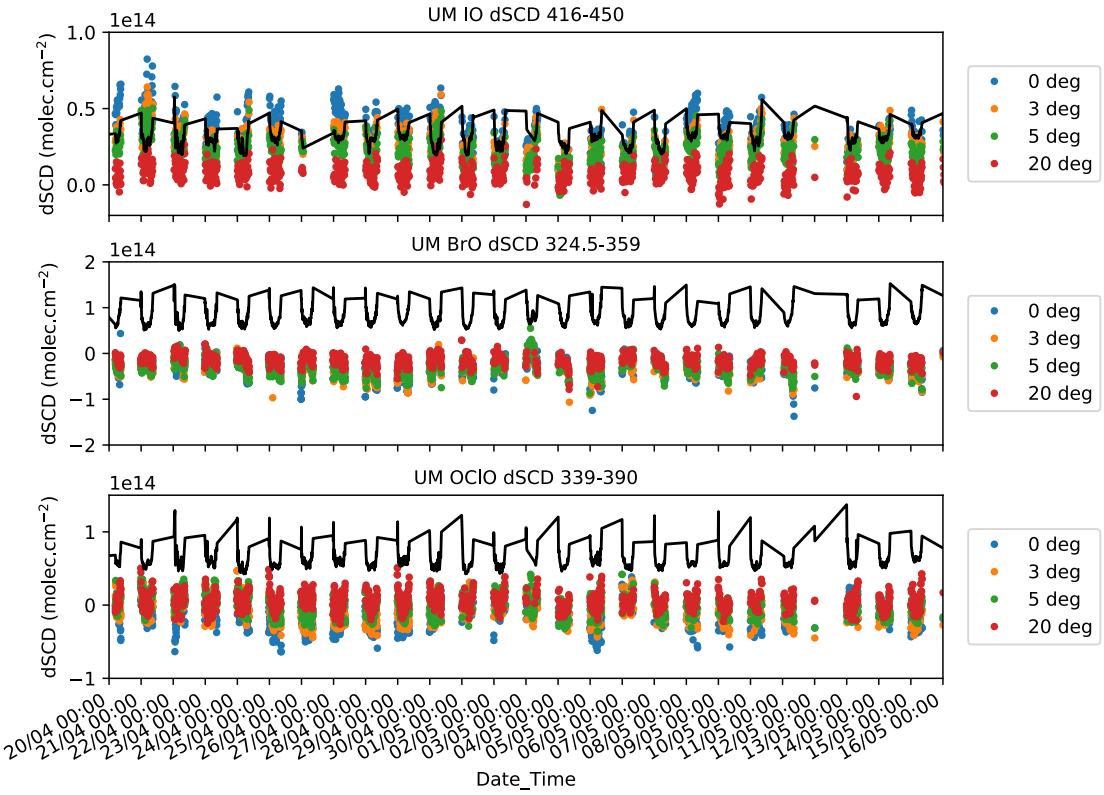

Figure 6.5: Timeseries of halogen oxide differential slant column densities for selected elevation angles, from the Garden Island campaign: top to bottom IO, BrO, OClO. The black solid line indicates the detection limit calculated using the residual RMS, for the 0° elevation angle. 'UM' denotes that the University of Melbourne MAX-DOAS was used at Garden Island.

6.2.2 Aerosol retrieval results

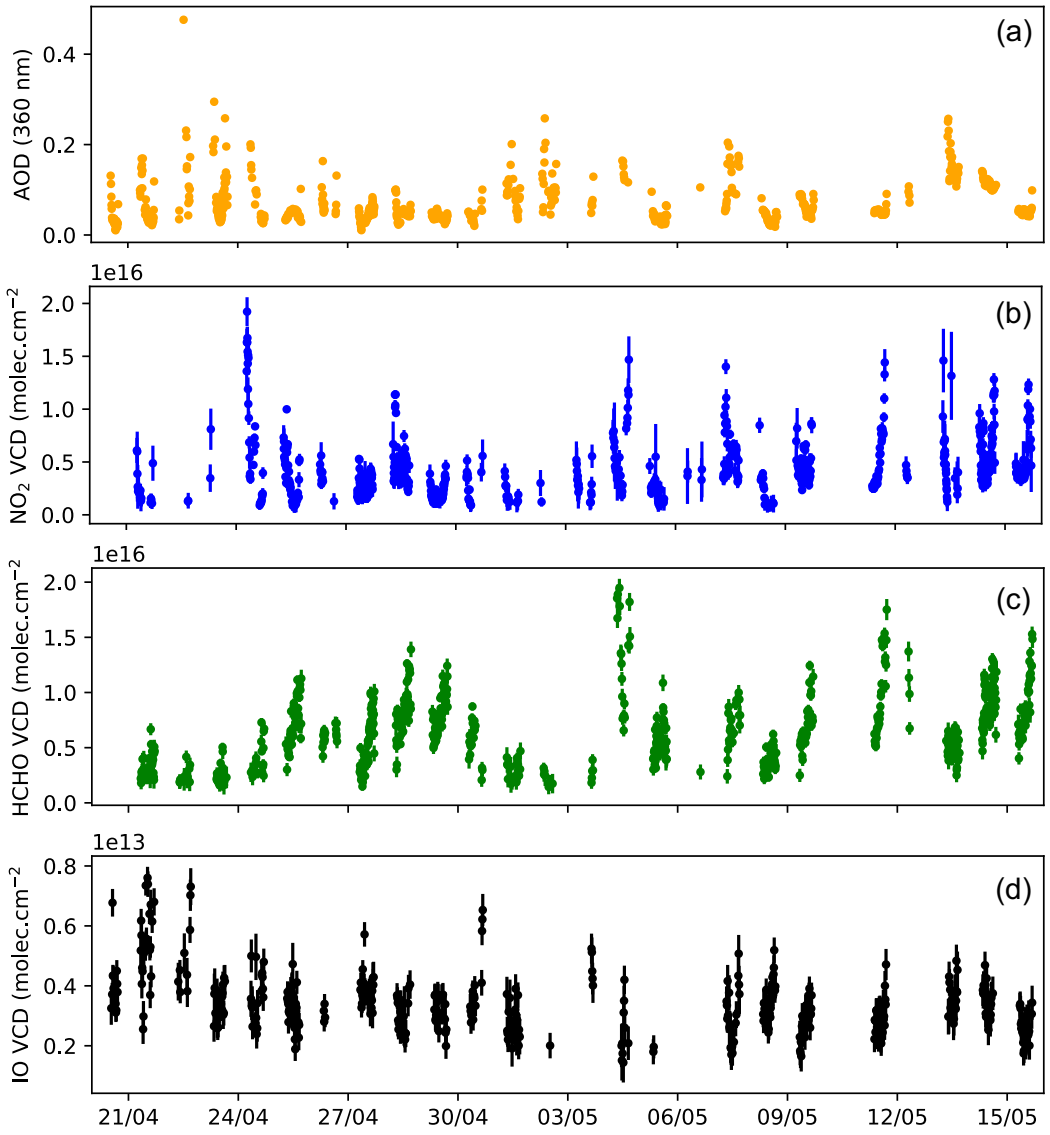

Figure 6.6: Timeseries of vertical column densities, calculated using HEIPRO from MAX-DOAS dSCDS at Garden Island, for (a) aerosols (i.e. AOD), (b) NO_2, (c) HCHO and (d) IO.

Aerosol vertical profiles and total columns (i.e. aerosol optical depth, AOD) were successfully retrieved throughout the campaign, using differential slant columns of O_4, as shown in the timeseries in figure 6.6(a). During the measurement period, considering the cloud filtered data as shown in figure 6.6, AOD ranged from 0.48-0.010, with a mean $\pm$ standard deviation of 0.070 ± 0.047. As shown in the example vertical profile heatmaps in figure 6.7, the vertical distribution of aerosol extinction at Garden Island

was variable depending on prevailing conditions. Results from 23rd of April are typical of aerosol vertical profiles with wind coming from the ocean sector, with moderate aerosol extinction up to 0.4 km^{-1}, often retrieved at altitudes between 0.5-1 km. This is considered to most likely indicate a prevalence of clouds around the horizon under these conditions (see example image illustrating the phenomenon on 1st May, since camera was not working on 23rd April). This illustrates the difficulty interpreting clouds using MAX-DOAS measurements; in cases such as 1st May and 23rd April, the cloud filtering algorithm misses these clouds because the 30° elevation angle sees blue sky while the horizon is cloudy. In future work, it would be ideal to investigate more sophisticated cloud-filtering algorithms, or make use of devices such as all-sky cameras, to either more confidently exclude or better classify results under different cloudy conditions.

Considering for example the aerosol heatmap (figure 6.7(b)) and the photo in figure 6.8 from 29th April, the aerosol retrieval returns very low aerosol extinction at all altitudes with mean airflow from the Australian continent. A particularly interesting example is highlighted in the aerosol heatmap and photo from 4th May, when a smoke plume from a nearby control burn exercise surrounded the whole Perth region including Garden Island. The aerosol heatmap captures the vertical extent of the smoke plume as it evolves with the expanding boundary layer in the early morning, before diminishing with the onset of a wind change around midday. These case studies demonstrate the ability of MAX-DOAS technique to provide vertically resolved aerosol information for the range of conditions and events experienced at Garden Island.

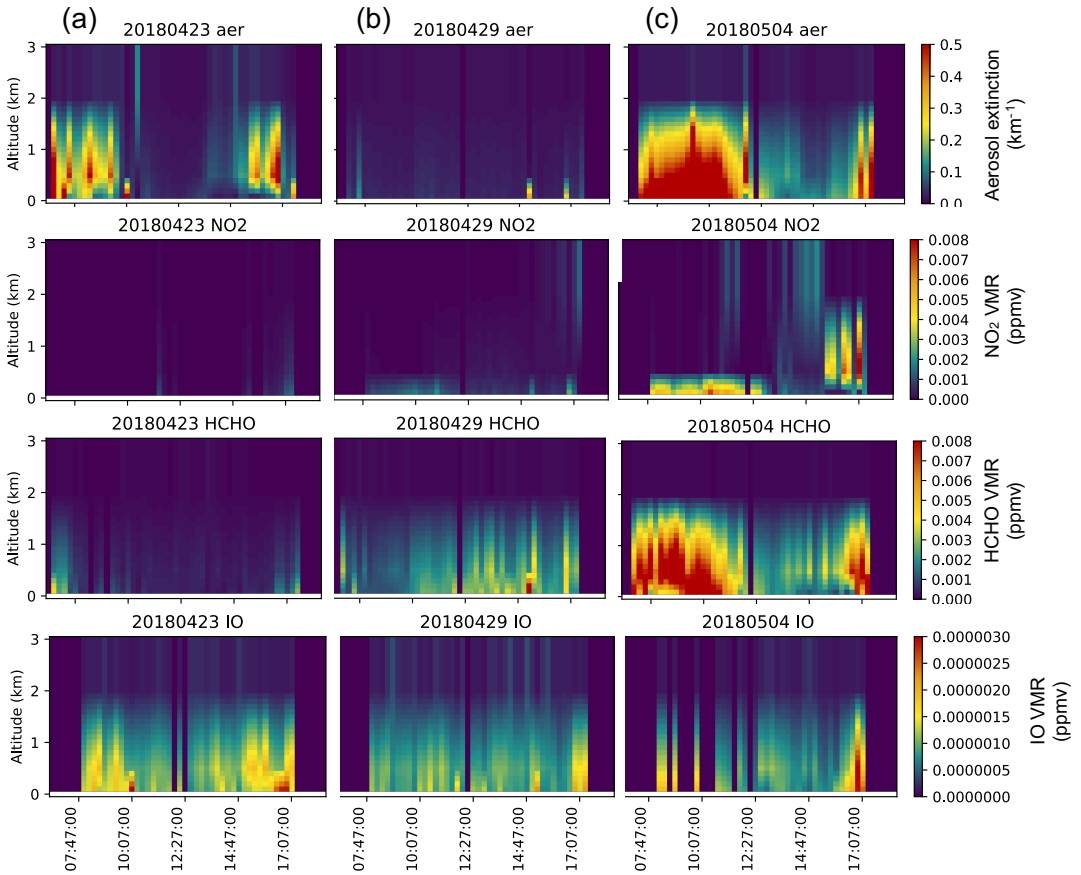

Figure 6.7: Example vertical profile heatmaps, output from HEIPRO MAX-DOAS retrievals at Garden Island, for (from top) aerosol extinction, NO_2 VMR, HCHO VMR, IO VMR. (a) results from 23rd April, a day with winds from the ocean sector, (b) 29th April, a day with winds from the land sector and (c) 4th May, a day with wind from the land sector bringing a large smoke plume over the measurement site.

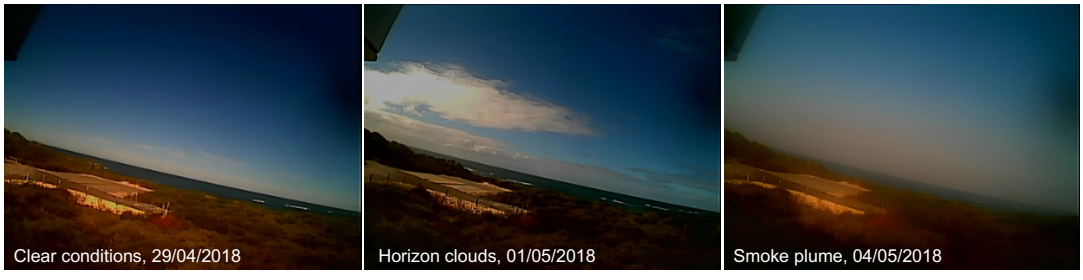

Figure 6.8: Three photos from the MAX-DOAS at Garden Island: (left) from 29th April, (b) from 1st May, (c) from 4th May.

6.2.3 NO_2 at Garden Island

NO_2 was measured using the MAX-DOAS throughout the campaign as shown in the timeseries in figure 6.6(b). VCDs ranged from 7.77×10^{14} to 1.92×10^{16} molecules.cm^{-2} with a mean $\pm$ standard deviation of $4.20 \times 10^{15} \pm 2.79 \times 10^{15}$ molecules.cm^{-2}. As illustrated in the example vertical profile heatmaps in figure 6.7 most of the NO_2 vertical column was retrieved in the lowest two retrieval levels, i.e. below 400 m altitude. The corresponding range of mixing ratios in the lowest retrieval layer was 0.14-16.34 ppb with a mean $\pm$ standard deviation of 2.26 $\pm$ 2.23 ppb. The average NO_2 concentration measured at Garden Island were much lower than at Broadmeadows at the same time of year (chapter 5) as expected given that the measurements in Melbourne were next to a strong primary NO_x source. The main source of NO_2 is broadly expected to be the urban area of Perth/Fremantle located to the north-west and west of the measurement site. In particular, large industrial sites including an oil refinery and chemical plant in Kwinana directly to the west, the port of Fremantle, and shipping around Garden Island (itself a naval base) are likely to be large NO_x sources. The polar bivariate plot in figure 6.9 clearly shows that NO_2 VMR is highest when the wind comes from the direction of these urban and industrial areas, clearly showing that Garden Island measurements are sampling the urban outflow of Perth.

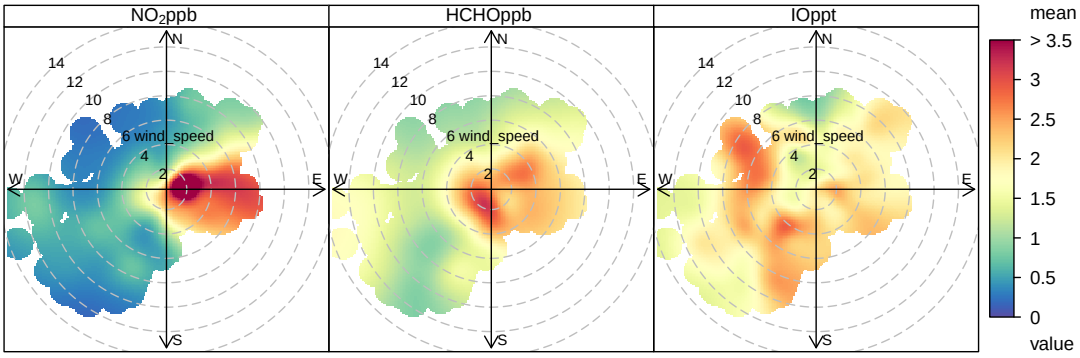

Figure 6.9: Polar bivariate plots of NO_2, HCHO and IO VMR retrieved from Garden Island MAX-DOAS data. Note that NO_2 and HCHO results are in ppb, while IO is in ppt.

Comparison of in-situ and MAX-DOAS NO_2

NO_2 was also measured using an in-situ NO_x analyser at Garden Island, providing an opportunity for a highly localised validation of the MAX-DOAS NO_2 VMR. In addition to DOAS retrieval of NO_2 in the UV region (wavelength range 338-370 nm) as discussed in chapter 2, the results from using an alternative visible wavelength range (460-490 nm, see e.g. Kreher et al. (2020)) were also tested here. Aerosol profiles using O_4 dSCDs from the same visible wavelength range were used in the visible NO2 retrievals. As shown in the scatterplot in figure 6.10, the visible and UV methods for MAX-DOAS NO_2 retrieval compare well temporally, with an R^2 correlation coefficient of 0.92, however the slope is 0.81 suggesting the visible retrieval is biased low relative to the UV retrieval. This may be due to higher residual RMS in the visible than UV region meaning that lower NO_2 slant columns are reported. The lower visible NO_2 retrieval may also relate to longer pathlengths of visible photons due to lower scattering than UV photons, although this effect should largely be accounted for by the use of aerosol profiles calculated from O_4 dSCDs in the same wavelength range. Compared to the in-situ results, each of the UV and visible MAX-DOAS retrievals have a slope of around 0.7 and R^2 correlation coefficient around 0.5. The general underestimation by the MAX-DOAS relative to the in-situ measurements is expected because it reports an average VMR across the lowest 200 m of the atmosphere, compared to a ground level observation. The importance of this effect should be enhanced by the fact that significant NO_2 appears to be transported across the water from the mainland, allowing for pollution plume evolution including mixing, sea-breeze and boundary layer dynamics. To address concerns over the low correlation coefficients, the average diurnal cycle of NO_2 over the course of the campaign from in-situ, UV and visible methods has been plotted in figure 6.10(d). Within the 95% confidence intervals, all methods observe the same average diurnal cycle of NO_2, which has a strong maximum in the early morning followed by a decrease across the course of the day. This figure suggests that the MAX-DOAS does not capture the extremes, either high or low, of daytime NO_2 VMR, and under-represents the rate of NO_2 loss throughout the day, which would result from the MAX-DOAS being more sensitive to boundary layer evolution and other mixing dynamics. It further indicates that existence of a strong diurnal cycle in surface NO_2 relative to higher levels of the boundary layer, for which the MAX-DOAS but not the in-situ instrument has sensivity.

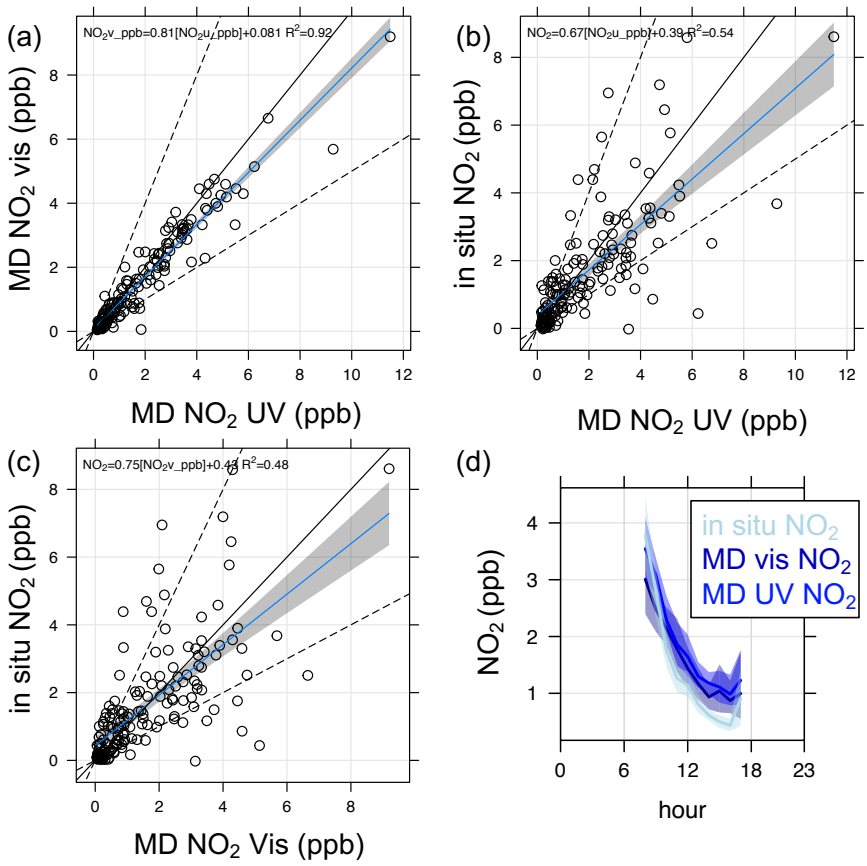

Figure 6.10: Scatterplots for NO_2 mixing ratio: (a) comparing NO_2 from UV and visible MAX-DOAS retrievals, (b) in-situ vs visible MAX-DOAS results and (c) in-situ vs UV MAX-DOAS results. (d) shows average diurnal cycles of NO_2 from in-situ, UV and visible MAX-DOAS retrievals.

Considering polar bivariate plots of concentration, windspeed and direction provides another interesting comparison between in-situ and MAX-DOAS trace gas measurements. As shown in figure 6.9, NO_2 is observed in a 'wedge' shape of wind directions between north-east to south-east. In contrast, in-situ NO_2 and NO are observed in two distinct 'lobes' of wind direction from the north east and south east (see figure C.1. The difference in polar bivariate plots is again a function of different vertical resolutions, with in-situ measurements capturing only surface NO_2 and the MAX-DOAS averaging NO_2 from 0-200 m. This implies vertical gradient of transported NO_2: the MAX-DOAS sees more from due east than the in-situ measurements suggesting this fraction has been transported aloft.

6.2.4 HCHO

The formaldehyde timeseries (figure 6.6(c)) at Garden Island shows some more striking day-to-day variation than NO_2. The range of VCDs was $1.44 \times 10^{15} - 1.95 \times 10^{16}$ molecules.cm^{-2} and a mean $\pm$ standard deviation of $6.40 \times 10^{15} \pm 3.12 \times 10^{15}$ molecules.cm^{-2}. In the 0-200 m retrieval layer, this corresponded to a mixing ratio range of 0.57-11.45 ppb with a mean $\pm$ standard deviation of 2.17 ± 1.66 ppb. Therefore the average formaldehyde levels during the Garden Island campaign were higher than at the same time of year in Melbourne. Interestingly, given that HCHO is higher at GI than Melbourne and glyoxal was below the detection limit, the glyoxal/formaldehyde ratio will be significantly lower in this location than reported in chapter 5 for Broadmeadows and perhaps closer to the ranges reported in other places around the world (see (Kaiser et al., 2015) and references therein, and discussion in chapter 5).

Biogenic isoprene and monoterpene emissions are expected to be a key formaldehyde source for Garden Island, with large tracts of forest extending southwards from Perth down to the south-west corner of Western Australia. Agricultural emissions of methane may also play a role in forming formaldehyde, and there is potential for significant anthropogenic VOC emissions from nearby industry and shipping. Biomass burning may also be a key contributor to formaldehyde in this location and at this time of year: as discussed for the Melbourne region in chapter 5, autumn is a key time for fuel reduction burning in Australia and this was occuring in the Perth region during the campaign. For example, the example vertical profile heatmap in figure 6.7(c) for 4th May shows the large plume of formaldehyde coincident with the aerosol plume when smoke shrouded the GI site. For this smokey day, the correlation between formaldehyde VCD and aerosol optical depth was examined. As discussed in Paton-Walsh et al. (2005) and Paton-Walsh et al. (2004), and observationally characterised using MAX-DOAS measurements in Melbourne (chapter 5), the correlation between these two species has been identified as an indicator of biomass burning in Australia. For the 4th of May, total least squares regression found a slope of 2.1×10^{16} and R^2 of 0.9 (see figure C.2 in Appendix C). This slope is similar to, but slightly less than, those observed in the Melbourne MAX-DOAS measurements and in Sydney and Wollongong (Paton-Walsh et al., 2004, 2005) which were between $2.5 - 3.5 \times 10^{16}$. The differences in slopes perhaps reflect differences in vegetation burning, although in each location eucalyptus trees would be expected to dominate, or could reflect differences in the age of the smoke at the measurement location. Nevertheless this is a further observational confirmation of the theory advanced by Paton-Walsh et al. (2004) that correlations between AOD and HCHO may be useful in helping to constrain VOC emissions on the basis of AOD measurements.

The polar bivariate plot for HCHO surface VMR in figure 6.9 does not present a clear picture of formaldehyde source directions. HCHO levels are lowest with strong winds from the ocean sectors and are generally higher with wind from the land sector, as expected, while strongest HCHO levels are found for very low wind speeds. There are

two possible interpretations for this observation: (a) local HCHO production which could be driven either by local VOC emissions from shipping or by local conversion of other VOCs to HCHO at this location (e.g. by NO), or (b) if the HCHO is transported it is associated with very stable weather patterns and consequent low wind speeds. The sources and implications of formaldehyde at Garden Island will be discussed in greater detail in the modelling section below.

6.2.5 Iodine monoxide

Iodine monoxide vertical columns were successfully retrieved throughout the campaign as illustrated in figure 6.6(d). IO was found to be consistently between 1.44×10^{12} and 7.60×10^{12} molecules.cm^{-2} with a mean and standard deviation of $3.37 \times 10^{12} \pm 9.87 \times 10^{11}$ molecules.cm^{-2}. The profile retrieval found a consistent vertical gradient for IO as shown in figure 6.7 with highest concentration at the surface and practically all the IO contained in the lowest 1.5 km of the atmosphere. Volume mixing ratios in the lowest retrieval layer ranged from 0.58-5.54 ppt with a mean and standard deviation of 2.03 $\pm$ 0.57 ppt. The IO measured at Garden Island therefore falls well within the range of expected marine background levels, as summarised in detail in Saiz-Lopez et al. (2012) and references therein. In particular, previous literature reports of IO mixing ratios in the Australian region include Großmann et al. (2013) who found a range of 0.72-1.5 ppt from ship-based MAX-DOAS measurements in the Western Pacific, and Allan et al. (2000) who reported IO ranging from 0-2.5 ppt at Cape Grim in Tasmania.

The key sources of IO to the atmosphere are believed to be halogenated hydrocarbons released by oceanic algae (Saiz-Lopez et al., 2012). These include compounds such as CH_3I, C_2H_5I and C_3H_7I which quickly photolyse once in the atmosphere; for example:

$$CH_3I + hv \longrightarrow CH_3 + I \qquad \{50\}$$

The liberated iodine can go on to react with ozone

$$I + O_3 \longrightarrow IO + O_2 \qquad \{51\}$$

It is believed that marine boundary layer (MBL) background concentrations around 2 ppt, as found by Großmann et al. (2013) and others, are sufficient to indicate that iodine is likely to be a major global tropospheric ozone sink. The polar bivariate plot for IO at Garden Island, shown in figure 6.9, shows some contribution to IO from all wind directions but strongest concentration with winds from the western sector, consistent with measuring a background marine source at this island location.

Significant organoiodide and IO production around exposed seaweed and sea-grasses has previously been observed in other coastal locations around the world, most notably

Mace Head in Ireland (Commane et al., 2011; Saiz-Lopez et al., 2012). In Commane et al. (2011), a strong anticorrelation between tidal height and IO was observed, as kelp beds became exposed at low tide. In that study, much higher IO mixing ratios were found, up to 49 ppt. Notwithstanding the likely differences in marine biology between Ireland and Western Australia, which were outside the scope of this study, the IO levels measured at GI are more indicative of background MBL conditions than local production. Furthermore, when Fremantle tide gauge (the closest available) values were plotted against the retrieved IO mixing ratio at Garden Island in figure 6.11, no significant (anti-)correlation was observed at the 95 % confidence level.

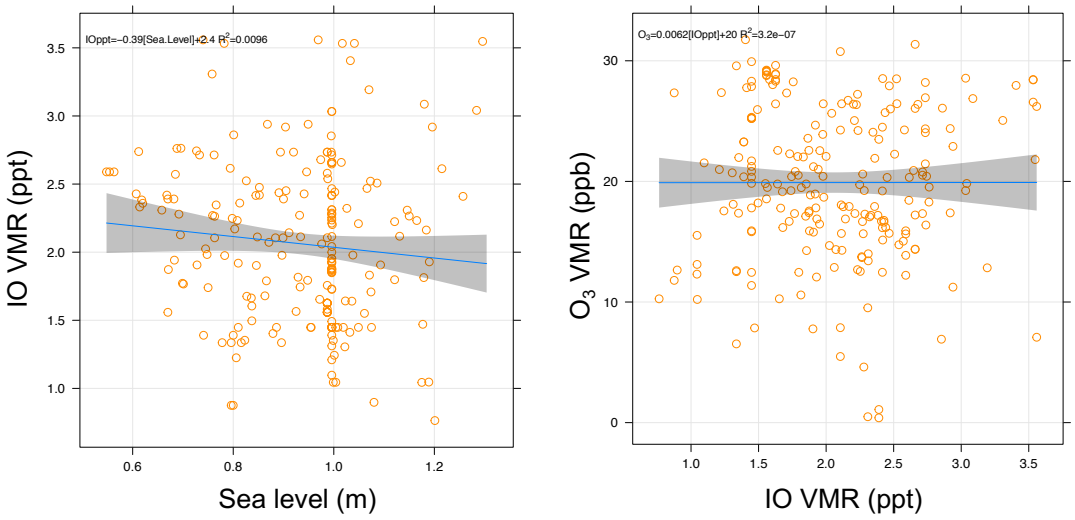

Figure 6.11: Scatterplots showing hourly averaged iodine monoxide mixing ratio vs (left) sea level at the Port of Fremantle and (right) in-situ ozone mixing ratio.

Because reactive iodine is known to deplete tropospheric ozone in the MBL and produce IO (reactions 50 and 51), we investigated whether there was a relationship between IO mixing ratio and in-situ measured ozone at GI. Anticorrelations were found for O_3 and IO in open ocean measurements by Großmann et al. (2013) and Mahajan et al. (2012). However, it is clear in figure 6.11 that there is no relationship at Garden Island between the two. Considering the polar bivariate plots of IO (figure 6.9 and in-situ O_3 (figure C.1 in Appendix C), some conditions including wind from the south, west and north-west do seem to give both high IO and low O_3, however this observation can in no way imply a causal link. Despite the lack of conclusive evidence, any influence of iodine chemistry may well be masked by ozone formation and destruction processes due to NO_x and VOCs in the urban and continental outflow. The presence of NO_x at this location may also serve to help recycle, rather than destroy, tropospheric ozone because IO reacts with NO:

$$IO + NO \longrightarrow I + NO_2 \quad \{52\}$$

Therefore reactive iodine can shift the NO/NO_2 ratio through reaction 52, with more NO_2 promoting tropospheric ozone production. In addition to influencing tropospheric ozone, reactive iodine is also thought to play a role in oxidation capacity by promoting OH formation from HO_2 radicals:

$$IO + HO_2 \longrightarrow HOI + O_2 \quad \{53\}$$

$$HOI + hv \longrightarrow OH + I \quad \{54\}$$

Because IO shifts the balance of the HO_x cycle through reactions 53 and 52, rather than being a primary HO_x producer, it is difficult to calculate its influence without measured HO_2 concentrations.

6.3 Lagrangian chemistry-trajectory modelling

The aim of a Lagrangian photochemical model is to evolve atmospheric composition in an air parcel along a precalculated meteorological trajectory. Therefore such models are an intermediary between stationary box models and fully-resolved chemical transport models. The main advantage of using a Lagrangian chemistry-trajectory approach is that it allows for more thorough treatment of advection, spatial emissions variation and meteorology than a box model, while being computationally much more straightforward than a full chemical transport model. Disadvantages of this approach include that mixing must be parameterised because turbulence within and surface stretching/folding of the air parcel cannot be well resolved by considering an 'isolated' box.

6.3.1 Introduction to CiTTyCAT

The Lagrangian chemistry-trajectory model chosen to aid interpretation of the GI observations was the Cambridge Tropospheric Trajectory model of Chemistry And Transport, known as CiTTyCAT (Pugh et al., 2012). CiTTyCAT has been used to study a wide variety of atmospheric chemistry problems including trace gas lifetimes, tropospheric ozone formation and secondary particle formation; see Pugh et al. (2012) and references therein for details of the model design and particular modelling experiments.

The key elements of the CiTTyCAT model are shown in the schematic in figure 6.12.

6.3.2 WRF-Chem modelling

Modelling of the entire Garden Island campaign period was undertaken using the Weather Research and Forecasting model, coupled with chemistry (WRF-Chem) by

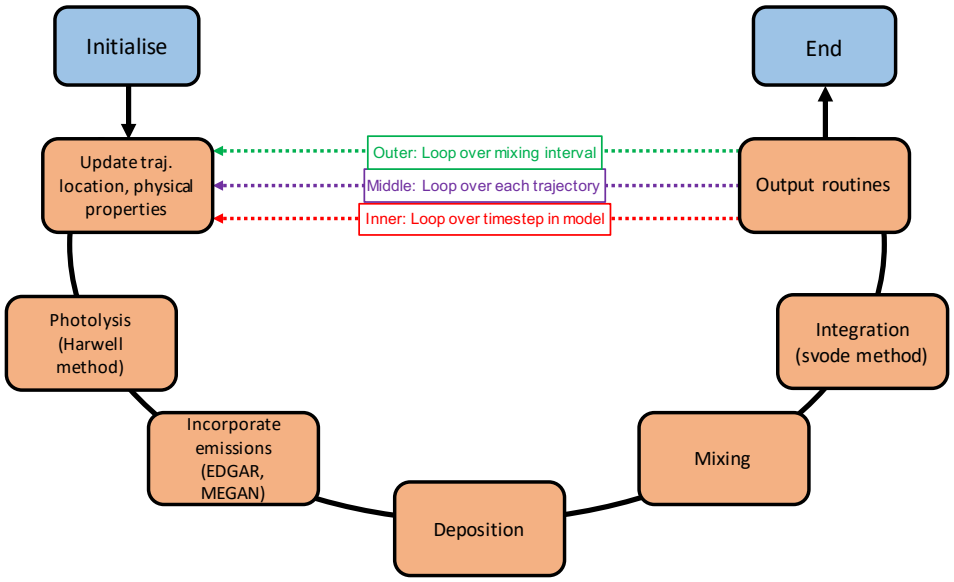

Figure 6.12: Schematic of the CiTTyCAT model showing the key elements and loops. Figure adapted from Pugh et al. (2012).

Dr Steve Utembe (Utembe, 2019). WRF-Chem is a popular regional-scale atmospheric chemical transport model (CTM) that is widely used for atmospheric research with a wide choice of chemical and physical parameterisations available. Version 3.9.1 was used in this study. The Lambert conformal projection was used to map the model grid to Earth's surface in a three nested configuration set-up with outermost to innermost domains at horizontal resolutions of 27, 9, and 3km, respectively.

Meteorological fields, initial and lateral boundary conditions were taken from Australia Bureau of Meteorology's ACCESS-R re-analyses. The meteorological output from WRF was used as the input for calculating back trajectories to be used in CiTTyCAT.

6.3.3 HYSPLIT back trajectories

Back trajectory analysis allows a fictitious 'air parcel' to be traced backwards in time using gridded meteorological data. These trajectories allow a more detailed analysis of the airmass characteristics associated with specific aerosol or chemistry events, beyond simply the in-situ wind speed and direction. For the Garden Island campaign, the input gridded meteorology was supplied by the WRF model. Trajectories were run 5 days back in time, starting every hour from the AIRBOX location. Example trajectories are shown in figure 6.13, chosen from periods representative of the two dominant wind sectors highlighted in figure 6.3. In these examples, the oceanic and terrestrial sectors indicated by the in-situ wind direction are confirmed by the five-day back trajectory.

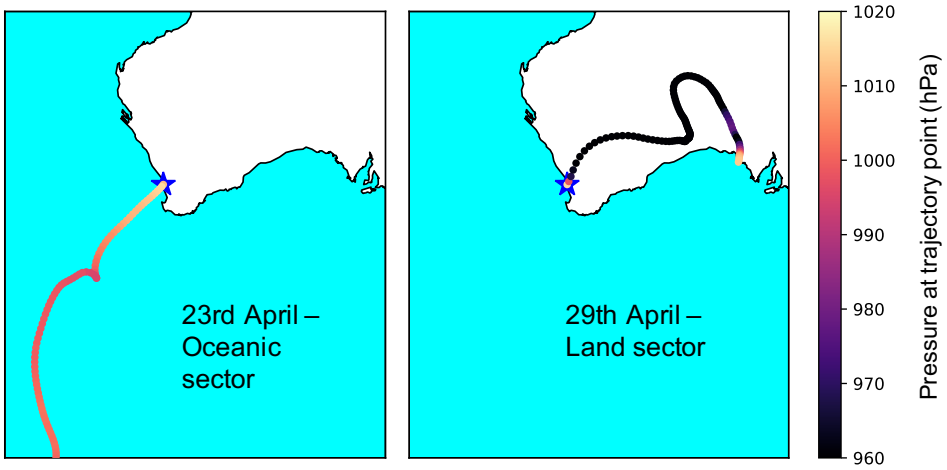

Figure 6.13: Two example trajectories, run 5 days back from Garden Island using the HYSPLIT model, initiated with meteorological data from the WRF model and used in turn for the CiTTyCAT modelling study.

6.3.4 Comparison between observations and CiTTyCAT

Firstly, in order to assess the ability of CiTTyCAT to accurately model the atmospheric chemistry at Garden Island, trajectory endpoint trace gas mixing ratios were compared with observations as shown in figure 6.14. The observations shown here are in-situ ozone and NO_2 along with MAX-DOAS formaldehyde. Measurements up to the 3rd of May are shown because several days thereafter were impacted by bushfire smoke which could not be captured by CiTTyCAT. It is apparent in figure 6.14(a) that the diurnal cycle for ozone is generally well reproduced by CiTTyCAT with maximum values overnight and minimum values in the middle of the day due to strong daytime photolysis. However the modelled O_3 is consistently higher than the observations; average modelled O_3 across the plotted period was 34.7 ppb compared to 23.7 ppb for measurements. The difference is most pronounced in the middle of the day suggesting that there is a missing daytime O_3 sink in the model. Several sensitivity tests were trialled to identify a reason for the discrepancy including increasing dry deposition, increasing actinic flux, reducing aerosol optical depth, increasing NO_x emissions and setting the model initial ozone concentration to zero. Doubling the actinic flux and doubling NO_x emissions were the only tests to produce a noticeable decrease in daytime modelled O_3 (see figure X in Appendix C) and even these did not explain the discrepancy with observations.

It is possible that iodine chemistry may help explain the difference between observed and modelled ozone. Although no clear trend linking ozone to iodine monoxide was observed in figure 6.11, this need not exclude the possibility of iodine playing an important role alongside NO_x and VOCs in determining ozone budgets. In future work it would be very interesting to add an estimate of oceanic iodine emissions to CiTTyCAT to see if this might help explain the apparent missing daytime O_3 sink.

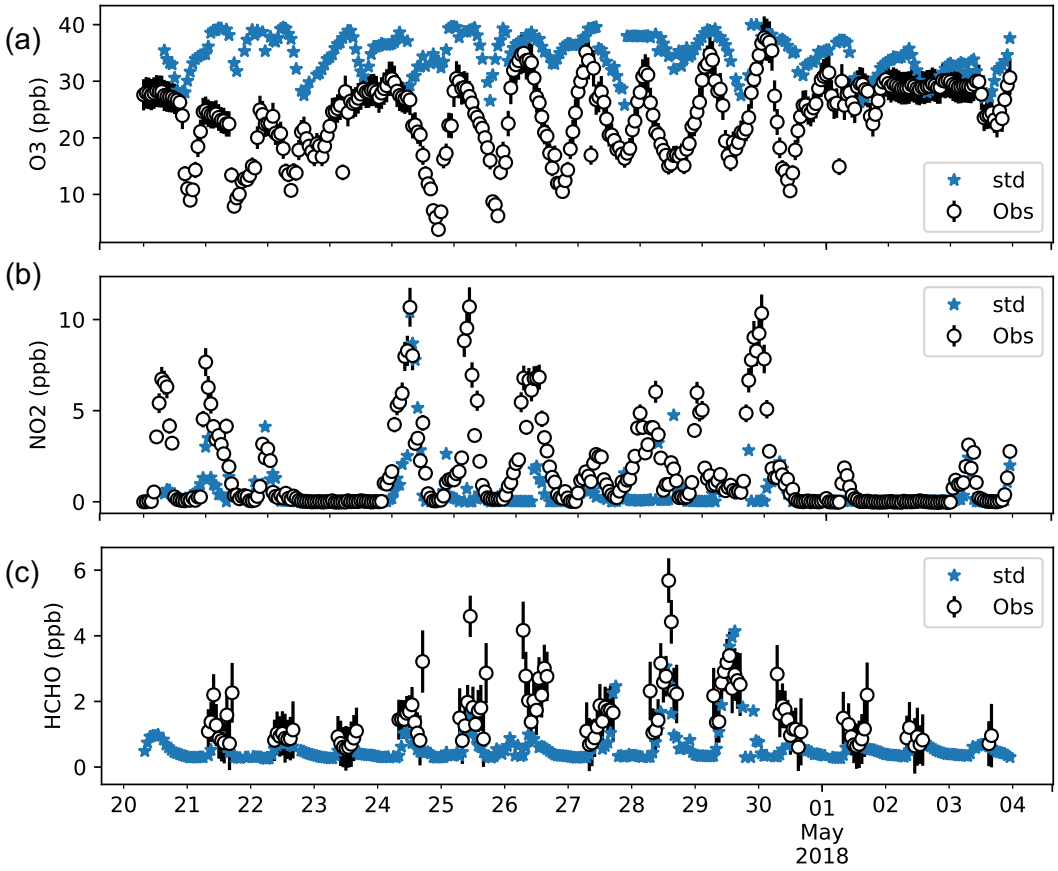

Figure 6.14: Timeseries comparison of Garden Island trace gas observations with CiTTyCAT (standard settings) output. In (a) the observations are in-situ ozone mixing ratio, (b) in-situ NO_2 and (c) MAX-DOAS lowest-layer retrieved formaldehyde mixing ratio.

In figure 6.14(b), NO_2 modelled and in-situ observations are shown. Some daytime measured spikes are captured by the model such as on 21st and 24th April, some are partially captured such as on 26th, and some like the 25th are not captured at all. The overall average of modelled NO_2 is less than a third of the observations, 0.49 ppb compared to 1.60 ppb. It is a similar story for NO, with an observational average of 0.25 ppb compared to modelled average of 0.11 ppb. This hit-and-miss outcome for NO_x likely highlights a key model limitation in that emissions come from the EDGAR emissions grid as a trajectory passes over regardless of, and unmodulated by, any diurnal emissions pattern. This will make it difficult to capture the timing of NO_x concentration maxima when trajectories pass over the urban area of Perth. In addition, the proximity of the GI site to shipping lanes makes it highly likely that some peak NO_x events are caused by ships which would be completely missed by CiTTyCAT. In the observations, largest peaks in NO_2 correspond temporally with largest dips in O_3 suggesting that while a doubling of NO_x emissions did not address the modelled ozone shortfall, missed or mistimed NO_x-titration events may hold the key to capturing the magnitude of the

ozone variation.

Of the model-measurement comparisons, formaldehyde seems to be the best as seen in figure 6.14(c). Both the magnitude and diurnal pattern of HCHO are well represented by CiTTyCAT on several days including 24th, 27th, 28th and 29th of April, all days on which trajectories were predominantly from the land sector. An average across the plotted period suggests the MAX-DOAS observations were double the CiTTyCAT values, 1.59 ppb compared to 0.79 ppb. Note however that this difference actually falls within the average uncertainty on the HCHO lowest layer mixing ratio from the HEIPRO retrieval of 0.69 ppb. HCHO is expected to stem mostly from oxidation of biogenic VOCs (when trajectories have passed over land) and, unlike NO_x and anthropogenic VOCs there is a temporal variation in CiTTyCAT for biogenic VOCs through temperature dependence of emissions in MEGAN. Therefore it makes sense that the formaldehyde comparison is the most successful in reproducing the diurnal cycle, and gives some confidence in using this model for further understanding the role of biogenic VOCs on oxidation chemistry at the Garden Island site.

On days with winds coming from the ocean sector, HCHO is observed higher than models especially in the early mornings (see for example 21-23 April and 1-2 May). The polar bivariate plot in figure 6.9 indicates background MBL mixing ratios between 0.5-1 ppb, consistent with previous studies in various places around the world (e.g. Ayers et al. (1997), Vigouroux et al. (2009), Mahajan et al. (2010), Peters et al. (2012)). Mahajan et al. (2010) found that formaldehyde observations at Cape Verde, which ranged from 350 to 550 ppt, were reproduced by a photochemical box model primarily considering methane and non-methane hydrocarbon oxidation. The non-methane VOC precursors were hypothesised to be long-lived anthropogenic emissions from Europe or North America. Such anthropogenic contributions are unlikely for the marine trajectories at Garden Island (see figure 6.13 for example) given the much lower land and population density of this part of the world compared to the Northern Hemisphere. Therefore background MBL formaldehyde mixing ratios up to 1 ppb at GI may indicate marine HCHO sources not accounted for in CiTTyCAT. These could include diesel VOC emissions from shipping in the area, or isoprene which is known to have marine biogenic emission sources (see Shaw et al. (2010) and references therein).

6.3.5 Sensitivity studies in CiTTyCAT

Emissions from EDGAR and MEGAN are the primary drivers of chemistry in CiTTyCAT so some sensitivity studies were undertaken to ascertain that the model responded as expected to varying emissions. The tests are listed in table 6.1 and are briefly described here: anthropogenic VOC emissions in EDGAR turned off ('ax0') and doubled ('ax2'), NO_x emissions in EDGAR turned off ('nx0') and doubled ('nx2') and the same for isoprene and monoterpene emissions in MEGAN ('ix0', 'ix2', 'mx0' and 'mx2' respectively). Because these emissions stem only from the land, the period considered for the tests was 24-29 April when trajectories predominantly came from the land sector.

Figure 6.15 shows the results of each test compared to the standard scenario in which emissions were unchanged. Altering NO_x emissions was the biggest influence on NO_2 levels as expected. While the mean NO_2 level fell and rose when emissions were cut and doubled respectively, in the case of doubling the result was highly variable as indicated by the huge (one standard deviation) errorbar. Clearly doubling the amount of NO_x while keeping VOCs the same is a non-linear process which does not simply result in double the concentration of NO_2.

Test label	Test details
std	standard CiTTyCAT settings
ax0	Anthropogenic VOCs $\times 0$
ax2	Anthropogenic VOCs $\times 2$
mx0	Monoterpene emissions $\times 0$
mx2	Monoterpene emissions $\times 2$
ix0	Isoprene emissions $\times 0$
ix2	Isoprene emissions $\times 2$
nx0	NO_x emissions $\times 0$
nx2	NO_x emissions $\times 2$
sfx2	Solar flux $\times 2$
aert1	Aerosol profile $\times 0.1$ at all altitudes
icO30	O_3 initial conc. $= 0$
ddep1	O_3 dry deposition $\times 2$

Table 6.1: Details and labels of the CiTTyCAT sensitivity studies.

The highly variable NO_x response may be due to the importance of isoprene-driven chemistry at this location. This is highlighted by the fact that adjusting isoprene emissions was the the largest influence on OH radicals and formaldehyde, and the second largest influence after NO_x emissions on ozone. Changes in monoterpene and anthropogenic VOC emissions had very little influence on modelled HCHO, ozone or OH concentration. Therefore on the evidence of these sensitivity tests, CiTTyCAT predicts isoprene to be the dominant driver of VOC chemistry in the Western Australian region.

In figure 6.16 the sensitivity study results have also been compared to observations to ascertain if emissions may help explain model-measurement discrepancies. As discussed above, ozone was modelled much too high and none of the emission sensitivity tests made a significant impact. In the case of NO_x, doubling emissions resulted in modelled NO_2 that much more closely matched measurements, however at the same time this caused significant overestimation of NO. Altering anthropogenic VOCs and monoterpene emissions caused no change in the model-measurement comparison for any species. The most notable result was that doubling isoprene emissions resulted in

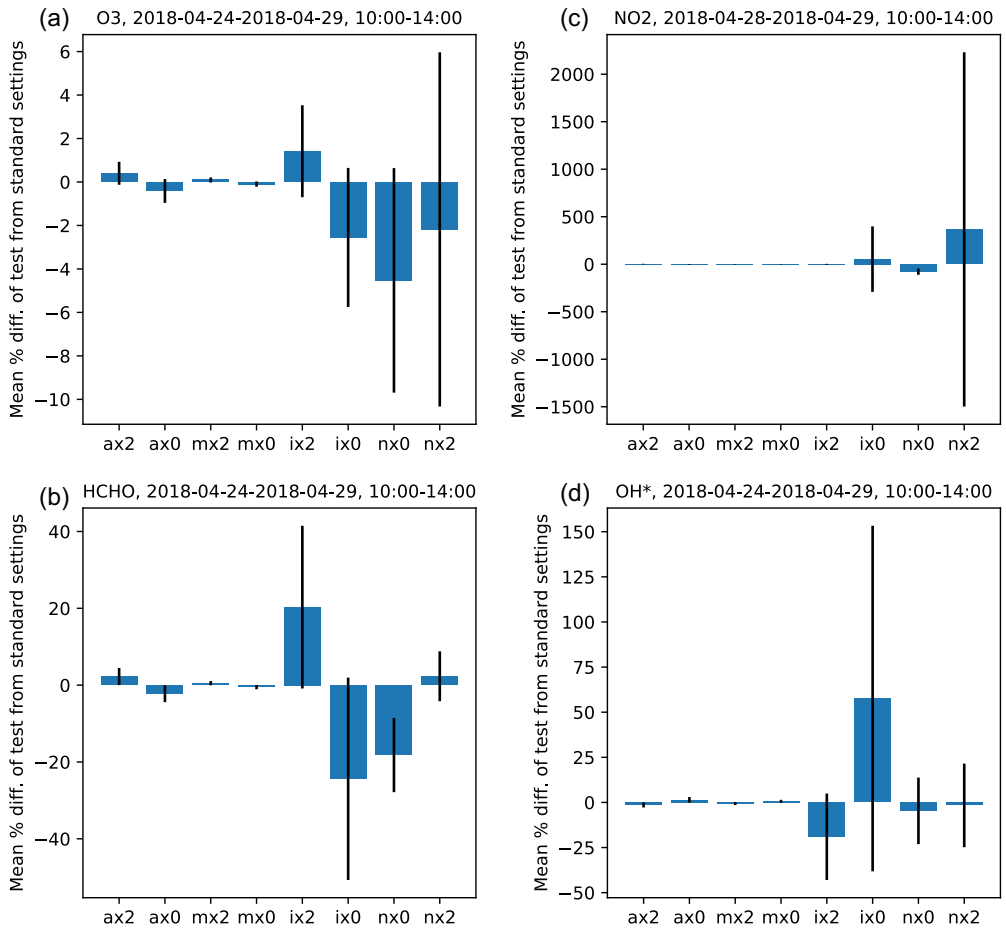

Figure 6.15: Bar charts showing results of CiTTyCAT sensitivity studies where the effect of each test is expressed as an average percentage difference to 'cc1', the standard model run scenario. Errorbars represent the standard deviation. Test details are outlined in table 6.1. (a) shows ozone, (b) HCHO, (c) NO_2 and (d) OH.

an increase in HCHO; in the standard scenario formaldehyde was modelled about 40% lower than observations, and doubling isoprene emissions led on average to modelled HCHO doubling and therefore being 20% lower than the MAX-DOAS measurements. This suggests that MEGAN may be underestimating isoprene emissions from Western Australian forests.

6.4 Discussion

6.4.1 Importance of isoprene in oxidation chemistry

It is clear from the sensitivity study bar charts presented in figure 6.15 that isoprene chemistry is expected to play a key role in oxidation chemistry in this region. In

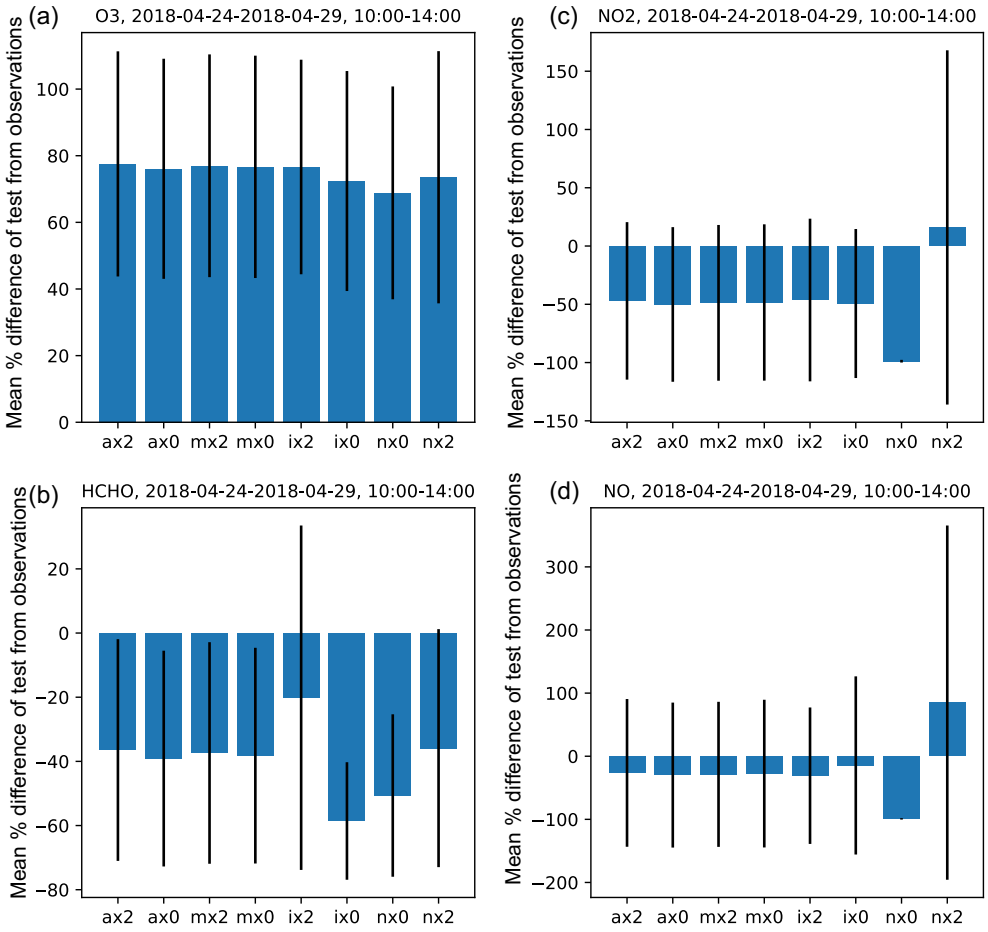

Figure 6.16: Bar charts showing results of CiTTyCAT sensitivity studies where the effect of each test is expressed as an average percentage difference to observations. Errorbars represent the standard deviation. Test details are outlined in table 6.1. (a) shows ozone, (b) HCHO, (c) NO_2 and (d) NO.

particular, altering isoprene emissions cause the largest changes in formaldehyde and OH levels. The primary importance of isoprene in producing formaldehyde fits with the discussion of formaldehyde observed with MAX-DOAS measurements in Melbourne (chapter 5). It is also in line with the finding of the global modelling study by Pfister et al. (2008) that isoprene represents by far the most significant source of formaldehyde across Australia.

To illustrate the importance of isoprene emissions from Australia's eucalyptus forests more broadly, trace gas mixing ratios along one example trajectory have been plotted in figure 6.17. This trajectory travelled from the Nullabor region of South Australia across Western Australia over the course of the five day trajectory, as depicted in figure 6.13. Emissions sensitivity tests are shown for the emissions turned-off case, to highlight the primary influence on each gas concentration. As the 'air parcel' travels across the

arid, sparsely vegetated and even more sparsely populated interior of the continent, emissions of precursors are practically zero and hence none of the emissions tests make any difference to mixing ratios. As the trajectory approaches the west of Western Australia in the last two days however, it passes over vegetation and the influence of isoprene chemistry in the model is clearly seen. As anticipated, removing isoprene reduces HCHO to the same levels as when the trajectory was passing over arid areas, and background methane oxidation is the primary HCHO precursor. Strikingly, only when isoprene emissions are turned off are significantly higher OH levels seen, implying that isoprene and its secondary products collectively represent the largest OH sink. In fact, summing over all OH loss processes along this trajectory showed that 99 % of OH loss events were due to isoprene and its secondary oxidation products, far eclipsing reactions with CO, CH_4 and monoterpenes.

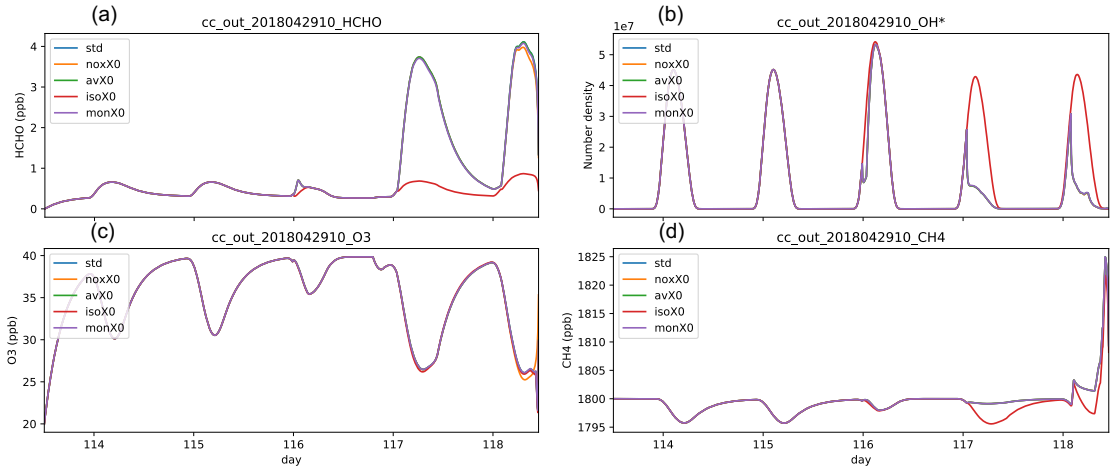

Figure 6.17: Timeseries of CiTTyCAT modelled mixing ratios along one example trajectory which arrived at Garden Island on 29th April (and is depicted in figure 6.13. (a) shows HCHO, (b) OH, (c) O_3 and (d) CH_4. In each case the plots show the results of sensitivity studies in which NO_x, anthropogenic VOC, isoprene and monoterpene emissions were successively turned off.

In a trajectory such as this, the isoprene degradation mechanism driven by OH oxidation will be responsible for delivery of large amounts of many secondary VOCs from rural areas to the Perth urban region. Such high biogenic VOC levels help promote NO_x limited ozone production conditions in Australian cities as found in chapter 5 for Melbourne and for Sydney in Utembe et al. (2018). For periods in which the wind came from the land sector, except for low windspeeds directly from the urban area, the MAX-DOAS determined $HCHO/NO_2$ ratio indicated that ozone production conditions were also predominantly NO_x limited at Garden Island (see figure C.3 in Appendix C). While no high episodes of poor ozone air quality were recorded during this campaign, it is anticipated that on hot summer days NO_x-limited pollution events similar to Melbourne and Sydney are possible.

In addition to implying ozone production potential, the importance of isoprene chemistry highlighted by this model study has climate implications. This is because OH is the primary oxidant for methane, an important greenhouse gas. As shown in figure 6.17 when isoprene emissions are turned off and OH stays high in the middle of the day, CH_4 mixing ratios decrease. Because biogenic isporene emissions depend on temperature (see e.g. Guenther et al. (2012)) it is plausible that isoprene emissions may be expected to increase in a warming world, which would divert OH away from reaction with methane, representing a potential global warming feedback. This further serves to highlight the importance of biogenic VOCs in the isoprene-hotspot that is Australia.

6.4.2 Modelled OH production

Because CiTTyCAT typically has the ozone mixing ratio too high compared to observations (a) it is difficult to believe the magnitude of the ozone mediated OH production from ozone and (b) that contribution swamps all other OH production mechanisms. However, a deeper look reveals an important contribution to OH production in CiTTyCAT from nitrogen oxides and VOCs. In chapter 5, concentrations of HONO and HCHO were found to be higher than at Garden Island and sufficient to eclipse ozone photolysis in OH production. For Broadmeadows in April, midday HO_x production was on average around 2×10^6 $cm^{-3}.s^{-1}$ due to each of formaldehyde and ozone, overshadowed by HONO photolysis at around 6×10^6 $cm^{-3}.s^{-1}$. In the CiTTyCAT simulations, as shown along an example trajectory in figure 6.18, the HO_x production due to NO_x and VOCs has been combined. Contributions from NO_x, primarily HONO photolysis, reach up to 2×10^5 $cm^{-3}.s^{-1}$ while the contributions from VOCs, including HCHO photolysis are at most half of this. Therefore, the currently available emissions for Western Australia imply primary OH production from VOCs and NO_x an order of magnitude less than observed in Melbourne. Because ozone is overestimated and because HONO was predominantly below the MAX-DOAS detection limit, it is difficult to validate the accuracy of these OH production simulations, however, this could be achieved in future work for both the Garden Island and Melbourne campaigns with appropriate emission inventories.

6.4.3 Iodine chemistry and OH

As highlighted in reactions 53 and 54, the presence of IO indicates a reactive halogen mediated OH source. The OH production is through photolysis of HOI which, as reaction 53 details can be formed by reaction of IO and HO_2 and is considered to be a key reservoir iodine species. HOI also forms through reaction of I^- and ozone at, and direct emission from, the ocean surface (Carpenter et al., 2013). A simple estimation of the OH production potential from iodine comes from assuming a HOI concentration equal to the campaign average IO mixing ratio of around 2 ppt. Assuming HOI to be of similar concentration as IO is reasonable given the background marine boundary

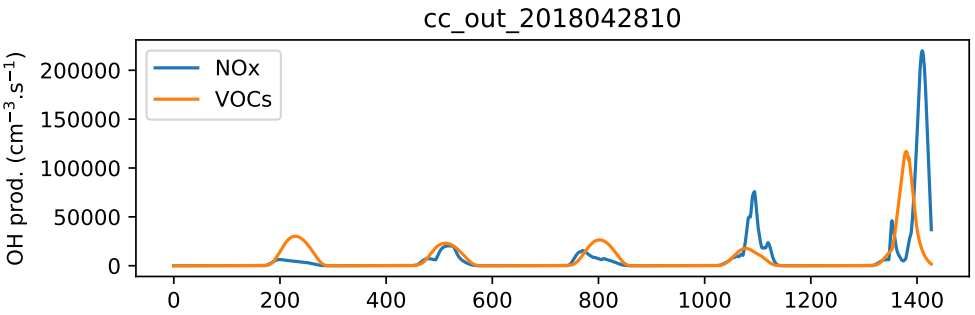

Figure 6.18: Timeseries of CiTTyCAT modelled hydroxyl radical production rate along one example trajectory (arriving GI 28th April, 10:00 UTC), stemming from NO_x (primarily HONO) and VOCs (biogenic and anthropogenic contributions combined).

layer iodine chemistry simulations of Vogt et al. (1999) found HOI to be the dominant daytime inorganic form of atmospheric iodine. Using the TUV model as described previously in chapter 5, the HOI photolysis rate J(HOI) was calculated to be 6.8×10^{-3} s^{-1} at solar zenith angle 33 as was the case at midday in the middle of the GI campaign. The OH production is given by:

$$P(\mathrm{OH})_{\mathrm{HOI}} = J(\mathrm{HOI}) \times [\mathrm{HOI}] \tag{6.1}$$

which equates to 1.4×10^{-2} ppt.s^{-1} or approximately 3.3×10^{5} cm^{-3}.s^{-1}. This is two orders of magnitude lower than the OH production rates discussed at Broadmeadows in chapter 5 and at GI in the previous section from VOCs and NO_x , however, potentially an important OH source in their absence in the remote marine boundary layer.

6.4.4 A note on glyoxal

As discussed above, unfortunately residual RMS values in the visible spectral fitting windows were too high for confident retrieval of glyoxal slant columns. Interestingly, using the CiTTyCAT configuration described, glyoxal was predicted to be present in appreciable quantities on several days of the campaign as shown in figure 6.19(a). At Broadmeadows, glyoxal was consistently retrieved above 1×10^{14} molecules.cm^{-2} ($\approx$ 0.05 ppb). CiTTyCAT modelled glyoxal above 0.05 ppb between 24-30 April suggesting that given the current state of knowledge of emissions, it should have been detectable by the MAX-DOAS at Garden Island.

One possible reason for the non-detection of glyoxal could be that a strong sink exists. The lack of glyoxal detection at all hours of the day (i.e. all solar zenith angles and light conditions) makes it unlikely that a particularly strong photolytic or OH reaction sink could be responsible. Instead, the formation of secondary organic aerosol (SOA) from glyoxal reactions or heterogeneous uptake may play a role as was found for example in

Mexico City by Volkamer et al. (2007). This is a particularly interesting proposition given the coastal location of Garden Island and the "salting-in" effect which enhances uptake of glyoxal on aqueous aerosols under slightly saline conditions (Kurtén et al., 2015). Understanding the potential for SOA formation to explain the lack of glyoxal here, through modelling of SOA and salting-in and/or a measurement technique with a lower glyoxal detection limit, would make for very interesting future work.

Figure 6.19(b) shows that the expected glyoxal-formaldehyde ratio (R_{gf}) ranged from $\approx 10^{-5}$ when winds came from the ocean (e.g. 22-23 April) to between 0.05-0.10 with winds coming from the land. Using the sensitivity studies, in figures 6.19(b) and (c) it is clear that in CiTTyCAT, anthropogenic VOC emissions are the main influence on glyoxal mixing ratios and therefore the R_{gf}. The importance of anthropogenic emissions on R_{gf} fits with the observations and discussion in Chapter 5.

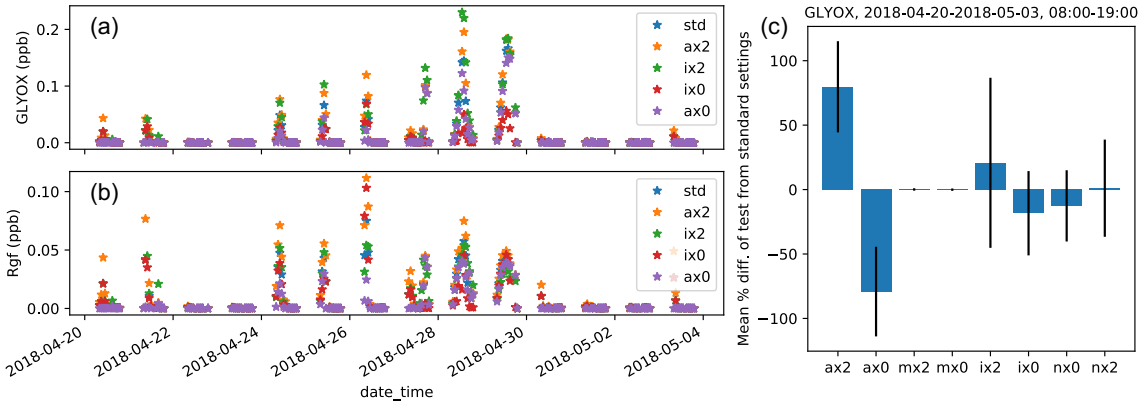

Figure 6.19: (a) Timeseries of CiTTyCAT modelled glyoxal mixing ratios at the Garden Island site for the first part of the campaign, plotted for a range of sensitivity tests. (b) Timeseries over the same period of the modelled ratio between glyoxal and formaldehyde (R_fn) mixing ratios. (c) Bar chart showing the influence of sensitivity tests on glyoxal mixing ratio. Test details are outlined in table 6.1.

6.5 Garden Island summary and future work

The 2018 AIRBOX campaign at Garden Island is a rich dataset of atmospheric aerosol and chemistry information. In this chapter, the MAX-DOAS results have been presented from that campaign and placed in the context of influence on oxidation chemistry alongside Lagrangian chemistry-trajectory modelling.

Formaldehyde, nitrogen dioxide and iodine monoxide were measured using the MAX-DOAS at Garden Island. HCHO and NO_2 concentrations were higher in airmasses originating from the land and urban/industrial directions as expected, and in combination suggested ozone production conditions in this region would mostly be NO_x limited as found previously in Melbourne. Bushfire smoke from controlled burnoffs was

observed clearly in the MAX-DOAS vertical profiles of HCHO and AOD, and, also consistent with results in Melbourne, a strong correlation between HCHO column and AOD was observed. IO showed no distinct variation with windspeed and direction, and no (anti-)correlation with in-situ O_3, rather suggesting the presence of a uniform background marine boundary layer iodine cycle.

Meteorological back trajectories were computed using the HYSPLIT model, run over high resolution meteorological output from WRF, and these were used in turn to initiate Lagrangian chemistry-trajectory modelling using CiTTyCAT for the first time in Australia. The modelling study highlighted that the NO_x emissions currently available for Western Australia through EDGAR are insufficient to reproduce the observed NO_2 and NO at this location. This likely hinders the ability to model ozone concentrations, which were consistently higher than observations in this study. Despite this, CiTTyCAT had some success modelling formaldehyde mixing ratios. The model study suggests that HCHO levels at this location depend almost entirely on isoprene emissions, secondarily on methane and secondary VOC oxidation and hardly at all on monoterpene emissions. The emissions sensitivity studies in CiTTyCAT also demonstrated the importance of isoprene emissions as an OH radical sink, therefore influencing oxidation capacity and enhancing methane lifetimes. The potential for primary OH production by iodine (specifically HOI), implied by the presence of IO at Garden Island, was briefly discussed. While it was found that OH production due to HOI is likely two orders of magnitude less than from NO_x and VOC cycles, and therefore insignificant at this location, it may be an important factor in the global remote marine boundary layer if such IO levels are ubiquitous.

The short but rich Garden Island dataset, and the modelling study presented here, provide fertile ground for future work. The observation of iodine monoxide and underrepresentation of ozone in CiTTyCAT raises the question of whether iodine chemistry may be an important O_3 sink in this location: adding an iodine emissions estimate to CiTTyCAT would be an interesting way to study this. It would also be good in future work to re-run these simulations with an updated Western Australian anthropogenic emissions inventory to see if this satisfactorily resolves the underestimation of NO_x and overestimation of ozone. The CiTTyCAT model shows promise for addressing questions relating to the glyoxal-formaldehyde ratio, under current literature discussion, in particular the competing role of anthropogenic and biogenic VOCs. This work shows that, despite the limitations, combining MAX-DOAS observations with chemistry-trajectory modelling has great potential to inform our understanding of oxidation chemistry in these unique Australian environments. Therefore it would be ideal to expand this work in future studies, running CiTTyCAT in other Australian locations, to test our mechanistic understanding of the NO_x and VOC chemistry underpinning OH and O_3 production.

Chapter 7

Comparison and validation of formaldehyde columns

In the previous chapters, the MAX-DOAS technique has demonstrated utility providing ground-based data to inform understanding of Australian oxidation chemistry. In recent years, advances in remote sensing and satellite technology have brought space-based observations to the forefront of atmospheric science. Compared to in-situ or ground-based remote sensing methods, space-based instrumentation can provide the global coverage required by climate and chemical transport models. Satellite-borne instruments for measuring trace gases such as nitrogen dioxide and formaldehyde use the same DOAS principles as described for MAX-DOAS, albeit using an entirely different viewing geometry. Because satellite DOAS measures scattered light which has undergone two transects of the Earth's atmosphere, the radiative transfer calculations are more complicated and the sensitivity at different altitudes is different to MAX-DOAS. MAX-DOAS measurements are most sensitive in the boundary layer, which, because of emission from the Earth's surface, is typically the region of highest trace gas concentrations. Therefore, in addition to measurements in its own right, MAX-DOAS can play an important role in understanding atmospheric composition through validation of for satellite trace gas results.

This chapter will focus on comparisons of formaldehyde vertical column densities at two locations: the remote Lauder atmospheric observatory in New Zealand and the suburban Broadmeadows site in Melbourne. At Lauder, formaldehyde is measured both using infrared spectroscopy and UV spectroscopy (MAX-DOAS), both of which can be compared to satellite results. At Broadmeadows, formaldehyde is measured using MAX-DOAS as outlined in chapter 5 of this thesis. MAX-DOAS has previously been used in formaldehyde VCD validation studies for several different satellites including GOME (Chance et al., 2000; Thomas et al., 1998), GOME-2 (Hoque et al., 2018b; De Smedt et al., 2015), SCIAMACHY (Vigouroux et al., 2009) and OMI (Lee et al., 2015; De Smedt et al., 2015; Kurosu et al., 2007). The focus of satellite comparisons

in this work will be for the TROPospheric Monitoring Instrument (TROPOMI), on the European Space Agency's Sentinel-5P satellite, which was launched in October 2017 (Veefkind et al., 2012). This study represents the first attempt at MAX-DOAS - TROPOMI comparison in the southern hemisphere.

7.1 Outline of measurements at Lauder

A 1D Envimes MAX-DOAS system is installed on the roof of the NIWA building at the Lauder atmospheric observatory. The instrument and its performance at international intercomparison campaigns has been highlighted in Chapter 4. In design and operation it is essentially identical to the University of Melbourne and Broadmeadows MAX-DOAS instruments detailed in other parts of this thesis. In this chapter, MAX-DOAS vertical column density results are presented from November 2016 to January 2019, largely overlapping with the timeseries at Broadmeadows. The dataset is broken only for the NIWA MAX-DOAS to attend TIMTAM in February 2017.

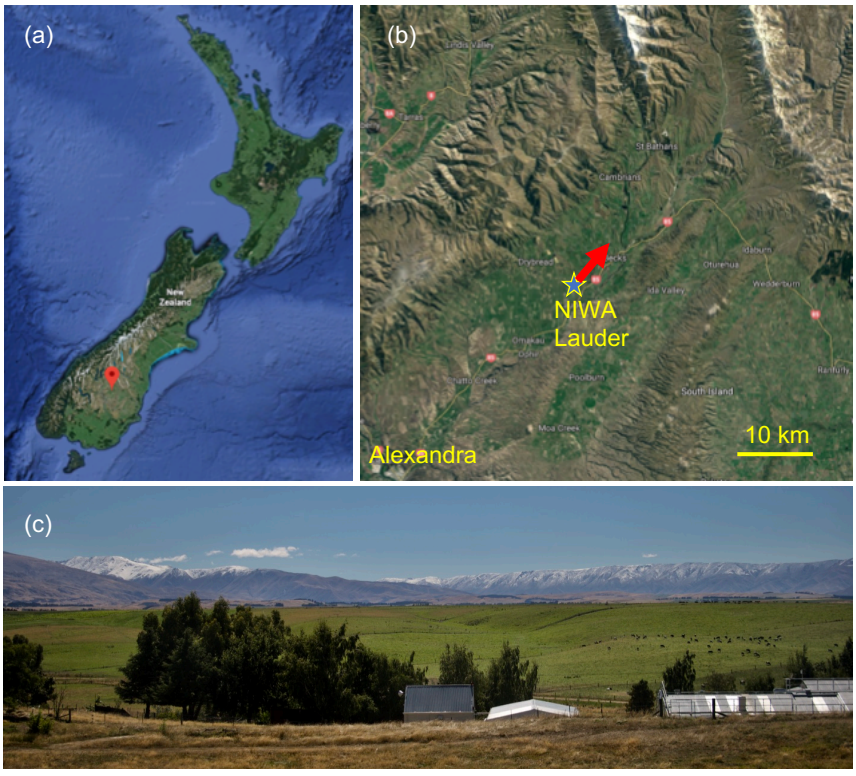

Figure 7.1: (a) Map of New Zealand showing the location of Lauder (red pin) in the South Island. (b) Map zoomed in to Central Otago showing the location of NIWA Lauder (blue star) and viewing direction of the MAX-DOAS (red arrow) towards St Bathans and the Dunstan Range. (c) Photo over the NIWA Lauder buildings, in the MAX-DOAS viewing direction, towards Mt St Bathans and the Dunstan Range (*Maps sourced from Google Maps, photo by R.Ryan*).

Lauder (lat. -45.038°, lon. 169.682°, elevation 370 m ASL) is located in the Central Otago region of New Zealand's South Island as shown in figures 7.1(a) and (b). It a remote location surrounded by intensively irrigated farmland, ringed by distant mountain ranges and lying approximately 30 km north-east of the nearest large town, Alexandra. The photo in figure 7.1(c) provides a scale for the St Bathans and Dunstan Ranges to the North East, relative to the NIWA Lauder buildings. Of note for MAX-DOAS measurements is that elevation angles $< 2^o$ are impacted by these mountains. The NIWA site at Lauder is part of the Network for the Detection of Atmospheric Composition Change (NDACC) network (https://www.ndsc.ncep.noaa.gov/).

Similarly to Broadmeadows, Lauder has regular co-located meteorological, radiation, ozone sonde and Dobson ozone measurements. Aerosol optical depth is measured using a sun-photometer with data submitted to the Skynet International Data Center (www.skynet-isdc.org). As well as this, in-situ O_3, HCHO, NO, NO_2 and HCHO vertical profiles calculated from fourier-transform infrared spectra are also collected, providing an ideal dataset for comparison with the MAX-DOAS measurements.

7.1.1 Formaldehyde measurements at Lauder

FTIR

Formaldehyde absorbs infrared radiation as well as UV, making it accessible to fourier transform infrared spectroscopy (FTIR). FTIR measurements have been made since the 1990s at Lauder, as described originally in Jones et al. (1994). The retrieval of HCHO from a 1992-2005 FTIR dataset was described in detail in Jones et al. (2009), wherein a mean total column amount of 4.9×10^{15} molec.cm^{-2} and strong seasonal cycle with summer peak was found. Using a box model, it was found that methane oxidation alone could not explain the magnitude of the summer peak. Isoprene was hypothesised as a potential source of HCHO in this location but aside from this, observations of atmospheric formaldehyde and information on its sources in New Zealand are sparse. An example FTIR formaldehyde retrieval from 8th January 2018 is shown in figure 7.2, including a priori and retrieved profiles below 10 km. In fact, the retrieval grid used for FTIR measurements extends to 100 km. In the corresponding averaging kernels below 10 km, it can be seen that HCHO from the FTIR technique has highest sensitivity around 10 km and in the upper troposphere rather than the boundary layer, in direct contrast to MAX-DOAS measurements (Vigouroux et al., 2009; Jones et al., 2009).

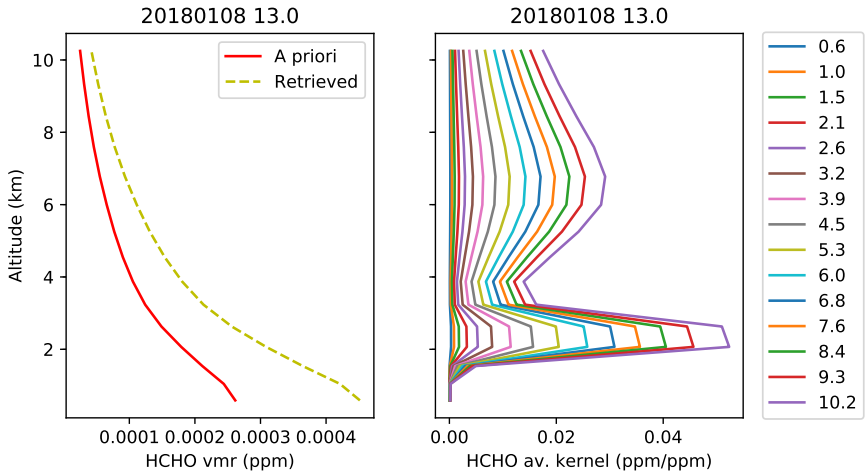

Figure 7.2: Example FTIR profile retrieval from 1 pm local time on 8th January 2018 at Lauder. The left hand panel shows a priori and retrieved HCHO profiles in the lowest 10 km, the right hand panel shows the corresponding averaging kernels.

MAX-DOAS

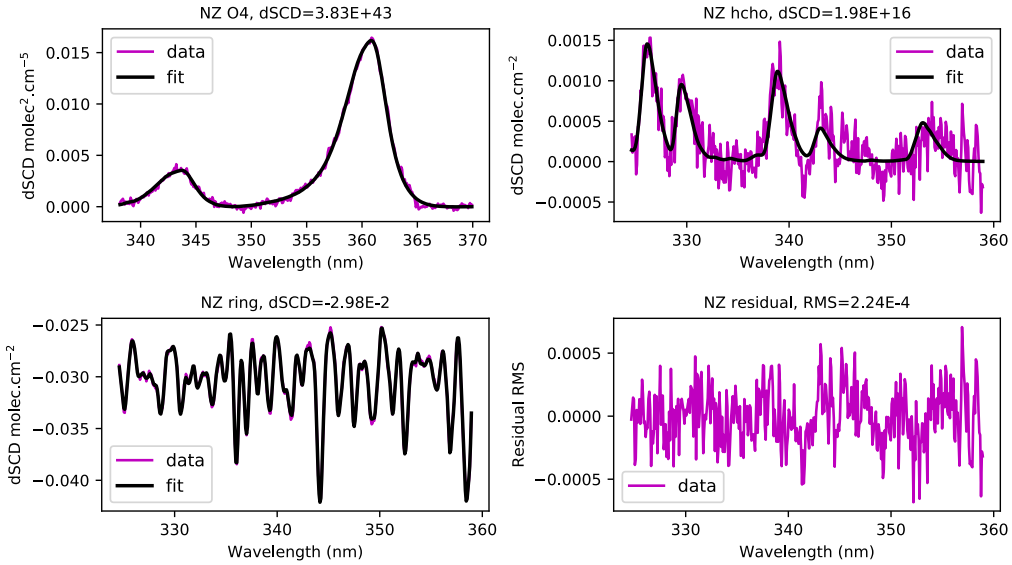

Figure 7.3: Example QDOAS fits from Lauder MAX-DOAS data, 1st January 2018 at solar zenith angle 30^o and elevation angle 3^o. Top row: O_4 (338-370 nm wavelength range), HCHO (324.5-359 nm wavelength range). Bottom row: ring and residual spectra (both in the 324.5-359 nm wavelength range).

Formaldehyde was detected throughout the measurement period in the DOAS analysis, using the same DOAS settings as described for Broadmeadows in the previous chapter.

An exemplary HCHO fit from noon on a clear Lauder day is shown in figure 7.3, along with the residual RMS and fits for O_4 and the Ring effect. As shown in this figure, residual RMS was very low at Lauder giving good confidence in the spectral analysis. The average residual RMS across the whole measurement period for 3^o elevation angles was 3.5×10^{-4}, 1.0×10^{-4} less than Broadmeadows. Accordingly, the formaldehyde detection limit was lower than at Broadmeadows, with a value (calculated using the method described in the previous chapter) of 3.8×10^{14} molecules.cm^{-2}.

Settings for retrieving formaldehyde vertical profiles in the HEIPRO profile retrieval algorithm were mostly the same as described for Broadmeadows although the a priori profile parameters were varied because of the lower expected HCHO VCD and surface concentration at Lauder compared to Melbourne. Three formaldehyde retrieval scenarios were tested in HEIPRO for Lauder. The standard test case (test 00) used HEIPRO retrieved aerosol profiles, and HCHO a priori parameters of 1.5 km scale height, 0.4 ppb surface mixing ratio and relative error of 1.0. Test 01 was designed to test the influence of the aerosol retrieval on HCHO results. It used the same a priori settings as test 00 but fixed the aerosol profile to have aerosol optical depth of 0.05 contained in a box shaped profile up to 1.5 km. Test 02 was designed for direct comparison with FTIR results by using the HEIPRO retrieved aerosol profiles, but the same a priori profile as FTIR formaldehdye retrieval. Figure 7.4(a) shows the total least squares regression of test 00 and test 01. There is good agreement with R^2 correlation coefficient of 0.93 and slope of 0.96. The offset is 2.8×10^{15} molec.cm^{-2}, indicating that using a fixed aerosol profile slightly increases the total HCHO column retrieved. There is also excellent agreement (slope = 0.97 and $R^2 = 0.96$, figure 7.4(b) for test 02 and test 01, however the offset is higher at 4.4×10^{15} molec.cm^{-2} in this case. This is expected because the FTIR a priori is higher than the MAX-DOAS a priori especially at altitudes above 2 km, allowing more weight to be given to the higher altitudes in test 02 than test 00. The deviation of slopes from unity in each case is still well within the mean VCD uncertainty of 15 % for each test. It can therefore be determined that within uncertainty, the MAX-DOAS HCHO VCD is independent of the a priori and aerosol profile choices. For the standard test case, method 00, the range of formaldehyde vertical columns was 1.37×10^{15} to 6.18×10^{15} molec.cm^{-2} with a mean value of 3.13×10^{15} molec.cm^{-2}, peaking in summer months. Therefore HCHO was detected throughout the measurement period well above the calculated MAX-DOAS detection limit.

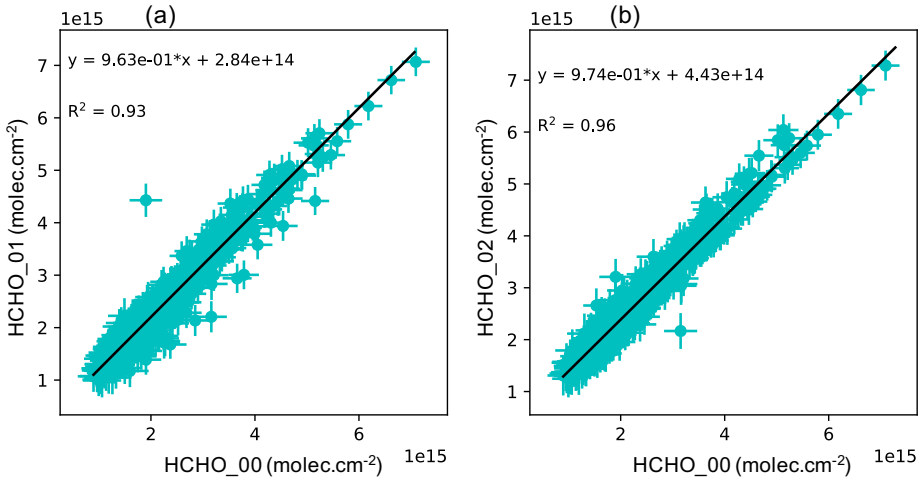

Figure 7.4: Comparison scatter plots for MAX-DOAS formaldehyde retrieval methods at Lauder. The x-axis in each plot indicates test 00, with standard HCHO retrieval settings. The y-axis indicates (a) test 01 designed to examine the influence of the aerosol profiles on the trace gas retrieval, and (b) test 02 which uses the a priori HCHO profile from FTIR analysis.

As illustrated in the example retrieval (standard method "00") in figure 7.5(a), good agreement was generally achieved found between modelled and measured HCHO dSCDs in HEIPRO. However, it is clear in the averaging kernels that the information content of the MAX-DOAS formaldehyde retrievals at Lauder was much lower than at Broadmeadows, with notably poorer sensitivity to the lowest retrieval layers. This is likely exacerbated by the fact that 2^o is the lowest available elevation angle. The highest sensitivity was found around 0.9 km altitude, and the monthly averaged vertical profile plot (figure 7.5(b)) shows that summer vertical HCHO profile maxima are retrieved consistently at this altitude. In winter, HCHO VMR is lower than summer across all altitudes, rather than, for example, being compressed in the boundary layer.

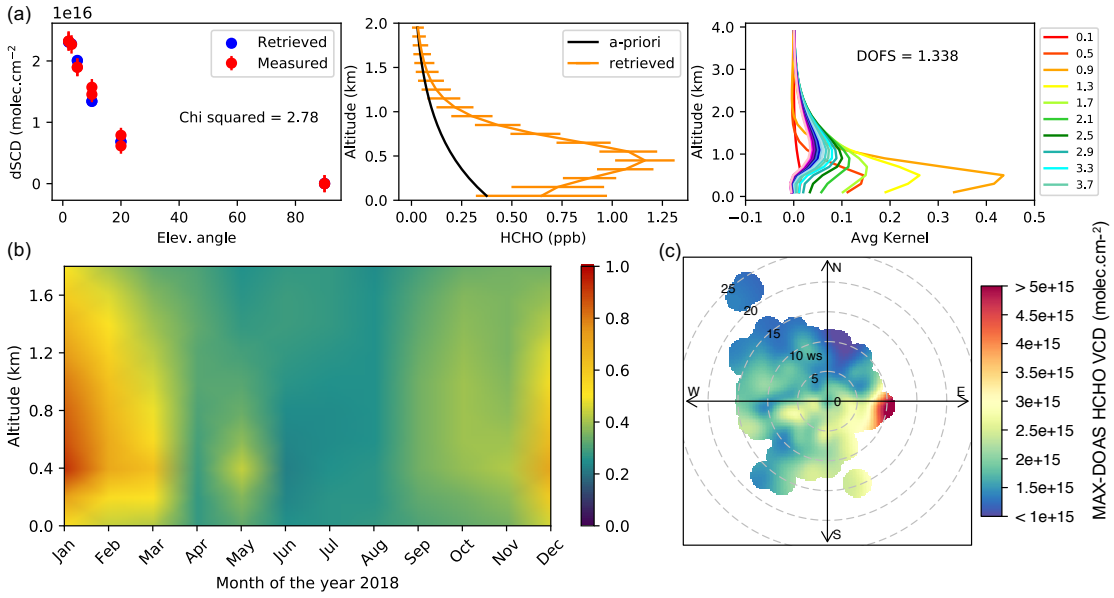

Figure 7.5: (a) An example MAX-DOAS formaldehyde retrieval from 1st January 2018 at Lauder, showing the modelled and measured values, retrieved and a priori vertical profile and averaging kernels. (b) Monthly averaged midday HCHO vertical profiles, and (c) polar bivariate plot showing the HCHO VCD as a function of wind speed and direction. All HCHO profiles in this figure retrieved using standard retrieval settings (method 00).

Given the minimal low-altitude information content, the following discussion of formaldehyde at Lauder and comparison with FTIR and satellite measurements will focus on total vertical column amounts rather than surface mixing ratios. HCHO results were filtered for the presence of cloud using the SkyNet radiometer data which reports a cloud flag parameter. To determine potential source directions, the HCHO VCD measured with MAX-DOAS was plotted as a function of wind speed and direction as shown in figure 7.5(c). This plot shows a maximum column amounts with moderate wind speeds from the south-west, south-south-east and especially easterly directions. In this MAX-DOAS dataset, the easterly maximum seems slightly misleading since windroses over this period show that wind comes from this direction less than 10 % of the time. However, the same key source directions including the strong 'easterly maximum' are observed in polar bivariate plots of the 2001-2019 FTIR dataset (not shown). There is a large variation in vegetation types across New Zealand's South Island, including temperate rainforest in the west, dryland agricultural in the Central Otago region and intensive irrigated pasture in much of the east, south and south east, which might be expected to produce different volatile organic emissions and formaldehyde amounts. On the available evidence it could be hypothesised that the agricultural eastern sector is a stronger source of formaldehyde than the forested the west coast.

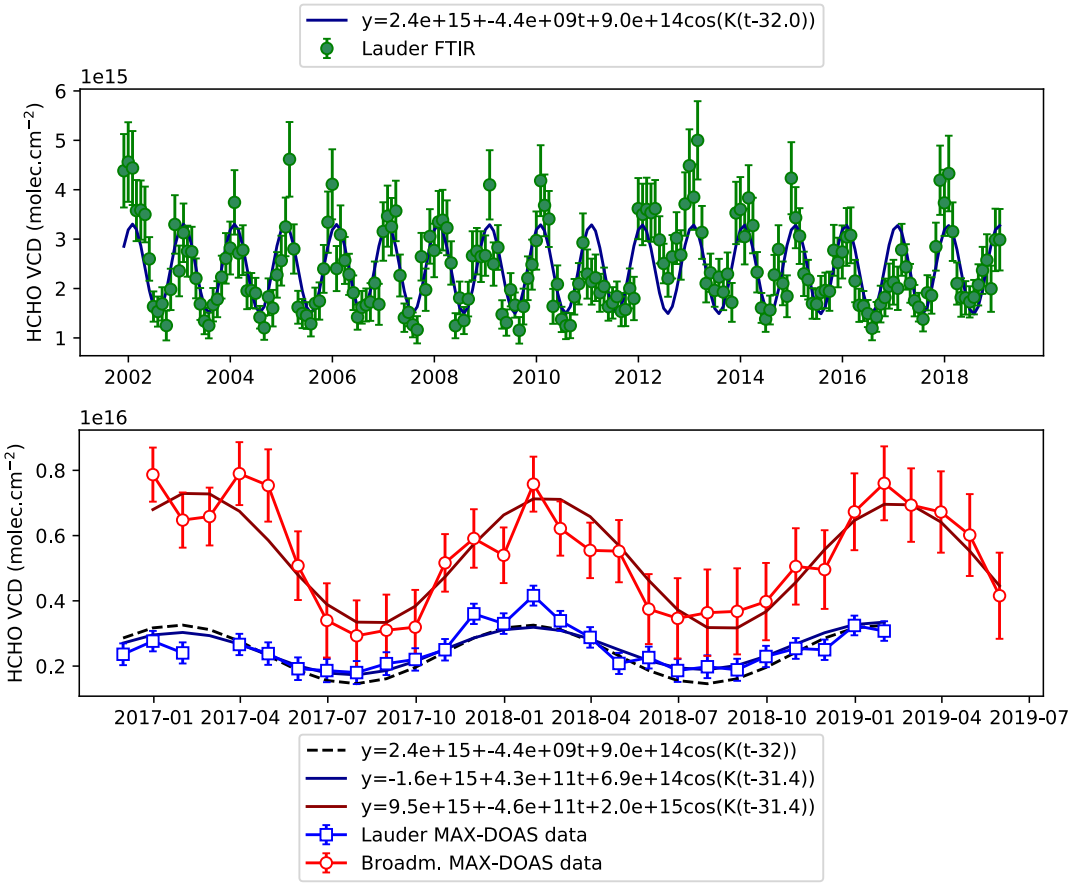

Figure 7.6: (a) Timeseries of monthly averaged formaldehyde total column measurements at Lauder from 2001-2019 measured with FTIR. Included is a cosine fit to this data highlighting the seasonal cycle. (b) Timeseries of monthly averaged formaldehyde vertical column densities from MAX-DOAS measurements at Broadmeadows (red points) and Lauder (blue squares). Cosine fits to each dataset are also plotted, along with the cosine fit from the 2001-2019 FTIR results in (a) (dashes).

Lauder vs Melbourne HCHO

Following the example of Jones et al. (2009), the seasonal cycle of formaldehyde vertical columns was fitted with a cosine function described by the following equation:

$$C(t) = a_0 + a_1 t + a_2 \cos K(t - \phi) \tag{7.1}$$

where $C(t)$ is the formaldehyde vertical column as a function of time (in units of days since 1st January 1992), ϕ is the phase term with units of day of the year and $K = 2\pi/365$. Also fitted in the regression are a_2 (amplitude of the seasonal cycle), a_0 (the initial mean column amount) and a_1 (the magnitude of the linear trend in HCHO over time), as shown for the 2001-2019 FTIR HCHO columns from Lauder in figure 7.6. The

a_1 term is found to be small and slightly negative, -4.4×10^9 implying a very slight negative trend to HCHO columns over the 2001-2019 measurement period. The phase of the cosine fit is 32 days suggesting that peak formaldehyde at Lauder occurs on the 1st of February on average. In figure 7.6(b) the magnitude of the formaldehyde VCD at Lauder, as measured by the MAX-DOAS, was lower on average in all seasons than at Broadmeadows. The amplitude of the seasonal cycle is also smaller, although the phase is very similar (31.4 days) which perhaps indicates that similar seasonally-dependent sources of formaldehyde at each location. In figure 7.6(b), the cosine fit to the 2001-2019 FTIR data has been included (black dashed line) indicating that the MAX-DOAS 2.5 year results have a slightly lower seasonal amplitude but essentially the same phase as the FTIR results. In the following section, a more rigorous comparison of HCHO columns from FTIR and MAX-DOAS will be undertaken.

7.2 HCHO comparisons

In this section, formaldehyde vertical columns from MAX-DOAS measurements are compared to FTIR and satellite measurements taken at the same time.

7.2.1 MAX-DOAS vs FTIR at Lauder

To date, one paper highlights a comparison between MAX-DOAS and FTIR formaldehyde columns, from the tropical Reunion Island Vigouroux et al. (2009). In that paper, the comparison period was four months. In this work, co-located measurements over a period of 25 months are compared, from November 2016 to January 2019, allowing a comparison two full seasonal cycles of formaldehyde at this background location. The comparison method used here has been adapted from Vigouroux et al. (2009) and Rodgers and Connor (2003). In order to account for the fact that the FTIR instrument is sensitive to the HCHO column over a greater range of the atmosphere than the MAX-DOAS (as evident from the averaging kernels in figures 7.5(a) and 7.2 respectively), the FTIR columns have been smoothed by the MAX-DOAS averaging kernels. To facilitate this, the MAX-DOAS total averaging kernels were interpolated onto the FTIR retrieval grid, which is the coarser retrieval tropospheric retrieval grid. The equation for the smoothing is given by:

$$\mathbf{X}^{smooth} = \mathbf{X}_a + \mathbf{A}_M(\mathbf{p} - \mathbf{p_a}) \tag{7.2}$$

where $\mathbf{X}_a$ is the a priori FTIR total column, $\mathbf{p}$ is the FTIR volume mixing ratio (VMR) profile, $\mathbf{p_a}$ is the a priori FTIR VMR profile. $\mathbf{X}^{smooth}$ is the FTIR total column smoothed by the MAX-DOAS averaging kernels $\mathbf{A}_M$, which have units of VMR/VMR. To quantify the agreement between instruments, daily average columns of results between noon and 2 pm local time are examined here. A timeseries of the results is presented in figure 7.7(a), showing that both techniques, including the FTIR before and after smoothing,

capture the same seasonal cycle at Lauder. The differences between the FTIR and the MAX-DOAS (mean ± standard deviation) were $-7.58 \pm 26.54\%$ considering the original FTIR columns, and $-0.44 \pm 31.86\%$ considering the smoothed FTIR columns. These absolute differences were lower on average than the combined error on the differences of the columns, calculated according to $E_{TC} = \sqrt{E_{MAX-DOAS}^2 + E_{FTIR}^2}$, where E_{FTIR} and $E_{MAX-DOAS}$ are the combined random and systematic errors of each instrument. For the whole timeseries the mean combined error on the differences was 21.7 %. The differences between FTIR and MAX-DOAS columns here are consistent with the results found in the Reunion Island comparison (Vigouroux et al., 2009). In contrast to their study, here the smoothing was found to improve the mean difference but increase the standard deviation of the difference. The higher standard deviations of the differences at Lauder likely reflect the much longer comparison period, incorporating variations across a much wider range of atmospheric conditions. The good agreement within error between the two techniques is further examined by total least squares regression in figure 7.7(b) and (c) for the smoothed and original FTIR columns respectively. Consistent with the improved mean difference post-smoothing, the slope of the regression is closer to one, and the offset is an order of magnitude smaller, in the smoothed compared to the original case. Practically no change is observed in the R^2 correlation coefficient post smoothing. Considering monthly instead of daily averages, R^2 values were 0.53 and 0.51 for MAX-DOAS compared to pre- and post-smoothing FTIR respectively. Throughout the measurement period, there are two key periods of discrepancy: February-March 2017 and November-December 2018. In each case, the MAX-DOAS over-represents the FTIR by a factor of about 1.5.

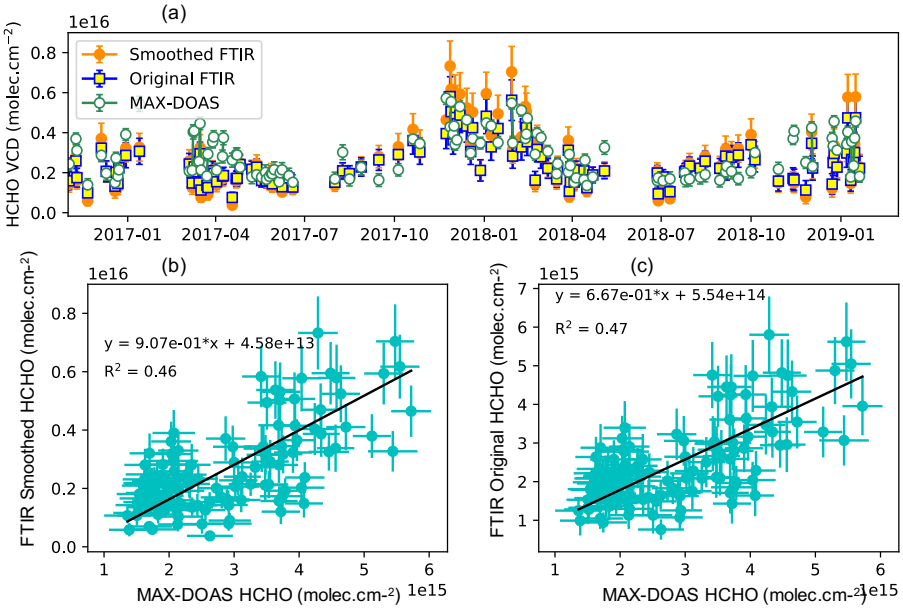

Figure 7.7: (a) Timeseries comparison of MAX-DOAS and FTIR HCHO vertical columns (both original values and smoothed with MAX-DOAS averaging kernels) from November 2016 to January 2019. Results are daily average column amounts from measurements between 12:00 and 2:00 pm local time. (b) Scatter plot comparison of MAX-DOAS HCHO VCDs with smoothed FTIR results. (c) same as (b) but with original FTIR HCHO columns.

7.2.2 MAX-DOAS vs Satellite

In this section, MAX-DOAS formaldehyde columns are compared with satellite results. Firstly, Lauder HCHO MAX-DOAS columns are examined alongside results from the TROPospheric Monitoring Instrument (TROPOMI satellite). Following the example of MAX-DOAS vs satellite formaldehyde comparisons in Hoque et al. (2018b) and De Smedt et al. (2015), absolute values of the vertical columns are compared rather than profiles. Downloaded TROPOMI data was first regridded to 0.1×0.1^o, meaning that average columns in an area about 20 km^2 around the MAX-DOAS measurement site were used. The recommended quality control (QC) filtering was applied, excluding retrieved values where the QC flag was less than 0.5 (on a scale of 0-1), and cloudy scenes as determined by the satellite results were also excluded from the comparisons. At both Lauder and Broadmeadows, the satellite overpass was around 13:00 local time, so MAX-DOAS results between 12:00 and 14:00 were averaged for the comparisons.

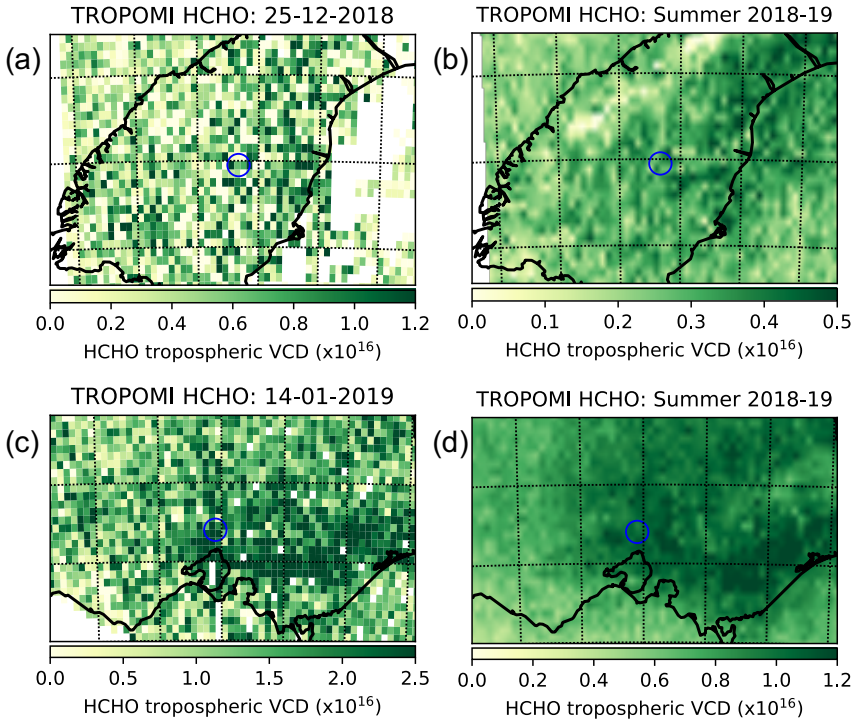

Figure 7.8: Examples of TROPOMI 0.1×0.1^o gridded output. The blue circles indicate the MAX-DOAS measurement locations. The grid lines drawn are at 1^o latitude and longitude intervals. (a) Example retrieval from the South Island of New Zealand, 24th of December 2018. (b) All New Zealand retrievals from December 2018-February 2019 averaged. (c) Example from Victoria, 14th January 2019, and (d) all Victorian retrievals from December 2018-February 2019 averaged. Note that the colour bar scale is different for each plot to emphasise the spatial patterns.

TROPOMI reports an uncertainty on the column amount, however it was found that this uncertainty was highly correlated with the magnitude of the column amount. Therefore, we estimated the uncertainty on the satellite column retrievals from the number of retrievals contributing to the averaged column in the 0.1×0.1^o grid box (number per cell, N_{pc}) and the standard deviation of those retrievals (S_T): $E_{sat} = \frac{S_T}{\sqrt{N_{pc}}}$. More information was available from TROPOMI over Broadmeadows than the Lauder, with the average N_{pc} across the comparison period and considering TROPOMI pixels 1^o either side of the ground-based station, of 1.18 in New Zealand and 2.76 in Melbourne. Final compared results filtered for out pixels with $N_{pc} < 1$, giving a used average N_{pc} of 1.84 for Lauder and 2.94 for Broadmeadows. The discrepancy in N_{pc} could be due to more cloud over New Zealand than Victoria, or because HCHO columns over Lauder are low enough to be approaching background levels and the TROPOMI detection limit. TROPOMI results showed greater spatial variation over New Zealand than Victoria, as illustrated in the example map in figure 7.8(a). This is reflected

in the standard deviation (S_T) of HCHO retrievals contributing to the 'Lauder' and 'Broadmeadows' TROPOMI columns; the mean $\pm S_T$ was $1.66 \times 10^{15} \pm 1.50 \times 10^{15}$ and $7.53 \times 10^{15} \pm 1.10 \times 10^{15}$ for Lauder and Broadmeadows respectively. Overall, these factors combined to give a high mean percentage error for Lauder TROPOMI columns of 129 %, while for Broadmeadows it was only 9.7%.

Nevertheless, the average summer 2018-19 TROPOMI retrieval map for the central New Zealand South Island shown in figure 7.8(b), supports the above conclusion from the MAX-DOAS measurements that highest formaldehyde amounts are in the agricultural eastern parts of the island. There are no discernible HCHO 'hot spots', for example along the thickly forested west coast or sout-western Fiordland region. The New Zealand Alps are highlighted in this figure by the lack of formaldehyde, possibly due to minimal vegetation in this region and because the satellite retrieval will not work over areas of high albedo (i.e. snow). The inference that formaldehyde is close to background levels is supported by the fact that average summer column amounts over the Tasman Sea and Pacific Ocean off the coast of the South Island appear similar to those over land. In comparison, the average summer 2018-19 map from Victoria highlights some clear features especially high formaldehyde production from the densely forested regions in the east of the state. The irrigated agricultural land north of Melbourne stands out compared to the drier grazing country in the west and north-west, and as with New Zealand the alpine area (north east) is distinguished by lower formaldehyde as a result of lower vegetation cover. These observations are in agreement with the source regions for formaldehyde deduced from the Broadmeadows MAX-DOAS measurements in the previous chapter.

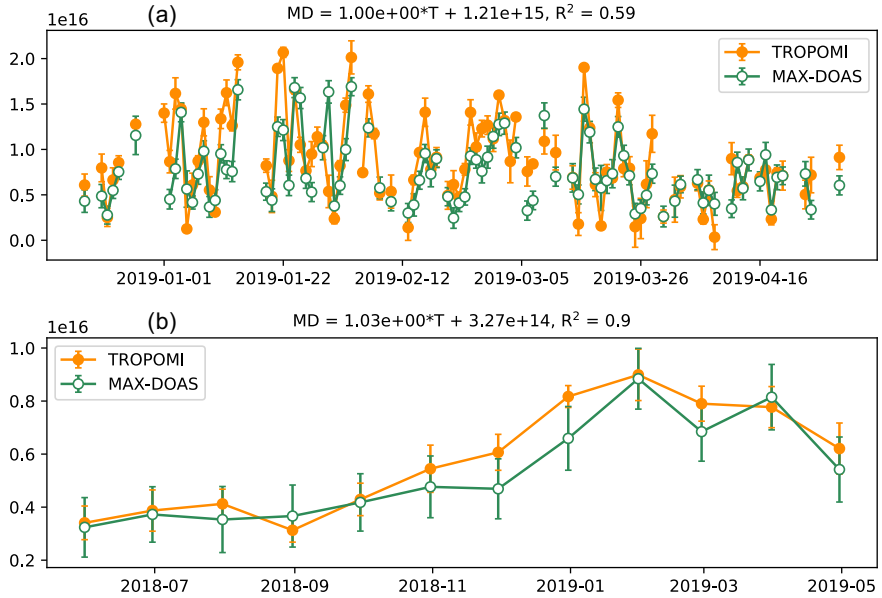

Figure 7.9: Timeseries comparisons for MAX-DOAS and TROPOMI. Figure titles indicate the equation describing a total least-squares linear regression fit for the two datasets. (a) Timeseries of daily averaged HCHO vertical columns at Broadmeadows from 12/12/2018 to 15/5/2019. (b) Timeseries of monthly averaged HCHO columns from Broadmeadows, May 2018-May 2019.

Formaldehyde columns from TROPOMI and MAX-DOAS at Broadmeadows were compared over the course of a year (May 2018-May 2019) and found to be in very good agreement both in terms of magnitude and temporal variation. During the summer and autumn, the period of highest formaldehyde on average in Melbourne, daily column amounts (12:00-14:00 local time) were compared as shown in figure 7.9 (a). Very good agreement was found from the total least squares regression analysis, with a slope of unity and R^2 of 0.59 suggesting the magntitude and day-to-day variation in summer HCHO columns is well captured by TROPOMI at this location. Across the whole comparison timeframe, the regression analysis for daily amounts yields a slope of 0.74 and R^2 of 0.39, with the daily variation not captured as well when HCHO columns are lower in winter. The same total least squares regression was carried out on monthly averaged data as shown in figure 7.9(b). The two methods compare very well, with slope close to unity at 1.03, R^2 of 0.9. On average, TROPOMI VCDs are 9 % higher than from the MAX-DOAS, but this difference is within the standard deviation of 12 %. The comparisons between TROPOMI and MAX-DOAS in Melbourne are excellent in light of previous validation studies, as listed in table 7.1. With slope and R^2 close to 1.0, for averaging only 10 km either side of the MAX-DOAS measurement location, the monthly results in Melbourne represent the most successful such validation attempt for formaldehyde vertical columns, suggesting that the greater resolution and updated retrieval processes of TROPOMI have resulted in improved HCHO column

accuracy.

This finding is highlighted by a comparison (2017-2019) at the same Broadmeadows location between OMI and the MAX-DOAS. As shown in figure 7.11, OMI does not clearly capture any of the seasonal formaldehyde variation in Melbourne, and as such fails to replicate the MAX-DOAS values. The errorbars shown in this figure are the quoted uncertainty on the OMI columns, and represent 67 % of the total column on average, perhaps due to the poorer resolution of OMI compared to TROPOMI, making observation of the seasonal cycle difficult in this data. Monthly OMI HCHO columns are on average 200 % higher than the MAX-DOAS (see table 7.1), far greater than any discrepancy reported in the literature for a MAX-DOAS vs satellite retrieval. One possibility for the disparity is inappropriate a priori profiles, which are calculated in OMI using chemical transport models. Knowing that formaldehyde production from isoprene and monoterpene emissions is poorly simulated in south-eastern Australia using standard VOC mechanisms (Emmerson et al., 2016, 2018), relying on these mechanisms to produce useful formaldehyde a priori profiles in this area may be problematic. Previous studies (e.g. De Smedt et al. (2015) and Wang et al. (2017b)) found that agreement between OMI and MAX-DOAS measurements was found when using the MAX-DOAS a priori profiles to retrieve satellite columns; it would be interesting in future work to do the same for satellite retrievals over Australia.

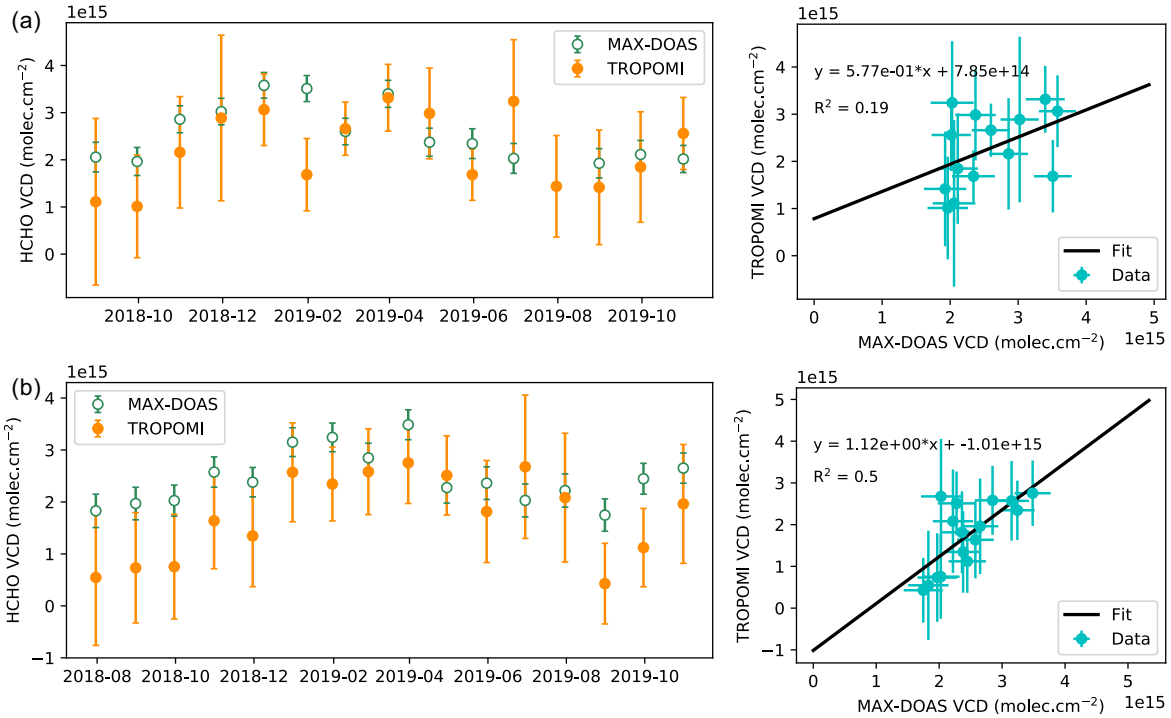

Figure 7.10: Comparison of monthly mean formaldehyde columns from TROPOMI and the MAX-DOAS at Lauder, with timeseries on the left and scatterplot of the same values on the right. (a) shows TROPOMI columns averaged 0.1^o either side of Lauder, (b) shows TROPOMI columns averaged 1^o either side of Lauder.

Finally, vertical formaldehyde columns have been compared for Lauder's MAX-DOAS vs TROPOMI, for the period July 2018-November 2019. As indicated in figure 7.8 TROPOMI retrievals were more spatially variable over Lauder than Broadmeadows, with fewer pixels per grid cell available for averaging. The lack of information greatly hampered the comparison, with not enough consistency to attempt a daily average point-for-point comparison as with Melbourne. Indeed, only 7 days per month on average were available for contributing to monthly means at Lauder, compared to 15 at Broadmeadows, due predominantly to missing TROPOMI pixels rather than poor midday MAX-DOAS retrievals. The number of days per month available for comparison was much greater in summer than in winter indicating the inherent difficulty of satellite remote sensing of trace gases close to the detection limit. Monthly mean comparisons are presented in figure 7.10, where only months with more than one day of data have been included. Because most winter months have less than five days of data contributing to the mean, their error is large, and also the results should be viewed purely for comparison purposes rather than as indicators of the absolute formaldehyde column at Lauder.

In figure 7.10(a) the monthly means are compared for TROPOMI pixels approximately

10 km either side of the measurement location. The slope of the regression of 0.58 indicates that TROPOMI significantly underestimates the MAX-DOAS at this location, in contrast to Melbourne where TROPOMI overestimated the MAX-DOAS. While the R^2 of 0.19 indicates at best a weak correlation between the two techniques, in all months except January 2019 the MAX-DOAS mean falls within the TROPOMI errorbars; the size of the TROPOMI errorbars makes interpretation of a seasonal cycle difficult in this dataset. A seasonal cycle is more apparent in the TROPOMI results taken 1^o (approx 100 km) either side of Lauder, as shown in figure 7.10(b), and reflected in the regression slope close to unity and improved R^2 from figure 7.10(a). Moving directly 1^o of latitude or longitude from Lauder takes one almost to the coast in all directions, hence, the TROPOMI results in figure 7.10(b) are effectively a southern-South Island HCHO average. Using all pixels across this large area dramatically increased the number of days available for comparison in each month, but high spatial variability still results in large standard deviation errorbars. The strong regression result indicates that the MAX-DOAS formaldehyde measurements at Lauder are generally a good indication of the background formaldehyde level across New Zealand's South Island. This is especially true in spring, summer and autumn where once again MAX-DOAS monthly means typically fall within the errorbars of TROPOMI.

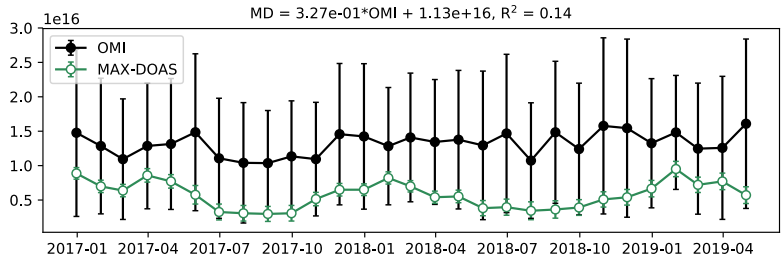

Figure 7.11: Timeseries of monthly averaged MAX-DOAS and OMI HCHO vertical columns at Broadmeadows from January 2017 to May 2019.

7.3 HCHO validation: summary and future work

This chapter presents comparison studies of MAX-DOAS formaldehyde measurements in two distinctly different environments: the remote Central Otago region in New Zealand and the suburban fringe area of Broadmeadows in Victoria. This work is the first long-term comparison and validation study undertaken using MAX-DOAS measurements in the Southern Hemisphere.

At Lauder, 25 months of MAX-DOAS measurements were compared with FTIR formaldehyde columns. Smoothing of the FTIR columns using the MAX-DOAS averaging kernels, to account for the different vertical sensitivities, was successfully carried according to the methodology outlined in Rodgers and Connor (2003) and Vigouroux et al. (2009). The seasonal cycle of formaldehyde at Lauder, with pronounced summer peak,

was clearly replicated by both sets of observations and the smoothed FTIR columns correlated more strongly than the original with the MAX-DOAS results. The phases (i.e. timing of the HCHO peak) of the seasonal cycle were very similar between Broadmeadows and Lauder suggesting similar HCHO sources, however the source strength at Lauder seems to be weaker with a lower seasonal cycle amplitude.

In the first TROPOMI - MAX-DOAS Southern Hemispheric validation study, TROPOMI performed especially well compared to the Broadmeadows monthly average columns, in terms of temporal variation and magnitude (R^2 = 0.9, slope = 1.03). In summer periods, daily variation was also well captured - a vast improvement on the comparison with OMI both for this location and in previous literature reports. Higher spatial variability and lower absolute amounts of HCHO made the comparison more difficult at Lauder. Nevertheless, broad seasonal variations were still captured for formaldehyde over New Zealand's south island which, within uncertainty, compared favourably to the magnitude of the MAX-DOAS observations.

The success of the TROPOMI validation study, especially over Melbourne, raises many exciting possibilities for future work. This study shows the importance of long-term timeseries MAX-DOAS measurements for satellite validation, and could be contributed to international validation efforts. This would begin to address the current Northern-Hemispheric bias in satellite validation studies. Moreover, this work has shown that improvements in satellite technology, culminating (at this point in time) in TROPOMI, mean that space-based HCHO measurements in the VOC-hotspot of south-eastern Australia can be believed, and will be useful for future studies of VOC oxidation chemistry. Ideally, this study should be extended to consider not only formaldehyde validation but also NO_2, HONO and glyoxal. With such assurance, the work on oxidation chemistry of O_3 and OH production begun using MAX-DOAS in chapter 5, can be expanded using satellite-DOAS, allowing the associated air quality and climate implications to be studied on a much grander scale.

Reference	Satellite	Location	Time period	Avgs	Max. distance (km)	Diff. ± std (%)	R^2	Slope
This study	TROPOMI	Lauder, NZ	May 2018-Jan 2019	Monthly	20	23.40±23.25	0.41	0.72
This study	TROPOMI	Melbourne, Australia	May 2018-May 2019	Monthly	10	-9.05±12.34	0.90	1.03
This study	OMI	Melbourne, Australia	Jan2017-May 2019	Monthly	50	-187±103	0.33	0.14
Tian et al. (2018)	OMI	Yangtze River Delta, China	Dec 2013-Dec 2016	Monthly	25	-	0.56	1.19
Chan et al. (2019)	OMI	Nanjing, China	Apr 2013-Apr 2017	Monthly	20	-	0.56	0.99
Wang et al. (2017b)	OMI	Wuxi, China	May 2011-Nov 2014	Daily	50	-	0.17	0.48
Wang et al. (2017b)	GOME-2	Wuxi, China	May 2011-Nov 2014	Daily	50	-	0.18	0.61
Hoque et al. (2018b)	GOME-2	Pantnagar, India	Feb-Nov 2017	Monthly	50	-	0.50	-
Vigouroux et al. (2009)	SCIAMACHY	Reunion Island	Jul 2004-Jul 2005	Daily	500	-11.2±30.5	-	-

Table 7.1: Results from this and previous literature studies comparing formaldehyde vertical columns from MAX-DOAS and satellite retrievals. Note that 'Diff' is for MAX-DOAS - satellite. Slope is the gradient (m) of the linear regression for MAX-DOAS = $m\times$Satellite + C.

Chapter 8

Conclusion

The work in this thesis has achieved the research aims set out in section 1.6 of the Introduction:

1. To establish the utility of MAX-DOAS measurements for the study of atmospheric chemistry in Australasia,

2. To determine the key drivers and sources of atmospheric oxidation capacity in Australia and

3. To identify the chemical sources and physical conditions associated with tropospheric ozone pollution in Australia.

This thesis represents the first long term comprehensive study of MAX-DOAS measurements in Australasia. The utility of the MAX-DOAS measurements was first demonstrated by undertaking a range of sensitivity studies to optimise the data collection and analysis protocols. In chapter 2, the physics underpinning differential optical absorption spectroscopy was presented followed by sensitivity studies examining a range of DOAS settings. Key outcomes of chapter 2 included that using the 324.5-359 nm wavelength range rather than 336-359 was preferable for formaldehyde and that the optimum wavelength range for nitrous acid was 339-372 nm. Iodine monoxide was best fitted between 416-450 nm incorporating four strong absorption bands. The number of wavelength calibration bins used in the QDOAS wavelength calibration routine was found to be important to overall residual RMS, with 20 bins found to be optimal in the UV region, although no clear optimum number of bins was found in the visible region. The sensitivity studies in the visible region highlighted the importance of including vibrational Raman scattering especially for N_2, suggested that the HITEMP water lines perform better in IO and glyoxal retrievals than the updated Polyansky et al. (2018) cross section, and demonstrated that the Thalman and Volkamer (2013) O_4 gives most stable retrieval results for IO. In summary, these DOAS tests demonstrated convincing spectral retrievals of O_4, NO_2, HCHO, HONO, CHOCHO and IO which gave confidence in the slant column observations underlying the results of this thesis.

In chapter 3 the background and settings for vertical column and profile retrieval from MAX-DOAS slant columns using HEIPRO was presented. The key result from the sensitivity studies in chapter 3 was optimisation of, and uncertainty estimates from, aerosol and trace gas a priori parameters. Trace gas retrievals were found to have minimal dependence on carry-over aerosol retrieval uncertainty, and overall less than 10 % uncertainty on retrieved vertical columns can be attributed to uncertainty in the a priori parameters. A range of quality assurance parameters were also discussed in chapter 3 including the filtering results by retrieval information content and chi squared. An empirical cloud filtering algorithm based on clear-sky colour index measurements was also outlined.

The utility of the MAX-DOAS measurements to provide useful and reliable atmospheric chemistry observations was also demonstrated in a range of validation exercises. The TIMTAM campaign (chapter 4 brought together four Envimes MAX-DOAS instruments for a week of simultaneous measurements in Melbourne. This allowed some instrumental problems to be addressed, especially the pointing accuracy of the instruments, highlighting the importance of elevation angle calibration. The campaign also facilitated a comparison of slant and vertical columns which highlighted an instrumental uncertainty of around 10 %.

Further validation exercises included a comparison of NO_2 in-situ and MAX-DOAS measurements in both Melbourne (chapter 5 and at Garden Island (chapter 6), for both of which the diurnal variation and magnitude of NO_2 surface mixing ratios were well captured. For HCHO, MAX-DOAS vertical columns were compared with FTIR measurements at Lauder in New Zealand (chapter 7) and found to agree within the uncertainty in terms of magnitude and seasonality. The formaldehyde comparison was extended in chapter 6 to consider satellite results. At Broadmeadows, excellent temporal agreement was found between TROPOMI and the MAX-DOAS in seasonal variation, and also in terms of daily variation in summer. TROPOMI HCHO was more sparsely retrieved over the South Island of New Zealand, but within this uncertainty TROPOMI also captured the seasonal variation of HCHO observed by the MAX-DOAS. These studies represented the first long term MAX-DOAS-satellite validation in the Southern Hemisphere.

To address the second research aim, MAX-DOAS measurements of HCHO, HONO, NO_2, CHOCHO and IO at Broadmeadows and Garden Island were examined alongside in-situ ozone and meteorological measurements. The primary drivers of air quality and oxidation chemistry at Broadmeadows were analysed using photolysis rate equations and by calculating characteristic ratios of tropospheric constituents in chapter 5. HONO photolysis was found to be the most significant contributor to hydroxyl radical production in the boundary layer in all months, contributing on average between 45-50 % of OH production. HCHO and ozone photolysis were significant OH producers in summer, especially on the hottest days when HCHO was often present at sufficient levels to overtake HONO as the primary surface HO_x source. The vertical profiling

capability of the MAX-DOAS technique showed that while HONO typically dominated the OH production close to the surface, ozone and formaldehyde photolysis were the dominant mechanisms at higher altitudes.

To understand O_3 formation, the broad VOC and nitrogen oxide drivers of the ozone smog cycle were studied using the ratio of HCHO:NO_2. At Broadmeadows it was found that ozone production conditions are usually VOC-limited because of significant nearby road transport NO_x emissions. However, with significant VOC emissions on hot summer days (as indicated by high observed HCHO levels), the ozone production regime was found to tend towards being NO_x-limited. This finding, in line with previous literature modelling studies of ozone production in Australia, highlights that a reduction in severe ozone smog events in Melbourne would be possible with effective NO_x-emission controls. This finding is especially important given the increased likelihood of extreme temperature events due to climate change in the future.

In addition to examining the primary HO_x producers HONO, HCHO and O_3, the sources of these molecules were studied by considering relationships to key meteorological variables and their respective seasonal and diurnal cycles. At Broadmeadows, NO_2 appeared to be dominated by traffic emissions from the adjacent road corridors, with a winter-peaking seasonal cycle. Despite being close to major road corridors, NO_2 levels did not exceed guideline WHO or Australian NEPM standards. The HONO diurnal cycle showed a clear and consistent midday peak at levels that cannot be explained using standard HONO formation mechanisms involving NO_2, NO and OH. The midday HONO mixing ratios correlate with soil moisture levels supporting the theory that soil-based emissions may be an important HONO source. The HCHO seasonal cycle at Broadmeadows had a strong summer maximum and overall exhibited an exponential temperature dependence. Therefore, despite likely contributions to local VOC levels from anthropogenic and biomass burning sources, oxidation of biogenic VOCs from rural and forested areas east and north of Melbourne were identified as the most important formaldehyde source. The seasonal variation of glyoxal was much less pronounced than HCHO suggesting that CHOCHO may be more dependent on local anthropogenic VOC emissions. Maximum CHOCHO concentrations in Autumn may be related to VOCs associated with fuel-reduction biomass burning. A consistent value of glyoxal to formaldehyde around 10 % is high by literature standards elsewhere in the world and may suggest that monoterpenes make up a large proportion of the biogenic VOCs in Melbourne.

MAX-DOAS measurements of HCHO, NO_2 and IO (HONO and CHOCHO were not found above the detection limit) were conducted at Garden Island in Western Australia during a short, four week campaign in 2018. HCHO and NO_2 mixing ratios were greater in air from the continental sector, whereas IO mixing ratios were fairly constant from all directions suggesting a ubiquitous background marine boundary layer IO level was measured rather than a strong local source. The levels of NO_2 and HCHO implied NO_x-limited O_3 production conditions at Garden Island. Bushfire smoke plumes

were clearly observed using the MAX-DOAS vertical profile technique and there was a strong correlation between HCHO column and AOD which is consistent with previous measurements on Australia's east coast. as observed.

The HYSPLIT model was used to calculate meteorological back trajectories from high-resolution WRF output, and these were used in turn as input for the CiTTyCAT Lagrangian chemistry-trajectory model. Sensitivity studies using this model showed the EDGAR NO_x emissions significantly underestimate the observed NO_x mixing ratios and NO at Garden Island. As a result, due to missing NO_x-titration, ozone levels were modelled higher than observed. However, CiTTyCAT was better able to simulate the magnitude and diurnal cycle of HCHO, with these model runs suggesting that HCHO at Garden Island depends almost entirely on isoprene chemistry. The emissions sensitivity studies in CiTTyCAT also highlighted the importance of isoprene as a sink for OH radical sink, thereby influencing methane lifetimes and oxidation capacity overall. The presence of IO at Garden Island raised the possibility of iodine-mediated OH production, specifically by HOI, but this mechanism was found to be two orders of magnitude less than from NO_x and VOC cycles at the observed IO concentrations. No clear evidence of iodine driven O_3 destruction was found, however a more detailed speciated iodine study would be required over long timescales to address this fully.

In this thesis, the MAX-DOAS technique has been applied to a range of Australasian atmospheric chemistry topics. Through method development, comparison campaigns and validation with external remote sensing and in-situ measurements, the technique has shown to provide reliable results over timescales ranging from daily measurements to yearly cycles. The interpretation of MAX-DOAS results alongside meteorological measurements has allowed a comprehensive analysis of the most likely sources of aerosol optical depth, HCHO, HONO, IO, NO_2 and glyoxal in remote, urban and coastal environments. This study has highlighted the important role of HONO and HCHO in HO_x production in Australia for the first time. Through HCHO and NO_2 measurements this work has provided observational constraints on ozone production regimes which can be used to inform air quality policy into the future. In a world where the threats of climate change and air pollution are increasingly real, it is hoped that this thesis contributes meaningfully to the growing body of atmospheric chemistry knowledge in Australasia.

Appendix A

Relating to methodology and TIMTAM chapters

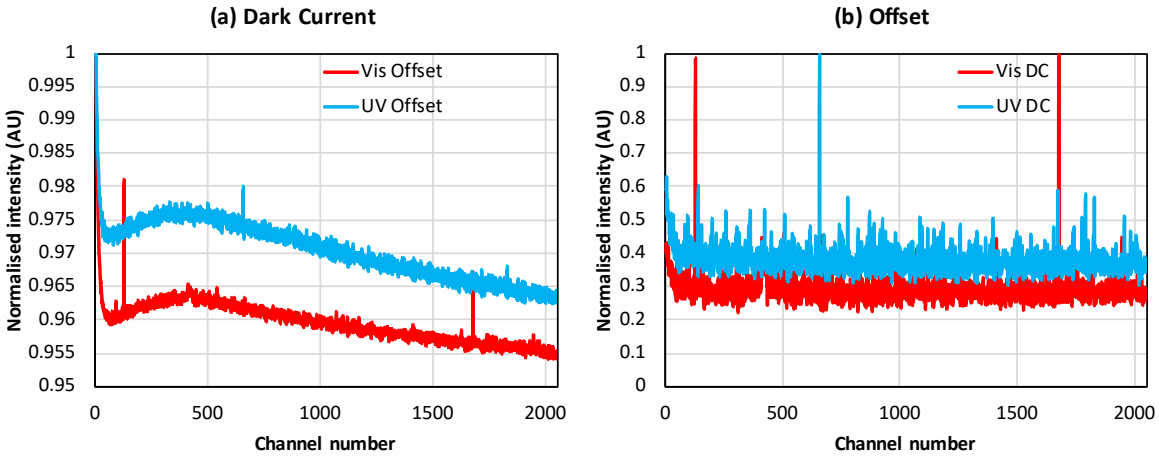

Figure A.1: Example calibration spectra from the University of Melbourne Envimes MAX-DOAS: (a) Dark current and (b) offset spectra.

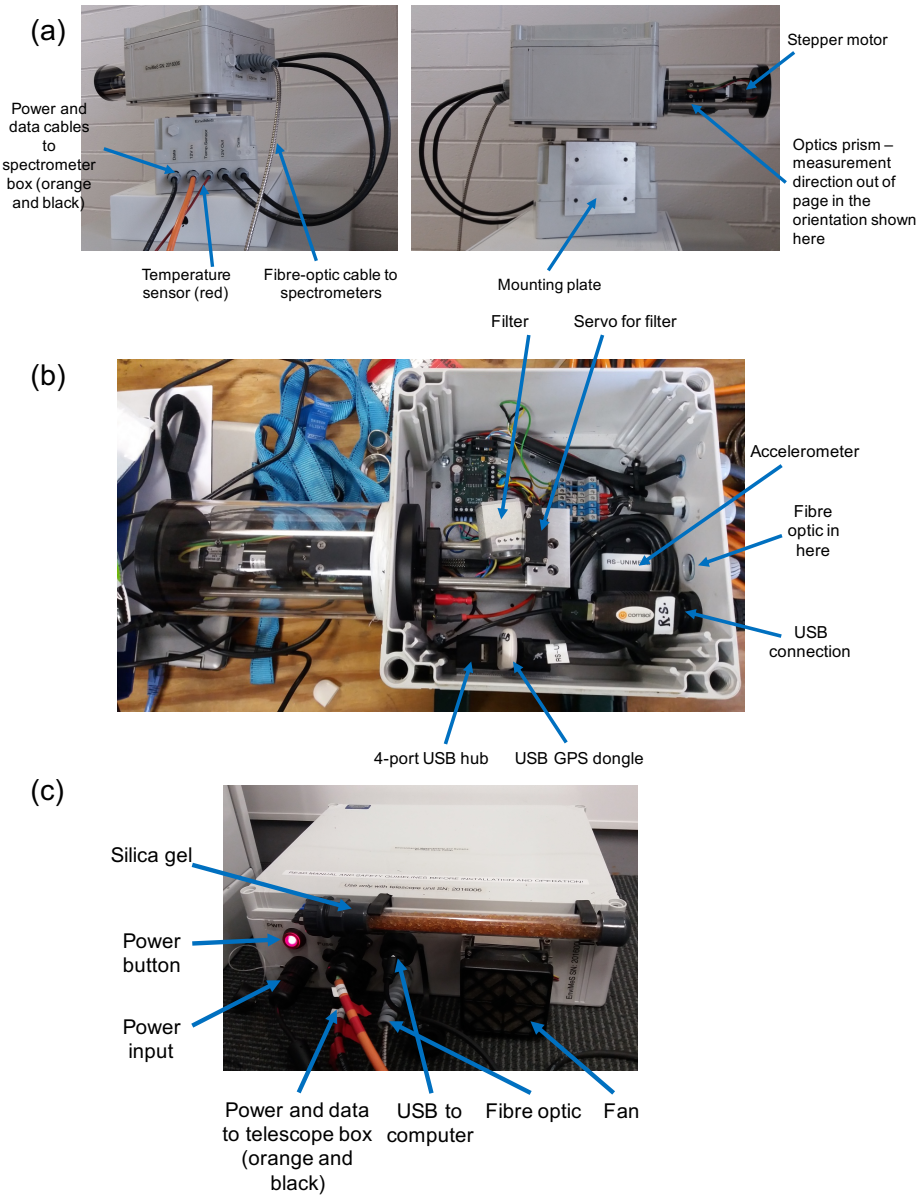

Figure A.2: (a) Annotated diagram of the University of Melbourne Envimes 2D MAX-DOAS optics head, (b) the inside of the optics head, (c) the spectrometer unit

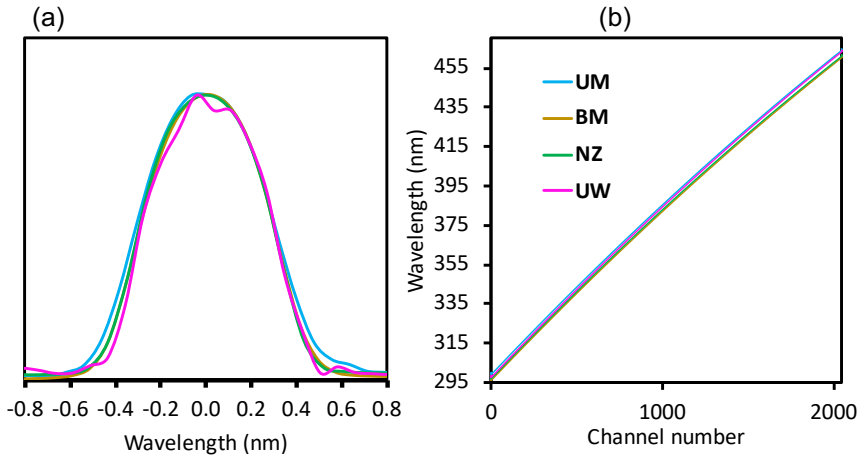

Figure A.3: Lineshape functions (left) and wavelength calibrations (right) for each of the TIMTAM Envimes MAX-DOAS instruments (UV spectrometer only), calculated from mercury lamp spectra

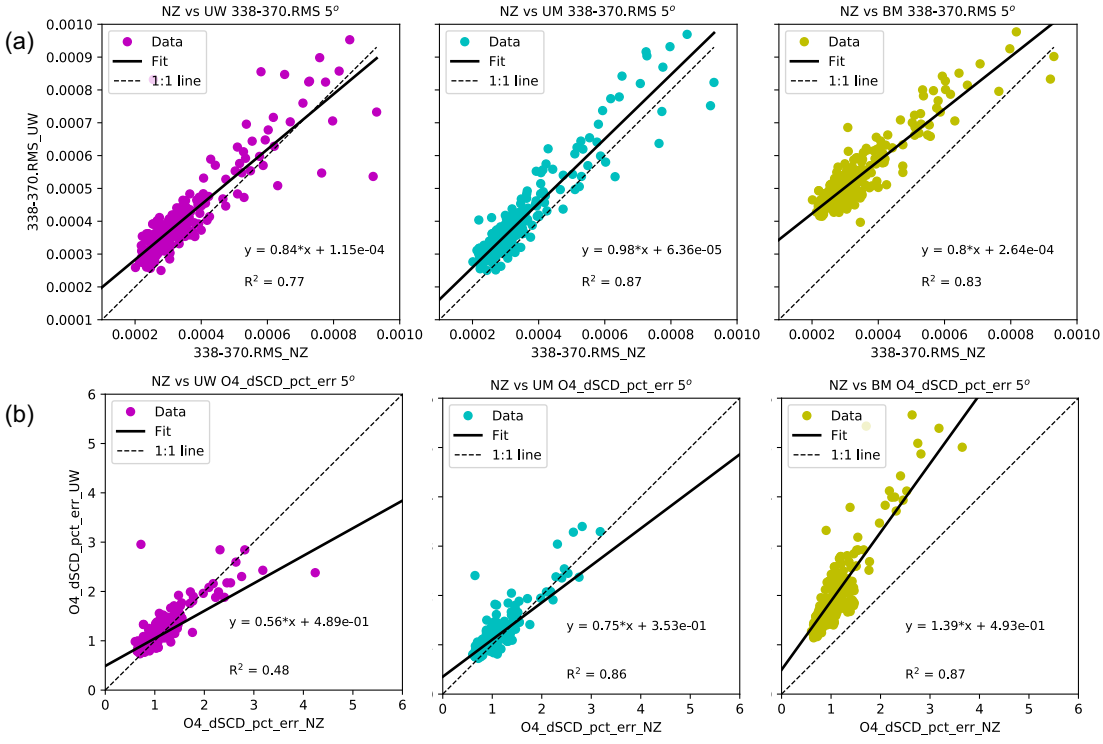

Figure A.4: Scatter plots showing correlations between NZ measurements (x-axis) and BM, UW and UM respectively, for (a) residual RMS and (b) percentage fit error (fit error/dSCD). All 5^o elevation angle results in the period 16-20 February 2017 are plotted.

Appendix B

Relating to Broadmeadows data analysis

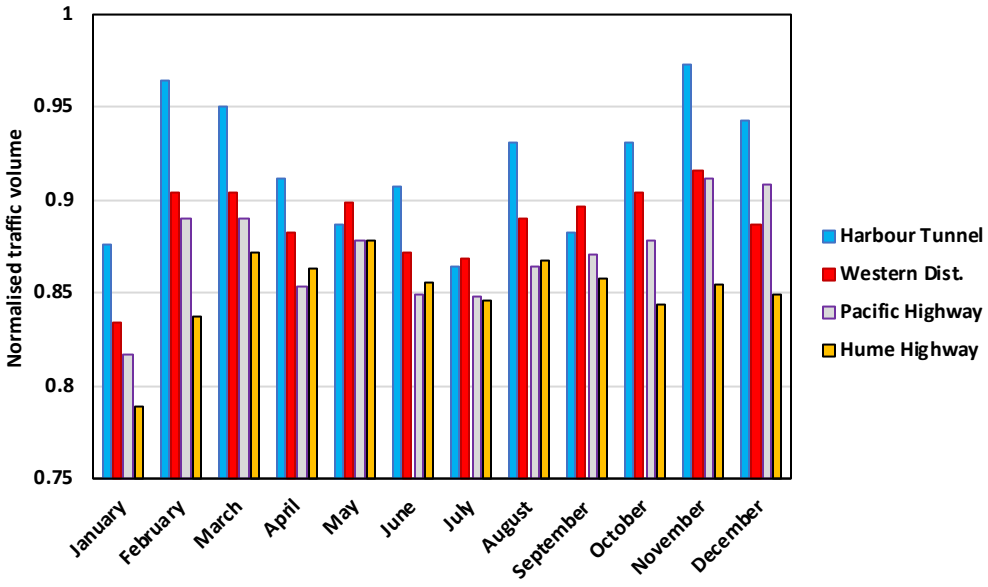

Figure B.1: Monthly average traffic volume on four major roads in inner Sydney, normalised to the maximum monthly traffic volume at each location, from data taken between 2010-2018. The road count locations are the Sydney Harbour Tunnel in Central Sydney, the Western Distributor at Glebe in the inner west, the Pacific Highway at Roseville in the north and the Hume Highway at Bankstown in the south-west.

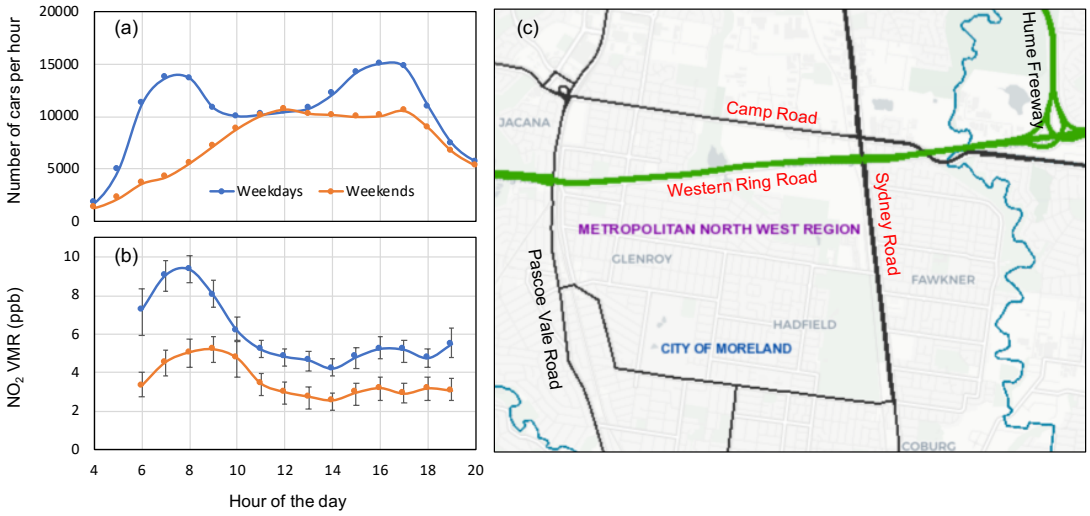

Figure B.2: Comparison of NO_2 diurnal cycle with aggregate traffic volume data for the Western Ring Road, Camp Road and Sydney Road.

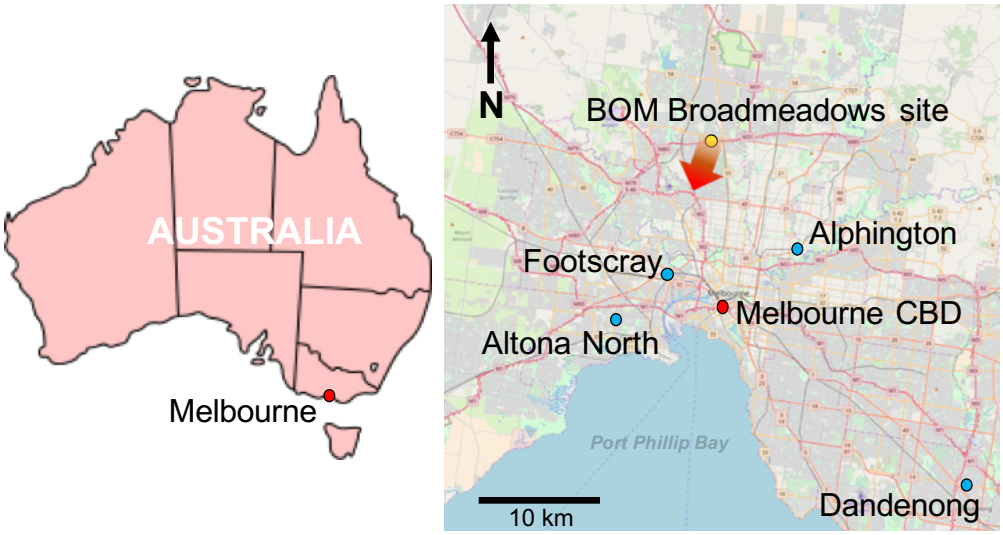

Figure B.3: Figure adapted from Ryan et al. (2018) showing (left) location of Melbourne in Australia and (right) the location of Broadmeadows relative to the Melbourne Metropolitan EPA air quality monitoring stations used for validation of MAX-DOAS NO_2 results.

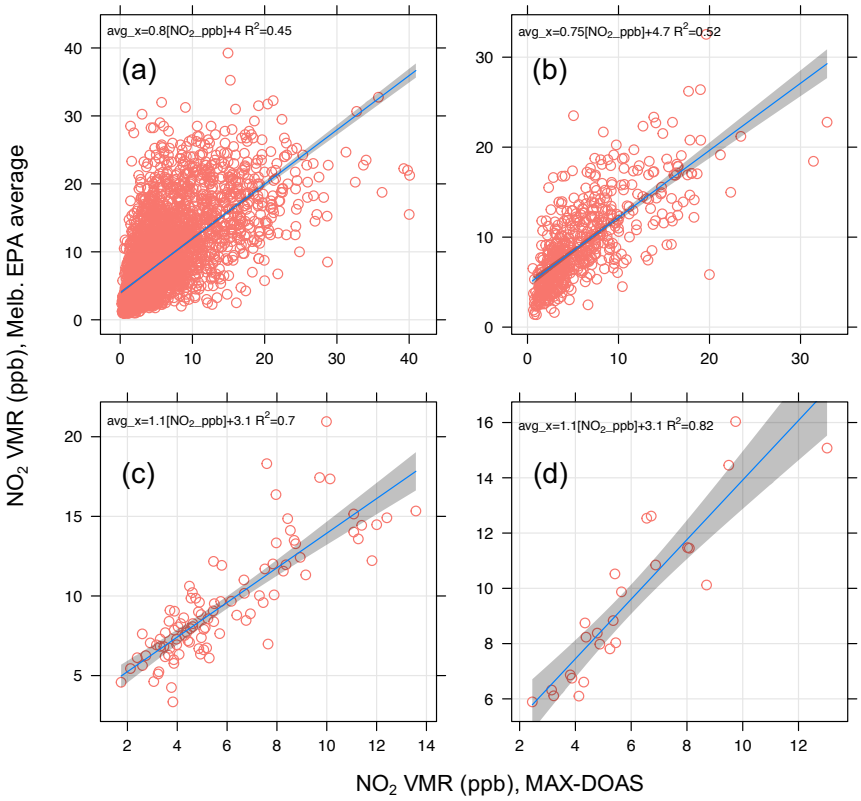

Figure B.4: Scatterplots showing correlation between NO_2 measured by the MAX-DOAS at Broadmeadows and in-situ NO_2 averaged across Melbourne metropolitan EPA monitoring stations. (a) shows hourly average comparison, (b) daily average comparison, (c) weekly averages, (d) monthly averages.

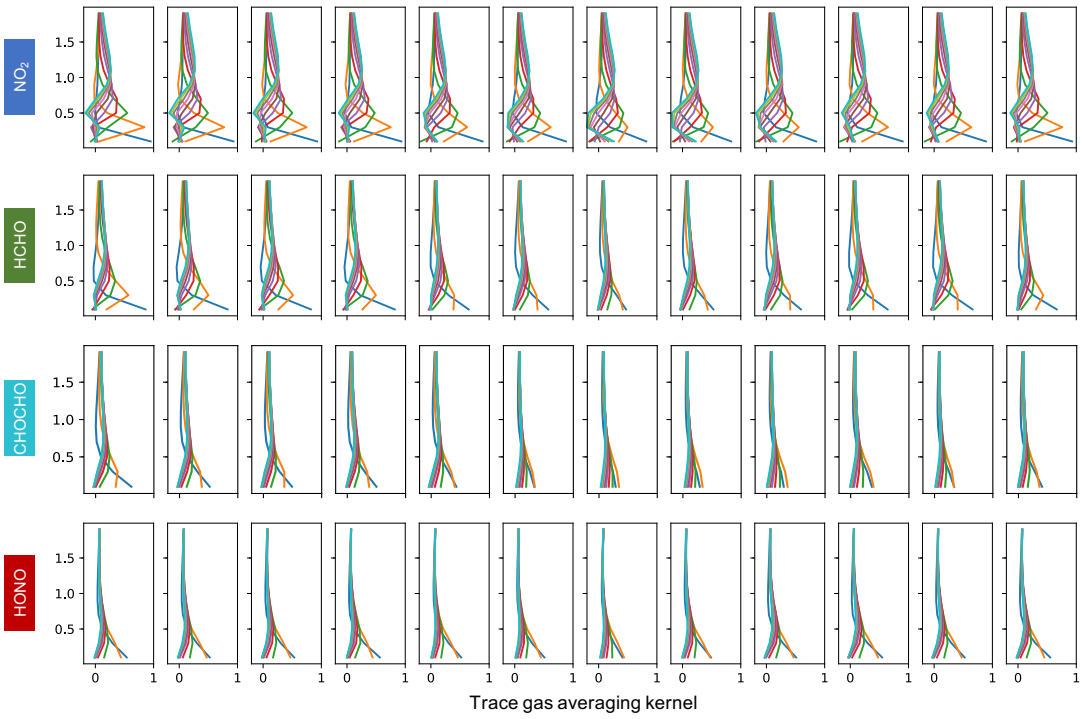

Figure B.5: Monthly averaged averaging kernels (lowest 2 km) for trace gases retrieved at Broadmeadows, 2018 data: top NO_2, middle HCHO and bottom HONO.

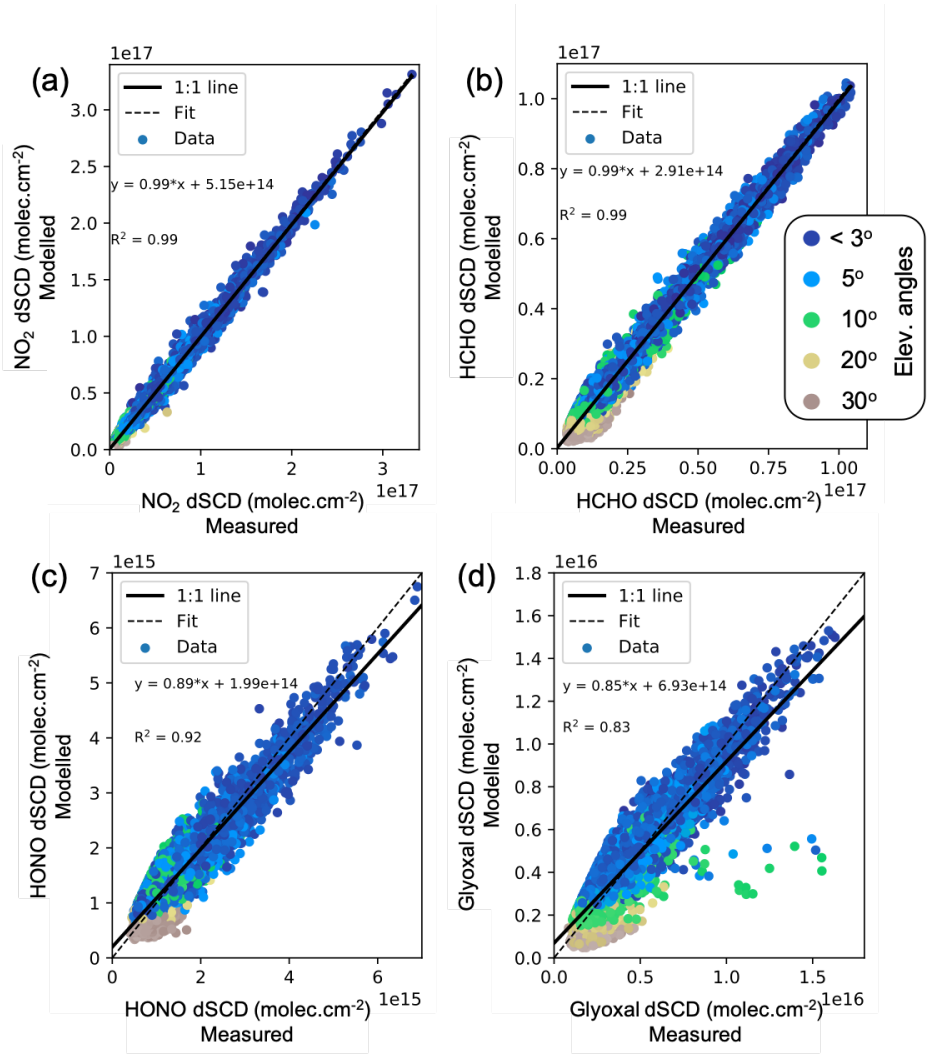

Figure B.6: Comparison of modelled and measured values for the four trace gases retrieved at Broadmeadows, demonstrating successful HEIPRO retrievals.

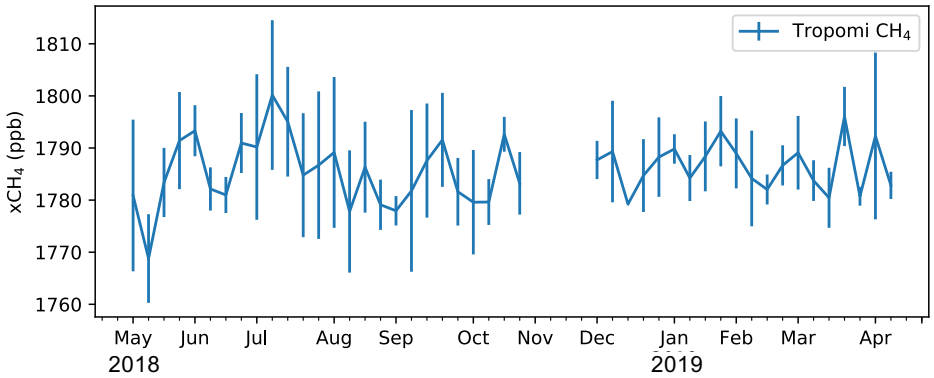

Figure B.7: Methane total column mixing ratios retrieved by the TROPOMI satellite from May 2018 to April 2019. Retrievals have been re-gridded to 0.25x0.25^o resolution then averaged spatially over the state of Victoria, then temporally to produce weekly mean values.

Table B.1: Compilation of urban HONO and NO_2 surface measurements from cities around the world. Average (avg) and maximum (max.) values are from diurnal cycles reported in the papers referenced, and therefore comparable with the diurnal cycle results in this work. It should be noted that the maximum HONO values reported from each paper listed occurred around or shortly after sunrise, as opposed to midday as in this work. * NOx reported rather than NO_2. LOPAP = long path absorption photometer, LP-DOAS = long path differential optical absorption spectrscopy, HPLC = high performance liquid chromatography, CIMS = chemical ionization mass spectrometery

Reference	Location	Season, year	HONO meas. technique	Midday avg HONO (ppbv)	Max. HONO (ppbv)	Midday avg NO_2 (ppv)
Lee et al. (2016)	London, UK	Summer 2012	LOPAP	0.4	0.6	15*
Michoud et al. (2014)	Paris, France	Summer 2009	Wet chemical	0.1	0.2	3
Acker and Möller (2007)	Rome, Italy	Spring 2001	Wet chemical	0.2	0.9	7
Hendrick et al. (2014)	Beijing, China	Summer 2008	MAX-DOAS	0.2	1.0	23
Huang et al. (2017)	Xi'an, China	Summer 2015	LOPAP	0.4	2.2	11
Wang et al. (2013)	Shanghai, China	Summer 2011-12	LP-DOAS	0.6	1.2	15
Xu et al. (2015)	Hong Kong	Summer 2011	LOPAP	0.8	1.0	23
Ren et al. (2003)	New York City, USA	Summer 2001	HPLC	0.4	1.0	25*
Pusede et al. (2015)	Pasadena, USA	Summer 2010	CIMS	0.3	1.1	15
Wong et al. (2012)	Houston, USA	Spring 2009	LP-DOAS	0.1	0.3	7
Elshorbany et al. (2009)	Santiago, Chile	Autumn 2005	LOPAP	1.7	3.7	30
This work	Melbourne, Australia	2016-2019	MAX-DOAS	0.14	0.8	4.5

Table B.2: Compilation of HCHO results from recent long term measurement campaigns recent papers (published 2014 or later) from various urban and rural locations around the world. NB: MD = MAX-DOAS, H = high performance liquid chromatography, WC = wet chemical methods where HCHO gas, added to a solution, is reacted with a coloured reagent that is then detected colourimetrically. U = Urban, R = Rural

Reference	Location, U/R	Period	Method	Monthly avg. range (ppb)	Mean, range (ppb)	Notes
This work	Melbourne, Australia, U	2016-2019	MD	0.8-1.9	1.59, 0.23-12.1	Summer max.
This work	Lauder, New Zealand, R	2016-2019	MD	0.45-0.57	0.54, 0.15-1.70	Summer max.
Benavent et al. (2019)	Madrid, Spain, U	2016 (full year)	MD	5-30	-	Autumn and winter max.
Hoque et al. (2018a)	Phimai, Thailand, R	2014-2016	MD	2-8	-	Dry season max.
Hoque et al. (2018b)	Pantnagar, India, U	2017 (Jan-Nov)	MD	2-6	-	Spring and autumn max.
Wang et al. (2017e)	Wuxi, China, U	2011-2014	MD	2-6	-	Summer max.
Hassan et al. (2018)	Cairo, Egypt, U	2014-2015	WC	19-33	-	Summer max.
Lui et al. (2017)	Hong Kong, China, U	2012-2013	H	-	2.78, 1.70-3.68	Autumn max.
de Blas et al. (2019)	Valderejo, Spain, R	Summer 2016	WC	-	1.42, 0.7-10	Max. on hottest days
Leuchner et al. (2016)	Schneefernerhaus, Germany, R	2012-2013	WC	-	0.58, 0.05-3.96	Summer max.
Yang et al. (2019)	Wuhan, China, U	2017 (full year)	H	-	3.46, 0.98-8.48	Summer max.
Guo et al. (2016)	Nanning, China, U	2011-2012	H	-	4.80, 1.00-10.43	Summer max.
Guo et al. (2014)	Qinzhou, China, U	2011-2012	H	-	4.74, 0.25-17.35	Summer max.

Table B.3: Compilation of validation studies comparing formaldehyde vertical column results for MAX-DOAS and satellite retrievals

Reference	Location	Satellite	Period	Avg	Slope	R^2	Bias (%)
This work	Melbourne, Australia	OMI	2016-2019	Monthly	3.05	0.14	+43.6
" "	Melbourne, Australia	TROPOMI	Dec 2018-May 2019	Daily	0.98	0.67	+15.1
" "	Lauder, NZ	OMI	2016-2019	Monthly	tbd	tbd	tbd
" "	Lauder, NZ	TROPOMI	2016-2019	Daily	tbd	tbd	tbd
Wang et al. (2017d)	Wuxi, China	OMI	2011-2014	Daily	0.48	0.17	-
" "	" "	GOME-2A	2011-2014	Daily	0.61	0.18	-
" "	" "	GOME-2B	2011-2014	Daily	1.03	0.53	-
De Smedt et al. (2015)	Beijing, Xianghe, China	OMI	2008-2013	Monthly	0.60	0.81	-
" "	" "	GOME-2	2008-2013	Monthly	0.80	0.64	-
Chan et al. (2019)	Nanjing, China	OMI	2013-2017	Monthly	0.99	0.56	-
Tian et al. (2018)	Hefei, Nanjing, Shanghai, China	OMI	2013-2016	Monthly	0.84	0.56	-
Vigouroux et al. (2009)	Reunion Island	SCIAMACHY	2004-2005	Monthly	-	-	-11.2
Wittrock et al. (2006)	Nairobi, Kenya	SCIAMACHY	Apr-Jul 2005	Monthly	-	-	-15.5
" "	Cabauw, Netherlands	SCIAMACHY	Apr-Jul 2005	Monthly	-	-	-12.9

Appendix C

Relating to Garden Island campaign

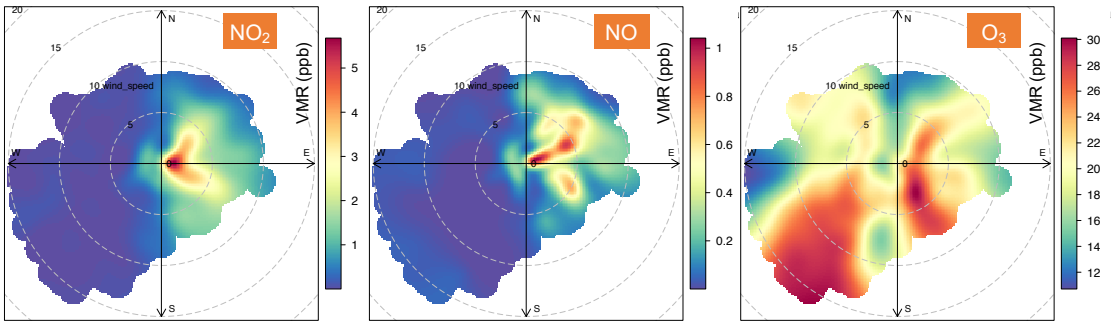

Figure C.1: Polar bivariate plots of insitu trace gas mixing ratio during the Garden Island campaign (NO_2, NO and O_3). Results taken only from daylight hours so as to be comparible with MAX-DOAS measurements.

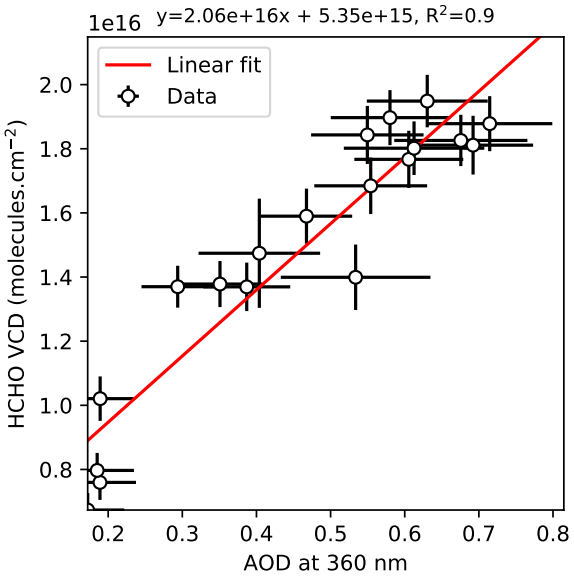

Figure C.2: Scatterplot of aerosol optical depth (AOD) vs formaldehyde VCD for 4th of May 2018 at Garden Island, a day on which a smoke plume blanketed the region. The plot title indicates the equation of the total least squares regression fit to the points.

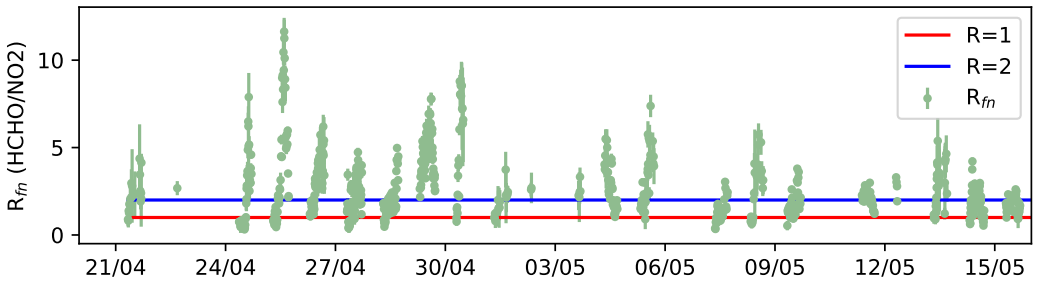

Figure C.3: Timeseries of the ratio of formaldehyde to NO_2 (R_{fn} during the Garden Island campaign.

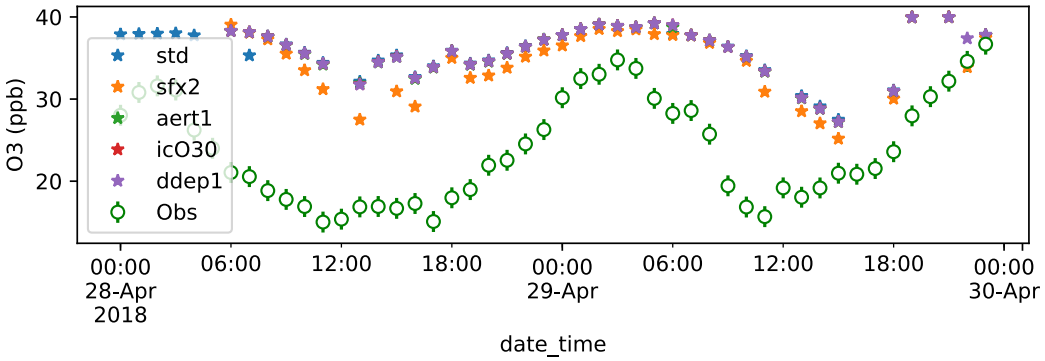

Figure C.4: Time series of ozone mixing ratios, output from CiTTyCAT for in a range of sensitivity tests. The sensitivity test details are outlined in table 6.1 in chapter 6

.

List of acronyms

AERONET: AErosol RObotic NETwork

AMF: Air Mass Factor

AOD: Aerosol Optical Depth

ASL: Above Sea Level

Asy: Aerosol asymmetry parameter

AU: Arbitrary Units

bVOC: Biogenic VOC

BIRA: Belgian Institute for Space Aeronomy

BOM: Australian Bureau of Meteorology

CCD: Charge Coupled Device

CCN: Cloud Condensation Nuclei

CiTTyCAT: Cambridge Tropospheric Trajectory model of Chemistry And Transport

CFC: Chlorofluorocarbon

CI: Colour index

CINDI: Cabauw Intercomparison of Nitrogen Dioxide Instruments

CTM: Chemical Transport Model

DMS: Dimethyl Sulfide

DOAS: Differential Optical Absorption Spectroscopy

dSCD: Differential Slant Column Density

dOD: Differential Optical Depth

DoFs: Degrees of freedom for signal

EA: Elevation Angle

Envimes: Environmental Measurement Systems

FTIR: Fourier Transform InfraRed spectroscopy

GI: Garden Island, Western Australia

GOME: Global Ozone Monitoring Experiment

HEIPRO: HEIdelberg PROfile retrieval algorithm

HO_x: Oxides of hydrogen (i.e. OH + HO_2)

ITCZ: Intertropical convergence zone

lat.: Latitude

LIDAR: LIght Detection And Ranging

lon.: Longitude

MAD-CAT: MAX-DOAS Comparison campaign for Aerosols and Trace gases

MAX-DOAS: Multi-axis DOAS

MEGAN: Model of Emissions of Gases and Aerosols from Nature

MODIS: Moderate Resolution Imaging Spectroradiometer (Satellite)

NIWA: National Institute of Water and Atmosphere research (New Zealand)

NO_x: Oxides of nitrogen (i.e. NO + NO_2)

NZ: New Zealand

OMI: Ozone Monitoring Instrument (Satellite)

PBL: Planetary Boundary Layer

ppb: Parts per billion (mixing ratio)

ppt: Parts per trillion (mixing ratio)

QDOAS: DOAS software developed at BIRA

RHS: Reactive Halogen Species

RMS: Root Mean Squared

RRS: Rotational Raman Scattering

RTE: Radiative Transfer Equation

RTM: Radiative Transfer Model

SCD: Slant Column Density

SCIATRAN: Scanning Imaging Absorption radiative TRANsfer model

SSA: Single scattering albedo

SZA: Solar Zenith Angle

TIMTAM: Trans-Tasman Intercomparison of MAX-DOAS Trace gas and Aerosol Measurements

TROPOMI: TROPOspheric Monitoring Instrument

UM: University of Melbourne

UW: University of Wollongong

UV: Ultraviolet (radiation)

VCD: Vertical Column Density

Vis: Visible (radiation)

VMR: Volume Mixing Ratio

VOC: Volatile Organic Compound

VRS: Vibrational Raman Scattering

WA: Western Australia

XSC: Cross section correction factor

Bibliography

Acker, K. and Möller, D. (2007). Atmospheric variation of nitrous acid at different sites in Europe. *Environmental Chemistry*, 4(4):242–255.

Acker, K., Möller, D., Wieprecht, W., Meixner, F. X., Bohn, B., Gilge, S., Plass-Dülmer, C., and Berresheim, H. (2006). Strong daytime production of OH from HNO2 at a rural mountain site. *Geophysical Research Letters*, 33(2).

Alicke, B., Geyer, A., Hofzumahaus, A., Holland, F., Konrad, S., Pätz, H. W., Schäfer, J., Stutz, J., Volz-Thomas, A., and Platt, U. (2003). OH formation by HONO photolysis during the BERLIOZ experiment. *Journal of Geophysical Research: Atmospheres*, 108(D4):PHO 3–1–PHO 3–17.

Alicke, B., Platt, U., and Stutz, J. (2002). Impact of nitrous acid photolysis on the total hydroxyl radical budget during the Limitation of Oxidant Production/Pianura Padana Produzione di Ozono study in Milan. *Journal of Geophysical Research: Atmospheres*, 107(D22):LOP 9–1–LOP 9–17.

Allan, B. J., McFiggans, G., Plane, J. M., and Coe, H. (2000). Observations of iodine monoxide in the remote marine boundary layer. *Journal of Geophysical Research: Atmospheres*, 105(D11):14363–14369.

Ayers, G. P., Gillett, R. W., Granek, H., de Serves, C., and Cox, R. A. (1997). Formaldehyde production in clean marine air. *Geophysical Research Letters*, 24(4):401–404.

Baidar, S., Hardesty, R. M., Kim, S.-W., Langford, A. O., Oetjen, H., Senff, C. J., Trainer, M., and Volkamer, R. (2015). Weakening of the weekend ozone effect over california's south coast air basin. *Geophysical Research Letters*, 42(21):9457–9464.

Barnett, A. G., Williams, G. M., Schwartz, J., Best, T. L., Neller, A. H., Petroeschevsky, A. L., and Simpson, R. W. (2006). The effects of air pollution on hospitalizations for cardiovascular disease in elderly people in Australian and New Zealand cities. *Environmental health perspectives*, 114(7):1018.

Behrens, L. K., Hilboll, A., Richter, A., Peters, E., Alvarado, L., Kalisz Hedegaard, A. B., Wittrock, F., Burrows, J. P., and Vrekoussis, M. (2019). Detection of outflow of formaldehyde and glyoxal from the African continent to the Atlantic Ocean with a MAX-DOAS instrument. *Atmospheric Chemistry and Physics*, 19(15):10257–10278.

Benavent, N., Garcia-Nieto, D., Wang, S., and Saiz-Lopez, A. (2019). MAX-DOAS measurements and vertical profiles of glyoxal and formaldehyde in Madrid, Spain. *Atmospheric Environment*, 199:357–367.

Boersma, K., Jacob, D. J., Trainic, M., Rudich, Y., DeSmedt, I., Dirksen, R., and Eskes, H. (2009). Validation of urban NO_2 concentrations and their diurnal and seasonal variations observed from the SCIAMACHY and OMI sensors using in situ surface measurements in Israeli cities. *Atmospheric Chemistry and Physics*, 9(12):3867–3879.

Boucher, O., Randall, D., Artaxo, P., Bretherton, C., Feingold, G., Forster, P., Kerminen, V. M., Kondo, Y., Liao, H., Lohmann, U., Rasch, P., Satheesh, S. K., Sherwood, S., Stevens, B., and Zhang, X. Y. (2013). Clouds and Aerosols. In Stocker, T. F., Qin, D., Plattner, G. K., Tignor, M., Allen, S. K., Boschung, J., Nauels, A., Xia, Y., Bex, V., and Midgley, P. M., editors, *Climate Change 2013: The Physical Science Basis. Contribution of Working Group I to the Fifth Assessment Report of the Intergovernmental Panel on Climate Change*, pages 571–658. Cambridge University Press, Cambridge, United Kingdom and New York, NY, USA.

Carpenter, L. J., MacDonald, S. M., Shaw, M. D., Kumar, R., Saunders, R. W., Parthipan, R., Wilson, J., and Plane, J. M. (2013). Atmospheric iodine levels influenced by sea surface emissions of inorganic iodine. *Nature Geoscience*, 6(2):108–111.

Carslaw, D., Beevers, S., Westmoreland, E., Williams, M., Tate, J., Murrells, T., Stedman, J., Li, Y., Grice, S., Kent, A., and Tsagatakis, I. (2011). Trends in NO_x and NO_2 emissions and ambient measurements in the UK. Scientific Report.

Carslaw, D. C., Murrells, T. P., Andersson, J., and Keenan, M. (2016). Have vehicle emissions of primary NO_2 peaked? *Faraday Discussions*, 189:439–454.

Chan, K., Wiegner, M., Wenig, M., and Pöhler, D. (2018). Observations of tropospheric aerosols and NO_2 in Hong Kong over 5 years using ground based MAX-DOAS. *Science of the Total Environment*, 619:1545–1556.

Chan, K. L., Wang, Z., Ding, A., Heue, K.-P., Shen, Y., Wang, J., Zhang, F., Shi, Y., Hao, N., and Wenig, M. (2019). MAX-DOAS measurements of tropospheric NO_2 and HCHO in Nanjing and a comparison to ozone monitoring instrument observations. *Atmospheric Chemistry and Physics*, 19(15):10051–10071.

Chan Miller, C., Gonzalez Abad, G., Wang, H., Liu, X., Kurosu, T., Jacob, D., and Chance, K. (2014). Glyoxal retrieval from the ozone monitoring instrument. *Atmospheric Measurement Techniques*, 7(11):3891–3907.

Chance, K., Palmer, P. I., Spurr, R. J., Martin, R. V., Kurosu, T. P., and Jacob, D. J. (2000). Satellite observations of formaldehyde over North America from GOME. *Geophysical Research Letters*, 27(21):3461–3464.

Chance, K. V. and Spurr, R. J. D. (1997). Ring effect studies: Rayleigh scattering,

including molecular parameters for rotational Raman scattering, and the Fraunhofer spectrum. *Applied Optics*, 36(21):5224–5230.

Clémer, K., Van Roozendael, M., Fayt, C., Hendrick, F., Hermans, C., Pinardi, G., Spurr, R., Wang, P., and De Mazière, M. (2010). Multiple wavelength retrieval of tropospheric aerosol optical properties from MAXDOAS measurements in Beijing. *Atmospheric Measurement Techniques*, 3(4):863–878.

Commane, R., Seitz, K., Bale, C. S. E., Bloss, W. J., Buxmann, J., Ingham, T., Platt, U., Pöhler, D., and Heard, D. E. (2011). Iodine monoxide at a clean marine coastal site: observations of high frequency variations and inhomogeneous distributions. *Atmospheric Chemistry and Physics*, 11(13):6721–6733.

Cushing, N. (2020). Even for an air pollution historian like me, these past weeks have been a shock. *The Conversation*.

de Blas, M., Ibáñez, P., García, J. A., Gómez, M. C., Navazo, M., Alonso, L., Durana, N., Iza, J., Gangoiti, G., and de Cámara, E. S. (2019). Summertime high resolution variability of atmospheric formaldehyde and non-methane volatile organic compounds in a rural background area. *Science of the Total Environment*, 647:862–877.

De Smedt, I., Stavrakou, T., Hendrick, F., Danckaert, T., Vlemmix, T., Pinardi, G., Theys, N., Lerot, C., Gielen, C., Vigouroux, C., Hermans, C., Fayt, C., Veefkind, P., Müller, J.-F., and Van Roozendael, M. (2015). Diurnal, seasonal and long-term variations of global formaldehyde columns inferred from combined OMI and GOME-2 observations. *Atmospheric Chemistry and Physics*, 15(21):12519–12545.

DiGangi, J., Henry, S., Kammrath, A., Boyle, E., Kaser, L., Schnitzhofer, R., Graus, M., Turnipseed, A., Park, J., and Weber, R. (2012). Observations of glyoxal and formaldehyde as metrics for the anthropogenic impact on rural photochemistry. *Atmospheric Chemistry and Physics*, 12(20):9529–9543.

Dignon, J. and Hameed, S. (1989). Global emissions of nitrogen and sulfur oxides from 1860 to 1980. *JAPCA*, 39(2):180–186.

Doherty, R. M. (2015). Atmospheric chemistry: Ozone pollution from near and far. *Nature Geoscience*, 8(9):664–665.

Donaldson, M. A., Berke, A. E., and Raff, J. D. (2013). Uptake of gas phase nitrous acid onto boundary layer soil surfaces. *Environmental Science Technology*, 48(1):375–383.

Donaldson, M. A., Bish, D. L., and Raff, J. D. (2014). Soil surface acidity plays a determining role in the atmospheric-terrestrial exchange of nitrous acid. *Proceedings of the National Academy of Sciences*, 111(52):18472.

Donner, S., Kuhn, J., Van Roozendael, M., Bais, A., Beirle, S., Bösch, T., Bognar, K., Bruchkouski, I., Chan, K. L., Dörner, S., Drosoglou, T., Fayt, C., Frieß, U., Hendrick, F., Hermans, C., Jin, J., Li, A., Ma, J., Peters, E., Pinardi, G., Richter, A., Schreier,

S. F., Seyler, A., Strong, K., Tirpitz, J.-L., Wang, Y., Xie, P., Xu, J., Zhao, X., and Wagner, T. (2020). Evaluating different methods for elevation calibration of MAX-DOAS (Multi AXis Differential Optical Absorption Spectroscopy) instruments during the CINDI-2 campaign. *Atmospheric Measurement Techniques*, 13(2):685–712.

Duncan, B. N., Lamsal, L. N., Thompson, A. M., Yoshida, Y., Lu, Z., Streets, D. G., Hurwitz, M. M., and Pickering, K. E. (2016). A space based, high resolution view of notable changes in urban NO_x pollution around the world (2005–2014). *Journal of Geophysical Research: Atmospheres*, 121(2).

Duncan, B. N., Yoshida, Y., Damon, M. R., Douglass, A. R., and Witte, J. C. (2009). Temperature dependence of factors controlling isoprene emissions. *Geophysical Research Letters*, 36(5).

Duncan, B. N., Yoshida, Y., Olson, J. R., Sillman, S., Martin, R. V., Lamsal, L., Hu, Y., Pickering, K. E., Retscher, C., and Allen, D. J. (2010). Application of OMI observations to a space-based indicator of NOx and VOC controls on surface ozone formation. *Atmospheric Environment*, 44(18):2213–2223.

Elshorbany, Y., Kurtenbach, R., Wiesen, P., Lissi, E., Rubio, M., Villena, G., Gramsch, E., Rickard, A., Pilling, M., and Kleffmann, J. (2009). Oxidation capacity of the city air of Santiago, Chile. *Atmospheric Chemistry and Physics*, 9(6):2257–2273.

Emmerson, K. M., Cope, M. E., Galbally, I. E., Lee, S., and Nelson, P. F. (2018). Isoprene and monoterpene emissions in south-east Australia: comparison of a multi-layer canopy model with MEGAN and with atmospheric observations. *Atmospheric Chemistry and Physics*, 18(10):7539–7556.

Emmerson, K. M., Galbally, I. E., Guenther, A. B., Paton-Walsh, C., Guerette, E.-A., Cope, M. E., Keywood, M. D., Lawson, S. J., Molloy, S. B., Dunne, E., Thatcher, M., Karl, T., and Maleknia, S. D. (2016). Current estimates of biogenic emissions from eucalypts uncertain for southeast Australia. *Atmospheric Chemistry and Physics*, 16(11):6997–7011.

EPA, V. (2013). Future air quality in Victoria Future air quality in Victoria – Final report. Scientific Report.

Finlayson-Pitts, B. J. and Pitts Jr, J. N. (1999). *Chemistry of the upper and lower atmosphere: theory, experiments, and applications*. Academic Press.

Fischer, E. V., Jacob, D. J., Yantosca, R. M., Sulprizio, M. P., Millet, D. B., Mao, J., Paulot, F., Singh, H. B., Roiger, A., Ries, L., Talbot, R. W., Dzepina, K., and Pandey Deolal, S. (2014). Atmospheric peroxyacetyl nitrate (PAN): a global budget and source attribution. *Atmospheric Chemistry and Physics*, 14(5):2679–2698.

Fischer, H., Kormann, R., Klüpfel, T., Gurk, C., Königstedt, R., Parchatka, U., Mühle, J., Rhee, T. S., Brenninkmeijer, C. A. M., Bonasoni, P., and Stohl, A. (2003).

Ozone production and trace gas correlations during the June 2000 MINATROC intensive measurement campaign at Mt. Cimone. *Atmospheric Chemistry and Physics*, 3(3):725–738.

Fish, D. J. and Jones, R. L. (1995). Rotational Raman scattering and the ring effect in zenith-sky spectra. *Geophysical Research Letters*, 22(7):811–814.

Fleischmann, O. C., Hartmann, M., Burrows, J. P., and Orphal, J. (2004). New ultraviolet absorption cross-sections of BrO at atmospheric temperatures measured by time-windowing Fourier transform spectroscopy. *Journal of Photochemistry and Photobiology A: Chemistry*, 168(1):117–132.

Franco, B., Hendrick, F., Van Roozendael, M., Müller, J.-F., Stavrakou, T., Marais, E. A., Bovy, B., Bader, W., Fayt, C., Hermans, C., Lejeune, B., Pinardi, G., Servais, C., and Mahieu, E. (2015). Retrievals of formaldehyde from ground-based FTIR and MAX-DOAS observations at the Jungfraujoch station and comparisons with GEOS-Chem and IMAGES model simulations. *Atmospheric Measurement Techniques*, 8(4):1733–1756.

Fraser, A., Chan Miller, C., Palmer, P. I., Deutscher, N. M., Jones, N. B., and Griffith, D. W. T. (2011). The Australian methane budget: Interpreting surface and train-borne measurements using a chemistry transport model. *Journal of Geophysical Research: Atmospheres*, 116(D20).

Fried, A., McKeen, S., Sewell, S., Harder, J., Henry, B., Goldan, P., Kuster, W., Williams, E., Baumann, K., Shetter, R., and Cantrell, C. (1997). Photochemistry of formaldehyde during the 1993 Tropospheric OH Photochemistry Experiment. *Journal of Geophysical Research: Atmospheres*, 102(D5):6283–6296.

Frieß, U., Klein Baltink, H., Beirle, S., Clemer, K., Hendrick, F., Henzing, B., Irie, H., de Leeuw, G., Li, A., Moerman, M. M., van Roozendael, M., Shaiganfar, R., Wagner, T., Wang, Y., Xie, P., Yilmaz, S., and Zieger, P. (2016). Intercomparison of aerosol extinction profiles retrieved from MAX-DOAS measurements. *Atmospheric Measurement Techniques*, 9(7):3205–3222.

Frieß, U., Monks, P. S., Remedios, J. J., Rozanov, A., Sinreich, R., Wagner, T., and Platt, U. (2006). MAX-DOAS O_4 measurements: A new technique to derive information on atmospheric aerosols: 2. Modeling studies. *Journal of Geophysical Research: Atmospheres*, 111(D14).

Fu, T.-M., Jacob, D. J., Wittrock, F., Burrows, J. P., Vrekoussis, M., and Henze, D. K. (2008). Global budgets of atmospheric glyoxal and methylglyoxal, and implications for formation of secondary organic aerosols. *Journal of Geophysical Research: Atmospheres*, 113(D15).

Fuentes, J. D., Lerdau, M., Atkinson, R., Baldocchi, D., Bottenheim, J., Ciccioli, P., Lamb, B., Geron, C., Gu, L., Guenther, A., Sharkeyj, T. D., and Stockwell, W.

(2000). Biogenic hydrocarbons in the atmospheric boundary layer: a review. *Bulletin of the American Meteorological Society*, 81(7):1537–1576.

Geddes, J. A., Martin, R. V., Boys, B. L., and van Donkelaar, A. (2015). Long-term trends worldwide in ambient NO_2 concentrations inferred from satellite observations. *Environmental Health Perspectives*, 124(3):281–289.

George, C., Strekowski, R., Kleffmann, J., Stemmler, K., and Ammann, M. (2005). Photoenhanced uptake of gaseous NO_2 on solid organic compounds: a photochemical source of HONO? *Faraday Discussions*, 130:195–210.

Gielen, C., Van Roozendael, M., Hendrick, F., Pinardi, G., Vlemmix, T., De Bock, V., De Backer, H., Fayt, C., Hermans, C., and Gillotay, D. (2014). A simple and versatile cloud-screening method for MAX-DOAS retrievals. *Atmospheric Measurement Techniques*, 7(10):3509.

Grainger, J. F. and Ring, J. (1962). Anomalous Fraunhofer Line Profiles. *Nature*, 193(4817):762–762.

Grange, S. K., Farren, N. J., Vaughan, A. R., Rose, R. A., and Carslaw, D. (2019). Strong temperature dependence for light-duty diesel vehicle NOx emissions. *Environmental Science & Technology*.

Großmann, K, K., Frieß, U., Peters, E., Wittrock, F., Lampel, J., Yilmaz, S., Tschritter, J., Sommariva, R., Glasow, R. v., and Quack, B. (2013). Iodine monoxide in the Western Pacific marine boundary layer. *Atmospheric Chemistry and Physics*, 13(6):3363–3378.

Guenther, A., Jiang, X., Heald, C., Sakulyanontvittaya, T., Duhl, T., Emmons, L., and Wang, X. (2012). The Model of Emissions of Gases and Aerosols from Nature version 2.1 (MEGAN2. 1): an extended and updated framework for modeling biogenic emissions. *Geoscientific Model Development*, 5(6):1471–1492.

Guo, S., Chen, M., and Tan, J. (2016). Seasonal and diurnal characteristics of atmospheric carbonyls in Nanning, China. *Atmospheric Research*, 169:46–53.

Guo, S.-J., Chen, M., He, X.-L., Yang, W.-W., and Tan, J.-H. (2014). Seasonal and diurnal characteristics of carbonyls in urban air in Qinzhou, China. *Aerosol and Air Quality Research*, 14:1653–1664.

Hafeez, F., Frost, A., Vaze, J., Dutta, D., Smith, A., and Elmahdi, A. (2015). A new integrated continental hydrological simulation system. *Water: Journal of the Australian Water Association*, 42(3):75.

Harrison, A. W. and Kendall, D. J. W. (1974). Fraunhofer Line Filling In (3855–1455 A). *Canadian Journal of Physics*, 52(11):940–944.

Hassan, S. K., El-Abssawy, A. A., and Khoder, M. I. (2018). Effect of Seasonal Variation

on the Levels and Behaviours of Formaldehyde in the Atmosphere of a Suburban Area in Cairo, Egypt. *Asian Journal of Atmospheric Environment (AJAE)*, 12(4).

He, C., Murray, F., and Lyons, T. (2000). Monoterpene and isoprene emissions from 15 Eucalyptus species in Australia. *Atmospheric Environment*, 34(4):645–655.

Heckel, A., Richter, A., Tarsu, T., Wittrock, F., Hak, C., Pundt, I., Junkermann, W., and Burrows, J. (2005). MAX-DOAS measurements of formaldehyde in the Po-Valley. *Atmospheric Chemistry and Physics*, 5(4):909–918.

Hendrick, F., Müller, J.-F., Clémer, K., Wang, P., Mazière, M. D., Fayt, C., Gielen, C., Hermans, C., Ma, J., and Pinardi, G. (2014). Four years of ground-based MAX-DOAS observations of HONO and NO_2 in the Beijing area. *Atmospheric Chemistry and Physics*, 14(2):765–781.

Hendrick, F., Van Roozendael, M., Kylling, A., Petritoli, A., Rozanov, A., Sanghavi, S., Schofield, R., von Friedeburg, C., Wagner, T., Wittrock, F., Fonteyn, D., and De Mazière, M. (2006). Intercomparison exercise between different radiative transfer models used for the interpretation of ground-based zenith-sky and multi-axis DOAS observations. *Atmospheric Chemistry and Physics*, 6(1):93–108.

Henze, D., Seinfeld, J., Ng, N., Kroll, J., Fu, T.-M., Jacob, D. J., and Heald, C. (2008). Global modeling of secondary organic aerosol formation from aromatic hydrocarbons: high-vs. low-yield pathways. *Atmospheric Chemistry and Physics*, 8(9):2405–2420.

Hermans, C., Vandaele, A., Fally, S., Carleer, M., Colin, R., Coquart, B., Jenouvrier, A., and Merienne, M.-F. (2003). Absorption cross-section of the collision induced bands of oxygen from the UV to the NIR. In *Weakly interacting molecular pairs: unconventional absorbers of radiation in the atmosphere*, pages 193–202. Springer.

Hesterberg, T. W., Bunn, W. B., McClellan, R. O., Hamade, A. K., Long, C. M., and Valberg, P. A. (2009). Critical review of the human data on short-term nitrogen dioxide (NO_2) exposures: evidence for NO_2 no-effect levels. *Critical reviews in toxicology*, 39(9):743–781.

Hönninger, G. and Platt, U. (2002). Observations of BrO and its vertical distribution during surface ozone depletion at Alert. *Atmospheric Environment*, 36(15–16):2481–2489.

Hönninger, G., von Friedeburg, C., and Platt, U. (2004). Multi axis differential optical absorption spectroscopy (MAX-DOAS). *Atmospheric Chemistry and Physics*, 4(1):231–254.

Hoque, H., Irie, H., and Damiani, A. (2018a). First MAX-DOAS Observations of Formaldehyde and Glyoxal in Phimai, Thailand. *Journal of Geophysical Research: Atmospheres*, 123(17):9957–9975.

Hoque, H. M. S., Irie, H., Damiani, A., Rawat, P., and Naja, M. (2018b). First simulta-

neous observations of formaldehyde and glyoxal by MAX-DOAS in the Indo-Gangetic Plain region. *SOLA*, 14:159–164.

Huang, R.-J., Yang, L., Cao, J., Wang, Q., Tie, X., Ho, K.-F., Shen, Z., Zhang, R., Li, G., and Zhu, C. (2017). Concentration and sources of atmospheric nitrous acid (HONO) at an urban site in Western China. *Science of The Total Environment*, 593:165–172.

Irie, H., Kanaya, Y., Akimoto, H., Iwabuchi, H., Shimizu, A., and Aoki, K. (2008). First retrieval of tropospheric aerosol profiles using MAX-DOAS and comparison with lidar and sky radiometer measurements. *Atmospheric Chemistry and Physics*, 8(2):341–350.

Irie, H., Takashima, H., Kanaya, Y., Boersma, K., Gast, L., Wittrock, F., Brunner, D., Zhou, Y., and Roozendael, M. V. (2011). Eight-component retrievals from ground-based MAX-DOAS observations. *Atmospheric Measurement Techniques*, 4(6):1027–1044.

Jacob, D. (1999). *Introduction to Atmospheric Chemistry*. Princeton University Press.

Jang, M., Czoschke, N. M., Lee, S., and Kamens, R. M. (2002). Heterogeneous atmospheric aerosol production by acid-catalyzed particle-phase reactions. *Science*, 298(5594):814–817.

Javed, Z., Liu, C., Khokhar, M. F., Xing, C., Tan, W., Subhani, M. A., Rehman, A., and Tanvir, A. (2019). Investigating the impact of glyoxal retrieval from MAX-DOAS observations during haze and non-haze conditions in Beijing. *Journal of Environmental Sciences*, 80:296–305.

Jiménez, R., Martilli, A., Balin, I., Van den Bergh, H., Calpini, B., Larsen, B., Favaro, G., and Kita, D. (2000). Measurement of formaldehyde (HCHO) by DOAS: Intercomparison to DNPH measurements and interpretation from Eulerian model calculations. In *Proceedings of A&WMA 93rd Annual Conference, Salt Lake City (UT), Paper*, volume 829.

Jin, X., Fiore, A. M., Murray, L. T., Valin, L. C., Lamsal, L. N., Duncan, B., Folkert Boersma, K., De Smedt, I., Abad, G. G., Chance, K., and Tonnesen, G. S. (2017). Evaluating a Space-Based Indicator of Surface Ozone-NOx-VOC Sensitivity Over Midlatitude Source Regions and Application to Decadal Trends. *Journal of Geophysical Research: Atmospheres*, 122(19):10,439–10,461.

Johansson, M., Rivera, C., Foy, B. d., Lei, W., Song, J., Zhang, Y., Galle, B., and Molina, L. (2009). Mobile mini-DOAS measurement of the outflow of NO_2 and HCHO from Mexico City. *Atmospheric Chemistry and Physics*, 9(15):5647–5653.

Jones, N., Koike, M., Matthews, W., and McNamara, B. (1994). Southern hemisphere mid-latitude seasonal cycle in total column nitric acid. *Geophysical Research Letters*, 21(7):593–596.

Jones, N., Riedel, K., Allan, W., Wood, S., Palmer, P., Chance, K., and Notholt, J. (2009). Long-term tropospheric formaldehyde concentrations deduced from ground-based fourier transform solar infrared measurements. *Atmospheric Chemistry and Physics*, 9(18):7131–7142.

Kaiser, J., Wolfe, G. M., Min, K. E., Brown, S. S., Miller, C. C., Jacob, D. J., deGouw, J. A., Graus, M., Hanisco, T. F., Holloway, J., Peischl, J., Pollack, I. B., Ryerson, T. B., Warneke, C., Washenfelder, R. A., and Keutsch, F. N. (2015). Reassessing the ratio of glyoxal to formaldehyde as an indicator of hydrocarbon precursor speciation. *Atmospheric Chemistry and Physics*, 15(13):7571–7583.

Keywood, M., Cope, M., Meyer, C. M., Iinuma, Y., and Emmerson, K. (2015). When smoke comes to town: The impact of biomass burning smoke on air quality. *Atmospheric Environment*, 121:13–21.

Khokhar, M., Naveed, S., Butt, J., and Abbas, Z. (2016). Comparative Analysis of Atmospheric Glyoxal Column Densities Retrieved from MAX-DOAS Observations in Pakistan and during MAD-CAT Field Campaign in Mainz, Germany. *Atmosphere*, 7(5):68.

Kleffmann, J. (2007). Daytime sources of nitrous acid (HONO) in the atmospheric boundary layer. *ChemPhysChem*, 8(8):1137–1144.

Kleffmann, J., Gavriloaiei, T., Hofzumahaus, A., Holland, F., Koppmann, R., Rupp, L., Schlosser, E., Siese, M., and Wahner, A. (2005). Daytime formation of nitrous acid: A major source of OH radicals in a forest. *Geophysical Research Letters*, 32(5).

Kleinman, L. I. (1994). Low and high NOx tropospheric photochemistry. *Journal of Geophysical Research: Atmospheres*, 99(D8):16831–16838.

Kreher, K., Van Roozendael, M., Hendrick, F., Apituley, A., Dimitropoulou, E., Frieß, U., Richter, A., Wagner, T., Lampel, J., Abuhassan, N., Ang, L., Anguas, M., Bais, A., Benavent, N., Bösch, T., Bognar, K., Borovski, A., Bruchkouski, I., Cede, A., Chan, K. L., Donner, S., Drosoglou, T., Fayt, C., Finkenzeller, H., Garcia-Nieto, D., Gielen, C., Gómez-Martín, L., Hao, N., Henzing, B., Herman, J. R., Hermans, C., Hoque, S., Irie, H., Jin, J., Johnston, P., Khayyam Butt, J., Khokhar, F., Koenig, T. K., Kuhn, J., Kumar, V., Liu, C., Ma, J., Merlaud, A., Mishra, A. K., Müller, M., Navarro-Comas, M., Ostendorf, M., Pazmino, A., Peters, E., Pinardi, G., Pinharanda, M., Piters, A., Platt, U., Postylyakov, O., Prados-Roman, C., Puentedura, O., Querel, R., Saiz-Lopez, A., Schönhardt, A., Schreier, S. F., Seyler, A., Sinha, V., Spinei, E., Strong, K., Tack, F., Tian, X., Tiefengraber, M., Tirpitz, J.-L., van Gent, J., Volkamer, R., Vrekoussis, M., Wang, S., Wang, Z., Wenig, M., Wittrock, F., Xie, P. H., Xu, J., Yela, M., Zhang, C., and Zhao, X. (2020). Intercomparison of NO_2, O_4, O_3 and HCHO slant column measurements by MAX-DOAS and zenith-sky UV–visible spectrometers during CINDI-2. *Atmospheric Measurement Techniques*, 13(5):2169–2208.

Kurosu, T. P., Chance, K., Liu, X., Volkamer, R., Fu, T.-M., Millet, D., Jacob, D. J., and Levelt, P. (2007). Seasonally resolved global distributions of glyoxal and formaldehyde observed from the Ozone Monitoring Instrument on EOS Aura. *Proceeding of Anais XIII Simpósio Brasileiro de Sensoriamento Remoto*, 21(26):6461.

Kurtén, T., Elm, J., Prisle, N. L., Mikkelsen, K. V., Kampf, C. J., Waxman, E. M., and Volkamer, R. (2015). Computational study of the effect of glyoxal–sulfate clustering on the henry's law coefficient of glyoxal. *The Journal of Physical Chemistry A*, 119(19):4509–4514.

Lampel, J. (2014). *Measurements of reactive trace gases in the marine boundary layer using novel DOAS methods*. PhD thesis, University of Heidelberg.

Lampel, J., Frieß, U., and Platt, U. (2015). The impact of vibrational Raman scattering of air on DOAS measurements of atmospheric trace gases. *Atmospheric Measurement Techniques*, 8(9):3767–3787.

Lampel, J., Pöhler, D., Polyansky, O. L., Kyuberis, A. A., Zobov, N. F., Tennyson, J., Lodi, L., Frieß, U., Wang, Y., and Beirle, S. (2017). Detection of water vapour absorption around 363 nm in measured atmospheric absorption spectra and its effect on DOAS evaluations. *Atmospheric Chemistry and Physics*, 17(2):1271–1295.

Lee, H., Ryu, J., Irie, H., Jang, S.-H., Park, J., Choi, W., and Hong, H. (2015). Investigations of the diurnal variation of vertical HCHO profiles based on MAX-DOAS measurements in Beijing: Comparisons with OMI vertical column data. *Atmosphere*, 6(11):1816–1832.

Lee, J., Whalley, L., Heard, D., Stone, D., Dunmore, R., Hamilton, J., Young, D., Allan, J., Laufs, S., and Kleffmann, J. (2016). Detailed budget analysis of HONO in central London reveals a missing daytime source. *Atmospheric Chemistry and Physics*, 16(5):2747–2764.

Leighton, P. A. (1961). *Photochemistry of air pollution*. Academic Press.

Lelieveld, J., Dentener, F., Peters, W., and Krol, M. (2004). On the role of hydroxyl radicals in the self-cleansing capacity of the troposphere. *Atmospheric Chemistry and Physics*, 4(9/10):2337–2344.

Lelieveld, J. and Dentener, F. J. (2000). What controls tropospheric ozone? *Journal of Geophysical Research: Atmospheres*, 105(D3):3531–3551.

Leser, H., Hönninger, G., and Platt, U. (2003). Max-doas measurements of bro and no2 in the marine boundary layer. *Geophysical Research Letters*, 30(10).

Leuchner, M., Ghasemifard, H., Lüpke, M., Ries, L., Schunk, C., and Menzel, A. (2016). Seasonal and diurnal variation of formaldehyde and its meteorological drivers at the GAW site Zugspitze. *Aerosol and Air Quality Research*, 16:801–815.

Lewis, S. C. and Karoly, D. J. (2013). Anthropogenic contributions to Australia's record summer temperatures of 2013. *Geophysical Research Letters*, 40(14):3705–3709.

Lewis, S. C. and King, A. D. (2015). Dramatically increased rate of observed hot record breaking in recent Australian temperatures. *Geophysical Research Letters*, 42(18):7776–7784.

Li, J., Mao, J., Min, K.-E., Washenfelder, R. A., Brown, S. S., Kaiser, J., Keutsch, F. N., Volkamer, R., Wolfe, G. M., Hanisco, T. F., Pollack, I. B., Ryerson, T. B., Graus, M., Gilman, J. B., Lerner, B. M., Warneke, C., de Gouw, J. A., Middlebrook, A. M., Liao, J., Welti, A., Henderson, B. H., McNeill, V. F., Hall, S. R., Ullmann, K., Donner, L. J., Paulot, F., and Horowitz, L. W. (2016). Observational constraints on glyoxal production from isoprene oxidation and its contribution to organic aerosol over the southeast united states. *Journal of Geophysical Research: Atmospheres*, 121(16):9849–9861.

Li, X., Brauers, T., Häseler, R., Bohn, B., Fuchs, H., Hofzumahaus, A., Holland, F., Lou, S., Lu, K., and Rohrer, F. (2012). Exploring the atmospheric chemistry of nitrous acid (HONO) at a rural site in Southern China. *Atmospheric Chemistry and Physics*, 12(3):1497–1513.

Li, X., Brauers, T., Hofzumahaus, A., Lu, K., Li, Y. P., Shao, M., Wagner, T., and Wahner, A. (2013). MAX-DOAS measurements of NO_2, HCHO and CHOCHO at a rural site in Southern China. *Atmospheric Chemistry and Physics*, 13(4):2133–2151.

Li, X., Rohrer, F., Hofzumahaus, A., Brauers, T., Häseler, R., Bohn, B., Broch, S., Fuchs, H., Gomm, S., and Holland, F. (2014). Missing gas-phase source of HONO inferred from Zeppelin measurements in the troposphere. *Science*, 344(6181):292–296.

Lieschke, K. J., Fisher, J. A., Paton-Walsh, C., Jones, N. B., Greenslade, J. W., Burden, S., and Griffith, D. W. (2019). Decreasing Trend in Formaldehyde Detected From 20-Year Record at Wollongong, Southeast Australia. *Geophysical Research Letters*, 46(14):8464–8473.

Lin, Y. C., Schwab, J. J., Demerjian, K. L., Bae, M.-S., Chen, W.-N., Sun, Y., Zhang, Q., Hung, H.-M., and Perry, J. (2012). Summertime formaldehyde observations in New York City: Ambient levels, sources and its contribution to HO_x radicals. *Journal of Geophysical Research: Atmospheres*, 117(D8).

Linfoot, S., Quigley, S., and Riley, M. (2005). Ozone events in Sydney—Implications for standard setting and investigation of control strategies. In *Proceedings of the 17th International Clean Air & Environment Conference, Hobart, Tasmania*, pages 3–6.

Liou, K.-N. (2002). *An introduction to atmospheric radiation*. Academic Press, California, USA, 2 edition.

Loh, Z., Law, R., Haynes, K., Krummel, P., Steele, L., Fraser, P., Chambers, S., and Williams, A. (2015). Simulations of atmospheric methane for Cape Grim, Tasmania,

to constrain southeastern Australian methane emissions. *Atmospheric Chemistry and Physics*, 15(1):305–317.

Lui, K., Ho, S. S. H., Louie, P. K., Chan, C., Lee, S., Hu, D., Chan, P., Lee, J. C. W., and Ho, K. (2017). Seasonal behavior of carbonyls and source characterization of formaldehyde (HCHO) in ambient air. *Atmospheric environment*, 152:51–60.

MacDonald, S., Oetjen, H., Mahajan, A., Whalley, L., Edwards, P., Heard, D., Jones, C., and Plane, J. (2012). DOAS measurements of formaldehyde and glyoxal above a south-east Asian tropical rainforest. *Atmospheric Chemistry and Physics*, 12(13):5949–5962.

MacIntyre, E. A., Gehring, U., Mölter, A., Fuertes, E., Klümper, C., Krämer, U., Quass, U., Hoffmann, B., Gascon, M., Brunekreef, B., Koppelman, G. H., , Beelen, R., Hoek, G., Birk, M., de Jongste, J. C., Smit, H. A., Cyrys, J., Gruzieva, O., Korek, M., Bergström, A., Agius, R. M., de Vocht, F., Simpson, A., Porta, D., Forastiere, F., Badaloni, C., Cesaroni, G., Esplugues, A., Fernández-Somoano, A., Lerxundi, A., Sunyer, J., Cirach, M., Nieuwenhuijsen, M. J., Pershagen, G., and Heinrich, J. (2013). Air pollution and respiratory infections during early childhood: an analysis of 10 European birth cohorts within the ESCAPE Project. *Environmental Health Perspectives*, 122(1):107–113.

Madronich, S. and Flocke, S. (1999). *The role of solar radiation in atmospheric chemistry*, pages 1–26. Springer.

Mahajan, A. S., Gómez Martín, J. C., Hay, T. D., Royer, S.-J., Yvon-Lewis, S., Liu, Y., Hu, L., Prados-Roman, C., Ordóñez, C., Plane, J. M. C., and Saiz-Lopez, A. (2012). Latitudinal distribution of reactive iodine in the Eastern Pacific and its link to open ocean sources. *Atmospheric Chemistry and Physics*, 12(23):11609–11617.

Mahajan, A. S., Whalley, L. K., Kozlova, E., Oetjen, H., Mendez, L., Furneaux, K. L., Goddard, A., Heard, D. E., Plane, J. M., and Saiz-Lopez, A. (2010). DOAS observations of formaldehyde and its impact on the HO_x balance in the tropical Atlantic marine boundary layer. *Journal of Atmospheric Chemistry*, 66(3):167.

Marais, E. A., Jacob, D. J., Jimenez, J. L., Campuzano-Jost, P., Day, D. A., Hu, W., Krechmer, J., Zhu, L., Kim, P. S., Miller, C. C., Fisher, J. A., Travis, K., Yu, K., Hanisco, T. F., Wolfe, G. M., Arkinson, H. L., Pye, H. O. T., Froyd, K. D., Liao, J., and McNeill, V. F. (2016). Aqueous-phase mechanism for secondary organic aerosol formation from isoprene: application to the southeast united states and co-benefit of SO_2 emission controls. *Atmospheric Chemistry and Physics*, 16(3):1603–1618.

Martin, R. V., Fiore, A. M., and Van Donkelaar, A. (2004). Space-based diagnosis of surface ozone sensitivity to anthropogenic emissions. *Geophysical Research Letters*, 31(6).

Meller, R. and Moortgat, G. K. (2000). Temperature dependence of the absorption cross

sections of formaldehyde between 223 and 323 K in the wavelength range 225–375 nm. *Journal of Geophysical Research: Atmospheres*, 105(D6):7089–7101.

Meszaros, E. (1999). *Fundamentals of Atmospheric Aerosol Chemistry*. Akademiai Kiado, Budapest.

Meusel, H., Kuhn, U., Reiffs, A., Mallik, C., Harder, H., Martinez, M., Schuladen, J., Bohn, B., Parchatka, U., and Crowley, J. N. (2016). Daytime formation of nitrous acid at a coastal remote site in Cyprus indicating a common ground source of atmospheric HONO and NO. *Atmospheric Chemistry and Physics*, 16(22):14475–14493.

Meusel, H., Tamm, A., Kuhn, U., Wu, D., Leifke, A. L., Fiedler, S., Ruckteschler, N., Yordanova, P., Lang-Yona, N., and Pöhlker, M. (2018). Emission of nitrous acid from soil and biological soil crusts represents an important source of HONO in the remote atmosphere in Cyprus. *Atmospheric Chemistry and Physics*, 18(2):799–813.

Michoud, V., Colomb, A., Borbon, A., Miet, K., Beekmann, M., Camredon, M., Aumont, B., Perrier, S., Zapf, P., and Siour, G. (2014). Study of the unknown HONO daytime source at a European suburban site during the MEGAPOLI summer and winter field campaigns. *Atmospheric Chemistry and Physics*, 14(6):2805–2822.

Mishra, R. K., Shukla, A., Parida, M., and Pandey, G. (2016). Urban roadside monitoring and prediction of CO, NO_2 and SO_2 dispersion from on-road vehicles in megacity Delhi. *Transportation Research Part D: Transport and Environment*, 46:157–165.

Molina, M. J. and Rowland, F. S. (1974). Stratospheric sink for chlorofluoromethanes: chlorine atomcatalysed destruction of ozone. *Nature*, 249(5460):810–812.

Neuman, J., Trainer, M., Brown, S., Min, K., Nowak, J., Parrish, D., Peischl, J., Pollack, I., Roberts, J., and Ryerson, T. (2016). HONO emission and production determined from airborne measurements over the Southeast US. *Journal of Geophysical Research: Atmospheres*, 121(15):9237–9250.

Organisation for Economic Co-operation and Development (2016). *Emissions of air pollutants*. Accessed: 26.02.2020.

Ortega, I., Berg, L. K., Ferrare, R. A., Hair, J. W., Hostetler, C. A., and Volkamer, R. (2016). Elevated aerosol layers modify the O2–O2 absorption measured by ground-based MAX-DOAS. *Journal of Quantitative Spectroscopy and Radiative Transfer*, 176:34–49.

Oswald, R., Behrendt, T., Ermel, M., Wu, D., Su, H., Cheng, Y., Breuninger, C., Moravek, A., Mougin, E., and Delon, C. (2013). HONO emissions from soil bacteria as a major source of atmospheric reactive nitrogen. *Science*, 341(6151):1233–1235.

Palmer, P. I., Abbot, D. S., Fu, T.-M., Jacob, D. J., Chance, K., Kurosu, T. P., Guenther, A., Wiedinmyer, C., Stanton, J. C., Pilling, M. J., Pressley, S. N., Lamb, B., and Sumner, A. L. (2006). Quantifying the seasonal and interannual variability of

North American isoprene emissions using satellite observations of the formaldehyde column. *Journal of Geophysical Research: Atmospheres*, 111(D12).

Parker, R., Boesch, H., Cogan, A., Fraser, A., Feng, L., Palmer, P. I., Messerschmidt, J., Deutscher, N., Griffith, D. W. T., Notholt, J., Wennberg, P. O., and Wunch, D. (2011). Methane observations from the Greenhouse Gases Observing SATellite: Comparison to ground-based TCCON data and model calculations. *Geophysical Research Letters*, 38(15).

Paton-Walsh, C., Emmons, L., and Wilson, S. R. (2010). Estimated total emissions of trace gases from the Canberra Wildfires of 2003: a new method using satellite measurements of aerosol optical depth & the MOZART chemical transport model. *Atmospheric Chemistry and Physics*, 10(12):5739–5748.

Paton-Walsh, C., Jones, N., Wilson, S., Meier, A., Deutscher, N., Griffith, D., Mitchell, R., and Campbell, S. (2004). Trace gas emissions from biomass burning inferred from aerosol optical depth. *Geophysical Research Letters*, 31(5).

Paton-Walsh, C., Jones, N. B., Wilson, S. R., Haverd, V., Meier, A., Griffith, D. W., and Rinsland, C. P. (2005). Measurements of trace gas emissions from Australian forest fires and correlations with coincident measurements of aerosol optical depth. *Journal of Geophysical Research: Atmospheres*, 110(D24).

Pearce, J. L., Beringer, J., Nicholls, N., Hyndman, R. J., Uotila, P., and Tapper, N. J. (2011). Investigating the influence of synoptic-scale meteorology on air quality using self-organizing maps and generalized additive modelling. *Atmospheric Environment*, 45(1):128–136.

Peters, E., Wittrock, F., Großmann, K., Frieß, U., Richter, A., and Burrows, J. (2012). Formaldehyde and nitrogen dioxide over the remote western Pacific Ocean: SCIAMACHY and GOME-2 validation using ship-based MAX-DOAS observations. *Atmospheric Chemistry and Physics*, 12(22):11179–11197.

Pfister, G., Emmons, L., Hess, P., Lamarque, J., Orlando, J., Walters, S., Guenther, A., Palmer, P., and Lawrence, P. (2008). Contribution of isoprene to chemical budgets: A model tracer study with the NCAR CTM MOZART-4. *Journal of Geophysical Research: Atmospheres*, 113(D5).

Pinardi, G., Van Roozendael, M., Abuhassan, N., Adams, C., Cede, A., Clémer, K., Fayt, C., Frieß, U., Gil, M., and Herman, J. (2013). MAX-DOAS formaldehyde slant column measurements during CINDI: intercomparison and analysis improvement. *Atmospheric Measurement Techniques*, 6(1):167–185.

Pinto, J., Dibb, J., Lee, B., Rappengluck, B., Wood, E., Levy, M., Zhang, R.-Y., Lefer, B., Ren, X.-R., and Stutz, J. (2014). Intercomparison of field measurements of nitrous acid (HONO) during the SHARP campaign. *Journal of Geophysical Research: Atmospheres*, 119(9):5583–5601.

Platt, U. and Stutz, J. (2008). *Differential Optical Absorption Spectroscopy*. Springer-Verlag Berlin Heidelberg, Berlin.

Polyansky, O. L., Kyuberis, A. A., Zobov, N. F., Tennyson, J., Yurchenko, S. N., and Lodi, L. (2018). ExoMol molecular line lists XXX: a complete high-accuracy line list for water. *Monthly Notices of the Royal Astronomical Society*, 480(2):2597–2608.

Prinn, R. G. (2003). The cleansing capacity of the atmosphere. *Annual Review of Environment and Resources*, 28(1):29–57.

Prinn, R. G., Huang, J., Weiss, R. F., Cunnold, D. M., Fraser, P. J., Simmonds, P. G., McCulloch, A., Harth, C., Salameh, P., O'Doherty, S., Wang, R. H. J., Porter, L., and Miller, B. R. (2001). Evidence for Substantial Variations of Atmospheric Hydroxyl Radicals in the Past Two Decades. *Science*, 292(5523):1882–1888.

Pugh, T. A. M., Cain, M., Methven, J., Wild, O., Arnold, S. R., Real, E., Law, K. S., Emmerson, K. M., Owen, S. M., Pyle, J. A., Hewitt, C. N., and MacKenzie, A. R. (2012). A Lagrangian model of air-mass photochemistry and mixing using a trajectory ensemble: the Cambridge Tropospheric Trajectory model of Chemistry And Transport (CiTTyCAT) version 4.2. *Geoscientific Model Development*, 5(1):193–221.

Pusede, S. E., VandenBoer, T. C., Murphy, J. G., Markovic, M. Z., Young, C. J., Veres, P. R., Roberts, J. M., Washenfelder, R. A., Brown, S. S., and Ren, X. (2015). An atmospheric constraint on the NO_2 dependence of daytime near-surface nitrous acid (HONO). *Environmental Science & Technology*, 49(21):12774–12781.

Qin, M., Xie, P., Su, H., Gu, J., Peng, F., Li, S., Zeng, L., Liu, J., Liu, W., and Zhang, Y. (2009). An observational study of the HONO–NO_2 coupling at an urban site in Guangzhou City, South China. *Atmospheric Environment*, 43(36):5731–5742.

Qin, Y. and Mitchell, R. (2009). Characterisation of episodic aerosol types over the Australian continent. *Atmospheric Chemistry and Physics*, 9(6):1943–1956.

Read, K. A., Mahajan, A. S., Carpenter, L. J., Evans, M. J., Faria, B. V. E., Heard, D. E., Hopkins, J. R., Lee, J. D., Moller, S. J., Lewis, A. C., Mendes, L., McQuaid, J. B., Oetjen, H., Saiz-Lopez, A., Pilling, M. J., and Plane, J. M. C. (2008). Extensive halogen-mediated ozone destruction over the tropical Atlantic Ocean. *Nature*, 453(7199):1232–1235.

Ren, X., Harder, H., Martinez, M., Lesher, R. L., Oliger, A., Simpas, J. B., Brune, W. H., Schwab, J. J., Demerjian, K. L., and He, Y. (2003). OH and HO_2 chemistry in the urban atmosphere of New York City. *Atmospheric Environment*, 37(26):3639–3651.

Rodgers, C. D. (1990). Characterization and error analysis of profiles retrieved from remote sounding measurements. *Journal of Geophysical Research: Atmospheres*, 95(D5):5587–5595.

Rodgers, C. D. (2000). *Inverse methods for atmospheric sounding: theory and practice*, volume 2. World Scientific.

Rodgers, C. D. and Connor, B. J. (2003). Intercomparison of remote sounding instruments. *Journal of Geophysical Research: Atmospheres*, 108(D3).

Roscoe, H. K., Van Roozendael, M., Fayt, C., du Piesanie, A., Abuhassan, N., Adams, C., Akrami, M., Cede, A., Chong, J., Clémer, K., Frieß, U., Gil Ojeda, M., Goutail, F., Graves, R., Griesfeller, A., Grossmann, K., Hemerijckx, G., Hendrick, F., Herman, J., Hermans, C., Irie, H., Johnston, P. V., Kanaya, Y., Kreher, K., Leigh, R., Merlaud, A., Mount, G. H., Navarro, M., Oetjen, H., Pazmino, A., Perez-Camacho, M., Peters, E., Pinardi, G., Puentedura, O., Richter, A., Schönhardt, A., Shaiganfar, R., Spinei, E., Strong, K., Takashima, H., Vlemmix, T., Vrekoussis, M., Wagner, T., Wittrock, F., Yela, M., Yilmaz, S., Boersma, F., Hains, J., Kroon, M., Piters, A., and Kim, Y. J. (2010). Intercomparison of slant column measurements of NO_2 and O_4 by MAX-DOAS and zenith-sky UV and visible spectrometers. *Atmospheric Measurement Techniques*, 3(6):1629–1646.

Rothman, L., Gordon, I., Barber, R., Dothe, H., Gamache, R., Goldman, A., Perevalov, V., Tashkun, S., and Tennyson, J. (2010). HITEMP, the high-temperature molecular spectroscopic database. *Journal of Quantitative Spectroscopy and Radiative Transfer*, 111(15):2139–2150.

Rothman, L., Gordon, I. E., Barbe, A., Benner, D. C., Bernath, P. F., Birk, M., Boudon, V., Brown, L. R., Campargue, A., Champion, J.-P., Chance, K., Coudert, L., Dana, V., Devi, V., Fally, S., Flaud, J.-M., Gamache, R., Goldman, A., Jacquemart, D., Kleiner, I., Lacome, N., Lafferty, W., Mandin, J., Massie, S., Mikhailenko, S., Miller, C., Moazzen-Ahmadi, N., Naumenko, O., Nikitin, A., Orphal, J., Perevalov, V., Perrin, A., Predoi-Cross, A., Rinsland, C., Rotger, M., Šimečková, M., Smith, M., Sung, K., Tashkun, S., Tennyson, J., Toth, R., Vandaele, A., and Vander Auwera, J. (2009). The HITRAN 2008 molecular spectroscopic database. *Journal of Quantitative Spectroscopy and Radiative Transfer*, 110(9-10):533–572.

Rozanov, V., Buchwitz, M., Eichmann, K.-U., De Beek, R., and Burrows, J. (2002). SCIATRAN-a new radiative transfer model for geophysical applications in the 240–2400 nm spectral region: The pseudo-spherical version. *Advances in Space Research*, 29(11):1831–1835.

Rozanov, V., Rozanov, A., Kokhanovsky, A., and Burrows, J. (2014). Radiative transfer through terrestrial atmosphere and ocean: Software package SCIATRAN. *Journal of Quantitative Spectroscopy and Radiative Transfer*, 133:13 – 71.

Ryan, R. G., Rhodes, S., Tully, M., Wilson, S., Jones, N., Frieß, U., and Schofield, R. (2018). Daytime HONO, NO_2 and aerosol distributions from MAX-DOAS observations in Melbourne. *Atmospheric Chemistry and Physics*, 18(19):13969–13985.

Saiz-Lopez, A., Plane, J. M., Baker, A. R., Carpenter, L. J., von Glasow, R.,

Gomez Martin, J. C., McFiggans, G., and Saunders, R. W. (2012). Atmospheric chemistry of iodine. *Chemical Reviews*, 112(3):1773–1804.

Saiz-Lopez, A. and von Glasow, R. (2012). Reactive halogen chemistry in the troposphere. *Chemical Society Reviews*, 41(19):6448–6472.

Samoli, E., Aga, E., Touloumi, G., Nisiotis, K., Forsberg, B., Lefranc, A., Pekkanen, J., Wojtyniak, B., Schindler, C., Niciu, E., Brunstein, R., Dodic Fikfak, M., Schwartz, J., and Katsouyanni, K. (2006). Short-term effects of nitrogen dioxide on mortality: an analysis within the APHEA project. *European Respiratory Journal*, 27(6):1129–1138.

Sander, R. (2015). Compilation of henry's law constants (version 4.0) for water as solvent. *Atmospheric Chemistry and Physics*, 15(8):4399–4981.

Sander, R., Keene, W., Pszenny, A., Arimoto, R., Ayers, G., Baboukas, E., Cainey, J., Crutzen, P., Duce, R., and Hönninger, G. (2003). Inorganic bromine in the marine boundary layer: a critical review. *Atmospheric Chemistry and Physics*, 3(5):1301–1336.

Sander, S., Golden, D., Kurylo, M., Moortgat, G., Wine, P., Ravishankara, A., Kolb, C., Molina, M., Finlayson-Pitts, B., and Huie, R. (2006). Chemical kinetics and photochemical data for use in atmospheric studies evaluation number 15. Technical report, Jet Propulsion Laboratory, National Aeronautics and Space Administration.

Serdyuchenko, A., Gorshelev, V., Weber, M., Chehade, W., and Burrows, J. (2014). High spectral resolution ozone absorption cross-sections. *Atmospheric Measurement Techniques*, 7(2):1867–8548.

Shang, J., Xu, W. W., Ye, C. X., George, C., and Zhu, T. (2017). Synergistic effect of nitrate-doped tio 2 aerosols on the fast photochemical oxidation of formaldehyde. *Scientific reports*, 7(1):1–9.

Shaw, S. L., Gantt, B., and Meskhidze, N. (2010). Production and emissions of marine isoprene and monoterpenes: a review. *Advances in Meteorology*, 2010.

Shepherd, T., Plummer, D., Scinocca, J., Hegglin, M., Fioletov, V., Reader, M., Remsberg, E., Von Clarmann, T., and Wang, H. (2014). Reconciliation of halogen-induced ozone loss with the total-column ozone record. *Nature Geoscience*, 7(6):443–449.

Shi, Q., Zhang, W., Ji, Y., Wang, J., Qin, D., Chen, J., Gao, Y., Li, G., and An, T. (2020). Enhanced uptake of glyoxal at the acidic nanoparticle interface: implications for secondary organic aerosol formation. *Environmental Science: Nano*, 7(4):1126–1135.

Sillman, S. (1995). The use of NO_y, H_2O_2, and HNO_3 as indicators for ozone-NO_x-hydrocarbon sensitivity in urban locations. *Journal of Geophysical Research: Atmospheres*, 100(D7):14175–14188.

Sillman, S., Logan, J. A., and Wofsy, S. C. (1990). The sensitivity of ozone to nitrogen oxides and hydrocarbons in regional ozone episodes. *Journal of Geophysical Research: Atmospheres*, 95(D2):1837–1851.

Simpson, R., Denison, L., Petroeschevsky, A., Thalib, L., and Williams, G. (2000). Effects of ambient particle pollution on daily mortality in Melbourne, 1991-1996. *Journal of Exposure Science and Environmental Epidemiology*, 10(5):1559–0631.

Simpson, R., Williams, G., Petroeschevsky, A., Best, T., Morgan, G., Denison, L., Hinwood, A., Neville, G., and Neller, A. (2005). The short term effects of air pollution on daily mortality in four Australian cities. *Australian and New Zealand Journal of Public Health*, 29(3):205–212.

Simpson, W., von Glasow, R., Riedel, K., Anderson, P., Ariya, P., Bottenheim, J., Burrows, J., Carpenter, L., Frieß, U., Goodsite, M., Heard, D., Hutterli, M., Jacobi, H.-W., Kaleschke, L., Neff, B., Plane, J., Platt, U., Richter, A., Roscoe, H., Sander, R., Shepson, P., Sodeau, J., Steffen, A., Wagner, T., and Wolff, E. (2007). Halogens and their role in polar boundary-layer ozone depletion. *Atmospheric Chemistry and Physics*, 4375.

Sinreich, R., Coburn, S., Dix, B., and Volkamer, R. (2010). Ship-based detection of glyoxal over the remote tropical Pacific Ocean. *Atmospheric Chemistry and Physics*, 10(23):11359–11371.

Souri, A. H., Nowlan, C. R., Wolfe, G. M., Lamsal, L. N., Miller], C. E. C., Abad, G. G., Janz, S. J., Fried, A., Blake, D. R., Weinheimer, A. J., Diskin, G. S., Liu, X., and Chance, K. (2020). Revisiting the effectiveness of HCHO/NO_2 ratios for inferring ozone sensitivity to its precursors using high resolution airborne remote sensing observations in a high ozone episode during the KORUS-AQ campaign. *Atmospheric Environment*, 224:117341.

Spietz, P., Martín, J. C. G., and Burrows, J. P. (2005). Spectroscopic studies of the I_2/O_3 photochemistry: Part 2. Improved spectra of iodine oxides and analysis of the IO absorption spectrum. *Journal of Photochemistry and Photobiology A: Chemistry*, 176(1):50–67.

Spinei, E., Cede, A., Herman, J., Mount, G. H., Eloranta, E., Morley, B., Baidar, S., Dix, B., Ortega, I., Koenig, T., and Volkamer, R. (2015). Ground-based direct-sun DOAS and airborne MAX-DOAS measurements of the collision-induced oxygen complex, O_2-O_2, absorption with significant pressure and temperature differences. *Atmospheric Measurement Techniques*, 8(2):793–809.

Stemmler, K., Ammann, M., Donders, C., Kleffmann, J., and George, C. (2006). Photosensitized reduction of nitrogen dioxide on humic acid as a source of nitrous acid. *Nature*, 440(7081):195.

Stutz, J., Kim, E., Platt, U., Bruno, P., Perrino, C., and Febo, A. (2000). UV visible

absorption cross sections of nitrous acid. *Journal of Geophysical Research: Atmospheres*, 105(D11):14585–14592.

Su, H., Cheng, Y., Oswald, R., Behrendt, T., Trebs, I., Meixner, F. X., Andreae, M. O., Cheng, P., Zhang, Y., and Pöschl, U. (2011). Soil nitrite as a source of atmospheric HONO and OH radicals. *Science*, 333(6049):1616–1618.

Tao, Y., Huang, W., Huang, X., Zhong, L., Lu, S.-E., Li, Y., Dai, L., Zhang, Y., and Zhu, T. (2011). Estimated acute effects of ambient ozone and nitrogen dioxide on mortality in the Pearl River Delta of southern China. *Environmental Health Perspectives*, 120(3):393–398.

Thalman, R. and Volkamer, R. (2013). Temperature dependent absorption cross-sections of O_2-O_2 collision pairs between 340 and 630 nm and at atmospherically relevant pressure. *Physical Chemistry Chemical Physics*, 15(37):15371–15381.

Thomas, W., Hegels, E., Slijkhuis, S., Spurr, R., and Chance, K. (1998). Detection of biomass burning combustion products in Southeast Asia from backscatter data taken by the GOME spectrometer. *Geophysical Research Letters*, 25(9):1317–1320.

Thomason, L., Poole, L., and Deshler, T. (1997). A global climatology of stratospheric aerosol surface area density deduced from Stratospheric Aerosol and Gas Experiment II measurements: 1984–1994. *Journal of Geophysical Research: Atmospheres*, 102(D7):8967–8976.

Tian, X., Xie, P., Xu, J., Li, A., Wang, Y., Qin, M., and Hu, Z. (2018). Long-term observations of tropospheric NO_2, SO_2 and HCHO by MAX-DOAS in Yangtze River Delta area, China. *Journal of Environmental Sciences*, 71:207–221.

Trewin, B. (2012). Techniques involved in developing the Australian Climate Observations Reference. *Extremes*, 19:14–9.

Utembe, S. (2019). personal communication.

Utembe, S., Rayner, P., Silver, J., Guérette, E.-A., Fisher, J., Emmerson, K., Cope, M., Paton-Walsh, C., Griffiths, A., Duc, H., Monk, K., and Scorgie, Y. (2018). Hot summers: Effect of extreme temperatures on ozone in Sydney, Australia. *Atmosphere*, 9(12):466.

van Deelen, R. (2007). *Rotational Raman scattering in the Earth's atmosphere*. PhD thesis, Vrije Universiteit.

Van Der A, R., Eskes, H., Boersma, K., Van Noije, T., Van Roozendael, M., De Smedt, I., Peters, D., and Meijer, E. (2008). Trends, seasonal variability and dominant NOx source derived from a ten year record of NO_2 measured from space. *Journal of Geophysical Research: Atmospheres*, 113(D4).

Vandaele, A. C., Hermans, C., Simon, P. C., Carleer, M., Colin, R., Fally, S., Merienne, M.-F., Jenouvrier, A., and Coquart, B. (1998). Measurements of the NO_2 absorption

cross section from 42000 cm^{-1} to 10000 cm^{-1} (238–1000 nm) at 220 K and 294 K. *Journal of Quantitative Spectroscopy and Radiative Transfer*, 59(3-5):171–184.

Veefkind, J., Aben, I., McMullan, K., Förster, H., De Vries, J., Otter, G., Claas, J., Eskes, H., De Haan, J., Kleipool, Q., van Weele, M., Hasekamp, O., Hoogeveen, R., Landgraf, J., Snel, R., Tol, P., Ingmann, P., Voors, R., Kruizinga, R., Vink, R., Visser, H., and Levelt, P. F. (2012). TROPOMI on the ESA Sentinel-5 Precursor: A GMES mission for global observations of the atmospheric composition for climate, air quality and ozone layer applications. *Remote Sensing of Environment*, 120:70–83.

Vigouroux, C., Hendrick, F., Stavrakou, T., Dils, B., De Smedt, I., Hermans, C., Merlaud, A., Scolas, F., Senten, C., Vanhaelewyn, G., Fally, S., Carleer, M., Metzger, J.-M., Müller, J.-F., Van Roozendael, M., and De Mazière, M. (2009). Ground-based FTIR and MAX-DOAS observations of formaldehyde at Reunion Island and comparisons with satellite and model data. *Atmospheric Chemistry and Physics*, 9(24):9523–9544.

Vlasenko, A., Macdonald, A. M., Sjostedt, S. J., and Abbatt, J. P. D. (2010). Formaldehyde measurements by Proton transfer reaction – Mass Spectrometry (PTR-MS): correction for humidity effects. *Atmospheric Measurement Techniques*, 3(4):1055–1062.

Vlemmix, T., Hendrick, F., Pinardi, G., De Smedt, I., Fayt, C., Hermans, C., Piters, A., Wang, P., Levelt, P., and Van Roozendael, M. (2015). MAX-DOAS observations of aerosols, formaldehyde and nitrogen dioxide in the Beijing area: comparison of two profile retrieval approaches. *Atmospheric Measurement Techniques*, 8(2):941–963.

Vlemmix, T., Piters, A., Berkhout, A., Gast, L., Wang, P., and Levelt, P. (2011). Ability of the MAX-DOAS method to derive profile information for NO_2: can the boundary layer and free troposphere be separated? *Atmospheric Measurement Techniques*, 4(12):2659–2684.

Vogel, L., Sihler, H., Lampel, J., Wagner, T., and Platt, U. (2013). Retrieval interval mapping: a tool to visualize the impact of the spectral retrieval range on differential optical absorption spectroscopy evaluations. *Atmospheric Measurement Techniques*, 6(2):275–299.

Vogt, R., Sander, R., Von Glasow, R., and Crutzen, P. J. (1999). Iodine chemistry and its role in halogen activation and ozone loss in the marine boundary layer: A model study. *Journal of Atmospheric Chemistry*, 32(3):375–395.

Volkamer, R., San Martini, F., Molina, L. T., Salcedo, D., Jimenez, J. L., and Molina, M. J. (2007). A missing sink for gas-phase glyoxal in mexico city: Formation of secondary organic aerosol. *Geophysical Research Letters*, 34(19).

Volkamer, R., Spietz, P., Burrows, J., and Platt, U. (2005). High-resolution absorption

cross-section of glyoxal in the UV–vis and IR spectral ranges. *Journal of Photochemistry and Photobiology A: Chemistry*, 172(1):35–46.

Vountas, M., Rozanov, V. V., and Burrows, J. P. (1998). Ring effect: impact of rotational Raman scattering on radiative transfer in earth's atmosphere. *Journal of Quantitative Spectroscopy and Radiative Transfer*, 60(6):943–961.

Vrekoussis, M., Wittrock, F., Richter, A., and Burrows, J. (2010). GOME-2 observations of oxygenated VOCs: what can we learn from the ratio glyoxal to formaldehyde on a global scale? *Atmospheric Chemistry and Physics*, 10(21):10145–10160.

Wagner, T., Apituley, A., Beirle, S., Dörner, S., Frieß, U., Remmers, J., and Shaiganfar, R. (2014). Cloud detection and classification based on MAX-DOAS observations. *Atmospheric Measurement Techniques*, 7(5):1289–1320.

Wagner, T., Beirle, S., and Deutschmann, T. (2009). Three-dimensional simulation of the Ring effect in observations of scattered sun light using Monte Carlo radiative transfer models. *Atmospheric Measurement Techniques*, 2(1):113–124.

Wagner, T., Beirle, S., Remmers, J., Shaiganfar, R., and Wang, Y. (2016). Absolute calibration of the colour index and O_4 absorption derived from Multi AXis (MAX-)DOAS measurements and their application to a standardised cloud classification algorithm. *Atmospheric Measurement Techniques*, 9(9):4803–4823.

Wagner, T., Dix, B., Friedeburg, C. v., Frieß, U., Sanghavi, S., Sinreich, R., and Platt, U. (2004). MAX-DOAS O4 measurements: A new technique to derive information on atmospheric aerosols—Principles and information content. *Journal of Geophysical Research: Atmospheres*, 109(D22).

Wang, C., Huang, X.-F., Han, Y., Zhu, B., and He, L.-Y. (2017a). Sources and potential photochemical roles of formaldehyde in an urban atmosphere in south china. *Journal of Geophysical Research: Atmospheres*, 122(21):11–934.

Wang, S., Cuevas, C. A., Frieß, U., and Saiz-Lopez, A. (2016). MAX-DOAS retrieval of aerosol extinction properties in Madrid, Spain. *Atmospheric Measurement Techniques*, 9(10):5089–5101.

Wang, S., Zhou, R., Zhao, H., Wang, Z., Chen, L., and Zhou, B. (2013). Long-term observation of atmospheric nitrous acid (HONO) and its implication to local NO_2 levels in Shanghai, China. *Atmospheric Environment*, 77:718–724.

Wang, Y., Beirle, S., Hendrick, F., Hilboll, A., Jin, J., Kyuberis, A. A., Lampel, J., Ang, L., Luo, Y., and Lodi, L. (2017b). MAX-DOAS measurements of HONO slant column densities during the MAD-CAT campaign: inter-comparison, sensitivity studies on spectral analysis settings, and error budget. *Atmospheric Measurement Techniques*, 10(10):1867–8548.

Wang, Y., Beirle, S., Hendrick, F., Hilboll, A., Jin, J., Kyuberis, A. A., Lampel, J., Li,

A., Luo, Y., Lodi, L., Ma, J., Navarro, M., Ortega, I., Peters, E., Polyansky, O. L., Remmers, J., Richter, A., Puentedura, O., Van Roozendael, M., Seyler, A., Tennyson, J., Volkamer, R., Xie, P., Zobov, N. F., and Wagner, T. (2017c). MAX-DOAS measurements of HONO slant column densities during the MAD-CAT campaign: inter-comparison, sensitivity studies on spectral analysis settings, and error budget. *Atmospheric Measurement Techniques*, 10(10):3719–3742.

Wang, Y., Beirle, S., Lampel, J., Koukouli, M., De Smedt, I., Theys, N., Li, A., Wu, D., Xie, P., Liu, C., Van Roozendael, M., Stavrakou, T., Müller, J.-F., and Wagner, T. (2017d). Validation of OMI, GOME-2A and GOME-2B tropospheric NO_2, SO_2 and HCHO products using MAX-DOAS observations from 2011 to 2014 in Wuxi, China: investigation of the effects of priori profiles and aerosols on the satellite products. *Atmospheric Chemistry and Physics*, 17(8):5007–5033.

Wang, Y., Lampel, J., Xie, P., Beirle, S., Li, A., Wu, D., and Wagner, T. (2017e). Ground-based MAX-DOAS observations of tropospheric aerosols, NO_2, SO_2 and HCHO in Wuxi, China, from 2011 to 2014. *Atmospheric Chemistry and Physics*, 17(3):2189–2215.

Wang, Y., Penning de Vries, M., Xie, P. H., Beirle, S., Dörner, S., Remmers, J., Li, A., and Wagner, T. (2015). Cloud and aerosol classification for 2.5 years of MAX-DOAS observations in Wuxi (China) and comparison to independent data sets. *Atmospheric Measurement Techniques*, 8(12):5133–5156.

Webb, C. and McMillan, A. (2020). Smoke haze makes Melbourne's air quality world's worst, for a time. *The Age*.

Whiteman, D. N., Melfi, S. H., and Ferrare, R. A. (1992). Raman lidar system for the measurement of water vapor and aerosols in the Earth's atmosphere. *Applied Optics*, 31(16):3068–3082.

WHO (2006). *Air quality guidelines: global update 2005: particulate matter, ozone, nitrogen dioxide, and sulfur dioxide*. World Health Organization.

WHO (2016). *Ambient air pollution: A global assessment of exposure and burden of disease*. World Health Organization.

Winters, A. J., Adams, M. A., Bleby, T. M., Rennenberg, H., Steigner, D., Steinbrecher, R., and Kreuzwieser, J. (2009). Emissions of isoprene, monoterpene and short-chained carbonyl compounds from Eucalyptus spp. in southern Australia. *Atmospheric Environment*, 43(19):3035–3043.

Wittrock, F., Richter, A., Oetjen, H., Burrows, J. P., Kanakidou, M., Myriokefalitakis, S., Volkamer, R., Beirle, S., Platt, U., and Wagner, T. (2006). Simultaneous global observations of glyoxal and formaldehyde from space. *Geophysical Research Letters*, 33(16).

Wojtal, P., Halla, J., and McLaren, R. (2011). Pseudo steady states of HONO measured

in the nocturnal marine boundary layer: a conceptual model for HONO formation on aqueous surfaces. *Atmospheric Chemistry and Physics*, 11(7):3243–3261.

Wolfe, G. M., Kaiser, J., Hanisco, T. F., Keutsch, F. N., de Gouw, J. A., Gilman, J. B., Graus, M., Hatch, C. D., Holloway, J., Horowitz, L. W., Lee, B. H., Lerner, B. M., Lopez-Hilifiker, F., Mao, J., Marvin, M. R., Peischl, J., Pollack, I. B., Roberts, J. M., Ryerson, T. B., Thornton, J. A., Veres, P. R., and Warneke, C. (2016). Formaldehyde production from isoprene oxidation across NO_x regimes. *Atmospheric Chemistry and Physics*, 16(4):2597–2610.

Wong, K., Tsai, C., Lefer, B., Haman, C., Grossberg, N., Brune, W., Ren, X., Luke, W., and Stutz, J. (2012). Daytime HONOvertical gradients during SHARP 2009 in Houston, TX. *Atmospheric Chemistry and Physics*, 12(2):1680–7316.

Xu, Z., Wang, T., Wu, J., Xue, L., Chan, J., Zha, Q., Zhou, S., Louie, P. K., and Luk, C. W. (2015). Nitrous acid (HONO) in a polluted subtropical atmosphere: Seasonal variability, direct vehicle emissions and heterogeneous production at ground surface. *Atmospheric Environment*, 106:100–109.

Yang, Z., Cheng, H., Wang, Z., Peng, J., Zhu, J., Lyu, X., and Guo, H. (2019). Chemical characteristics of atmospheric carbonyl compounds and source identification of formaldehyde in Wuhan, Central China. *Atmospheric Research*, 228:95–106.

Yilmaz, S. (2012). *Retrieval of atmospheric aerosol and trace gas vertical profiles using multi-axis differential optical absorption spectroscopy*. PhD thesis, IUP, Heidelberg University.

Young, P., Archibald, A., Bowman, K., Lamarque, J.-F., Naik, V., Stevenson, D., Tilmes, S., Voulgarakis, A., Wild, O., and Bergmann, D. (2013). Pre-industrial to end 21st century projections of tropospheric ozone from the Atmospheric Chemistry and Climate Model Intercomparison Project (ACCMIP). *Atmospheric Chemistry and Physics*, 13(4):2063–2090.

Yuhas, Y. (2016). Nasa astronaut Scott Kelly on his year in space: 'Maybe you do go bananas'. *The Guardian*.

Zeng, G., Williams, J. E., Fisher, J. A., Emmons, L., Jones, N. B., Morgenstern, O., Robinson, J., Smale, D., Paton-Walsh, C., and Griffith, D. W. (2015). Multimodel simulation of CO and HCHO in the Southern Hemisphere: comparison with observations and impact of biogenic emissions. *Atmospheric Chemistry and Physics*, 15:7217–7245.

Zhou, X., Zhang, N., TerAvest, M., Tang, D., Hou, J., Bertman, S., Alaghmand, M., Shepson, P. B., Carroll, M. A., and Griffith, S. (2011). Nitric acid photolysis on forest canopy surface as a source for tropospheric nitrous acid. *Nature Geoscience*, 4(7):1752–0908.

Zhu, L., Jacob, D. J., Keutsch, F. N., Mickley, L. J., Scheffe, R., Strum, M.,

González Abad, G., Chance, K., Yang, K., Rappenglück, B., Millet, D. B., Baasandorj, M., Jaeglé, L., and Shah, V. (2017). Formaldehyde (HCHO) as a hazardous air pollutant: Mapping surface air concentrations from satellite and inferring cancer risks in the United States. *Environmental science & technology*, 51(10):5650–5657.

Zhu, L., Jacob, D. J., Kim, P. S., Fisher, J. A., Yu, K., Travis, K. R., Mickley, L. J., Yantosca, R. M., Sulprizio, M. P., and Smedt, I. D. (2016). Observing atmospheric formaldehyde (HCHO) from space: validation and intercomparison of six retrievals from four satellites (OMI, GOME2A, GOME2B, OMPS) with SEAC 4 RS aircraft observations over the southeast US. *Atmospheric Chemistry and Physics*, 16(21):13477–13490.

Zhu, L., Jacob, D. J., Mickley, L. J., Marais, E. A., Cohan, D. S., Yoshida, Y., Duncan, B. N., Abad, G. G., and Chance, K. V. (2014). Anthropogenic emissions of highly reactive volatile organic compounds in eastern Texas inferred from oversampling of satellite (OMI) measurements of HCHO columns. *Environmental Research Letters*, 9(11):114004.

Zhu, Y., Chan, K. L., Lam, Y. F., Horbanski, M., Pöhler, D., Boll, J., Lipkowitsch, I., Ye, S., and Wenig, M. (2018). Analysis of spatial and temporal patterns of on-road NO_2 concentrations in Hong Kong. *Atmospheric Measurement Techniques*, 11(12):6719–6734.

Zielcke, J. (2015). *Observations of reactive bromine, iodine and chlorine species in the Arctic and Antarctic with differential optical absorption spectroscopy*. PhD thesis, IUP, Heidelberg University.